VOLUME 8 ISSUE 1 FEBRUARY 2023

IJEG

International Journal of Engineering and Geosciences

e-ISSN 2548-0960

Assist. Prof. Dr. Yelda TURKAN
Oregon State University,
USA

Dr. G. Sanka N. PERERA
Sabaragamuwa University Faculty of Geomatics
Sri Lanka

Dr. Hsiu-Wen CHANG
National Cheng Kung University, Department of Geomatics
Taiwan

The International Journal of Engineering and Geosciences (IJEG)

The International Journal of Engineering and Geosciences (IJEG) is a tri-annually published journal. The journal includes a wide scope of information on scientific and technical advances in the geomatics sciences. The International Journal of Engineering and Geosciences aims to publish pure and applied research in geomatics engineering and technologies. IJEG is a double peer-reviewed (blind) OPEN ACCESS JOURNAL that publishes professional level research articles and subject reviews exclusively in English. It allows authors to submit articles online and track his or her progress via its web interface. All manuscripts will undergo a refereeing process; acceptance for publication is based on at least two positive reviews. The journal publishes research and review papers, professional communication, and technical notes. IJEG does not charge for any article submissions or for processing.

CORRESPONDENCE ADDRESS
Journal Contact: engineeringandgeoscience@gmail.com

CONTENTS

Volume 8 - Issue 1

RESEARCH ARTICLES

International Journal of Engineering and Geosciences
https://dergipark.org.tr/en/pub/ijeg
e-ISSN 2548-0960

Comparison between random forest and support vector machine algorithms for LULC classification

Cengiz Avci [*1], **Muhammed Budak**[1], **Nur Yagmur**[1], **Filiz Bektas Balcik**[1]

[1]*Istanbul Technical University, Department of Geomatics Engineering, Türkiye*

Keywords
Remote sensing
Supervised Classification
Random Forest
Support Vector Machine
Wetland

Research Article
DOI: 10.26833/ijeg.987605

Received: 26.08.2021
Accepted: 30.11.2021
Published: 13.04.2022

Abstract

Nowadays, machine learning (ML) algorithms have been widely chosen for classifying satellite images for mapping Earth's surface. Support Vector Machine (SVM) and Random Forest (RF) stand out among these algorithms with their accurate results in the literature. The aim of this study is to analyze the performances of these algorithms on land use and land cover (LULC) classification, especially wetlands which have significant ecological functions. For this purpose, Sentinel-2 satellite image, which is freely provided by European Space Agency (ESA), was used to monitor not only the open surface water body but also around Marmara Lake. The performance evaluation was made with the increasing number of the training dataset. 3 different training datasets having 10, 15, and 20 areas of interest (AOI) per class, respectively were used for the classification of the satellite images acquired in 2015 and 2020. The most accurate results were obtained from the classification with RF algorithm and 20 AOIs. According to obtained results, the change detection analysis of Marmara Lake was investigated for possible reasons. Whereas the water body and wetland have decreased more than 50% between 2015 and 2020, crop sites have increased approximately 50%.

1. Introduction

In remote sensing, land use and land cover (LULC) maps are hugely demanded for land management and monitoring of natural resources such as wetlands, forest areas, grasslands [1]. The most significant way to produce LULC maps is to classify remotely sensed images using a variety of classification algorithms [2]. LULC maps, which are used in different fields such as agricultural tracking and city planning, are extremely important in sustainable monitoring and analyzing different ecosystems [3-4]. For the long-term change analysis generally, Landsat satellite images have been used because of providing free satellite images since the 1970s [5]. However, Sentinel-2 MSI satellite images have gained importance in the short-term change analysis [6]. With having 13 spectral band capacity, high spatial resolution between 10-60 meters, and having free access on a global scale, Sentinel-2 MSI provides a great advantage for researchers.

Many different classification methods have been developed and conducted such as unsupervised and supervised classification methods. With the development of machine learning (ML) algorithms, the accuracy and usage of classification methods have been increased. There are multiple ML algorithms used for the LULC classification, but random forest (RF) and support vector machine (SVM) algorithms have become prominent in the last years and have been widely used for that purpose [7-8]. These methods provide superior performance compared to traditional methods, especially in remote sensing applications [9]. However, these algorithms do not give the same results with different satellite data. The quality, number, and distribution of the training and test data sets have huge importance for the performance of the selected algorithm. It is important to compare applications to measure the performance of these algorithms based on the number of training and test points.

Google Earth Engine (GEE) has gained popularity in recent years. GEE makes geospatial analysis easy, enables processing satellite images using mathematical operations and many classification algorithms implemented. GEE provides to make global scale [10] and

* **Corresponding Author**

*(avcice16@itu.edu.tr) ORCID ID 0000-0002-6515-1059
(budakm16@itu.edu.tr) ORCID ID 0000-0003-4493-9936
(yagmurn@itu.edu.tr) ORCID ID 0000-0002-5915-6929
(bektasfi@itu.edu.tr) ORCID ID 0000-0003-3039-6846

Cite this article

Avcı, C. Budak, M. Yagmur, N., & Balcık, F. B. (2023). Comparison between random forest and support vector machine algorithms for LULC classification. International Journal of Engineering and Geosciences, 8(1), 01-10

local scale [11] water bodies and wetland analysis. Wang et al. [12] analyzed long-term surface water dynamics of the Yangtze River Basin using RF classification algorithm via GEE and Amani et al. [13] used GEE to create the wetland inventory of Canada by applying RF algorithm to satellite images.

The main objective of the study is the investigate the performance of machine learning algorithms in LULC classification of wetland by increasing the amount of the training dataset. For this purpose, RF and SVM algorithms were selected and applied to Sentinel-2 satellite images via the GEE platform. In the study, Marmara Lake, which is considered as one of the Nationally Important Wetlands in Turkey, was examined between the years of 2015 and 2020 as a test site and spatio-temporal analysis of the lake and its surroundings was investigated with the most accurate classification algorithm for short term change analysis.

2. Study area

In the study, classification performance analysis and LULC change analysis were applied on Marmara Lake. Marmara Lake is located in the Aegean Region, within the borders of Manisa province, between Salihli, Gölmarmara, and Ahmetli districts. Its depth is 3-4 m, and its altitude is 74 m. The lake, which was included in the wetland category according to the Regulation on the Conservation of Wetlands published in 2002, became a Nationally Important Wetland in 2017. Marmara Lake, which is economically important for the local community with fishing and tourism activities, has 162 bird species, 32 mammal species, and 355 different plant species in its ecosystem according to the report prepared in 2017 [14].

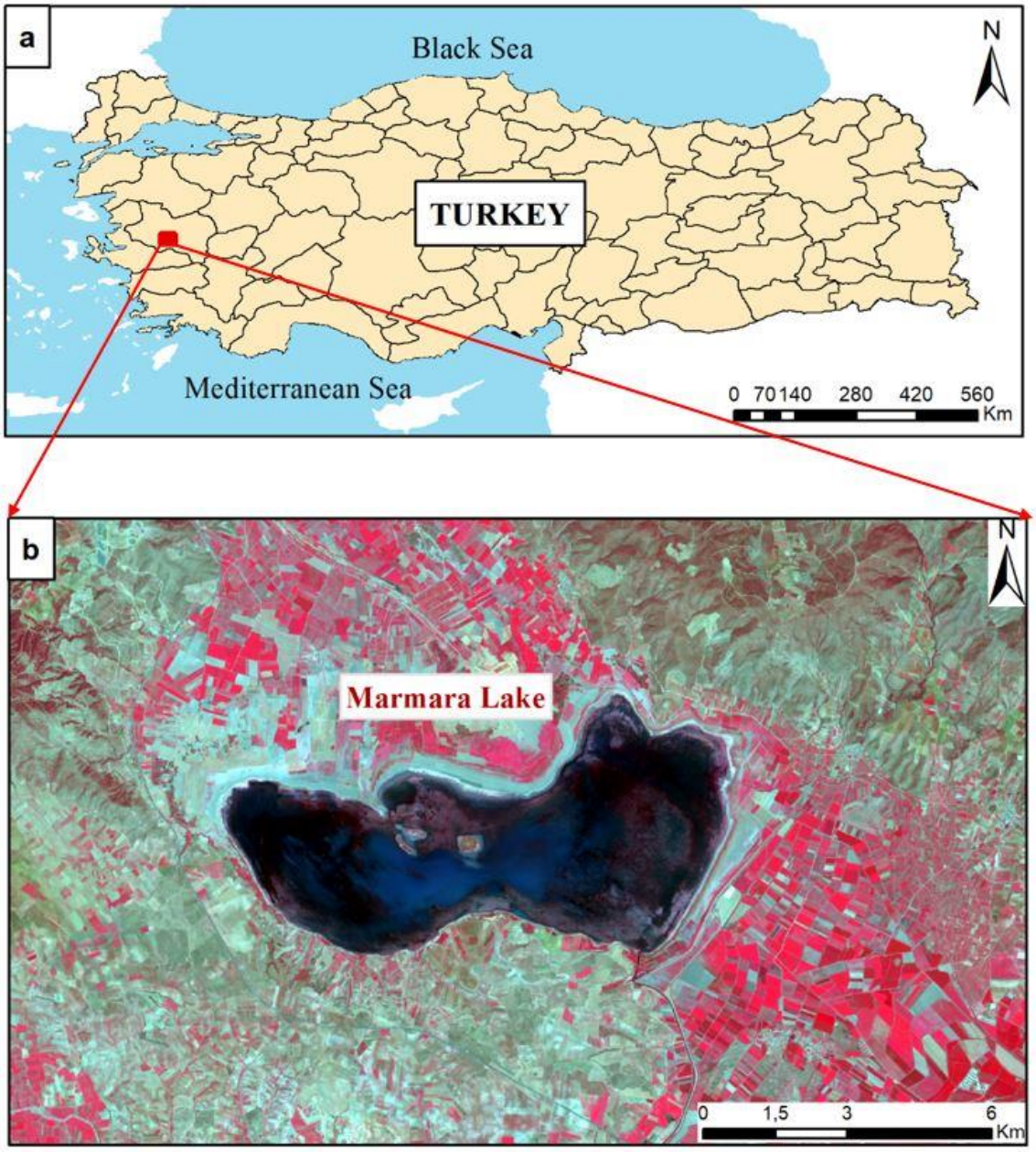

Figure 1. Study area

3. Dataset

Sentinel-2 MSI satellite images were used in the study for 2015 and 2020 years. It is freely available data and provides images since 2015. The Sentinel-2A satellite is a multispectral image with a medium spatial resolution developed by ESA. It has 13 spectral bands and the spatial resolution of them varies between 10 to 60 m. It also provides atmospherically corrected images. The detailed information is given in Table 1. In this study, satellite images acquired in the summer months were selected to use cloud-free images.

Table 1. Sentinel-2A MSI Information

Data	Sentinel-2A MSI
Spatial Resolution	B2-4, B8: 10 m B5-7, B8A, B11-12: 20 m B1, B9: 60 m
Spectral Resolution	B1: 443.9 nm, B2: 496.6 nm, B3: 560 nm, B4: 664.5 nm, B5: 703.9 nm, B6: 740.2 nm, B7: 782.5 nm, B8: 835.1 nm, B8A: 864.8 nm, B9: 945 nm, B11: 1613.7 nm, B12: 2202.4 nm
Radiometric Resolution	12 bits
Temporal Resolution	5 days
Used Dates	2015-07-30 2020-08-02

In general, one of the functions of these satellite sensors is mapping processes regarding LULC. CORINE (Coordination of information on the environment) Level 2 classes were considered in the classification process. CORINE is an inventory of European land cover split into 44 different land cover classes. Corine Level 2 classes are selected for the training data of the three dated images. According to spatial characteristics of the study area, four different classes in the CORINE Level 2 are selected by their order.

Classification algorithms were applied on the GEE platform using Sentinel-2 satellite images. GEE is a web-based system that enables access to a comprehensive catalog of satellite images, analysis, and visualization on a global scale. While the entire surface can be accessed, it provides freely accessible huge datasets including satellite image archive data for scientists and researchers. Provided data can be used in different remote sensing and geospatial analysis.

4. Methodology

Based on the GEE platform, two ML algorithms, SVM and RF, and different training data sets were used and compared. A flowchart of the study is given in Fig. 2 and conducted research steps were explained in the following sections.

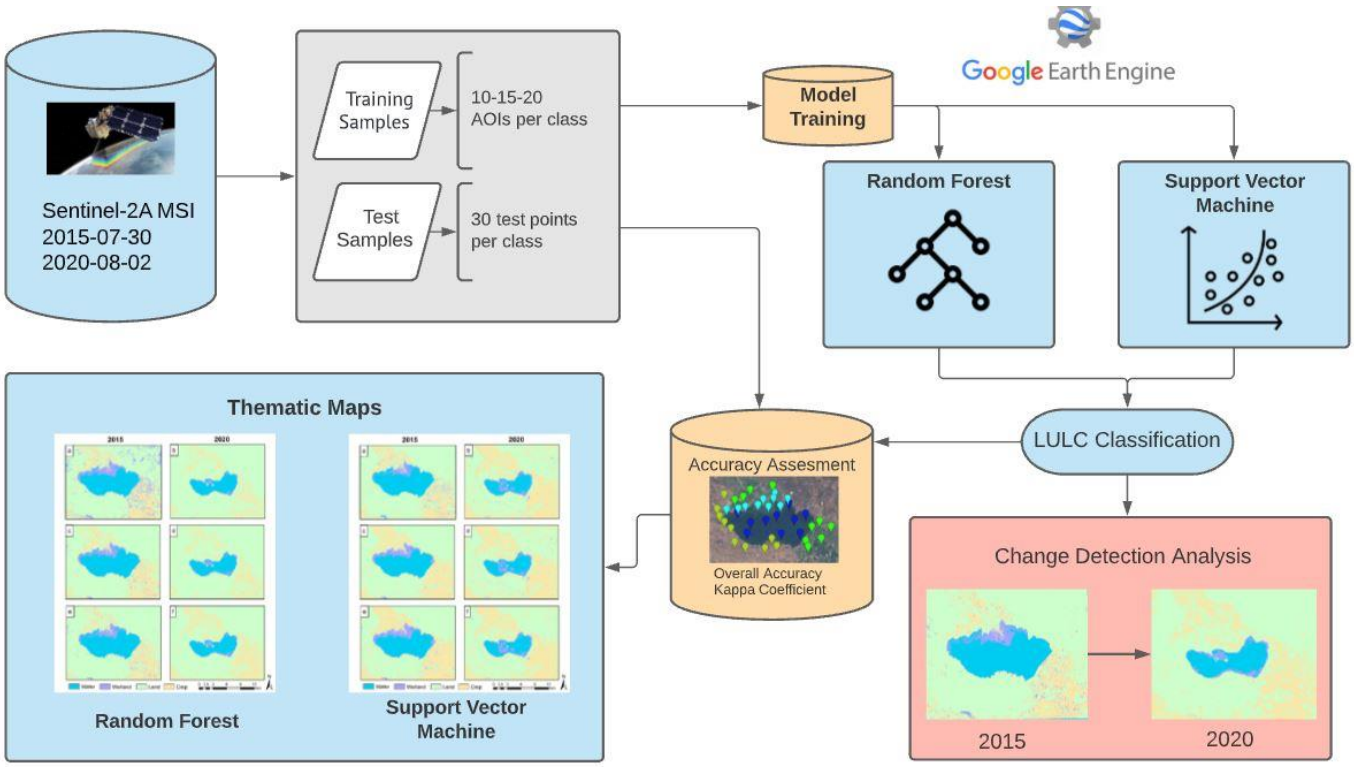

Figure 2. Flowchart of the study

In the first stage, RF classifier was used for mapping Marmara Lake. The RF classifier is a machine learning algorithm that combines many tree classifiers. To classify an input vector, each tree classifier generates a unit vote for the most common class in the tree [15]. RF, which is one of the most applied machine learning algorithms in classification studies [4,16] with a different type of data [17], increases the accuracy of the classification by creating more than one decision tree (Fig. 3). Several studies have shown that the RF classifier is capable of handling high data dimensionality and multi-linearity while still being fast and resistant to overfitting [18]. The

number of active variables in the random subset at each node and the number of trees in the forest are two parameters of RF. The number of active variables was set to the square root of the feature numbers whereas the number of trees was fixed to 25.

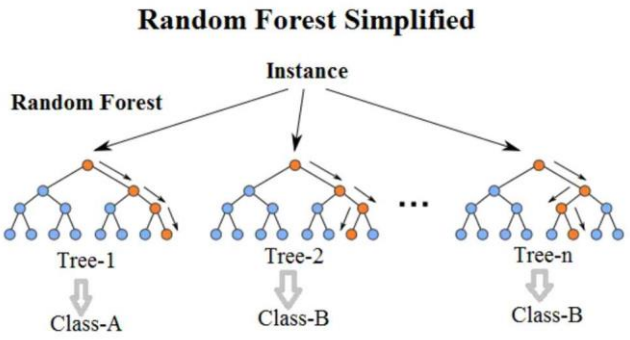

Figure 3. Random Forest Algorithm Architecture [18]

Since SVM is a supervised non-parametric statistical learning method, no assumptions about the underlying data distribution are made [19]. In the SVM algorithm, a hyperplane is created and the data is divided into two classes (Fig. 4). SVM is popular in remote sensing classification studies [20-21] and it is stated that SVM can be dealt with the classification of complex LULC [22]. For the SVM classifier, the radial basis kernel function was selected and the hyperparameters for gamma and cost were selected respectively 0.5 and 10.

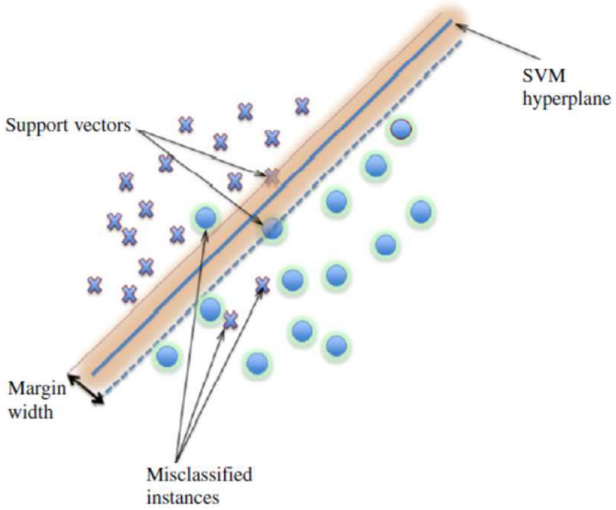

Figure 4. Support Vector Machine Algorithm Example [23]

Training datasets were collected on the GEE as polygons which are shown in Fig 5. The training area of interests (AOIs) for each class were selected as polygons which contain almost homogenous pixels in the area. To estimate the effect of training areas that are used on the classification they were separated into 3 different sized groups. The first group has the lowest area with 10 polygons and the second one has 15 polygons and the last one has the biggest area with 20 polygons. The effects of the increasing number of training data were evaluated. The results of the classification are different than each other.

These results can show us how much training area should be taken into classification to determine the best accuracy. Point data were used for the accuracy assessment (Fig. 5). The number of the training area and accuracy assessment points are given in Table 2 and the number of pixels in three data sets is given in Table 3. Classified satellite images are given in Fig. 6.

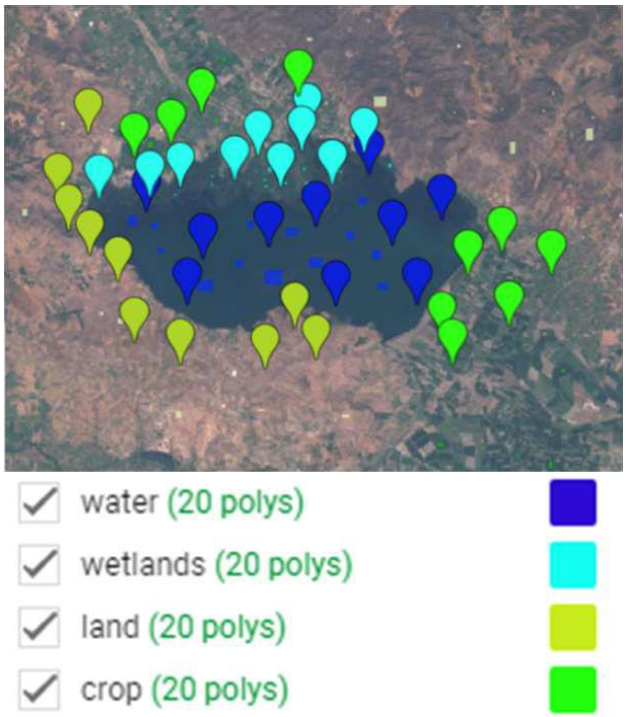

Figure 5. An example of AOIs for each Land Cover class collected with geometry tool in Google Earth Engine map.

Table 2. Detailed information of training and test data

Data	Date	AOI per class	Algorithm	Acc. points per class	Ass. class
Sentinel-2 MSI	2015	10 15 20	RF & SVM	30	
	2020	10 15 20		30	

Table 3. Number of pixels for each class 2015 and 2020

AOI/Class	Water	Wetlands	Land	Crop	Date
10	11159	1063	3714	1891	
15	16961	1141	3958	2177	2015
20	20679	1451	5769	2647	
10	4786	336	2269	740	
15	5483	396	2615	859	2020
20	6379	513	4325	1158	

Accuracy assessment shows the quality of the classification map. Therefore, overall accuracy (OA) and kappa coefficient (K) were calculated for each classification result using Eq.1-2.

$$OA = \frac{S_k}{S} \times 100 \quad (1)$$

where k represents the different AOI on the diagonal of the error matrix, Sk is the number of correctly classified samples, and S is the sample number.

$$K = \frac{p(\text{correct classification}) - p(\text{chance classification})}{1 - p(\text{chance classification})} \quad (2)$$

where p is proportion [24]. K values vary between 0 to 1 and values close to 1 show good classification.

5. Results and Discussion

The accuracy assessment results of LULC classification have been achieved using error matrices. In the accuracy assessment, four classified categories were considered: water, wetlands, land, and crop. Water defines the open surface area of the water body and the wetland class consists of the inland marshes. The land class covers the sparsely vegetated areas and the crop defines the heterogeneous agricultural area. LULC classes were created based on the CORINE. The overall accuracy (OA), and the kappa coefficient (K) was generated for each classification experiment and are given in Table 4.

In the accuracy assessment analysis, there are multiple methods to determine the number of test points as balanced or unbalanced. In studies with balanced and unbalanced training data sets, it has been observed that as the number of training pixels in each class increases, the model learns better and the classification accuracy increases in both data sets [25-26]. According to Thanh et al. [27] although the performance of balanced and unbalanced training datasets differs for both algorithms, the accuracy between the two models is approximately similar and high if the training sample is sufficient for the model. In our study, a direct link between pixel counts and accuracy was observed in parallel with these articles.

Table 4. Overall accuracy and kappa results of the classifications

AOI\	SVM		RF		Date
Model	OA (%)	Kappa	OA (%)	Kappa	
10	81.0	0.74	82.0	0.76	
15	88.0	0.83	86.0	0.81	2015
20	91.0	0.88	93.0	0.91	
10	80.8	0.74	81.7	0.76	
15	86.7	0.82	86.7	0.82	2020
20	91.7	0.89	92.5	0.90	

Besides the importance of the number of test sets, however, the distribution of the test sets is also important to more accurate analysis. For this purpose, test points should be homogeneously distributed. In this study, balanced test points were used (Table 2) and test points were homogeneously distributed. 30 test points were used per class and according to Story and Congalton [28] at least 30 samples are required to sufficiently populate the error matrix. According to Table 4, an increasing number of the training data improved the classification accuracy in both algorithms. However, the RF algorithm yielded slightly better overall accuracies with higher kappa coefficients (0.91 and 0.90, respectively) on both dates compared to the SVM algorithm. The best classification accuracy in both algorithms was obtained with 20 AOI on both dates. The error matrices of classification with 20 AOI are shown in Table 5. Water and wetland classes were mixed in the classification results.

The main reason is the mixed pixels that contain water and marshes on the coastal side of the lake. Additionally, the other mixed classes are land and crop. Because of having heterogeneous agricultural pattern, crop class mixed with the land class which contains sparsely vegetation. Classification results are shown in Fig. 7 and Fig. 8. Classification maps were produced considering CORINE color standards.

The areal change of the classes was calculated based on the RF classification results that were determined as the most accurate in the study. The areal coverage of the classes on both dates is given in Table 6. Marmara Lake, which is the Nationally Important Wetland, has lost more than half of the water and wetland (50.2% and 62.2%, respectively) since 2015. Most of these lost sites were converted to croplands.

Although the lake has been feeding 3 different sources, the water area has been decreasing in the last years. The first reason for that is the increase in irrigation demand [29]. According to the Turkish Statistical Institute [30], the agricultural area in the Gölmarmara, Ahmetli, and Salihli districts where the lake is located has increased approximately 3.3% between 2015 and 2020. This has caused an increase in water consumption for irrigation purposes.

The second reason is the withdrawal of groundwater sources. Although there is not enough information about groundwater resources, it is known that there are many illegal wells other than licensed wells [31].

The third and significant reason is the effects of the meteorological parameters. According to the Turkish State Meteorological Service [32], the annual precipitation average has decreased from 637.8 mm to 507.6 mm between 2015 and 2020 years on the national scale. In addition to precipitation, the annual temperature average has risen approximately 1 °C in the last 5 years.

6. Conclusion

In a conclusion, training data size and classification algorithms are important to achieve higher classification accuracy. In the study, it can be stated that the RF algorithm showed slightly better classification performance compared with the SVM algorithm. Increasing the number of training datasets improved the classification accuracy. Classification processes were applied to Sentinel-2 satellite images which have high spatial resolution data among the free available satellite images. All classification steps were implemented to the GEE and it makes processing satellite images easy with the increasing number of data and provides to rapidly access the results.

According to change detection analysis from the most accurate classification results, the area of the water body and wetland has dramatically decreased. Although the

lake is fed by different sources, the most likely causes of these significant decreases in the water body and wetland are climate change and unconscious irrigation. Additionally, it is observed that most of the dried lands were converted to the agricultural area in the study site.

This study has generated significant information about the LULC dynamics of Marmara Lake and its transformation during the last five years (2015–2020). It can be used as reference data for the decision-makers to protect water resources and nationally important wetlands. Additionally, this study was conducted for the summer season.

In future studies, water bodies and wetlands can be evaluated with seasonal and integrated with a different type of datasets which can improve the classification accuracy.

Table 5. Error matrices of RF and SVM classifications with 20 AOI

Error Matrix of RF 2015						
LULC Classes	Water	Wetlands	Land	Crop	Total	User Acc. (%)
Water	28	1	0	0	29	97.0
Wetlands	2	29	0	0	31	94.0
Land	0	0	27	2	29	93.0
Crop	0	0	3	28	31	90.0
Total	30	30	30	30	120	
Producer Acc. (%)	93.3	97.0	90.0	93.3		**93.0**
Error Matrix of RF 2020						
LULC Classes	Water	Wetlands	Land	Crop	Total	User Acc. (%)
Water	28	4	0	0	32	87.5
Wetlands	2	26	0	0	28	92.9
Land	0	0	28	1	29	96.6
Crop	0	0	2	29	31	93.5
Total	30	30	30	30	120	
Producer Acc. (%)	93.3	87.0	93.3	96.7		**92.5**
Error Matrix of SVM 2015						
LULC Classes	Water	Wetlands	Land	Crop	Total	User Acc. (%)
Water	27	3	0	0	30	90.0
Wetlands	3	27	0	0	30	90.0
Land	0	0	27	2	29	93.0
Crop	0	0	2	28	31	90.0
Total	30	30	30	30	120	
Producer Acc. (%)	90.0	90.0	90.0	93.3		**91.0**
Error Matrix of SVM 2020						
LULC Classes	Water	Wetlands	Land	Crop	Total	User Acc. (%)
Water	27	2	0	0	29	93.1
Wetlands	3	28	0	0	31	90.3
Land	0	0	27	2	29	93.1
Crop	0	0	3	28	31	90.3
Total	30	30	30	30	120	
Producer Acc. (%)	90.0	93.0	90.0	93.3		**91.7**

Figure 6. Sentinel-2A MSI RGB Imageries of 2015-07-30 and 2020-08-02

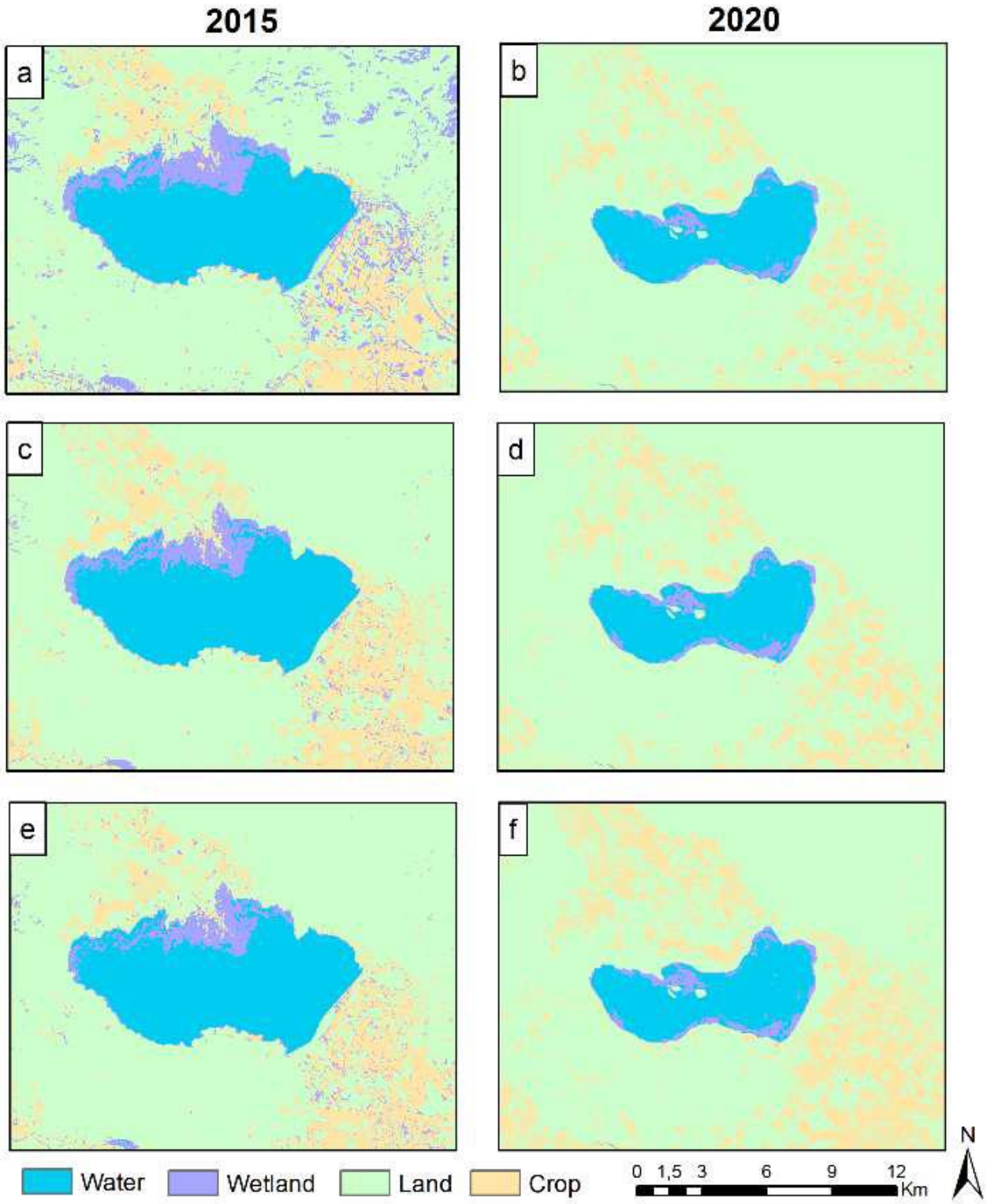

Figure 7. LULC classification results using RF classifier with 10 AOI (a-b), 15 AOI (c-d) and 20 AOI (e-f) for two dates

Table 6. Areal change of the lake between 2015 and 2020

Class/Area	2015 (ha)	2020 (ha)	Change (ha)	Change (%)
Water	5399.1	2689.3	-2709.8	- 50.2
Wetlands	1604.4	605.9	-998,5	- 62.2
Land	24199.7	25387.6	+1187,9	+ 4.9
Crop	5049.2	7569.5	+2520,3	+ 49.9

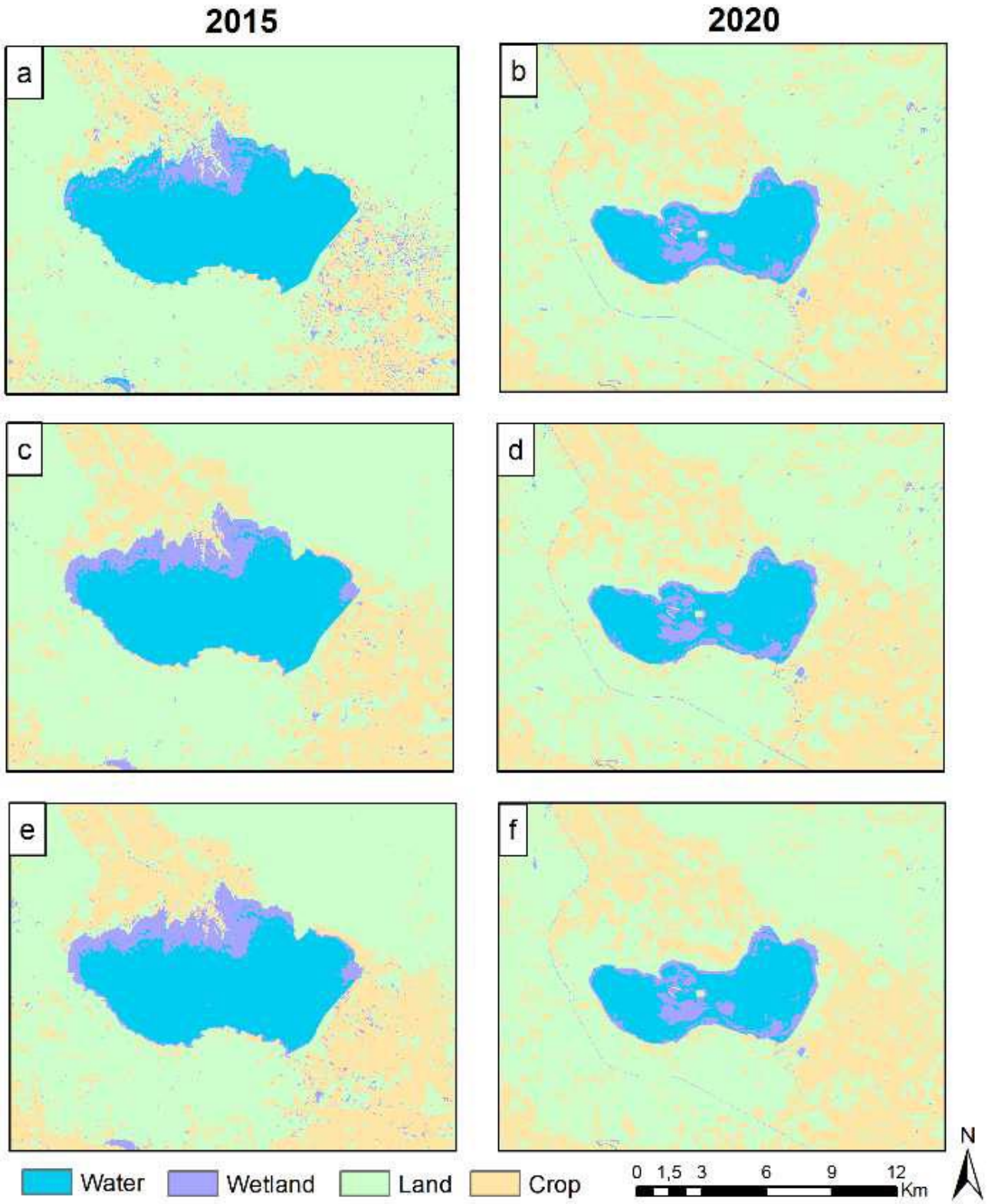

Figure 8. LULC classification results using SVM classifier with 10 AOI (a-b), 15 AOI (c-d) and 20 AOI (e-f) for two dates

Acknowledgement

The authors would like to acknowledge Sentinel-2 imagery from European Space Agency (ESA).

Author contributions

Cengiz Avcı: Methodology, Process, Writing **Muhammed Budak:** Methodology, Process, Writing **Nur Yağmur:** Process, Writing **Filiz Bektas Balcik:** Editing, Consultancy

Conflicts of interest

The authors declare no conflicts of interest.

References

1. DeFries, R. S., Foley, J. A., & Asner, G. P. (2004). Land-use choices: Balancing human needs and ecosystem function. Frontiers in Ecology and the Environment, 2(5), 249-257.
2. Kavzoglu, T., Tonbul, H., Erdemir, M. Y., & Colkesen, I. (2018). Dimensionality reduction and classification of hyperspectral images using object-based image analysis. Journal of the Indian Society of Remote Sensing, 46(8), 1297-1306.
3. Ekumah, B., Armah, F. A., Afrifa, E. K., Aheto, D. W., Odoi, J. O., & Afitiri, A. R. (2020). Assessing land use and land cover change in coastal urban wetlands of international importance in Ghana using Intensity Analysis. Wetlands Ecology and Management, 28(2), 271-284.
4. Basu, T., Das, A., Pham, Q. B., Al-Ansari, N., Linh, N. T. T., & Lagerwall, G. (2021). Development of an integrated peri-urban wetland degradation assessment approach for the Chatra Wetland in eastern India. Scientific reports, 11(1), 1-22.
5. Jamal, S., & Ahmad, W. S. (2020). Assessing land use land cover dynamics of wetland ecosystems using Landsat satellite data. SN Applied Sciences, 2(11), 1-24.
6. Hochreuther, P., Neckel, N., Reimann, N., Humbert, A., & Braun, M. (2021). Fully Automated Detection of Supraglacial Lake Area for Northeast Greenland Using Sentinel-2 Time-Series. Remote Sens. 2021, 13, 205.
7. Shih, H. C., Stow, D. A., & Tsai, Y. H. (2019). Guidance on and comparison of machine learning classifiers for Landsat-based land cover and land use mapping. International Journal of Remote Sensing, 40(4), 1248-1274.
8. Bangira, T., Alfieri, S. M., Menenti, M., & Van Niekerk, A. (2019). Comparing thresholding with machine learning classifiers for mapping complex water. Remote Sensing, 11(11), 1351.
9. Gislason, P. O., Benediktsson, J. A., & Sveinsson, J. R. (2006). Random forests for land cover classification. Pattern recognition letters, 27(4), 294-300.
10. Gorelick, N., Hancher, M., Dixon, M., Ilyushchenko, S., Thau, D., & Moore, R. (2017). Google Earth Engine: Planetary-scale geospatial analysis for everyone. Remote sensing of Environment, 202, 18-27.
11. Wang, Y., Ma, J., Xiao, X., Wang, X., Dai, S., & Zhao, B. (2019). Long-term dynamic of poyang lake surface water: a mapping work based on the Google earth engine cloud platform. Remote Sensing, 11(3), 313.
12. Wang, C., Jia, M., Chen, N., & Wang, W. (2018). Long-term surface water dynamics analysis based on Landsat imagery and the Google Earth Engine platform: A case study in the middle Yangtze River Basin. Remote Sensing, 10(10), 1635.
13. Amani, M., Mahdavi, S., Afshar, M., Brisco, B., Huang, W., Mohammad Javad Mirzadeh, S., ... & Hopkinson, C. (2019). Canadian wetland inventory using google earth engine: The first map and preliminary results. Remote Sensing, 11(7), 842.
14. MoAF (Ministry of Agriculture and Forestry) (2018). Wetland Managemant Plan of Marmara Lake. Ankara.
15. Breiman, L. (1999). Random forests. UC Berkeley TR567.
16. Berhane, T. M, Lane, C. R., Wu, Q, Autrey, B. C., Anenkhonov, O. A., Chepinoga, V. V., & Liu, H. (2018). Decision-tree, rule-based, and random forest classification of high-resolution multispectral imagery for wetland mapping and inventory. Remote sensing, 10(4), 580.
17. Dubeau, P., King, D. J., Unbushe, D. G., & Rebelo, L. M. (2017). Mapping the Dabus wetlands, Ethiopia, using random forest classification of Landsat, PALSAR and topographic data. Remote Sensing, 9(10), 1056.
18. Jagannath, V. (2020). "Random Forest Template for TIBCO Spotfire® - Wiki Page TIBCO Community." https://community.tibco.com/wiki/random-forest-template-tibco-spotfire
19. Vapnik, V. (1998). The support vector method of function estimation. In Nonlinear modeling (pp. 55-85). Springer, Boston, MA.
20. Qian, Y., Zhou, W., Yan, J., Li, W., & Han, L. (2015). Comparing machine learning classifiers for object-based land cover classification using very high resolution imagery. Remote Sensing, 7(1), 153-168.
21. Han, X., Pan, J., & Devlin, A. T. (2018). Remote sensing study of wetlands in the Pearl River Delta during 1995–2015 with the support vector machine method. Frontiers of Earth Science, 12(3), 521-531.
22. Pretorius, L., Brown, L. R., Bredenkamp, G. J. & van Huyssteen, C. W. (2016). The ecology and classification of wetland vegetation in the Maputaland Coastal Plain, South Africa. Phytocoenologia, 46(2), 125-139.
23. Burges, C. J. (1998). A tutorial on support vector machines for pattern recognition. Data mining and knowledge discovery, 2(2), 121-167.
24. Canty, M. J. (2014). Image analysis, classification and change detection in remote sensing: with algorithms for ENVI/IDL and Python. Crc Press.
25. Colditz, R. R. (2015). An evaluation of different training sample allocation schemes for discrete and continuous land cover classification using decision tree-based algorithms. Remote Sensing, 7(8), 9655-9681.
26. Mellor, A., Boukir, S., Haywood, A., & Jones, S. (2015). Exploring issues of training data imbalance and mislabelling on random forest performance for large area land cover classification using the ensemble margin. ISPRS Journal of Photogrammetry and Remote Sensing, 105, 155-168.

27. Thanh, Noi, P., & Kappas, M. (2018). Comparison of random forest, k-nearest neighbor, and support vector machine classifiers for land cover classification using Sentinel-2 imagery. Sensors, 18(1), 18.
28. Story, M., & Congalton, R. G. (1986). Accuracy assessment: a user's perspective. Photogrammetric Engineering and remote sensing, 52(3), 397-399.
29. Tubitak MAM (2013). Preparation Project of Basin Protection Action Plans, Gediz Basin. Project Report, Kocaeli.
30. TUIK, 2020. https://www.tuik.gov.tr/
31. Korbalta, H. (2019) Marmara Gölü Neden Kuruyor? Kent Akademisi, 12(3), 441-459.
32. MGM (2020). Analysis of meteorological parameters for Turkey. Accessed from: https://www.mgm.gov.tr/veridegerlendirme/il-ve ilceleristatistik.aspx?k=parametrelerinTurkiyeAnaliz i.

International Journal of Engineering and Geosciences
https://dergipark.org.tr/en/pub/ijeg
e-ISSN 2548-0960

Synoptic analysis of the January 2004 snowstorm: Example of Çanakkale

Mahmut Eşsiz [1], **Zahide Acar** [*1]

[1]*Çanakkale Onsekiz Mart University, Department of Geography, Türkiye*

Keywords
Radiosonde
Snowstorms
Synoptic Analysis

Research Article
DOI: 10.26833/ijeg.988115

Received: 28.08.2021
Accepted: 23.01.2022
Published: 13.04.2022

Abstract

Many natural disasters have occurred on the Earth we live in. Humans have always been in a struggle with these natural phenomena. Today, people are still struggling with atmospheric extreme events. One of the most important disasters like this is snowstorms that occur suddenly in winter. Especially countries in the middle belt (30-60 latitudes in the Northern Hemisphere) are constantly affected by snowstorms. Turkey, located in the Middle Belt, is also exposed to these storms during the winter season. From this perspective, the analysis of synoptic conditions and weather forecast is an important factor for risk analysis and take precautions for winter storms. Thus, the predictions made with the tracking of air masses and synoptic analysis make it easier to understand how the storm occurred. For this purpose, synoptic analyses were conducted to understand the development of the snowstorm that occurred in the high atmosphere in Çanakkale on January 20-30, 2004. This study examined how weather conditions change. Radiosonde data, surface maps, and daily bulletins provided from the Turkish State Meteorological Service were used in the study. Archival data were used to track air mass orbits using the Hysplit trajectory method. Stability and instability assessments of air masses were evaluated using the data from radiosonde stations using the K Index. Spatial analysis software was used to analyze the data and show the thematic distribution of topography. According to the findings, during the passage of a cold front of air masses coming from the north to Çanakkale on January 22, gusty winds began, suddenly dropped the temperatures, and began heavy snow events. Later, it turned into a blizzard and formed a type of snow.

1. Introduction

From the past to the present, finding solutions to environmental problems experienced by the destruction of nature along with the growing population is the greatest effort of humanity for a long time. Considering the relationship between man and space, the value of the interaction between them has emerged. Human-space interaction makes an inference through evaluations by developing different methods of its own.

Climate can be defined as the "synthesis of weather" over a long enough time period to determine its key statistical properties. More generally, it is the time-averaged state of the physical system that includes the atmosphere, hydrosphere, cryosphere, lithosphere, and biosphere and their interactions at many different time and space scales. The main areas that make up the climate system have a wide range of stabilization periods [1]. Turkey, a Mediterranean country, is a country located between three land continents such as Europe, Asia and Africa and surrounded by seas on three sides. The fact that the Black Sea, Aegean and Mediterranean basins are connected significantly affects the air masses and climate that come to the country. Turkey is under the influence of bipolar air mass, especially during the winter months. These are Maritime Polar (mP) and Continental Polar (Cp) air masses [2-8]. These polar air masses cause severe winters and snowstorms in the middle latitudes [9-12]. There is a high correlation between precipitation and storm intensity in the Mediterranean basin [13]. Stormy days display increasing trends in some regions where the wind is channeled by topographic effects such as Canakkale [14].

In January 2004, a severe snowstorm occurred in Çanakkale. Heavy snowfall and severe storms have turned northwestern Turkey into a disaster zone. Within

* **Corresponding Author**
(essizmahmut@gmail.com) ORCID ID 0000-0002-9219-7554
*(zacar@comu.edu.tr) ORCID ID 0000-0002-9174-0447

Cite this article
Eşsiz, M., & Acar, Z. (2023). Synoptic analysis of the January 2004 snowstorm: Example of Çanakkale. International Journal of Engineering and Geosciences, 8(1), 11-18

a day, temperatures of up to 15°C had dropped and heavy snowfall occurred. A strong winter storm formed along with strong winds. The problem of the study is to provide a good analysis and synthesis of the air masses available for blizzards. Previous studies have only assessed the catastrophic extent of the event [15]. The synoptic conditions that prepare the blizzard have never been studied, and there is a lack of knowledge in the literature. This study includes the climatology and effects of the blizzard that occurred in 2004 and affected the entire western Anatolia. It is believed that it will make a contribution to the literature with the scope of the study.

The snowstorm that occurred in January 2004 reached very effective dimensions in Çanakkale and the surrounding provinces. This severe snowstorm reached the size of a disaster and negatively affected the lives of the people of the region. In the Marmara Region, which is one of the most developed regions of Turkey, the snowstorm has reached the level of disaster. The January 2004 snow storm was felt very strongly in Çanakkale and the surrounding provinces. The purpose and scope of this study can be shown under the following headings.

• Determination of the effects of air masses in places where air masses pass by following the trajectory of the specified snowstorm, spatial distribution of the disaster,

• and the visual presentation of this with the map software program is the evaluation of the formation and development of the blizzard of January 20-30, 2004 by synoptic analysis.

2. Data and Method

Canakkale station was selected as the working area for the station scale assessment of the winter storm that was effective throughout western Anatolia (Figure 1).

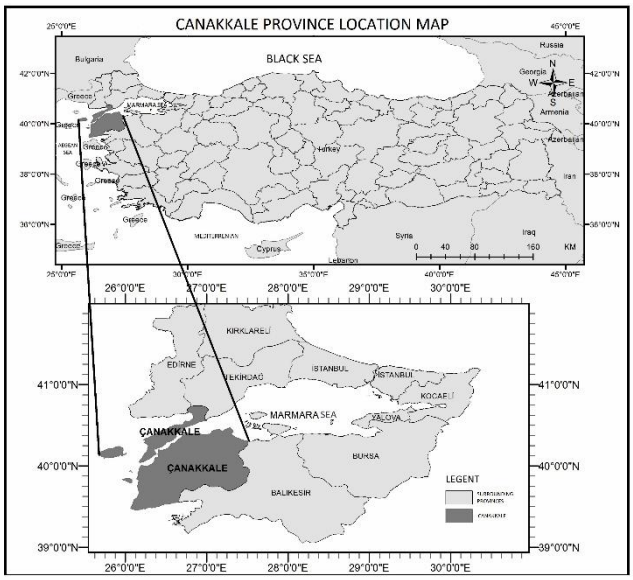

Figure 1. Çanakkale location map study area

The data used in the study are listed below. Daily and hourly data provided by Turkish State Meteorological Service. Hourly sea level pressure, temperatures, humidity, wind speed and wind direction, cloud amount and cloud base height data.

Daily Kadıköy/Istanbul radiosonde (rawinsonde) data. Daily bulletins (surface card and 500 hpa) and the HYSPLIT Reanalysis retro-orbit data model developed by NOAA (National Oceanic and Atmospheric Administration), and SKEW T LOG-P diagram sounding data of all stations in the World, shared publicly by the University of Wyoming [16]. In addition, 500 hpa geopotential altitude pressure distribution maps using Era5 satellite data from the European Center for medium-term weather forecasts (ECMWF) [17]. Synoptic analysis is based on radiosonde data and daily synoptic weather maps. Wind is the movement of air on the earth's surface. Winds play an important role in determining and controlling climate and weather [18].

Wind direction and speed maps [19], and 500 hpa geopotential elevation maps of the Global Forecast System (Gfs) numerical weather forecast model were used [20].

Graphs were created using hourly data (temperature, pressure, humidity, wind speed and direction, cloud base level, amount of cloud). The formation and development of air masses and the developmental stages of blizzards were analyzed and evaluated.

The Hybrid Single Particle Lagrange Integrated Orbit (HYSPLIT) instrument, developed by the National Oceanic and Atmospheric Administration (NOAA) Air Resources Laboratory, was used in this study to calculate retrograde trajectories to understand the development of intense blizzards. Trajectory analysis is a method used to determine the direction of arrival of air masses affecting a snowstorm and its path.

Trajectory analysis represents a method and framework used to analyze the physical processes that cause heavy winter precipitation. Therefore, this research effectively linked the varying concentration of components, the posterior trajectories identified using the HYSPLIT tool, to the physical processes that contribute to winter precipitation, as well as to the evolving large-scale circulation regimes. The origin of air masses was analyzed by calculating three-dimensional posterior orbits (or inverse orbits) using the HYSPLIT (Hybrid Single Particle Lagrangian Integrated Orbit) model from the Air Resources Laboratory (ARL). This model was chosen because it is widely used in international scientific research. For this study, reanalysis data for archival trajectories of the online version of HYSPLIT were used and run hourly, twice a day, during 15-30 January 2004 was determined as 48 hours. The isentropic considered, representing the transport by the air mass, are in surface, the 850 hPa and 500 hPa levels [21].

Within the scope of the study, the Skew T log P diagram data sets and graphics of all stations where the air masses pass, and the changes experienced by the air masses as they pass from one station to another station were evaluated. Calculations were made using the K index to determine the stability and unstability of the air. The calculation formula used for the index is as follows;

K= (T850-T500) + Td850 - (T700-Td700)
T 850: 850 mb dry bulb temperature,
Td850: 850 mb dew point temperature,
T700: 700 mb dry bulb temperature,
Td700: 700 mb dew point temperature,
T500: 500 mb is the dry chamber temperature.

The K index is among the most preferred indexes for determining the intensity of thunderstorms and storms in air masses. A temperature gradient of 850-500 mb, a dew point temperature of 850 mb for humidity in the lower troposphere, and a moisture distribution of 700 mb were presented together. The K index was constructed using data collected from radiosondes. With the addition of the dew point, it allows the determination of unstable air masses from the moisture in the lower levels to the upper level. The probability of occurrence of storm-thunderstorm for the K index is given in Table 1 [22-23].

Table 1. K Index Values

Values	Thunderstorm probability (%)
K<15	0
18-19	20% unlikely
20-25	20-40% isolated thunderstorm
26-29	50% widely scattered thunderstorms
30-35	85% numerous thunderstorms
K>36	100% chance for thunderstorms

3. Results

3.1. Change of Air Masses Due to Topography

Temperatures on land and sea change according to the seasons. Turkey has high windiness due to its location in the subtropical zone. Northwest Anatolia is one of the places where windiness is high in Turkey [3, 24-26]. In this section, the change experienced by the air masses that caused the January 2004 snowstorm is evaluated. The arrival paths of the air masses affecting the study area in Northwest Anatolia were determined using the Hyplit orbit model. The data obtained from the stations where the air masses pass was graphed by extracting the K index to determine the stability and instability situations. Radiosonde stations are homogeneously distributed in Turkey as in Europe. The spatial distribution of the radiosonde stations used in the study is shown in Figure 2. Stability and instability conditions are determined with the data obtained from the stations where the air masses pass. The change experienced by the air masses that were effective in the snowstorm that occurred in Çanakkale in January 2004 is presented visually.

January 20, 2004, according to the heights of the green air masses (red 0m, blue 1500m, green 5500m), their arrival trajectories to Çanakkale and the instability at the station they pass through are as in Figure 3. It is 16.5 at LGIR (Iraklion, Crete, Greece) station and 10.7 at Izmir station.

Figure 2. Geographical distribution of radiosonde stations in Turkey and surrounding countries [27].

The arrival trajectories to Çanakkale according to the altitudes of the air masses (red 0m, blue 1500m, green 5500m) on January 21, 2004, and the instability at the station it passes through are as shown in Figure 4. Instability changed to 5.5 at HEMM station (Mersa Matruh, Egypt), 26.3 at LGIR station (Iraklion, Crete, Greece), and 22.5 at IZMIR (Turkey) station.

The arrival trajectories of Çanakkale on 22 January 2004 according to the heights of the air masses (red 0m, blue 1500m, green 5500m) and the instability at the Istanbul station it passes through are as shown in figure 5. The air mass came from the north and the instability changed as 47.83 at Istanbul station (-3.9 at Poprad-Ganovce (Slovakia) station, -13.3 at LRBS (Bucharest, Romania) station).

According to the altitudes of the air masses (red 0m, blue 1500m, green 5500m) on January 23, 2004 and the instability of the station they passed, the trajectories of their arrival in Çanakkale are as in Figure 6. The air mass coming from the north (red 0m) changed to -8.7 at Budapest station, -11.6 when arriving at LHUD station (Szeged, Hungary), and -9.1 when passing through LRBS (Bucharest, Romania) station.

It is very important to evaluate the synoptic maps in order to see the conditions that created the January 2004 snowstorm and to reveal its effects. Global Forecast System (Gfs) Digital Weather Forecast Models and ECMWF (European Medium Term Weather Forecasts 507 Center) Era 5 satellite models were examined. On January 20, 2004, when viewed at 500 hPa level in Figure 7., a cold core trough path began to form towards Tunisia and Algeria, passing through Italy, where the EU region is formed, in the north of Turkey. The high-pressure ridge in the west also affects Turkey.

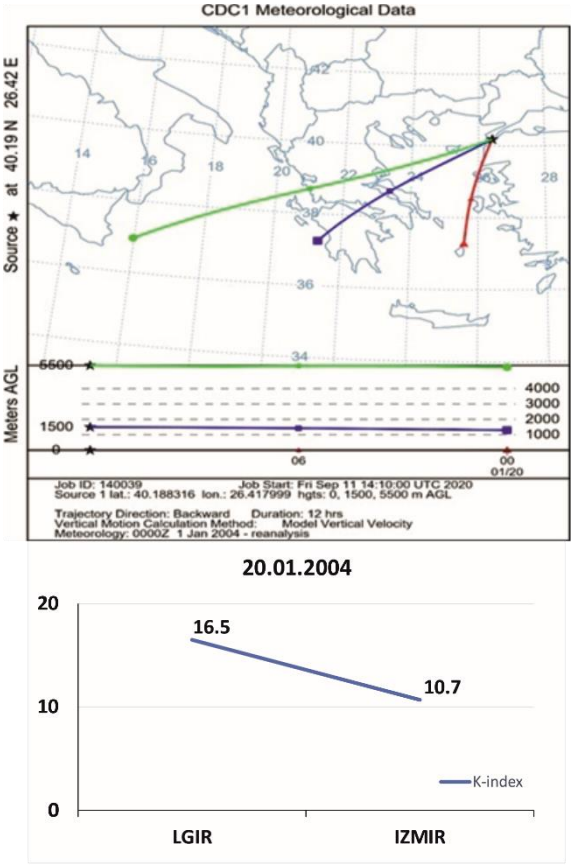

Figure 3. HYSPLIT Reanalysis Back trajectory analysis of 48 hours dated 20 January 2004 and k index analysis at stations where air masses pass

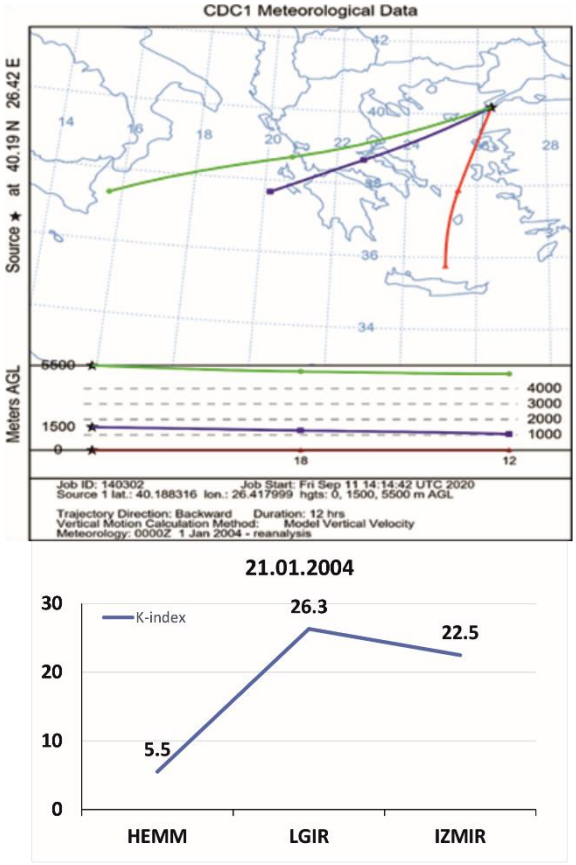

Figure 4. HYSPLIT Reanalysis Back trajectory analysis of 48 hours dated 21 January 2004 and k index analysis at stations where air masses pass

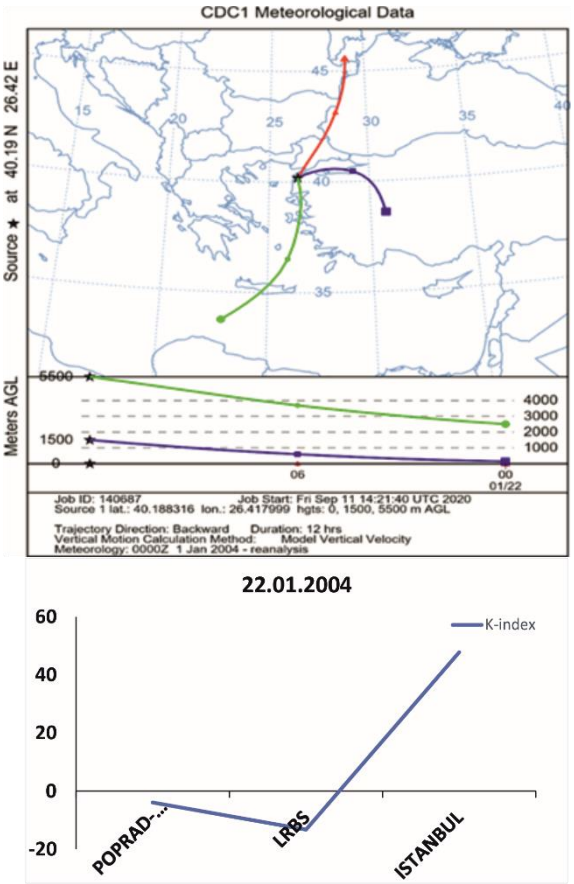

Figure 5. HYSPLIT Reanalysis Back trajectory analysis of 48 hours dated 22 January 2004 and k index analysis at stations where air masses pass

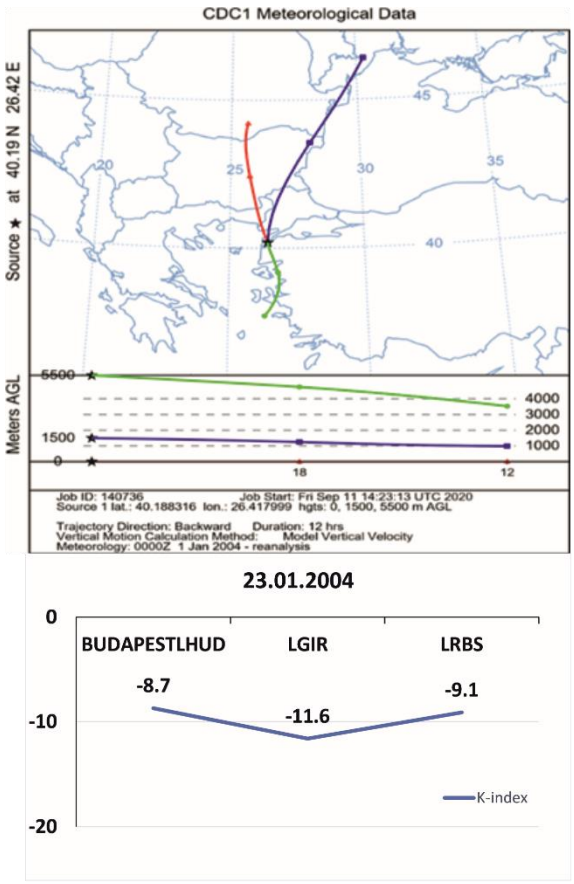

Figure 6. HYSPLIT Reanalysis Back trajectory analysis of 48 hours dated 22 January 2004 and k index analysis at stations where air masses pass

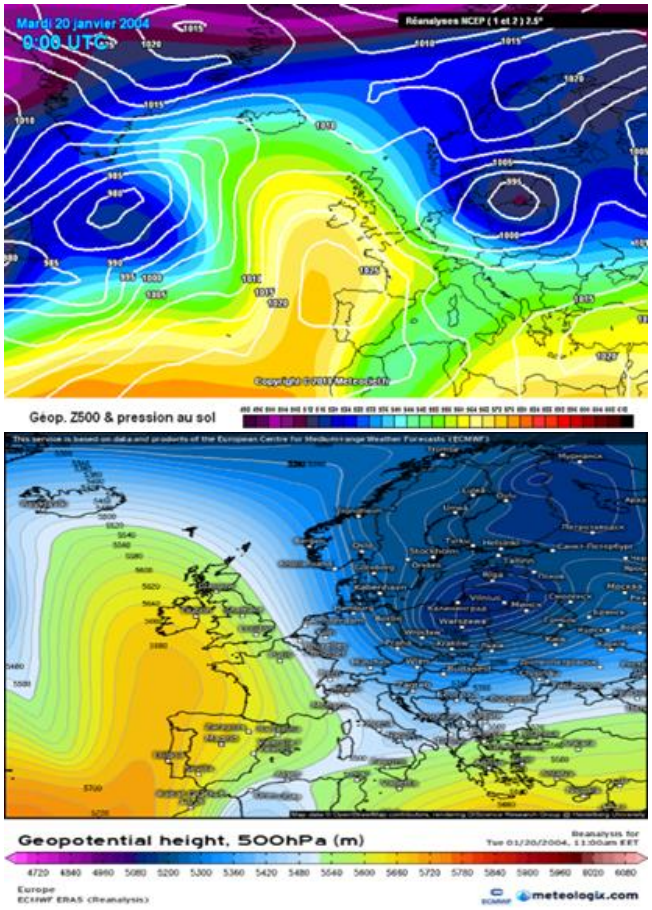

Figure 7. 20.01.2004 Global Forecast System (Gfs) 500 hPa Synoptic Map of the European Continent of the Digital Weather Forecast Model and ECMWF Era5 Satellite model 500 hPa geopotential elevation map

On January 20, 2004, the biggest effect on the transport of air masses was the wind. As indicated in the ECMWF Era5 Satellite model figure 8, the wind blows from south to north at a speed of 40-50 km/h towards the northwest of Turkey.

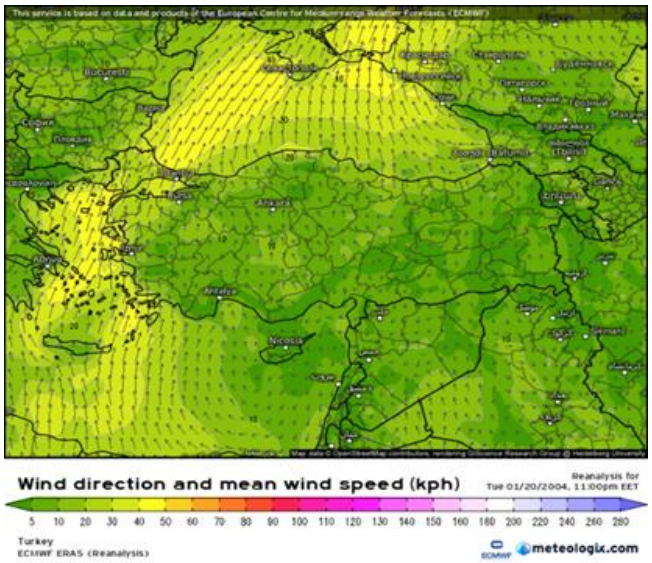

Figure 8. 20.01.2004 ECMWF Era5 Satellite model wind speed and wind direction map

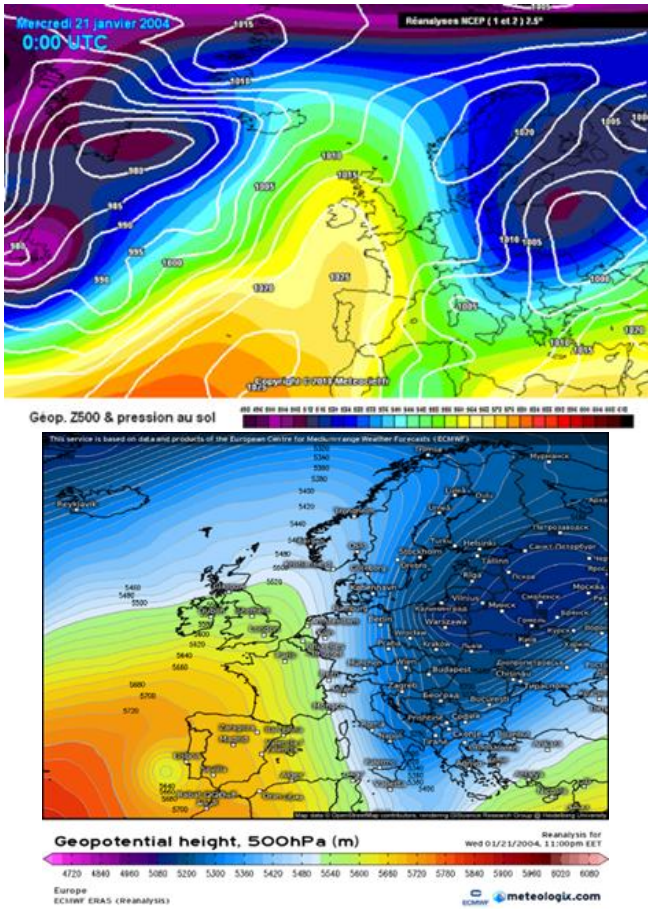

Figure 9. 21.01.2004 Global Forecast System (Gfs) 500 hPa Synoptic Map of the European Continent of the Digital Weather Forecast Model and ECMWF Era5 Satellite model 500 hPa geopotential elevation map

On January 21, 2004, the temperature in the Balkans dropped to -30 degrees, and a deep and cold trough extends to Italy. A frontal system was formed in the Mediterranean. The temperature and pressure gradient in the atmosphere is very strong. The cold-fronted mid-latitude cyclone in the north passes through Thrace and encounters the warm-fronted mid-latitude cyclone in the west. With the presence of a low-pressure system, a cold, rainy and stormy weather is effective on Turkey. With the entry of the cold front from the Balkans, snow in Thrace, Çanakkale region and northern Anatolia, heavy rain in the south and thunderstorms in Marmara are effective. During the passage of the cold front in the northwest of Turkey, the south-westerly wind became northerly (Figure 9 and 10).

On January 22, 2004, a very cold and deep trough deepened in northern Russia (Figure 11). The northern polar air mass affected the whole of Europe and a part of the Mediterranean basin, causing snowfall to begin in Thrace and northwestern Anatolia. With its intrusion towards the south, a pressure center of approximately 990 hpa was formed over Greece and the Aegean Sea, and a mid-latitude frontal area was formed.

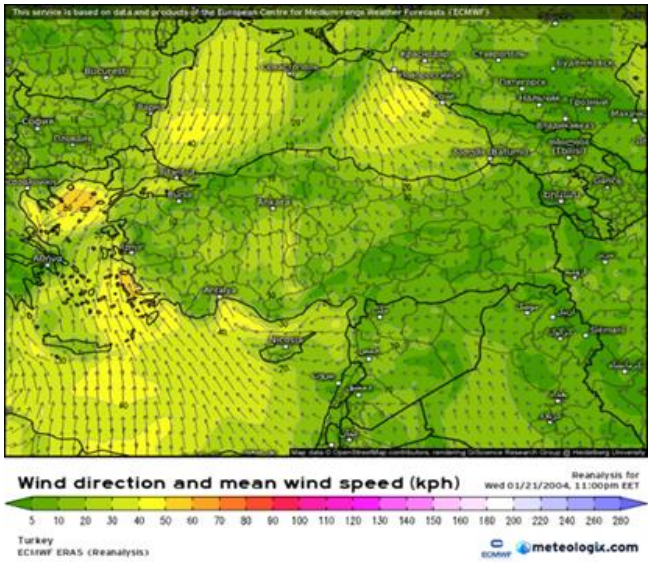

Figure 10. 21.01.2004 ECMWF Era5 Satellite model wind speed and wind direction map

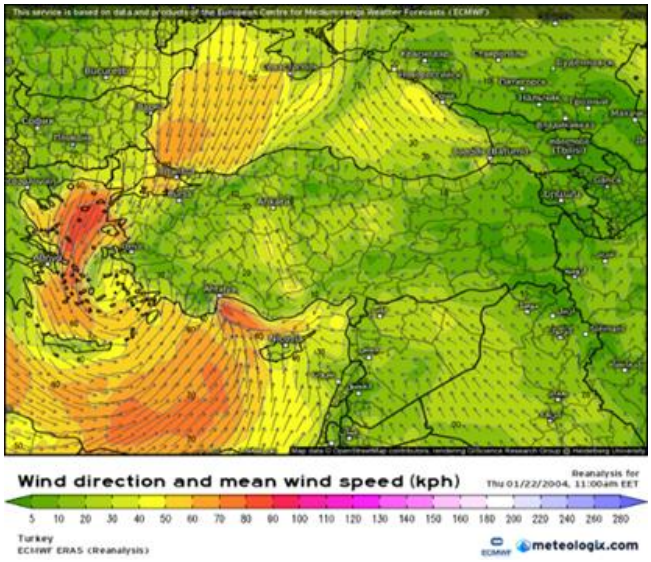

Figure 12. 22.01.2004 ECMWF Era5 Satellite model wind speed and wind direction map

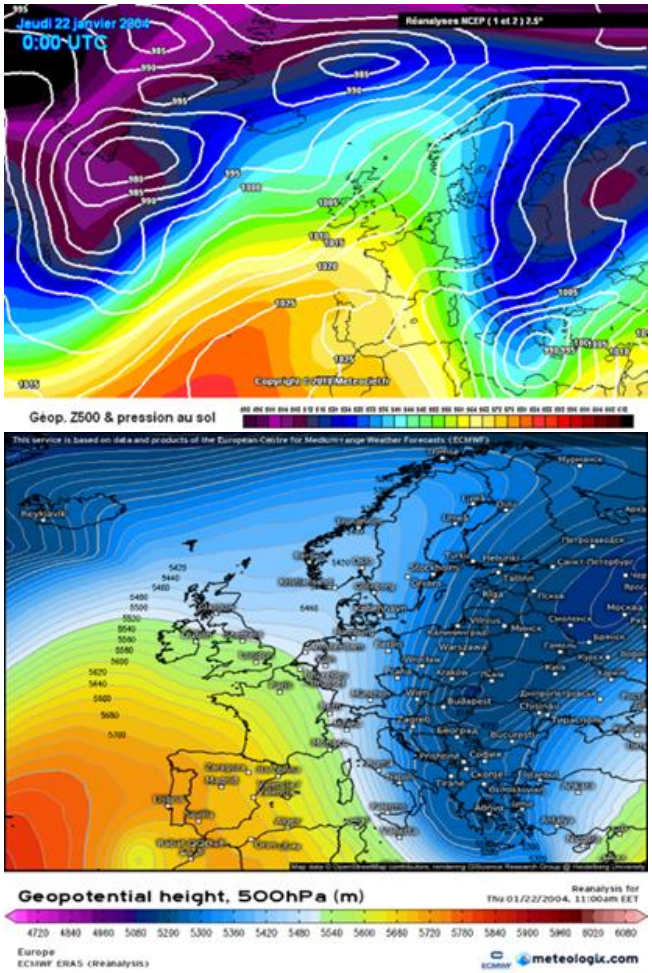

Figure 11. 22.01.2004 Global Forecast System (Gfs) 500 hPa Synoptic Map of the European Continent of the Digital Weather Forecast Model and ECMWF Era5 Satellite model 500 hPa geopotential elevation map

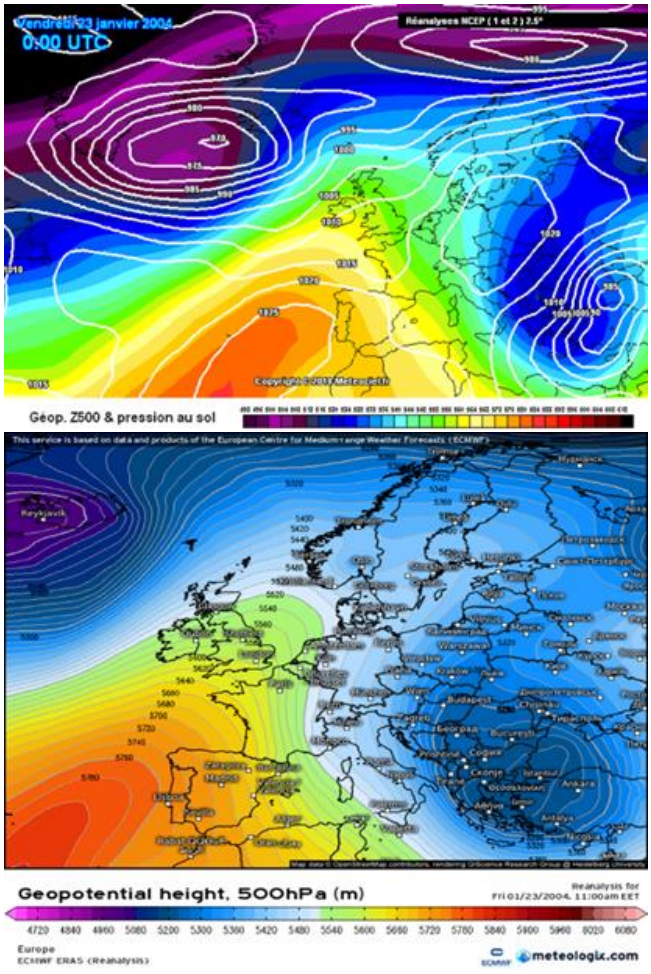

Figure 13. 23.01.2004 Global Forecast System (Gfs) 500 hPa Synoptic Map of the European Continent of the Digital Weather Forecast Model and ECMWF Era5 Satellite model 500 hPa geopotential elevation map

Snowfall, which started with the effect of northern sector air currents in Northwest Anatolia, increased the intensity of the wind together with the strong pressure gradient and turned into a snowstorm (Figure 12).

On January 23, 2004, the cold core, which expanded its influence in the Russian plains and settled in the Balkans and northwest of Turkey, formed a very cold and deep center. From this point of view, the low air temperature along with the mid-latitude cyclone has

increased the possibility of snowfall. When we look at Turkey in general, it has been under the influence of cold advection. It was very cold and rainy in most of Turkey. As of January 23, 2004, the cold weather in the northwest of Turkey is effective from the north and northeast sectors, but the wind speed has gradually weakened (Figure 13 and Figure 14).

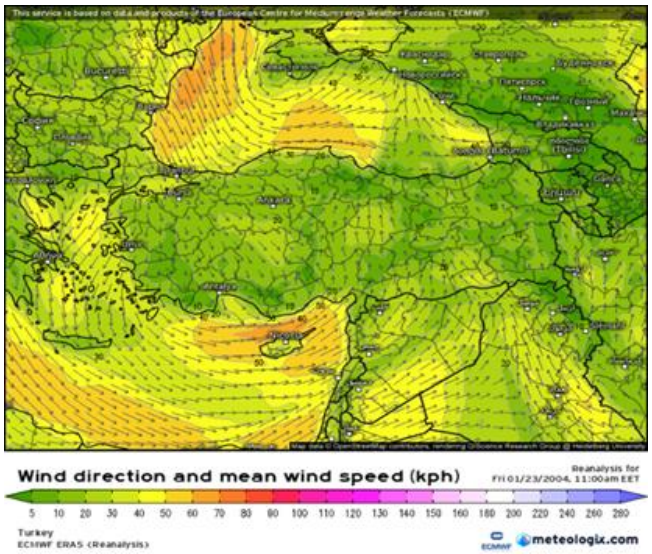

Figure 14. 23.01.2004 ECMWF Era5 Satellite model wind speed and wind direction map

The impact of the blizzard that occurred in January 2004 in the northwest of Turkey was materialized and evaluated with synoptic analyses. In figure 15, the hourly temperature, pressure and wind speed changes of the snowstorm and the effects of the snowstorm are visualized. 20-23 January are examined for storm details.

When the figures are examined, the snowstorm started on the morning of January 22 with the increase in wind speed with the temperature falling below 0 degrees on the night of January 21 and the pressure falling below 1000 hPa. Temperature Until January 26, the temperature is below 0 degrees. As the wind speed has fallen to 23 January (Figure 15).

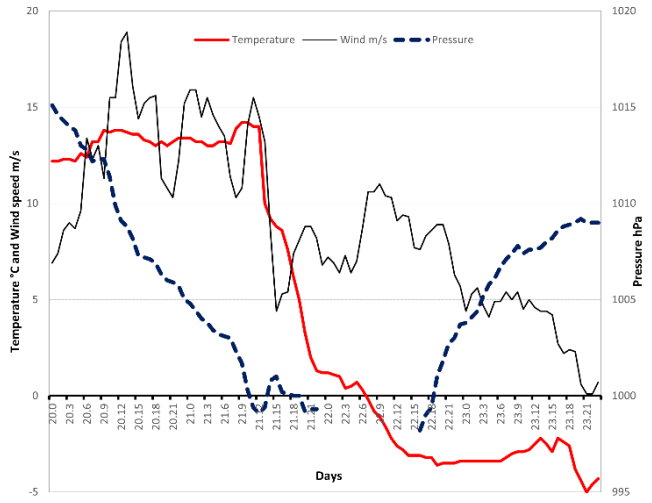

Figure 15. Analysis of hourly temperature, pressure and wind speed of 20-23 January 2004 Çanakkale snowstorm

4. Conclusion

Disasters are the results that occur according to the characteristics of the natural and social environment. There is an increase in disasters worldwide and in Turkey. The unavoidable increase in disasters causes more loss of life and property.

The snowstorm occurred in January 2004 in the Marmara region. However, many provinces in the Marmara region, especially Çanakkale, were affected by the snowstorm and experienced a disaster. The synoptic evaluation of the formation and development of the January 2004 snowstorm in Çanakkale is as follows:

Mid-latitude depressions are effective at an annual rate of 45% in the northwestern part of Turkey [8, 28]. Due to the displacement of the polar front to the south during the cold period, the effective rate of mid-latitude depressions increases in this period. The intensity and duration of the winter storm was strengthened by the presence of cold air introduced into the middle latitudes by the trough in the upper atmosphere.

The mid-latitude cyclone observed over the northern Aegean on 20-23 January 2004. The continuity and effectiveness of snowstorm and heavy snowfalls are related to the trough in the upper atmosphere. The trough is deepened by cold advection from the north. The k-index data from the skew t log p diagram vary across at stations. The values of the K index showed the stability and instability of the air masses. Accordingly, the instabilities of the air masses that caused the snow disaster are quite high in January 2004. According to the K-index of stations, there is a high probability of thunderstorms in northwest Turkey on January 21, 2004. On January 21-22, the air temperature dropped by about 10 degrees, and the storm was effective in the northwest of Turkey. Strong instability of the air mass was experienced snowfall and snowstorm in surrounding the northwestern part of Turkey.

Author contributions

Mahmut Eşsiz: Methodology, Writing-Original draft preparation, **Zahide Acar:** Conceptualization, Data curation, investigation, writing-reviewing and Editing.

Conflicts of interest

The authors declare no conflicts of interest.

References

1. Barry, R. G., & Carleton, A. M. (2001). Synoptic and Dynamic Climatology. Boca Raton: Taylor & Francis.
2. Şensoy, S. (2004). On the Flood Forecasting at the Bulgarian Part of. Ohrid, FY Republic of Macedonia, 1–10.
3. Gönençgil, B. (2008). Doğal süreçler açısından iklim değişikliği ve insan. İstanbul: Çantay Yayınevi.

4. Yılmaz, E., & Çiçek, İhsan. (2016). Thornthwaite climate classification of Turkey, Journal of Human Sciences, 13(3), 3973–3994.
5. Yılmaz, E., & Çiçek, İhsan. (2018). Detailed Köppen-Geiger climate regions of Turkey<p>Türkiye'nin detaylandırılmış Köppen-Geiger iklim bölgeleri. Journal of Human Sciences, 15(1), 225–242.
6. Acar Deniz, Z. Gönençgil, B., & Korucu Gümüşoğlu, N. (2017). Long-Term Changes in Hot and Cold Extremes in Turkey. *Istanbul University Journal of Geography, 37*, 57-67.
7. Acar Deniz, Z., & Gönençgil B. (2019). Extreme precipitation events in Turkey. Meteorological Journal, 2(22), 87-94.
8. Koç, T., (2001). Climate and Environment in Northwest Anatolia with Synoptic, Statistics and Application Dimensions. Istanbul: Çantay Bookstore.
9. Goree, P.A. & Younkin, R.S. (1966). Synoptic climatology of heavy snowfall over the central and eastern United States, Montly Weather Review, 94(11), 663-668.
10. Suriano, Z, & Leathers, D. J. (2017). Synoptic climatology of lake-effect snowfall conditions in the eastern Great Lakes region: synoptic climatology of lake-effect snowfall conditions. International Journal of Climatology, 37, 37: 4377-4389.
11. Mote, T., Gamble, D.W., Underwood, S.J., Bentley, M.L. (1997). Synoptic-Scale Features Common to Heavy Snowstorms in the Southeast United States, Weather and Forecasting, 12(1), 5-23.
12. Topuz, M., & Karabulut, M. (2016). Interrelation of Extreme Climatic Events with Air Masses in Antakya (Hatay, Turkey). International Journal of Humanities and Social Science Invention, 12;61-73.
13. Galanaki, E., Lagouvardos, K., Kotroni, V., Flaounas, E., & Argiriou, A. (2018). Thunderstorm climatology in the Mediterranean using cloud-to-ground lightning observations. Atmospheric Research, 207, 136–144.
14. Kurtulus, Y. F., & Acar, Z. (2021). Interannual variability of stormy day over Turkey. Journal of Geography, 42, 19-31.
15. Acar, Z , Gönençgil, B. (2022) Investigation of Extreme Precipitation indices in Turkey. Theorical and Applied Climatology, 147 (3-4). https://doi.org/10.1007/s00704-022-03971-3.
16. http://weather.uwyo.edu /upperair/sounding.html
17. https://meteologix.com/tr/reanalysis/ecmwf-era5
18. Britannica, T. Editors of Encyclopaedia (2020, March 28). wind. Encyclopedia Britannica. https://www.britannica.com/science/wind.
19. https://meteologix.com/tr/reanalysis/ecmwfera5/turkey/wind-mean-direction/20171113-1800z.html
20. https://www.meteociel.fr/modeles /archives/archives.php?day=13
21. https://www.ready.noaa.gov/ hypub-bin/trajasrc.pl
22. George, J.J. (1960). Weather Forecasting for Aeronautics. Academic Press, 410-415.
23. Stutevant, J.S. (1995). The Severe Local Storm Forecasting, Weather Scratch Meteorological Services; 1st edition. 978-096050408200.
24. Erinç, S. (1996). Klimatoloji ve Metodları, Alfa Yayınevi. İstanbul.
25. Erol, O. (1999). Genel klimatoloji (5. bs). İstanbul Üniversitesi yayınları no: Vol. 9. İstanbul: Çetinkaya Kitabevi.
26. Koçman, A. (1993). Türkiye İklimi, Ege Üniversitesi Edebiyat Fakültesi Yayınları: 72. İzmir.
27. http://weather.uwyo.edu/upperair
28. Flocas, H. A., Karacostas, Th. (2007). Cyclogenesis over the Aegean Sea: Identification and synoptic categories, Meteorological Applications, 3(1), 53-61.

International Journal of Engineering and Geosciences
https://dergipark.org.tr/en/pub/ijeg
e-ISSN 2548-0960

Evaluation of bioclimatic comfort area with heat index: A case study of Kocaeli

Efdal Kaya[*1]

[1]*Iskenderun Technical University, City and Region Planning, Türkiye*

Keywords
Bioclimatic Comfort
Heat Index
Inverse Distance Weight (IDW)
Kocaeli
QGIS 3.16 Software

Research/Review Article
DOI: 10.26833/ijeg.988452

Received: 30.08.2021
Accepted: 27.09.2021
Published: 13.04.2022

Abstract

The main reason for technological developments is to make human life more comfortable. Bioclimatic comfort areas are areas where people feel the most comfortable and comfortable in terms of climate. As a result of global climate changes, the temperature in the world is increasing day by day moreover increase in terms of people living in our country and other countries which the need for comfortable and comfortable spaces increases in all seasons. Bioclimatic comfort areas are the most needed in the summer months. However, the average temperature increases day by day in all seasons due to climate change. For this reason, within the scope of this study, the most suitable bioclimatic comfort areas were calculated with the HEAT index by using the average temperature and humidity maps for the fall, winter, spring, and summer seasons of 2019. While creating temperature and humidity maps, a point database was created for the neighborhoods in Kocaeli Province, temperature and humidity data were combined in this database. The temperature and humidity map for each season was open-source code the Inverse Distance Weighted (IDW) interpolation method in the QGIS 3.16 software was transformed into a map in raster format. The heat index was created by using temperature and relative humidity maps in raster format. Then, the relationship between the created heat index maps and morphological factors was examined.

1. Introduction

The most important factor affecting human life and relationships can be considered climate. Humans interact in various ways with their environment. It wants the environmental conditions to be suitable during this interaction. The suitability of these environmental conditions is directly related to the bioclimatic comfort zones.

When the accepted researches in the world are examined, people are comfortable in a certain temperature and humidity range and clean air environments. This range is defined as the comfort zone. Excessive or low temperature causes discomfort such as dry throat and burning in the eyes, as well as excessive humidity, which causes sweating and a feeling of suffocating warmth. In addition, the air in the environment should be clean and fresh. It is necessary to filter dust, smoke, pollen, and other harmful substances, and air circulation to bring clean air and remove polluted air [1].

The most appropriate values for the climatic comfort situation; For the summer months, the felt temperature values evaluated considering the absolute humidity are between 22.8 - 26.1 °C, while it is considered to be between 20.0 - 23.9 °C in the winter months. The temperature value ranges felt in the trial rooms were obtained subjectively with the experiments conducted on middle-aged groups. In these laboratory experiments, the individual's responses to temperature in indoor and outdoor environmental conditions were examined and the average temperature values felt were revealed.

The temperature felt by individuals in a space, which appears to be a completely separate atmospheric feature, is affected separately by all atmospheric features (humidity, wind, cloudiness, solar radiation, etc.). Due to this accumulative effect, the temperature of the air in an

* **Corresponding Author**
*(efdal.kaya@iste.edu.tr) ORCID ID 0000-0002-5553-0143

Cite this article
Efdal, K. (2023). Evaluation of bioclimatic comfort area with heat index: A case study of Kocaeli. International Journal of Engineering and Geosciences, 8(1), 19-25

area has a dominant effect on all beings in that area and represents all-climate elements [2- 12].

Factors affecting bioclimatic comfort; external factors are divided into three as factors that vary depending on the individual and other factors. External factors that affect bioclimatic comfort in an environment are air temperature, radiation, wind, and absolute humidity [13-18]. The parameters that vary depending on the individual are the temperature regulation of the metabolism depending on the activity, the activity level, and the clothing insulation [2, 3, 8, 11, 12, 19-28].

There are many approaches to calculating bioclimatic comfort. These approaches are generally based on the human heat balance model or the physiological approach. According to physiological approaches, the sum of the heat gained or produced by the body and the heat lost should be equal to zero. Factors with positive or negative values in this balance refer to the physiological and physical characteristics of the body and environmental factors [2-12, 29].

People spend a certain amount of energy to reach a bioclimatic comfort state or to adapt to their environment. According to the report of Çınar [30] the bioclimatic comfort state is; It is defined as the conditions in which a person can adapt to his environment by spending the least amount of energy. One of the most used methods in determining bioclimatic comfort is the "Bioclimatic Comfort Chart" developed by Olgyay [2-12, 19-26, 31].

According to Olgyay [32], the bioclimatic comfort value is; 21.0 – 27.5 °C temperature value in an open area, 30-65 % relative humidity and wind speeds up to 5 m/sec were taken as a combination and used in bioclimatic evaluation [2, 3, 6-12, 19-26].

In order to determine the bioclimatic comfort situation in space, first of all, it is necessary to determine and evaluate the temperature, relative humidity, radiation, and wind conditions. Besides these basic factors; The number of hot days, precipitation, diseases, and pests due to weather events, air pollution, and the amount of oxygen in the atmosphere also affect human comfort. "Bioclimatic Comfort" status can be determined by considering all of these effects [2, 3, 6-12, 19-26]. In this study, bioclimatic comfort areas were tried to be determined by using the heat index.

2. Bioclimatic Comfort

In many climatic indices, bioclimatic comfort status was evaluated depending on the combination of temperature, humidity, and wind elements, sometimes alone or all together. The most used criterion in determining comfort is 'Feel Temperature'. Thermal comfort is 80% effective in creating bioclimatic comfort. In this context, bioclimatic comfort has been examined as 'human temperature comfort' in many works of literature [21, 24-26, 31]. Bioclimatic comfort is accepted as the perceived temperature value of 17.0 – 24.9 °C depending on temperature, humidity, and wind in the middle latitudes where Turkey is located [22, 24-26, 34].

As Çınar [30] it is emphasized that the bioclimatic comfort status based on the temperature felt is a subjective value and varies according to space, time, and person. The temperature values felt at 15.0 – 27.0 °C in the evaluations; It was calculated for a person aged 25 years, indoors, with no health problems, normally dressed and not moving (Table 1). In outdoor conditions, these values can be 5°C, low or high.

Table 1. The temperature values felt in determining the bioclimatic comfort [21,22,24,25]

Sensed Temperature (°C)	Comfort Class
28>	Comfort is highly impaired
27-28	Comfort is disturbed
25-26.9	pass value (hot)
17-24.9	Comfort
15-16.9	pass value (cold)
15<	Comfort is disturbed

3. Method

The main material of the study are the climate data of Kocaeli Province. Climate data were obtained from the General Directorate of Meteorology. Kocaeli spatial boundary information was obtained from Kocaeli Metropolitan Municipality. The polygon data received from the relevant Municipality has been converted into a point database. A database was prepared for the analysis by assigning climate data to the database (Figure 1). The reason why the study was chosen as Kocaeli is that the climate of both the Marmara region and the Black Sea region is effective because it is located in the southern part of the Marmara Region. Materials used in the study: Temperature and relative humidity information for Kocaeli province.

WP1 Providing Data: The polygon type data obtained from Kocaeli Metropolitan Municipality was transferred to the QGIS 3.16 environment. It has been arranged by taking the average temperature and relative humidity values from the Provincial Meteorology Directorate. After the editing process was completed, it was saved in CSV format.

WP2 Transformation of Data: A dot was drawn in the middle of the polygon type data using QGIS 3.16 software. After the point data were prepared in excel and saved in CSV format, the average temperature and relative humidity values of the autumn, winter, spring, and summer months of 2019 were combined. By using the temperature and relative humidity values on the combined point data, it has been converted into a raster with the Inverse Distance Weighted interpolation method.

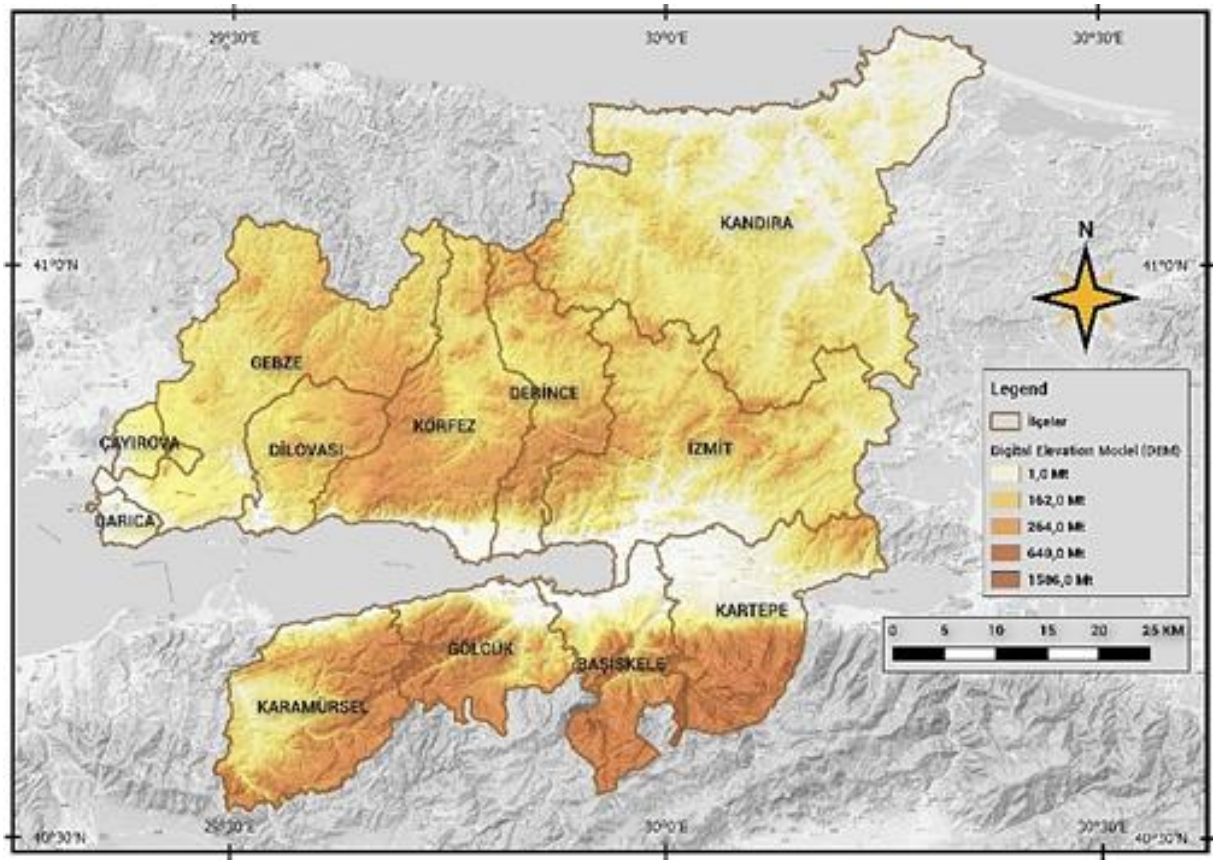

Figure 1. Location map of the study area

The workflow chart of the study is given in Figure 2.

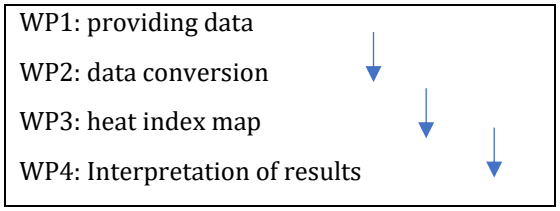

Figure 2. Work flow chart

WP3 Creating a Heat Index Map: The heat index is an index that combines the air temperature and relative humidity in shaded areas, the equivalent temperature perceived by the human, how warm it feels if the humidity is another value in the shade. The perceived air temperature is also known as the apparent temperature, the actual feel, or the felt temperature.

Effects of heat index (Shadow values)

• 26-32 °C caution: fatigue is possible with prolonged exposure and activity. Continued activity can cause heat cramps.

• 32-41 °C extreme caution: heat cramps and heat exhaustion are possible. Continued activity can cause heatstroke.

• 41-54 °C danger: heat cramps and heat exhaustion are likely. Heatstroke is likely with continued activity.

• hazard above 54 °C: heat stroke is inevitable.

How people are affected by temperature can be revealed with the heat index. The formula to be used during this study:

$$HI = 0.5 * \{T + 61.0 + [(T-68.0) * 1.2] + (RH*0.094)\}$$

HI: heat index
T: Temperature
RH: Relative Humidity

The calculation of the heat index is a refinement of a result obtained by multiple regression analysis conducted by lans P. Rothfusz [35] National Weather Service (NWS) technical supplement (SR 90-23). Rothfuss's regression equation, the symbol T represents the Fahrenheit unit of temperature measurement. The RH symbol represents relative humidity in percent and is the English abbreviation of relative humidity. However, if the temperature values in the heat index calculation are 80°F, the heat index calculations do not give accurate results, so Steadman's simplified formula is used [34].

While calculating the heat index, the calculation was made in °F in the first place, then the formula °C= (°F – 32) / 1.8 was converted to degrees Celsius (°C) in the raster calculator tool in QGIS 3.16.

4. Research Findings

The average temperature map and relative humidity maps required for the determination of bioclimatic comfort zones were created in Figure 3 and Figure 4 for each season in 2019.

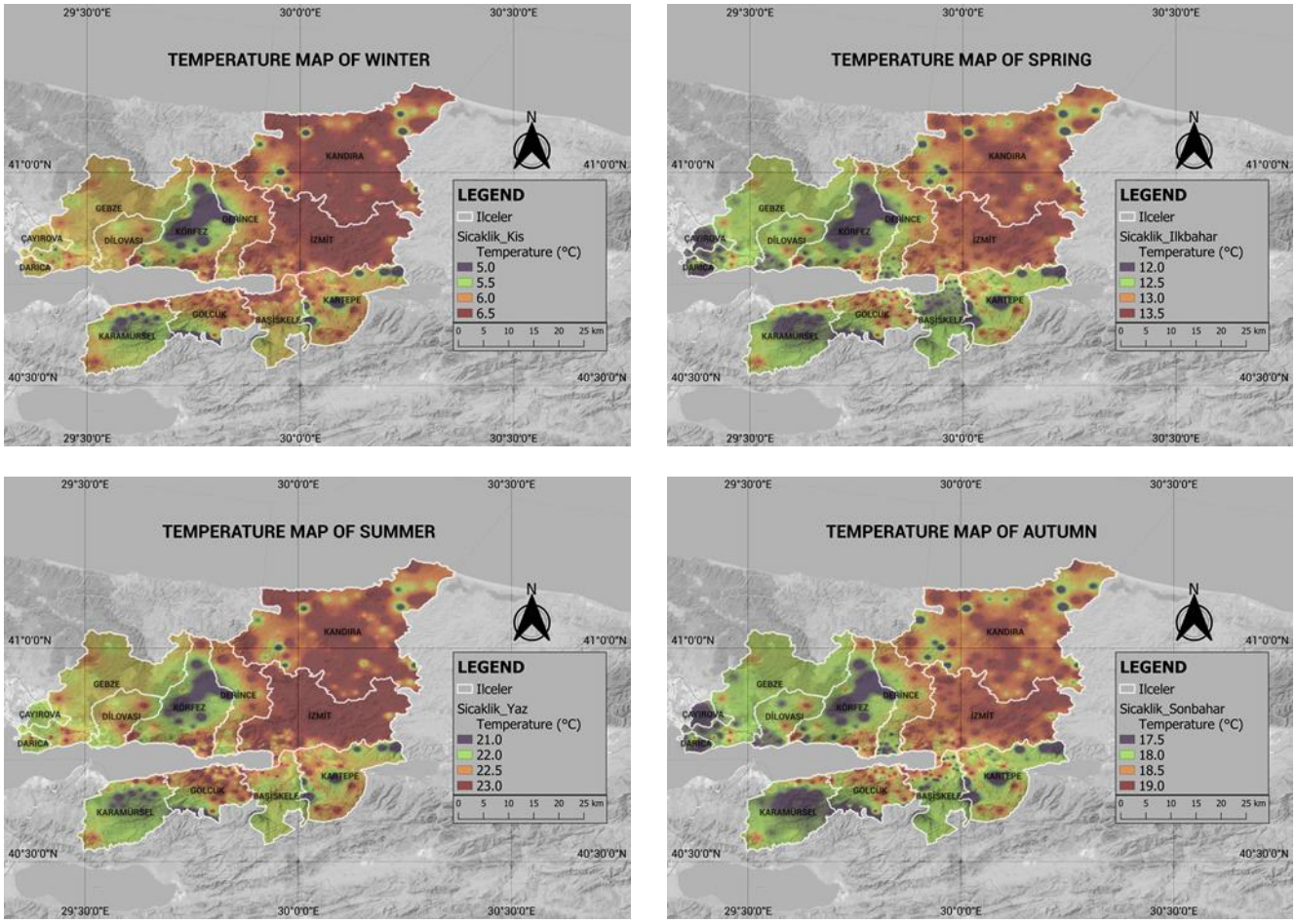

Figure 3. Average temperature maps for the four seasons of Kocaeli Province

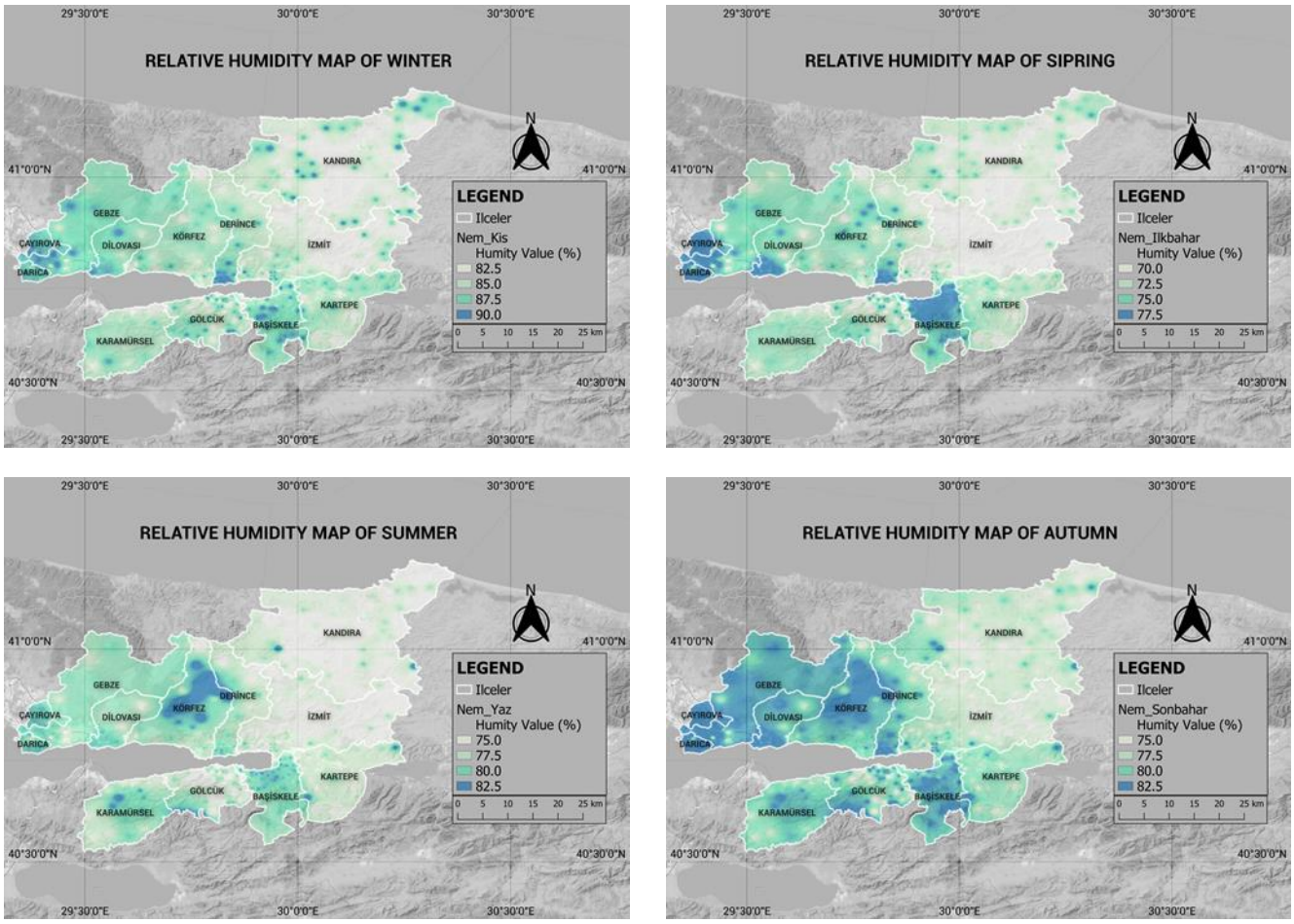

Figure 4. Average relative humidity maps for Kocaeli Province for four seasons

When the average temperature map is examined seasonally, the lowest temperature values for the autumn season are 14.58 °C, and the temperature values are low in the northern parts of the Gulf, Çayırova, Darıca, Dilovası, Gebze, and Karamürsel in the southern parts. The highest temperature is 20.16 °C in Izmit, Kandıra, Derince, partly in Gölcük and in the southern parts of Körfez District. In winter, temperatures vary between 7.77 and 2.04 °C. The lowest temperature in the winter period was observed in Çayırova, Körfez, Karamürsel, and partially in Gebze. The highest temperature is observed in İzmit, Kandıra, partially Gölcük Districts and northern parts of Başiskele District. The lowest temperature in the spring is seen in Başiskele, Çayırova, Darıca Districts and partially in Körfez District. The highest temperature is observed in İzmit, Kandıra, and partially Gölcük Districts. The lowest temperature in summer is seen in Başiskele, Çayırova, Darıca Districts and partially in Körfez and Gebze Districts. The highest temperature is observed in İzmit, Kandıra, and partially Gölcük Districts.

When the average relative humidity map is examined seasonally, the lowest humidity value for the autumn season is seen in Izmit, Kandıra Districts and partially in Gölcük, Karamürsel, Kartepe Districts. The highest humidity value is seen in Başiskele, Çayırova, Darıca, Derince, Dilovası and Gebze Districts.

The lowest humidity value in winter was seen in Izmit, Kandıra Districts and partially in Derince, Gölcük, Karamürsel, Kartepe and Körfez Districts. The highest humidity value is seen in Başiskele, Çayırova, Darıca, Dilovası and Gebze Districts.

The lowest humidity value in spring is seen in Izmit and Kandıra Districts, partially in Derince, Gölcük and Kartepe Districts. The highest humidity value is seen in Başiskele, Çayırova, Darıca, Dilovası, Gebze, Karamürsel, Körfez and partially Gölcük Districts.

The lowest humidity value in summer is seen in Izmit, Kandıra Districts, and partially in Derince and Gölcük Districts. The highest humidity value is seen in Başiskele, Çayırova, Darıca, Dilovası, Gebze, Karamürsel, Körfez and partially Gölcük Districts.

The bioclimatic comfort map created according to the heat index is shown in Figure 5.

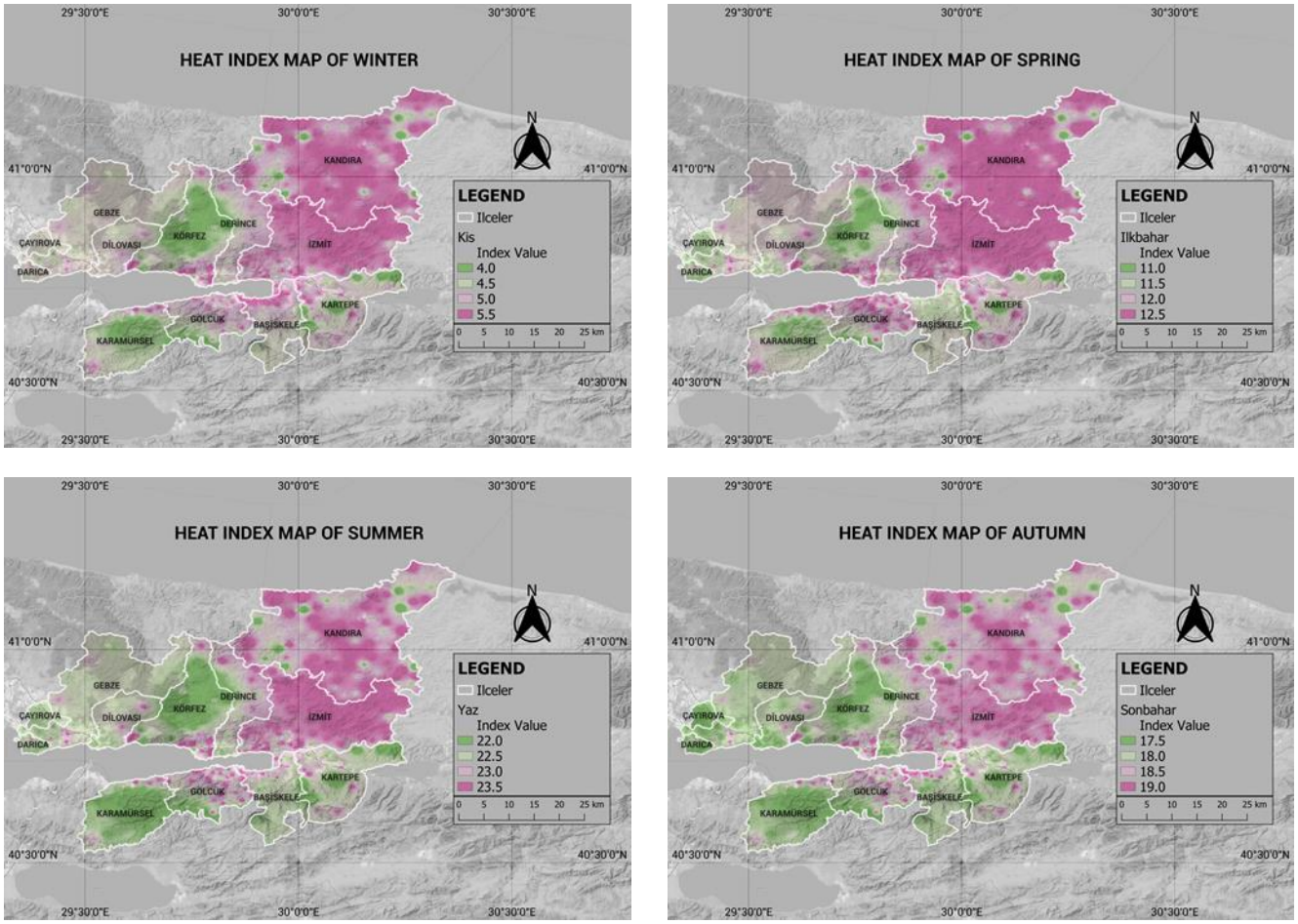

Figure 5. Bioclimatic comfort zone map according to the heat index

The relationship between comfort maps and topography was examined seasonally.

For the autumn season, the temperature index value in the high regions of Kartepe and Başiskele Districts is around 17 degrees. In the districts of Körfez, İzmit, Başiskele, and Gölcük near the sea, the temperature value is around 19 degrees.

For the winter season, the heat index value in the limited area in the districts in the high regions was around 5 degrees. The remaining fields have values close

to 0. In areas at altitudes close to the sea level, the temperature index was around 6 degrees.

For the spring season, the heat index value in the high regions was around 11 degrees. In areas at high sea level, the heat index was around 12.5.

For the summer season, there are very few places where the heat index value is high in high regions. In the regions close to the sea, especially in Gölcük, İzmit, and Körfez Districts, the temperature index is around 20 degrees, and the highest values are observed in the low-altitude seaside location of Gölcük District, almost all of the İzmit District and the majority of Kandıra District. This shows that they are the most uncomfortable areas according to the heat index in the summer seasons.

5. Discussion and conclusions

The seasonal heat index map for the province of Kocaeli for 2019 was created with relative humidity and temperature maps. There are many indices for the evaluation of bioclimatic comfort zones. With the heat index, comfort zones can be determined and they can shape the daily lives of living things.

According to the heat index results, the lowest heat index value for the autumn season is 14.3 degrees. The highest temperature is 20.3. It should not be exposed to a temperature for a long time in these range values. Fatigue is possible with activity.

According to the heat index results, the lowest heat index value for the winter season is 0.6 degrees. The highest temperature is 6.8. Since the air temperature is low, the heat index does not affect the winter season.

According to the heat index results, the lowest heat index value for the spring season is 8 degrees. The highest temperature is 13.6. When the heat index effects are examined, it is seen that it is comfortable.

According to the heat index results, the lowest heat index value for the summer season is 18.3 degrees. The highest temperature is 24.9. It should not be exposed to a temperature for a long time in these range values. Fatigue is possible with activity.

It should not be forgotten that the evaluation of the regions that provide bioclimatic comfort values in terms of settlement is very important for human health, and settlement areas should be determined by considering bioclimatic comfort in future planning studies for Kocaeli province.

Conflicts of interest

The authors declare no conflicts of interest.

References

1. Çınar, A. (2007). Psikometri nedir? Türk Tesisat Mühendisleri Derneği Isıtma, Soğutma, Havalandırma, Klima, Yangın ve Sıhhi Tesisat Dergisi, sayı 49 (s.ek 1-7).
2. Adiguzel, F., Cetin, M., Kaya, E., Simsek, M., Gungor, S., & Sert, E. B. (2020). Defining suitable areas for bioclimatic comfort for landscape planning and landscape management in Hatay, Turkey. Theoretical and Applied Climatology, 139(3), 1493-1503.
3. Bozdogan Sert, E., Kaya, E., Adiguzel, F., Cetin, M., Gungor, S., Zeren Cetin, I., & Dinc, Y. (2021). Effect of the surface temperature of surface materials on thermal comfort: a case study of Iskenderun (Hatay, Turkey). Theoretical and Applied Climatology, 144(1), 103-113
4. Cetin, M., Adiguzel, F., Gungor, S., Kaya, E., & Sancar, M. C. (2019). Evaluation of thermal climatic region areas in terms of building density in urban management and planning for Burdur, Turkey. Air Quality, Atmosphere & Health, 12(9), 1103-1112.
5. Cetin, M., Adiguzel, F., Kaya, O., & Sahap, A. (2018). Mapping of bioclimatic comfort for potential planning using GIS in Aydin. Environment, Development and Sustainability, 20(1), 361-375.
6. Cetin, M., Yildirim, E., Canturk, U., & Sevik, H. (2018). Chapter 25: investigation of bioclimatic comfort area of Elazig city centre. In book title: recent researches in science and landscape management. 324-333.
7. Cetın, M., & Zeren, I. (2016). Bioclimatic mapping of rural areas in Bozkurt, Turkey, for recreation. In VII International Scientific Agriculture Symposium," Agrosym 2016", 6-9 October 2016, Jahorina, Bosnia and Herzegovina. Proceedings (pp. 2924-2931). University of East Sarajevo, Faculty of Agriculture.
8. Cetin, M., & Zeren, I. (2016). Evaluation of the value of biocomfort for Kastamonu-Inebolu. In International conference GREDIT, 4-35.
9. Cetin, M., Sevik, H., & Zeren, I. (2017). Chapter 7_ Coastal biocomfort mapping for Doganyurt. OMICS, E-Books International, The Effects of Environmental Policies on Sustainability: Theory and Methods. Eds: Nurcan Kilinc-Ata, 51-55.
10. Gungor, S., Cetin, M., & Adiguzel, F. (2021). Calculation of comfortable thermal conditions for Mersin urban city planning in Turkey. Air Quality, Atmosphere & Health, 14(4), 515-522.
11. Zeren Cetin, I., Ozel, H. B., & Varol, T. (2020). Integrating of settlement area in urban and forest area of Bartin with climatic condition decision for managements. Air Quality, Atmosphere & Health, 13(8), 1013-1022.
12. Zeren Cetin, I. & Sevik, H. (2020). Investigation of the relationship between bioclimatic comfort and land use by using GIS and RS techniques in Trabzon. Environmental monitoring and assessment, 192(2), 1-14.
13. Atılgan İ., Ataer Ö. E. (2009). Isıl Konfor Analizinin Uygulanması. IX. Tesisat Mühendisliği Kongresi ve Sergisi Bildiri Kitabı, 571-581.
14. Fanger, P. O. (1972). Thermal comfort, analysis, and applications in environmental engineering. 5th Edition, McGraw-Hill,
15. Givoni B., (1976). Climate and Architecture. Van Nostrand Reinhold.
16. Höppe P. (1984). Die Energiebilanz des Menschen. Wiss. Mitt. Meteorol. Inst. Uni München, 43, 71- 75.

17. Landsberg H.E. (1972). The Assessment of Human Bioclimate, a Limited Reviewof Physical Parameters", World Meteorological Organization, Technical Note No.123, WMO-No. 331, 221-242.
18. Parsons K. C. (2003). Human thermal environments: the effects of hot, moderate, and cold environments on human health, comfort and performance. Taylor & Francis, 5, 258-271.
19. Çınar, İ., (1999). Fiziksel Planlamada Biyoiklimsel Veriler Kullanarak Biyokonforun Oluşturulması Üzerine Fethiye Merkezi Yerleşimi Üzerinde Araştırmalar. Yüksek Lisans Tezi, EÜ Fen Bilimleri Enstitüsü, 89s.
20. Cetin, M. (2019). The effect of urban planning on urban formations determining bioclimatic comfort area's effect using satellitia imagines on air quality: a case study of Bursa city. Air Quality, Atmosphere & Health, 12(10), 1237-1249.
21. Cetin, M. (2020). The changing of important factors in the landscape planning occur due to global climate change in temperature, Rain and climate types: A case study of Mersin City. Turkish Journal of Agriculture-Food Science and Technology, 8(12), 2695-2701.
22. Cetin, M. (2020). Climate comfort depending on different altitudes and land use in the urban areas in Kahramanmaras City. Air Quality, Atmosphere & Health, 13(8), 991-999.
23. Cetin, M. (2018, September). The finding of suitable biocomfort area mapping for Karabük City Center. In International Agricultural, Biological & Life Science Conference (pp. 295-299). 2018, September, Edirne.
24. Cetin, M. (2016). Determination of bioclimatic comfort areas in landscape planning: A case study of Cide Coastline. Turkish Journal of Agriculture-Food Science and Technology, 4(9), 800-804.
25. Cetin, M. (2015). Determining the bioclimatic comfort in Kastamonu City. Environmental monitoring and assessment, 187(10), 1-10.
26. Cetin, M., Topay, M., Kaya, L. G., & Yılmaz, B. (2010). Efficiency of bioclimatic comfort in landscape planning process: case of Kutahya. Süleyman Demirel Üniversitesi Orman Fakültesi Dergisi Seri A, (1), 83-95.
27. Matzarakis A., (2003). Assessing Climate for Tourism Purposes: Existing Methodsand Tools for The Thermal Complex. Meteorological Institute, University of Freiburg, 101-105.
28. Nikolopoulou M., Baker N., Steemers K. (2001). Açık alanlardaki kentsel alanlarda termal konfor: insan parametresini anlama. Solar Energy, 70(3),227-235
29. Blazejczyk K. (2005). New indices to assess thermal risks outdoors. [in:] I. Holmér, K.Kuklane, Ch. Gao (red.), Environmental Ergonomics XI", Proc. Of the 11th International Conference, 222-225, 22-26 May.
30. Çınar, İ. (2004). Biyoklimatik Konfor Ölçütlerinin Peyzaj Planlama Sürecinde Etkinliği Üzerinde Muğla-Karabağlar Yaylası Örneğinde Araştırmalar. Doktora tezi, Ege Üniversitesi Fen Bilimleri Enstitüsü, İzmir, 227s.
31. Evans, J. M. (2003). Evaluating comfort with varying temperature: a graphic design tool, Energy and Bulding, 35(2003) 87-93.
32. Olgyay, V., (1973). Desıgn wıth Clımate, Bıoclimatic Approach to Archıtectural Regıonalism. Prınceton Universsıty Press, New Jersey.
33. Koçman, A. (1991). İzmir'in Kentsel Gelişimini Etkileyen Doğal Çevre Faktörleri ve Bunlara İlişkin Sorunlar, Coğrafya Araştırmaları Dergisi, 3 s: 101, İzmir.
34. Steadman, R. G. (1994). Norms of Apparent Temperature in Australia. Aust. Met. Mag. 43, 1–16.
35. Rothfusz L. P., (1990). The Heat Index Equation (or, More Than You ever wanted to know about heat index). Technology Attachment, SR/SSD 90-23, NWS S. Reg. Headquarters, Forth Worth, TX.

International Journal of Engineering and Geosciences
https://dergipark.org.tr/en/pub/ijeg
e-ISSN 2548-0960

New approaches for outlier detection: The least trimmed squares adjustment

Hasan Dilmaç [*1], **Yasemin Şişman** [1]

[1]*Ondokuz Mayıs University, Department of Geomatics Engineering, Türkiye*

Keywords
The Least Square
Outliers
Robust Estimation
The Least Trimmed Squares

Research Article
DOI: 10.26833/ijeg.996340

Received: 18.09.2021
Accepted: 19.11.2021
Published: 13.04.2022

Abstract

Classical outlier tests based on the least-squares (LS) have significant disadvantages in some situations. The adjustment computation and classical outlier tests deteriorate when observations include outliers. The robust techniques that are not sensitive to outliers have been developed to detect the outliers. Several methods use robust techniques such as M-estimators, L_1- norm, the least trimmed squares etc. The least trimmed squares (LTS) among them have a high-breakdown point. After the theoretical explanation, the adjustment computation has been carried out in this study based on the least squares (LS) and the least trimmed squares (LTS). A certain polynomial with arbitrary values has been used for applications. In this way, the performances of these techniques have been investigated.

1. Introduction

In geodesy, for different purposes, many kinds of observations are done. Physical and geometric quantities such as angles, distances, heights, and gravity are measured and processed. In this case, a great number of data appears [1]. A quantity is always measured differently even though it is measured many times under the same conditions [2]. It is clear that observations are never equal to real value and they always contain an error. Thus, it is preferred that the observation number is bigger than the unknown number. In this case, the optimum solution must be made for a unique solution according to an aim function. This process is named adjustment computation [3-4].

The least-square (LS) is a conventional method for adjusting surveying measurements. It is one of the most adopted methods because of tradition and ease of computation [5-6]. But, outliers (observations with different distribution compared to the distribution of majority) negatively affect the LS method results [7].

Outliers in the observation group are encountered very often in applications [6]. The adjustment results with classical methods, which should meet some conditions like the normal distribution, are deteriorated. So, these outliers must be detected and eliminated from the observation group. Outlier tests are based on classical methods like Data-Snooping, Pope test and t-test [8-10]. These outlier tests are not robust against outliers. Therefore, new statistical methods have been sought instead of LS, which is sensitive to outliers [11].

The robust statistics deals with developing estimators insensitive to inconsistencies from basic assumptions in classical models [12]. Robust methods aim to find the results that would be found without outliers in the LS method to overcome the effects of outliers. Then, outliers can be detected through their residuals [13]. Many robust techniques have been developed. These techniques can be divided into classes by concepts of high-breakdown point, influence function, etc.

There are a lot of studies done on robust statistics. Some of them are assocaited with L_1-norm and M-estimators and some are associated with the other robust techniques [14-27].

The least trimmed squares (LTS) that is going to be emphasized in this study is a high-breakdown point estimator [6]. This study performs adjustment computations and outlier detection according to LS and LTS methods in different scenarios. Then, LS and LTS have been compared to determine the advantages and disadvantages of the methods.

* **Corresponding Author**

*(hasan.dilmac@omu.edu.tr) ORCID ID 0000-0001-6877-8730
(ysisman@omu.edu.tr) ORCID ID 0000-0002-6600-0623

Cite this article

Dilmaç, H., & Şişman, Y. (2023). New approaches for outlier detection: The least trimmed squares adjustment. International Journal of Engineering and Geosciences, 8(1), 26-31

2. Method and Material

2.1. Method

2.1.1. Adjustment Computation

The adjustment computation is performed to obtain unique values for the unknowns when there are redundant observations in a problem [28]. The adjustment is only performed when the observation number is more than the unknown number [4]. An objective function is selected to find the unique optimum solution [29]. Adjustment computation performed according to the objective function is an optimization problem, which minimizes the selected function [30]. A mathematical model representing the mathematical relationship of observations and unknowns is established [31]. The mathematical model accounts for an essential part of adjustment computation, and it is usually composed of two parts: a functional model and a stochastic model. When observations are made, a functional model is typically chosen to represent the physical situation. The stochastic model determines variances and covariances of the observations [3, 4, 28]. In the classical Gauss-Markov model, the functional and stochastic model can be expressed as below:

$$\begin{aligned} v &= Ax - l \\ P &= Q_{ll}^{-1} = \sigma_0^2 C_{ll}^{-1} \end{aligned} \quad (1)$$

Here $v, A, x, l, P, \sigma_0^2$ and C_{ll} are the residual vector, the coefficient matrix, unknown vector, the observation vector, the weight matrix, a priori variance, and the covariance matrix, respectively.

If the functional and stochastic models are correct, the adjustment computation gives optimal results [3].

2.1.2. The Least Squares Method

The LS is a method used in adjustment computation by minimizing the sum of the squared weighted residuals to get unique values with redundant measurements [4,32]. The objective function of LS can be given as follows:

$$v^T P v = \sum_{i=1}^{n} p_i v_i^2 \rightarrow min \quad (2)$$

where n is the number of observations. The steps of adjustment computation can be illustrated as in Figure 1.

The main problem of LS is that even one outlier might severely affect the LS method [33]. LS can propagate errors from one observation to another observation. Therefore, masking and swamping effects occur if there is more than one outlier in the data. A bad observation could seem like a good one because of the propagation of errors; this is called a masking effect. On the contrary, the good observation could seem bad; this is called the swamping effect [7]. There are classical outlier tests to detect outliers depending on the LS. Baarda test (Data-Snooping, W-test), Pope test (Tau test) and t-test are most common in geodesy [8,9,10,34,35,36]. Because the classical outlier tests are based on the LS, the results of these tests can be affected by outliers, too.

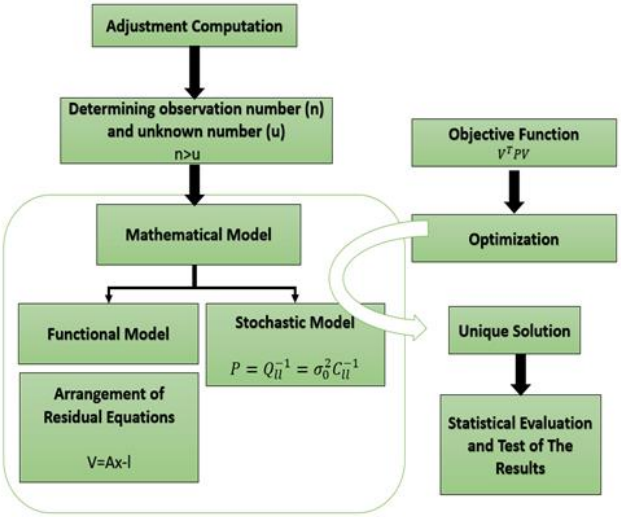

Figure 1. The steps of adjustment computation

2.1.3. Robust Estimation and Outlier Detection

Real data sets may contain outliers [37]. Therefore, robust methods that cannot be affected easily by outliers should be developed. Robustness usually means insensitivity to outliers [38].

There are many robust methods. L_1-norm is the oldest method of these robust methods. Then, M-estimators, R-Estimators, and L-Estimators appeared [6]. To compare the robustness of these methods, the 'breakdown point' concept has been used. The breakdown point means the smallest number of outliers, which may affect an estimator negatively [39]. The robust methods mentioned above don't have a high-breakdown point [6]. Because of this, generalised M-Estimators was developed. Then, Repeated Median, The Least Median of Squares (LMS) [40], S-Estimators, MM-Estimators, and The Least Trimmed Squares (LTS) were developed respectively [19,41,42].

2.1.4. The Least Trimmed Squares

The LTS was presented by Rousseeuw in 1987. This method is quite similar to LS except that the largest squared residuals are removed from the data [21]. The objective function of LTS can be given the following:

$$Min \sum_{i=1}^{h} P_i v_i^2 \quad (3)$$

Here, h is called as trimming constant and it determines the breakdown point of the LTS [43].

When h is approximately $h = \left[\frac{n}{2}\right] + \left[\frac{p+1}{2}\right]$ (n, number of observations; p, the number of regression parameters), the best robustness is achieved [6]. The LTS problem tries to find which result has the minimum sum of the squared residuals from $S = \binom{n}{h}$ subset of LS solutions [39]. There are two ways to solve the LTS

problem: Exact LTS solution and Approximate LTS solution. The exact LTS solution includes the searching through all subsets of S. But it is hardly possible to solve the Exact LTS solution unless the data size is small enough. On the other hand, the Approximate LTS solution searches through a certain number of subsets of S. [44,45]. In this study, the Exact LTS solution was selected because the data size is small enough.

The step of the Exact LTS solution can be illustrated as in Figure 2.

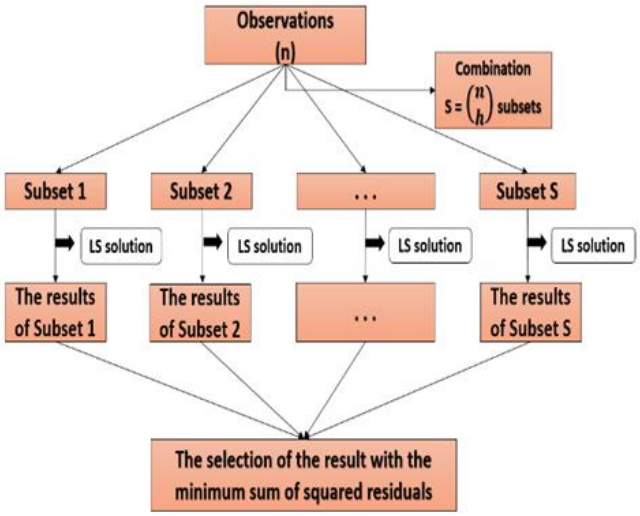

Figure 2. The steps of Exact LTS solution

In the first step, h is determined. Then, $S = \binom{n}{h}$ subsets are obtained. For all subsets, LS method is performed. Finally, the subset with a minimum sum of squared residuals is selected, and this subset's results are used.

2.2. Material

In numerical applications, a regression model such as $y = ax^2 + bx + c$ was used.

Here, a, b and c are regression coefficients. x is the independent variable; y is the dependent variable.

Regression coefficients a, b and c were taken as 2,3 and 5, respectively and y values were calculated according to x values that were chosen arbitrarily for ten observations. Two applications were made by adding random error and gross error to observations. In Application 1, both LS and LTS methods were performed using x and y values with random errors ($\pm 0 - 1$ unit interval). In LTS, h was taken as eight and $\binom{10}{8}$ solutions were made because two observations in the dataset would be simulated as the outlier. In Application 2, gross errors ($+5$ and $+10$ units) were added to y values (observations 3 and 9, respectively) and the outliers were simulated explicitly in this way to compare LS and LTS. Then, LS and LTS methods were performed again using those values. Additionally, classical outlier tests were applied to LS results to detect the outliers. Matlab was used for these solutions.

3. Results

When there is no outlier in observations, the results of LS and LTS are close to the real values and each other. (Table 1). This can be concluded by looking at regression parameters (a, b and c). But if examined more carefully, the regression parameters of the LTS are more accurate except c parameter.

Table 1. The regression results of Application 1

Methods	a	b	c	[VV]
LS	2.03	2.77	5.15	2.13
LTS	2.00	3.09	4.52	0.89

In Application 2, it is clear that the results of the LS are quite contaminated, and the sum of residuals squared increased very much (Table 2). The coefficients b and c of the LS in Application 2 are quite different from expected. The regression parameters of LTS in Application 2 has the results much closer to simulated parameters (2, 3 and 5, respectively) when compared to that of LS in Application 2. Also, the sum of residuals squared is relatively much smaller. It can be seen that the outliers affected the results of the LS regression in Application 2.

Table 2. The regression results of Application 2

Methods	a	b	c	[VV]
LS	2.23	0.28	12.82	89.49
LTS	2.06	2.51	5.44	1.53

Classical outlier tests were applied to detect outliers in the LS method in Application 2. Test values of observations and table values were computed and compared. Classical outlier tests are iterative and detect one outlier (observation with the highest test value) each time. So, two iterations were made in total. Observation 9 was detected as an outlier in Iteration 1 (Table 3).

Table 3. Iteration 1 results of the LS with classical outlier tests in Application 2

Observation	Test Value	Table Value	Result
1	0.1528	2.3646	Observation 9 is an outlier
2	0.0848		
3	0.4089		
4	0.6009		
5	0.1333		
6	2.2771		
7	0.2423		
8	0.1795		
9	12.5992		
10	0.1476		

In Iteration 2, there is no outlier detected. All test values are smaller than the table value (Table 4).

Table 4. Iteration 2 results of the LS with classical outlier tests in Application 2

Observation	Test Value	Table Value	Result
1	0.2875		
2	1.7702		
3	2.3752		
4	0.3710	2.4469	There is no outlier.
5	0.5186		
6	1.7479		
7	1.1552		
8	1.5683		
10	0.1169		

LS method and the classical outlier tests were affected by masking and swamping effects. Although the sum of residuals squared decreased, the regression parameters (especially *b* and *c*) are not close to their real values (Table 5).

Table 5. The regression results of LS results after the classical outlier tests in Application 2

Methods	a	b	c	[VV]
LS	2.15	1.65	7.0355	3.26

LTS method doesn't need classical outlier tests to detect outliers because the trimmed subset with the minimum sum of squared residuals tells us that the removed observations could be an outlier. Observations 3 and 9 were detected as an outlier in LTS method of Application 2. The results are presented in Table 6.

The residuals of the LS regression in Application 1 are small as expected. The effects of outliers on the residuals for the LS in Application 2 can be seen in Figure 3. It is seen that the gross errors added to the Observation 3 were distributed to the other observations in the LS method as a result of distribution of error.

Observations 3 and 9 were simulated as an outlier and classical outlier tests based on the LS method could detect only Observation 9 as outlier correctly. The error in Observation 3 was distributed to the other observations again. Therefore, it could not be detected as outlier (Figure 4).

Table 6. The outlier detection results of the LTS in Application 2

Observation	V (Residuals of Observations)	Result
1	0.1360	Observations 3 and 9 have the largest value of residuals. So, they are removed.
2	-0.6501	
4	-0.0890	
5	-0.6136	
6	0.1842	
7	0.7493	
8	-0.0458	
10	0.3291	

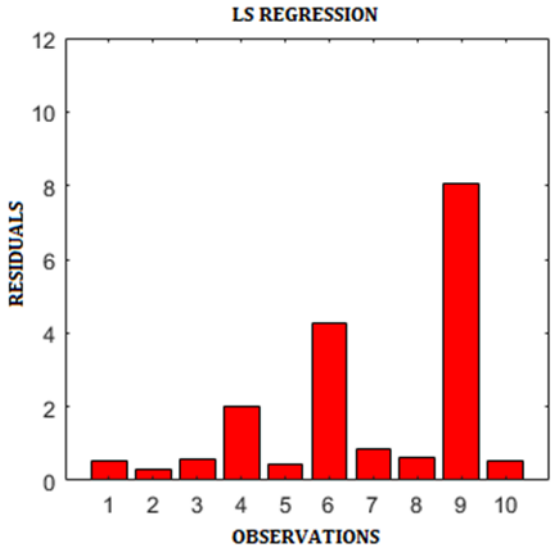

Figure 3. The residuals of the LS in Application 2 with all observations

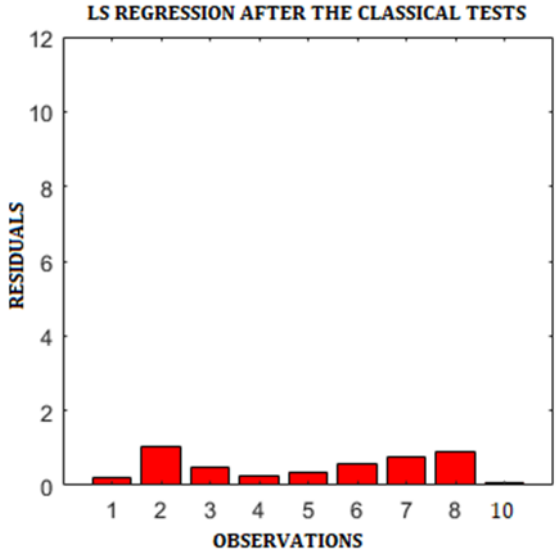

Figure 4. The residuals of the LS in Application 2 after the classical outlier tests

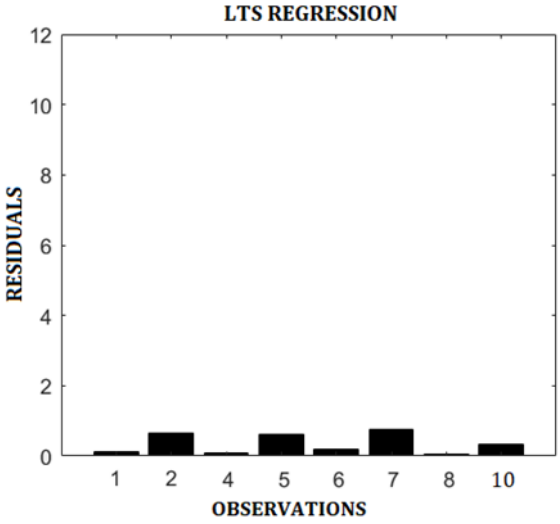

Figure 5. The residuals of LTS in Application 2

The outliers 3 and 9 were detected in the LTS and they were removed from the datasets. (Figure 5) The observations that are removed from the dataset in LTS could be interpreted as an outlier. But, the true selection of the trimming constant h plays a significant role in this. If h is not selected in a way that does not reflect the exact number of outliers, good observations may be removed from the datasets as in Application 1.

4. Discussion and Conclusion

In geodesy, the LS is usually used for adjustment computation. LS results are sufficient when there is no outlier in the observation group. But outliers may occur in observation. Because of this, robust methods have been developed. In this study, the LTS, which is a robust method and the LS were performed.

A regression model was used in this study to analyse the LS and the LTS method results using different scenarios. In Application 1, observations with only random errors were used. The LS and the LTS methods gave good results. But it can be said that the LTS has a little better result when the regression parameters in Table 1 are examined. The parameter a, b except c are closer to their real values and the sum of residuals squared of LTS is relatively smaller. In Application 2 where the simulated outliers were used, while LS results were affected badly from outliers, LTS results gave results close to ones in Application 1.

LTS results might be as good as LS results when observations do not contain any outliers. But it must be noted that the LTS could lead good observations to be eliminated from the dataset simultaneously. Therefore, it is essential to know exactly whether the dataset contains outliers and how many outliers it contains. On the other hand, the LTS can give much better results than the LS when observations have outliers because the LS method can distribute the outlier effect to the other points. It can be said that the LTS method could be more effective in general when compared to the LS. Besides, if the rate of outliers in a dataset is approximately or exactly known, the LTS can detect the outliers correctly without any additional outlier test.

Author contributions

Hasan Dilmaç: Conceptualization, Methodology, Writing-Original draft preparation, Software, Field study, Visualization **Yasemin Şişman:** Validation, Investigation, Writing-Reviewing and Editing.

Conflicts of interest

The authors declare no conflicts of interest.

References

1. Fan, H. (1997). Theory of errors and least squares adjusment. Royal Institute of Technology, 72, 100-44, Stockholm, Sweden.
2. Ingram, E. L. (1911). Geodetic surveying and the adjustment of observations (methods of least squares). McGraw-Hill Book Company, Inc. 370 Seventh Avenue, New York.
3. Ghilani, C. D. (2017). Adjustment computations: Spatial data analysis (Sixth edition). John Wiley ve Sons, Inc., Hoboken, New Jersey.
4. Mikhail, E. M. & Ackermann, F. E. (1976). Observations and least squares. Thomas Y. Crowell Company, Inc. 666 Fifth Avenue, New York.
5. Čížek, P. & Víšek, J. Á. (2005). Least Trimmed Squares. XploRe®—Application Guide,49-63. Springer, Berlin, Heidelberg.doi: 10.1007/978-3-642-57292-0_2
6. Rousseeuw, J. R. & Leroy, A. M. (1987). Robust Regression and Outlier Detection. John Wiley ve Sons, Inc.
7. Hekimoglu, S. (2005). Do Robust Methods Identify Outliniers More Reliably Than Conventional Tests for Outliniers? Zeitschrift für Vermessungwesen, 3, 174-180.
8. Baarda, W. (1968). A testing procedure for use in geodetic networks. Netherlands Geodetic Com., New Series, Delft, Netherlands, 2(5).
9. Pope, A. J. (1976). The statistics of residuals and the detection of outliers. NOAA Technical Report. NOS 65 NGS 1, U. S. Dept. of Commerce, Rockville, Md.
10. Koch, K. R. (1999). Parameter Estimation and Hypothesis Testing in Linear Models. 2nd Ed. Springer-Verlag, Berlin-Heidelberg, New York.
11. Yetkin, M. & Berber, M. (2013). Application of the sign-constrained robust least-squares method to surveying networks. Journal of Surveying Engineering, 139:1, 59-65. http://doi.org/10.1061/(ASCE)SU.1943-5428.0000088
12. Fabozzi, F. J., Focardi, S. M., Rachev, S. T. & Arshanapalli, B. G. (2014). *The Basics of Financial Econometric: Tools, Concepts and Asset Management Applications*. John Wiley ve Sons, Inc.
13. Rousseeuw, P. J. & Hubert, M. (2018). Anomaly detection by robust statistics. Wiley Interdisciplinary Reviews: Data Mining and Knowledge Discovery, 8:2, e1236. http://doi.org/10.1002/widm.1236
14. Bektas, S. & Sisman, Y. (2010). The comparison of L1 and L2-norm minimization methods. International Journal of the Physical Sciences, 5:11, 1721-1727. http://doi.org/10.5897/IJPS
15. Erdogan, B. (2014). An outlier detection method in geodetic networks based on the original observation. Boletim de Ciencias Geodesicas, 20:3, 578-589, http://doi.org/10.1590/S1982-21702014000300033
16. Giloni, A. & Padberg, M. (2001). Least Trimmed Squares Regression, Least Median Squares Regression and Mathematical Programming. *Matmetical and Computer Modelling*, 35:9-10, 1043-1060. http://doi.org/10.1016/S0895-7177(02)00069-9
17. Gui, Q. & Zhang, J. (1998). Robust biased estimation and its applications in geodetic adjustments. Journal of Geodesy, 72:7-8, 430-435. http://doi.org/10.1007/s00190005 0182
18. Hekimoglu, S. & Erenoglu, C. (2007). Jeodezik Ağlarda Uyuşumsuz Ölçülerin Klasik Yaklaşım ve Robust

Yöntemlerle Belirlenmesi. Jeodezi ve Jeoinformasyon Dergisi, 97, 3-14.
19. Hubert, M., Rousseeuw, P. J. & Van Aelst, S. (2008). High-breakdown robust multivariate methods. Statistical science, 23:1, 92-119. http://doi.org/10.1214/088342307000000087
20. İnal, C. & Yetkin, M. (2006). Robust yöntemlerle uyuşumsuz ölçülerin belirlenmesi. Selçuk Üniversitesi Mühendisler-Mimarlar Fakültesi Dergisi, 21, 3-4.
21. Knight, N. L. & Wang, J. (2009). A comparison of outlier detection procedures and robust estimation methods in GPS positioning. The Journal of Navigation, 62:4, 699-709 http://doi.org/10.1017/S0373463309990142
22. Sisman, Y. (2010). Outlier measurements analysis with the robust estimation. Scientific Research and Essays, 5:6, 668-678.
23. Sisman, Y. (2011). Parameter estimation and outlier detection with different estimation methods. Scientific Research and Essays, 6:7, 1620-1626 http://doi.org/10.5897/SRE10.1181.
24. Susanti, Y., Pratiwi, H., Sulistijowati, S., & Liana, T. (2014). M estimation, S estimation, and MM estimation in robust regression. International Journal of Pure and Applied Mathematics, 91:3, 349-360. http://doi.org/10.12732/jipam. v91i3.7
25. Valero, J. L. B., & Moreno, S. B. (2005). Robust estimation in geodetic networks. Física de la Tierra, 17, 7.
26. Yang, Y. (1999). Robust estimation of geodetic datum transformation. Journal of Geodesy, 73:5, 268-274. http://doi.org/10.1007/s001900050243
27. Yetkin, M. & Inal, C. (2011). L1 norm minimization in GPS networks. Survey Review, 43:323, 523-532. http://doi.org/10.1179003962611x131177 48892038
28. Ogundare, J. O. (2018). Understanding Least Squares Estimation and Geomatics Data Analysis. John Wiley ve Sons, Inc, 111 River Street, Hoboken, NJ 07030, USA
29. Sisman, Y. & Bektas, S. (2012). Linear regression methods according to objective functions. Acta Montanistica Slovaca, 17:3, 209-217.
30. Grafarend, E. W. & Sansò, F. (Editors) (2012). Optimization and design of geodetic networks. Springer Science & Business Media, Heidelberg, Berlin.
31. Schaffrin, B. (2019). Notes on Adjustment Computations Part I.
32. Wells, D., & Krakiwsky, E. (1971). The Method of least squares. University of New Brunswick: Canada
33. Muhlbauer, A., Spichtinger, P., & Lohmann, U. (2009). Application and comparison of robust linear regression methods for trend estimation. *Journal of Applied Meteorology and Climatology,* 48:9, 1961-1970. http://doi.org/10.1175/2009JAMC1851.1
34. Hekimoğlu, Ş., Erdogan, B., Soycan, M., & Durdag, U. M. (2014). Univariate Approach for Detecting Outliers in Geodetic Networks. Journals of Surveying Engineering, 140:2, 04014006, 1-8. http://doi.org/10.1061/(ASCE)SU.19435428.0000123
35. Kavouras, M. (1982). On the detection of outliers and the determination of reliability in geodetic networks. Department of Surveying Engineering Technical Report No. 87, University of New Brunswick, Fredericton, N.B., November.
36. Sisman, Y. (2005). Uyuşumsuz Ölçü Gruplarının Belirlenmesi Yöntemleri. Harita Dergisi, 133.
37. Rousseeuw, J. R. (1990). Robust estimation and identifying outliers. Handbook of statistical methods for engineers and scientists, 16-1.
38. Huber, P. J. (1981). Robust Statistics. John Wiley and Sons, Inc.
39. Hofmann, M., Gatu, C., & Kontoghiorghes, E. J. (2010). An Exact Least Trimmed Squares Algorithm for a Range of Coverage Values*, Journal of Computational and Graphical Statistics,* 19:1, 191-204, http://doi.org/10.1198/jcgs.2009.07091
40. Rousseeuw, P. J. (1984). Least Median of Squares Regression. Joırnal of the American Statistical Association, 79:388, 871-880. http://doi.org/10.1080/016 21459.1984.10477105
41. Toka, O., & Cetin, M. (2011). The comparing of S-estimator and M-estimators in linear regression. *Gazi University Journal of Science,* 24, 4, 747-752
42. Staudte, R. G., & Sheather, S. J. (2011). *Robust estimation and testing*. John Wiley ve Sons, Inc, 918.
43. Cizek P (2005). Least trimmed squares in nonlinear regression under dependence. *Journal of Statistical Planning,* 136, 3967-3988, http://doi.org/10.1016/j.jspi.2005.05.004
44. Cizek, P., & Visek, J. A. (2000): Least trimmed squares, SFB 373 Discussion Paper, No. 2000, 53, Humboldt University of Berlin, Interdisciplinary Research Project 373: Quantification and Simulation of Economic Processes, Berlin.
45. Rousseeuw, P. J., & Van Driessen, K. (2006). Computing LTS Regression for Large Data Sets. Data Min Knowl Disc 12, 29-45. https:/doi.org/10.1007/s10618-005-0024-4

International Journal of Engineering and Geosciences
https://dergipark.org.tr/en/pub/ijeg
e-ISSN 2548-0960

Investigating the length, area and volume measurement accuracy of UAV-Based oblique photogrammetry models produced with and without ground control points

Erdem Emin Maraş [*1], **Mohammad Noman Nasery** [2]

[1] *Samsun University, Department of Flight Training, Türkiye*
[2] *Ondokuz Mayis University, Department of Geomatics Engineering, Türkiye*

Keywords
Oblique photogrammetry
UAV
Photogrammetry
GCP

Research Article
DOI: 10.26833/ijeg.1017176

Received: 03.11.2021
Accepted: 21.02.2022
Published: 13.04.2022

Abstract

This study aimed to investigate the performance and sensitivity of 3D photogrammetric models generated without GCPs (ground control points). To determine whether the models with no GCPs retained accuracy in all terrain types as well as under varying climate or meteorological conditions, two separate studies were conducted in two areas with different characteristics (elevation, slope, topography, and meteorological differences). The study areas were initially modelled with GCPs and were later modelled without GCPs. Furthermore, some of the dimensions and areas within the modelled regions were measured using terrestrial techniques (with GPS/GNSS) for accuracy analyses. After regional modelling was conducted with and without GCPs, different territories with different slopes and geometric shapes were selected. Various length, area and volume measurements were carried out over the selected territories using both models (generated with and without GCPs). The datasets obtained from the measurement results were compared, and the measurements obtained using the models produced with GCPs were accepted as the true values. The length measurement results provided various levels of success. The first study area exhibited very promising length measurement results, with a relative error less than 1% and an RMSE (root mean square error) of 0.139 m. In the case of the area measurements, in the first study area (Sivas), a minimum relative error of 0.04% and a maximum relative error of 1.05% with an RMSE of 1.264 m^2 were obtained. In the second study areas (Artvin), a minimum relative error of 0.56% and a maximum relative error of 5.27% with an RMSE of 1.76 m^2 were achieved. Finally, in the case of the volume measurements, for the first study area (Sivas), a minimum relative error of 0.8% and a maximum relative error of 6.8% as well as an RMSE of 2.301 m^3 were calculated. For the second study area (Artvin), the minimum relative error of the volume measurements was 0.502%, and the maximum relative error was 2.01%, with an RMSE of 7.061 m^3.

1. Introduction

Photogrammetry, especially digital photogrammetry, is a versatile tool used for aerial surveys and is rapidly becoming the tool of choice for generating 3D realistic models from 2D photos for different engineering projects. Three-dimensional modelling via digital photogrammetry is based on a combination of vertical and inclined imagery. Oblique photogrammetry offers improved capabilities for the 3D reconstruction of different surfaces and terrains. Three-dimensional models obtained via oblique photogrammetry have widespread uses in different engineering fields, and their application area is expanding daily due to recent advances in technology, hardware, and software development. Currently, digital photogrammetry has numerous potential applications in areas such as surveying, civil engineering, urban planning, architecture, archaeology, mining, mass movement monitoring, industry, urban management, agriculture, and real estate.

Digital photogrammetry or three-dimensional (3D) mapping, the most famous discipline of the digital age, is expanding quickly and intensely around the world due to the low-cost facilities required for data acquisition and rapid workflow. Basically, UAV photogrammetry makes

* **Corresponding Author**

*(erdem.maras@samsun.edu.tr) ORCID ID 0000-0002-5205-1622
(nmnnasery@gmail.com) ORCID ID 0000-0000-0000-0000

Cite this article

Maraş, E. E., & Nasery, M. N. (2023). Investigating the length, area and volume measurement accuracy of UAV-Based oblique photogrammetry models produced with and without ground control points. International Journal of Engineering and Geosciences, 8(1), 32-51

the three-dimensionally (3D) reconstruction of objects via two-dimension (2D) photos possible. In addition, a model produced via oblique photogrammetry does not aim to just view and display the output object but also provides accurate geometric and spatial information about the object. In oblique photogrammetry, UAVs (unmanned aerial vehicles), also known as drones, are used to obtain aerial imagery. Recently, UAV photogrammetry has been used in different areas such as cultural heritage documentation [1-2], agriculture [3-4], architectural restoration [5-6], archaeology [7-8], mining [9-10], coastal habitat monitoring [11], and urban and infrastructure planning [12]. Older, challenging data acquisition methods have been eliminated by photogrammetry. Since 2D cadastre information does not meet today's needs, the world is moving into the 3D cadastre system, the name of which clearly shows that 3D information is needed for its applications and that such information could be supplied just with oblique photogrammetry [13-14]. Three-dimensional photogrammetric modelling plays an important role in designing three-dimensional city models as well as in urban management applications, especially during the city planning stage, it helps urban planners make optimal city plans.

Yılmaz [15] stated that the insufficiency of two-dimensional cadastre information for solving the problems occurring due to the lack of three-dimension information reveals the need for 3D cadastre implementation. Mueed Choudhury [16] used UAV-based oblique photogrammetry for the purpose of determining the characteristics of city trees, modelling a specific area for this purpose and determining the characteristics of city trees through this three-dimensional model. Wu et al. [17] used a new method in which aerial images were combined with terrestrial images, and they obtained good 3D city models with proper building geometries to obtain better 3D city models. One study called "Quantifying uncertainties in snow depth mapping from structure from motion photogrammetry in an alpine area" used the structures obtained from motion photogrammetry to characterise spatial uncertainties in snow depths [18]. For this purpose, a study was conducted at the Combe de Laurichard, which is located in the French Alps. Two different dates, June 1st, 2017 and October 5th, 2017, were chosen (one snow-on and one snow-off condition) for aerial data acquisition, and two DEMs (digital elevation models) from two datasets were constructed and compared; in this study, a method was presented for calculating spatially varying estimates of the snow depth precision and detection limits using repeated UAV surveys. Chudley et al. [19] called "High-accuracy UAV photogrammetry of ice sheet dynamics with no ground control points", the application of an alternative SFM-MVS (structure from motion-multi-view stereo) geolocation method called GNSS-supported aerial triangulation was presented; in this method, a carrier-phase GNSS receiver located onboard geo-references the SFM-MVS point cloud, significantly reducing the need for GCPs. Considering various flight configurations such as linear strips, radial strips and curved strips, the diverse obtained datasets were evaluated in terms of the density of the extracted point clouds and the distance between the reconstructed surface and control points [20].

Tomaštik et al. [21] conducted a study using a flight in the study area in which there was a 300-metre height difference; the vegetation cover in this region was forests. In this study, RMSE values were obtained as a result of comparing products such as orthophotos and digital surface models (DSMs) produced GCPs and without using GCPs, with these control points determined in the field. The RMSE values obtained by using GCP were between 8 cm and 20 cm horizontally and between 16 cm and 62 cm vertically. When the RMSE values obtained without using GCP were examined, the authors determined that, while the values varied between 6 cm and 9 cm horizontally, they varied between 8 cm and 15 cm vertically.

He et al. [22] obtained RMSE values of 1-3 cm horizontally and 4 cm vertically in a study area with different terrain types. Gerke and Przybilla [23] obtained horizontal and vertical RMSE values below 10 cm without using GCPs on a land surface with a maximum height difference of 50 metres. At the same time, they obtained similar results by using GCPs.

Türk and Öcalan [24], after establishing and marking 9 GCPs in the campus of Sivas Cumhuriyet University, a photogrammetric flight was performed by UAV equipped with PPK. Images obtained from this flight were processed by Pix4D, a photogrametric processing software, following different strategies as: with GCPs and without GCPs. The accuracy of the ortho-image produced using GCPs was obtained as 3.6 cm in horizontal and 5.0 cm in vertical.

2. Definition of problem

As a matter of fact, GCPs are a mandatory factor used to generate an accurate photogrammetric model, but what if GCPs cannot be marked due to location inaccessibility issues, such as lands with high slopes (canyons) or vertical structures (dam bodies), insufficient project budgets, areas with landslide risks or some other hazardous field situations such as glaciated environments? Modelling such land terrains and structures with GCPs is sometimes impossible or requires a vast budget. Should a photogrammetric model without GCPs be deemed as accurate as a model utilizing GCPs for some engineering applications?

3. The aim of this study

The purpose of this paper is to indicate the usability of photogrammetric models generated without GCPs in some engineering application such as length, area, and volume measurements.

For this purpose, two different areas with different characteristics were modelled with and without GCPs. The areas and lengths of these areas were measured using orthophotos, and the volumes were calculated from DEMs.

The measurements mentioned above were conducted over the same areas in both models produced with and without GCPs, and the results are discussed in detail.

4. Methods

A DJI Phantom 4 Pro Drone with a GPS/GLONASS satellite positioning system, a vertical hover accuracy of ±0.1 m and a horizontal hover accuracy of ±1.5 m and a 20 MP (Mega Pixel) camera were used for data acquisition in this study. In contrast, the use of real-time kinematic or post-processing kinematic enabled GNSS devices allows to improve the spatial accuracy to a range of several centimeters [25]. DJI Terra's Oblique Mission uses 5 flight routes to capture the same amount of data as that obtained using 5 cameras simultaneously on a drone. The 5 flight routes correspond to the 5 camera headings – downward, forward, backward, leftward, and rightward.

To measure the GCPs, a GEOMAX Zenith40-type GPS/COARS with 72 channels (GPS/GLONASS) was used in conjunction with a Maximum 36 satellite signal receiver; the satellite signal tracking capacity of GPS is L1, L2, L2C, and that in GLONASS is L1, L2.

The GNSS raw data were post-processed by RTKLib open-source software in the carrier-phase differential mode with respect to the CHC X91 model GNSS receiver mentioned in Section 5.1 as base station. The ratio of epochs with a fixed solution to total epochs of the GNSS trajectory solution is 99.17% and the mean standard deviation along x, y and z axes amounts to 8.4, 5.5 and 9.6 mm, respectively.

DJI RTK systems offer, due to the availability of the original satellite observation data as well as ephemeris data, the possibility of an improved position determination in post-processing. The necessary calculations can be performed using the free software RTKLIB [26]. RTKLIB is an open-source program package for standard and precise positioning with GNSS. RTKLIB consists of a portable program library and several APs (application programs) utilizing the library.

5. Case study

To investigate the usability of 3D (three-dimensional) photogrammetric models generated without GCPs, two studies were conducted in two different provinces of Turkey with different characteristics. The first area, Sivas, is located in southern Turkey with an elevation of 1650 m (above sea level), and the second area, Artvin, is located in north-eastern Turkey with an elevation of 450 m. The large elevation difference between these two regions as well as other varying factors such as meteorological differences, slope differences, terrain topography differences, etc., are applied to investigate whether the studied principle is applicable everywhere. The two areas were modelled one time with GCPs and another time without GCPs. The data acquisition process in both areas was as follows.

5.1. Sivas

This study region is presented in Fig. 1; research was conducted in Şuğul Canyon, located in the Sivas province of Turkey. Oblique imagery of this study area was obtained, and with the help of these data, the area was modelled with and without GCPs to compare the sensitivities of the two models in measuring the lengths, areas and volumes of the same regions.

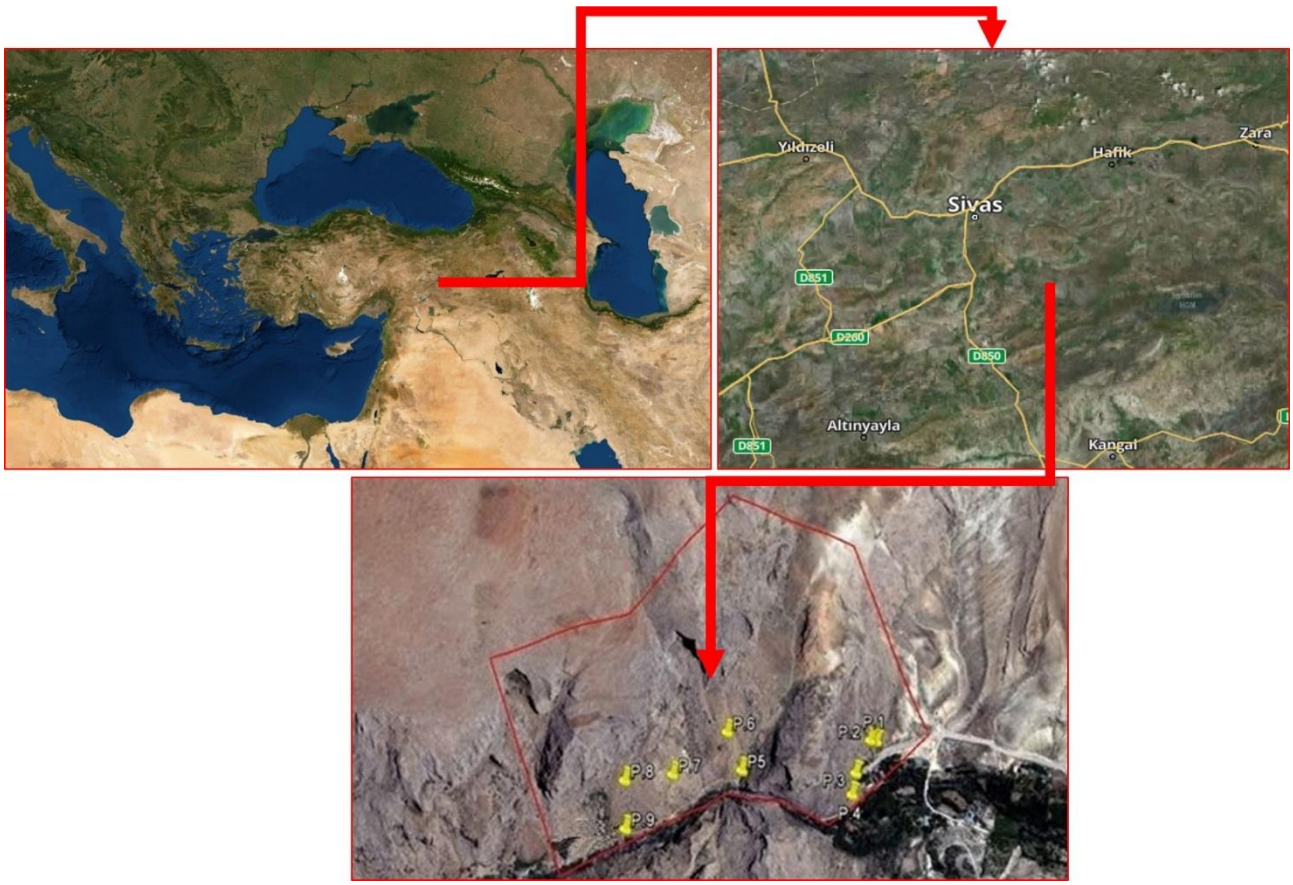

Figure 1. First study area Sivas, Gürün, Şuğul Canyon, Turkey

Figure 2. DJI Phantom 4Pro model UAV and CHC X91 model RTK-GNSS receiver used for data acquisition

Figure 3. Marking and measuring GCPs

To model the area with the oblique aerial photogrammetry method, a DJI Phantom 4 Pro model UAV was used (Fig. 2). Nine well-distributed GCPs were used to geo-reference the model. The GCP measurements were conducted with an RTK-GNSS receiver (CHC X91 GNSS model).

First, 9 well-distributed ground control points were established in the study area; during the establishment of these points, care was taken to ensure that they could easily be seen in the photos and were located away from any natural or artificial objects such as trees and buildings that would prevent these points from appearing in the pictures (Fig. 3).

After establishing the GCPs, the locations of these points were recorded in the Turkish National Reference System as TUREF/TM36 (ITRF96 in the universal system as EPSG: 5256) with a sensitivity of 2 cm; the obtained coordinates are given in Table 1.

Next, the flight plan and flight time were determined. Because the study area was mountainous, the appropriate flight time was determined as 12:00–14:00. Selecting this time frame allowed the effect of shading that would cause errors in the photogrammetric evaluation to be minimized. A DJI Phantom 4 Pro model UAV was used for the aerial photography; this Phantom 4 Pro was equipped with a 20-MP camera that could take photos with 4K quality and had a 1-inch sensor. The DJI Phantom 4 Pro model UAV camera is presented in Fig. 4.

Table 1. Coordinate list of ground control points

Point No.	X (m) East	Y (m) North	Z (m) Ellipsoidal Height
P.1	607223.539	4292394.086	1401.258
P.2	607217.702	4292407.654	1409.344
P.3	607141.923	4292390.866	1394.211
P.4	607094.008	4292376.559	1391.703
P.5	606994.953	4292671.055	1446.086
P.6	606986.964	4292597.873	1407.067
P.7	606845.780	4292703.114	1445.776
P.8	606793.686	4292683.833	1415.525
P.9	606664.304	4292784.330	1447.985

Figure 4. Phantom 4Pro UAV camera

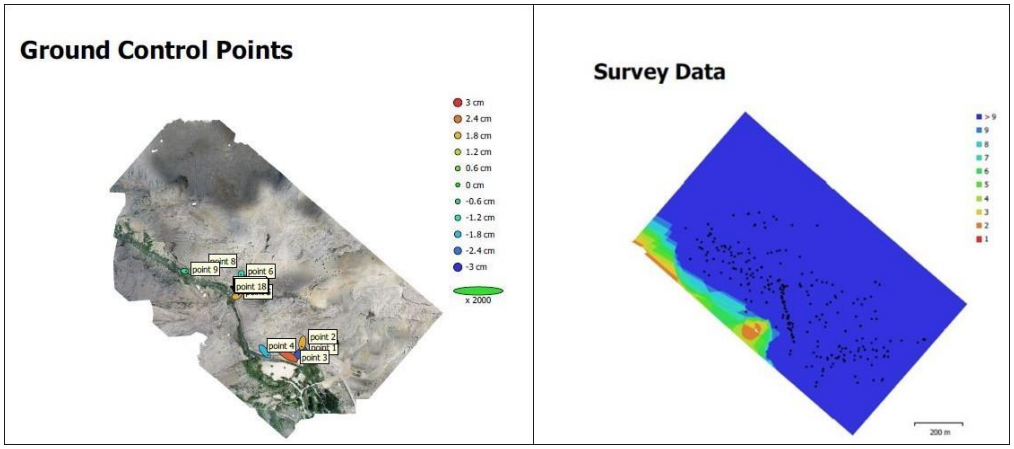

Figure 5. GCP positions and image overlap

The images were taken with the above-described UAV, and nadir and oblique images of the study area were obtained. The overlap in the imagery was 85%, and the forward overlap was 80%; these overlap percentages are sufficient to represent the topography and to virtually reconstruct the study area in three dimensions. The GCP positions and image overlap ratios are given graphically in Fig. 5.

The internal orientation parameters and camera calibration values used in the photogrammetric evaluation phase are presented in Table 2. The F values listed in this table indicate the focal length of the camera, Cx-Cy coordinates of the prime point, B1-B2 non-orthogonal transformation coefficients, K1-K2-K3 radial distortion values, and P1-P2 tangential distortion values. The GCP errors calculated by the Agisoft/Metashape and are given in Table 3.

Afterwards, the obtained aerial photographs were subjected to a photogrammetric evaluation, and the measured GCP coordinates were also used during this evaluation. Finally, the geometry of the subject area was reconstructed formally and computationally in virtual form. As a result of the evaluation, a dense cloud including 8,193,681 points with global coordinates, a 3D model, and an orthophoto and digital elevation model were obtained, as shown in Fig. 6.

Interpolation is a mathematics and statistical approach to estimation problems. In addition, in digital terrain modelling, interpolation is used to determine the elevation value of a given point benefiting from the known elevations of neighbouring points. There are two implicit assumptions behind interpolation techniques:

- The land surface is continuous and smooth.
- There is high correlation among neighbouring data points.

Interpolation is a basic technique in digital terrain modelling because it can be applied within various phases of the modelling process, such as in surface reconstructions, quality control, accuracy assessments, land analyses and implementations. In this study, a digital terrain model was produced by linear interpolation.

After a 3D model was generated with GCPs, a 3D model of the work area was again generated, this time without GCPs. The three-dimensional models created with and without GCPs are not presented separately as they are not visually different from each other.

5.2. Artvin

The second study site was the Artvin dam built on the Çoruh River, which is located in the Artvin province of Turkey (Fig. 7). Three-dimensional models of the area were generated by oblique photogrammetry, once with and once without GCPs.

To model this study area via aerial photogrammetry methods, a DJI Phantom 4 Pro model UAV was used. Five GCPs were used to geo-reference the model. The GCP measurements were conducted with a TRIMBLE R6 GPS (CORS/GNSS) receiver (Fig. 8). The coordinates of the GCPs were recorded in the Turkish National Reference System as TUREF/TM42 (3-degree) (ITRF96 in the universal system as EPSG: 5258) with a sensitivity of 2 cm, and the obtained coordinates are given in Table 4.

Table 2. Correlation matrix calculated by the Agisoft/Metahshape software

	Value	Error	F	Cx	Cy	B1	B2	K1	K2	K3	P1	P2
F	**3656.51**	0.04	1.00	0.00	0.20	-0.28	0.04	-0.21	0.25	0.23	0.00	-0.19
Cx	**-4.57**	0.08		1.00	0.01	-0.02	0.04	0.01	0.00	0.00	0.94	-0.01
Cy	**18.41**	0.06			1.00	-0.21	0.00	-0.03	0.02	-0.02	0.00	0.85
B1	**-7.25**	0.02				1.00	0.02	-0.02	0.00	0.00	-0.01	0.06
B2	**0.36**	0.02					1.00	0.00	0.00	0.00	-0.12	0.01
K1	**0.01**	0.01						1.00	-0.97	0.91	0.00	-0.04
K2	**-0.01**	0.01							1.00	-0.97	0.91	0.02
K3	**0.02**	0.01								1.00	0.00	-0.02
P1	**-0.01**	0.01									1.00	-0.01
P2	**-0.01**	0.01										1.00

Table 3. GCP errors calculated by the Agisoft/Metashape software

Label	X error (cm)	Y error (cm)	Z error (cm)	Total (cm)	Image (pix)
P.1	1.273	1.163	-2.676	3.184	0.320 (17)
P.2	-0.265	-1.345	1.950	2.384	0.299 (21)
P.3	-2.428	1.455	2.572	3.825	0.333 (15)
P.4	1.162	-1.346	-1.782	2.518	0.198 (22)
P.5	0.637	0.363	1.899	2.036	0.117 (5)
P.6	-0.113	-0.228	-1.186	1.213	0.201 (17)
P.7	-0.694	-0.402	0.301	0.858	0.087 (5)
P.8	0.479	-0.046	-0.851	0.977	0.067 (6)
P.9	0.017	0.190	0.491	0.527	0.063 (7)
Total	**1.058**	**0.912**	**1.727**	**2.221**	**0.246**

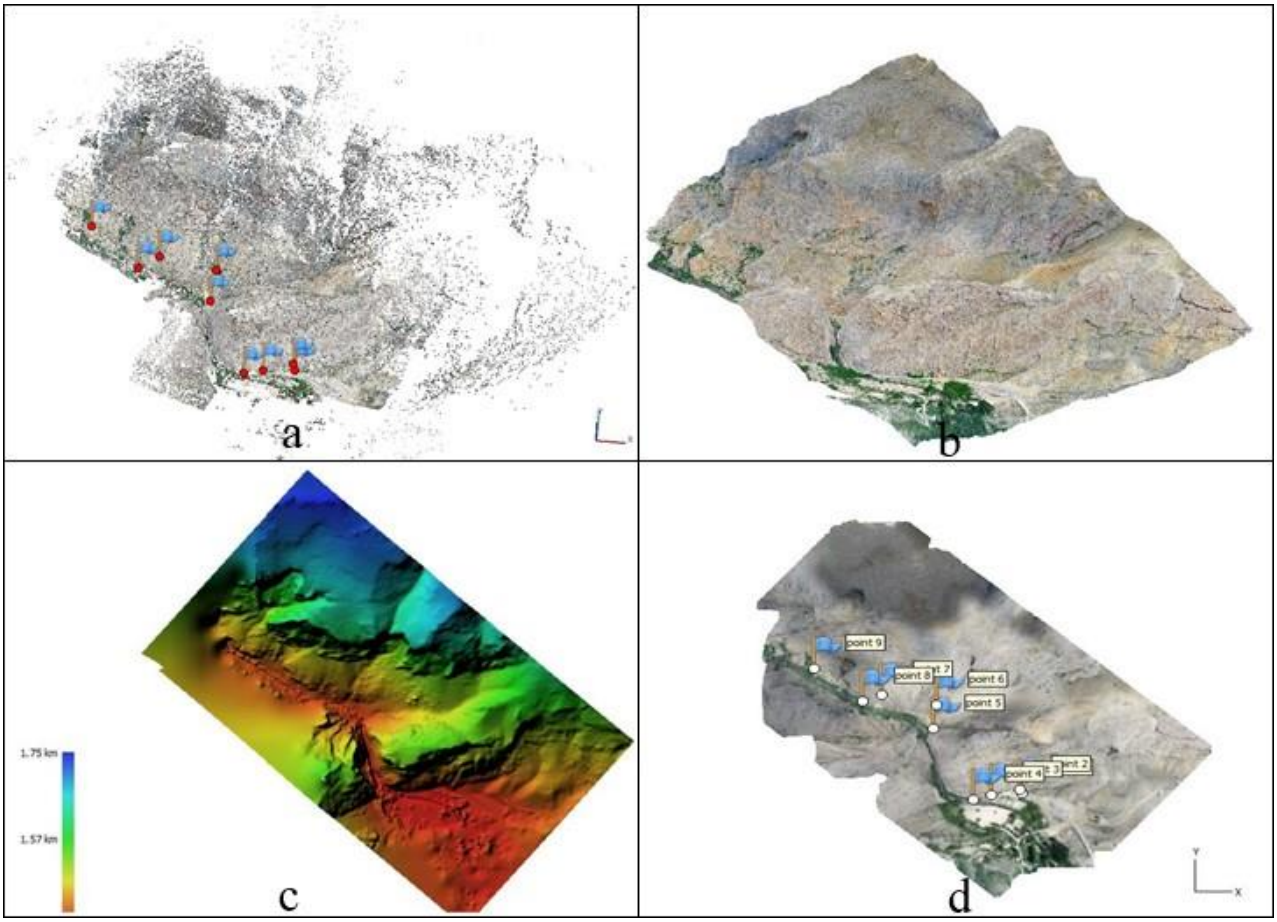

Figure 6. Results of photogrammetric evaluation a) Tie Points b) 3D model c) Digital Elevation Model d) Orthophoto

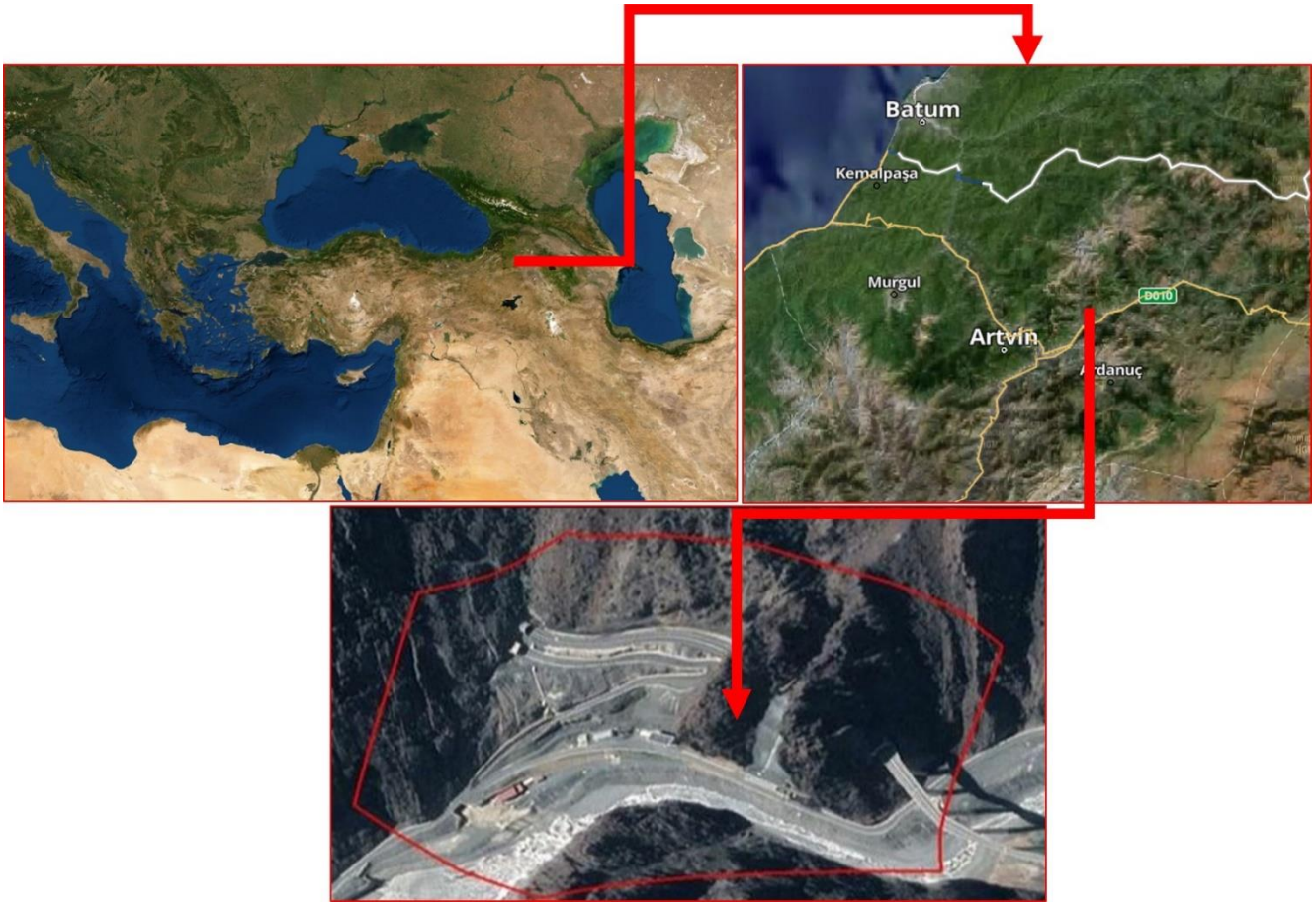

Figure 7. Second Study area Turkey, Artvin, Artvin Dam

Table 4. GCP coordinate list

Point No.	X (m) East	Y (m) North	Z (m) Ellipsoidal Height
P1	480173.041	4534136.386	408.183
P2	480193.098	4534080.037	395.799
P3	480188.260	4533962.940	397.686
P4	480112.801	4534002.926	442.610
P5	480095.596	4533966.277	446.039

Figure 8. Equipment used to obtain datasets

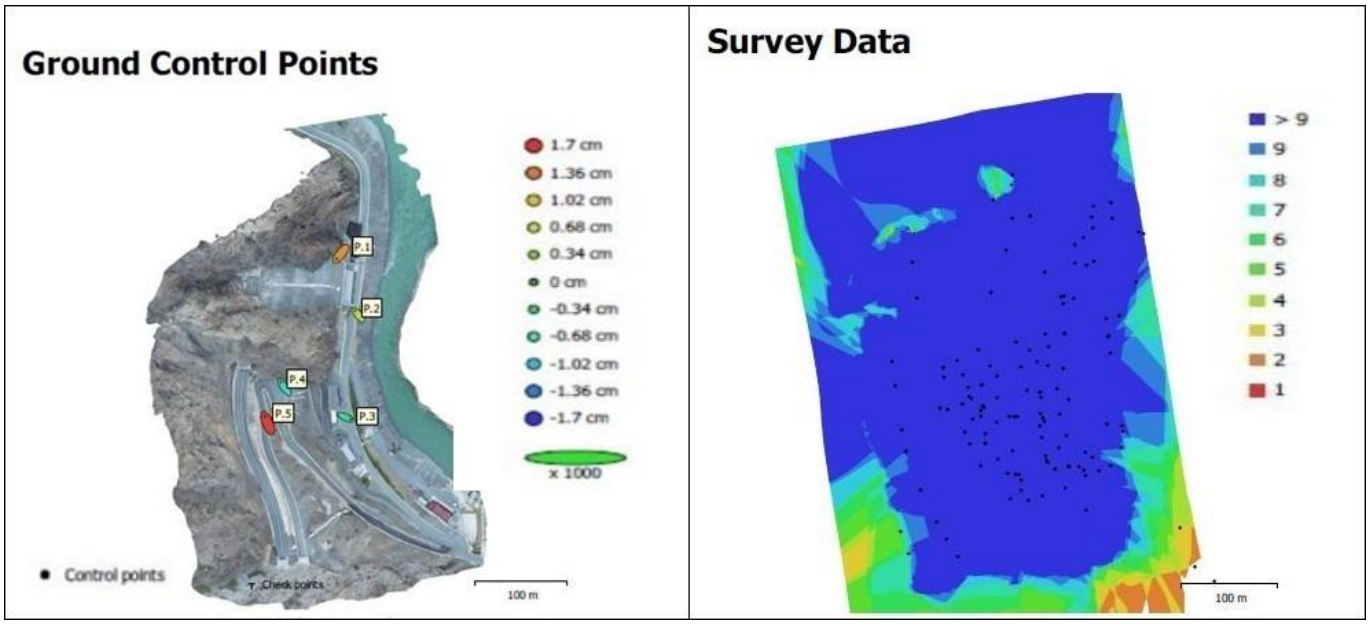

Figure 9. GCPs positions and image overlaps Orthophoto

The imagery was derived using the UAV in accordance with photogrammetric principles, and as a result, nadir and oblique images were obtained. The overlap in the imagery was 85%, and the forward overlap was 80%; these overlap percentages are sufficient to represent the topography and to virtually reconstruct the study area in three dimensions. The GCP positions and image overlap ratios are given in Fig. 9.

The positions and errors of the GCPs used during the photogrammetric evaluation, the image overlap ratios, the camera calibration coefficients and the correlation matrix are shown graphically in Fig. 9. The correlation matrix is given in Table 5. The GCP position errors were also calculated and are listed in Table 6.

Afterwards, the obtained aerial photographs were processed in accordance with photogrammetric principles, and the measured GCP coordinates were also used during the photogrammetric processing of the images. Finally, geometry of the subject area has been reconstructed formally and computationally in virtual form. As a result of this process, a dense cloud including 18,958,130 points with global coordinates, a 3D model, an orthophoto and a digital elevation model were obtained, as shown in Fig. 10.

After reconstructing the study area virtually in three dimensions using GCPs, a 3D model was generated without GCPs. The 3D models created with and without GCPs are not presented separately as they are not visually different from each other.

Table 5. Correlation matrix calculated by the Agisoft/Metashape software

	Value	Error	F	Cx	Cy	B1	B2	K1	K2	K3	P1	P2
F	**3649.93**	0.05	1.00	0.01	0.35	-0.09	0.05	-0.33	0.34	-0.31	-0.07	0.06
Cx	**-3.28**	0.06		1.00	0.12	0.03	0.04	0.01	-0.02	0.02	0.69	-0.23
Cy	**16.63**	0.06			1.00	-0.06	0.06	-0.03	0.01	0.00	0.32	-0.31
B1	**-0.28**	0.02				1.00	0.01	0.01	-0.02	0.02	0.01	-0.01
B2	**0.21**	0.02					1.00	0.00	0.00	0.00	-0.10	0.03
K1	**0.01**	0.01						1.00	-0.97	0.93	0.01	-0.01
K2	**-0.04**	0.01							1.00	-0.99	-0.02	0.01
K3	**0.07**	0.01								1.00	0.02	-0.01
P1	**-0.01**	0.01									1.00	0.79
P2	**-0.01**	0.01										1.00

Table 6. GCP position errors given by the Agisoft/Metashape software

Label	X error (cm)	Y error (cm)	Z error (cm)	Total (cm)	Image (pix)
P.l	-0.93064	-1.11915	1.23013	1.90573	0.321 (18)
P.2	-0.68080	0.83722	0.64880	1.25912	0.206 (21)
P.3	1.10243	-0.46048	-0.47225	1.28468	0.425 (14)
P.4	-0.78656	1.07360	-0.71107	1.50895	0.543 (8)
P.5	-0.61781	1.47969	1.62688	2.28427	0.245 (32)
Total	**0.84206**	**1.04953**	**1.03049**	**1.69484**	**0.320**

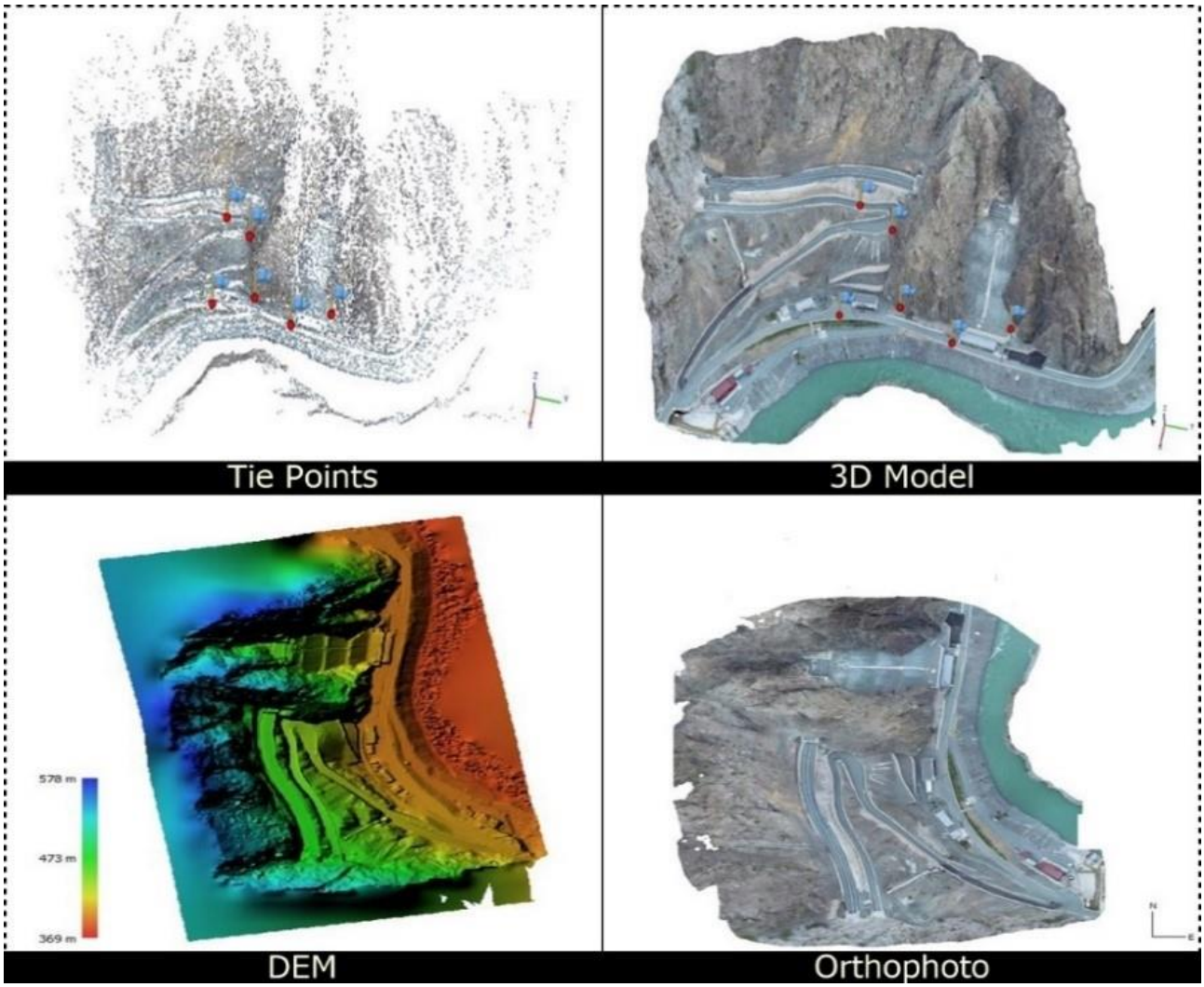

Figure 10. Tie Points, 3D Model, Digital Elevation Model and Orthophoto

6. Findings and Examination

In this section, an accuracy assessment is initially conducted for the models generated with GCPs. Afterwards, a comparison study is done among the final 3D models (one with GCPs and other without GCPs) obtained from the photogrammetric process. The length, area and volume measurements are selected as the comparison criteria. These measurements were collected in different areas using the models generated with and without GCPs, and at the end, these results were compared to the corresponding measurement conducted with terrestrial methods (GPS/GNSS), and the results are compared in detail.

6.1. Assessment of the length, area and volume measurements

6.1.1. First study area (Sivas) experimental studies

Length, area, and volume measurements of areas with different geometric shapes and slopes are carried out for the first study area.

6.1.2. Length measurement for accuracy analyse of model

Initially, two areas are selected for the accuracy analyses of the two models, length measurements are obtained for the study areas using the terrestrial method (using RTK (Real Time Kinematic/GNSS)), and the same areas are finally measured using the two models (the model with GCPs and the model without GCPs). The results of the measurements are given in Table 7.

As seen in Table 4, our model is sufficiently sensitive. Because the measurements are close enough to the data obtained with RTK/GNSS, the model generated with GCPs is sufficiently accurate, and since we could not measure all investigated areas with the terrestrial method in this study, the data obtained from the model with GCPs are accepted as true values, while the other data (obtained from the model without GCPs) are compared to these data. Different features are measured with both models, as shown in Fig. 11.

After the model accuracy is confirmed, measurements are conducted using both models in areas with different shapes. The measurements are provided in Table 8 and are further compared. The measurements obtained with the two models are graphically shown in Fig. 12.

Table 7. Length measurements obtained with different methods

Area Name	Reference (With GPS) (m)	With GCPs (m)	Without GCPs (m)	*RMSE (mm)*	Relative Error %
1	13.830	13.817	13.804	0.020	0.14
2	14.770	14.765	14.792	0.016	0.11

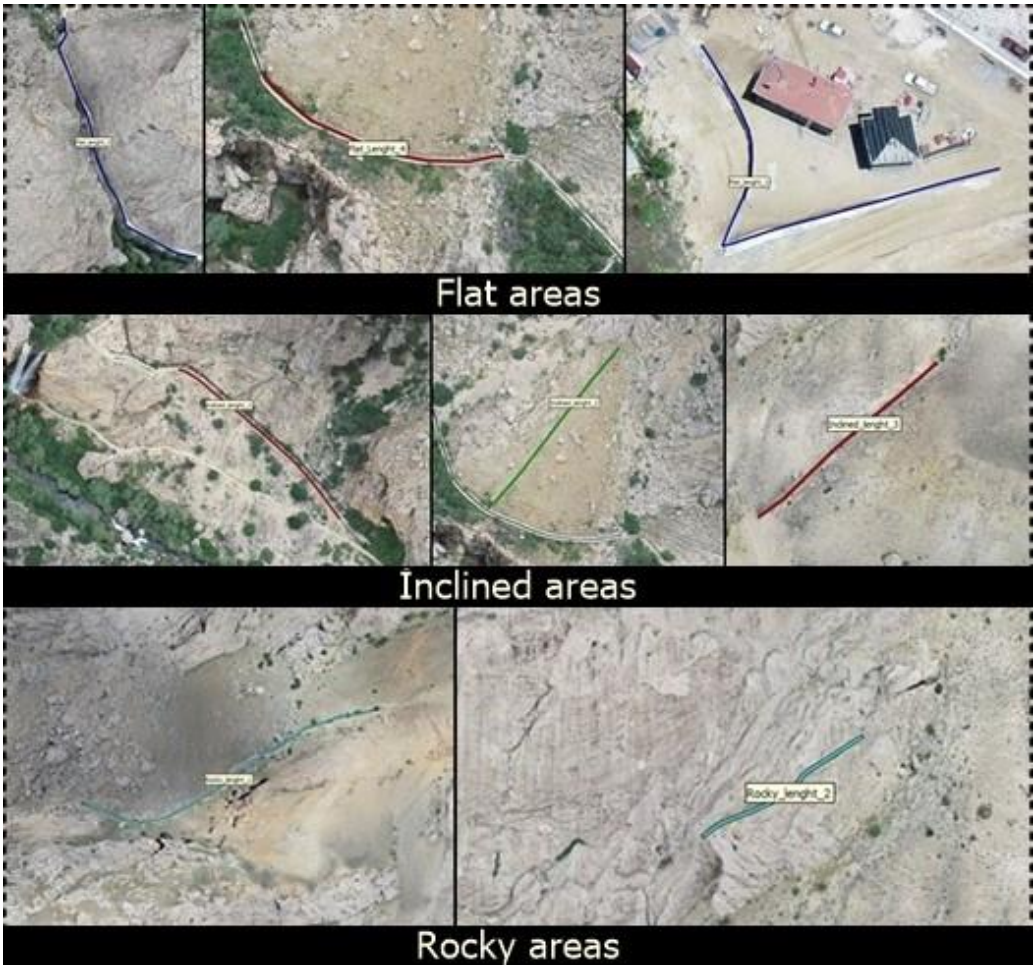

Figure 11. Length measurements of areas with different topography

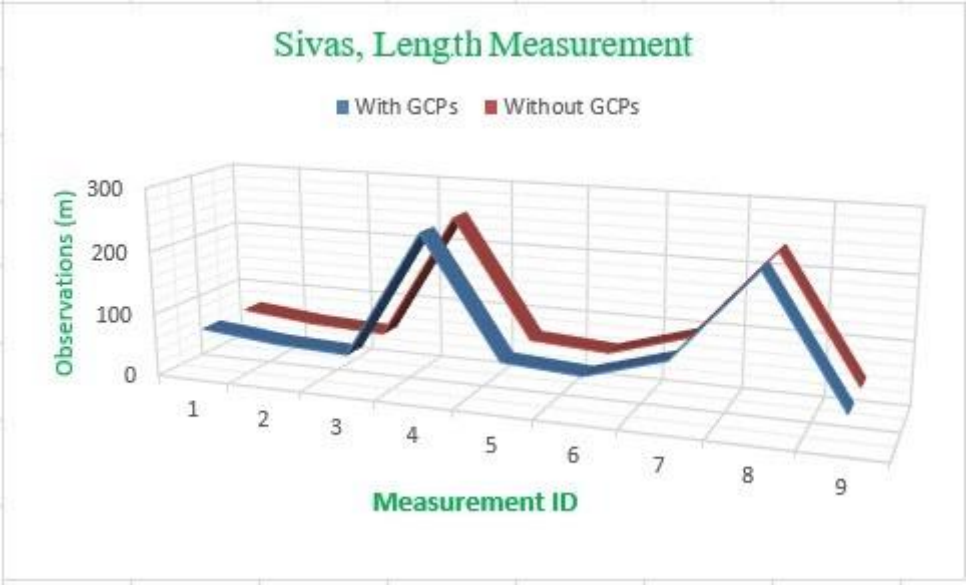

Figure 12. Measurements done in two models are graphically indicated

6.1.3. Length measurement for accuracy analyze of model

To observe the usability of the model produced without GCPs for the application of area measurements, 5 areas with different features are measured using both models, as shown in Fig. 13. The area measurement results are given in Table 9. The measurements conducted using the two models are shown graphically in Fig. 14.

Table 8. Length measurements obtained from two models of Sivas for the same areas

Area Type	With GCPs (m)	Without GCPs (m)	Δi (m)	Relative Error %	RMSE (m)
Flat Areas	72,418	72,470	-0,052	0,100	0,139
	60,518	60,558	-0,040	0,100	
	55,466	55,424	0,042	0,100	
Inclined Areas	253,182	253,083	0,099	0,040	
	69,644	69,746	-0,102	0,150	
	61,672	61,541	0,131	0,210	
Rocky Areas	98,036	98,230	-0,194	0,200	
	238,598	238,346	0,252	0,110	
	47,944	47,821	0,173	0,360	
		Mean	**0,121**	**0,126**	

Table 9. Area measurements carried out with both models for the same areas

First Study Area (Sivas) Measurements					
Observation No.	**With GCPs (m^2)**	**Without GCPs (m^2)**	**Δi (m^2)**	**Relative Error %**	**RMSE (m^2)**
Flat Areas	2789.200	2788.100	1.100	0.040	1.264
	682.526	683.594	-1.068	0.160	
	1277.400	1278.700	-1.300	0.100	
Inclined Areas	854.864	853.288	1.576	0.180	
	115.021	113.810	1.211	1.050	
		Mean	**1.251**	**0.306**	

Figure 13. Area measurements done over both models

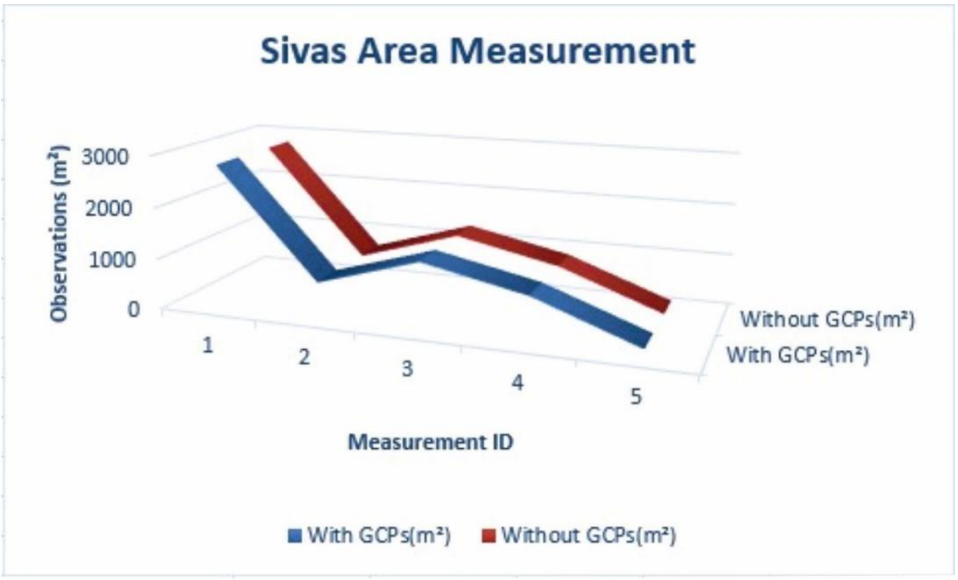

Figure 14. Measurements done in two models are showed graphically

6.1.4. Volume Measurements for Sivas

In order investigate the usability of the model generated without GCPs regarding volume measurements, the volumes of 4 different rocks were measured using both models, as shown in Fig. 15.

In Photoscan, the "reference surface" to be used for volume calculations can only be a plane. This surface can be defined in three ways:

- as an inclined flat surface interpolated by the vertices of the delimitation of the object (best-fit plane).
- as a horizontal flat surface with a moderate height determined by the heights of the vertices of the delimitation of the object (mean-level plane);
- as a horizontal flat surface at a reference height determined by the user (custom-level plane).

The results of the volume measurements are provided in Table 10 and Fig. 16.

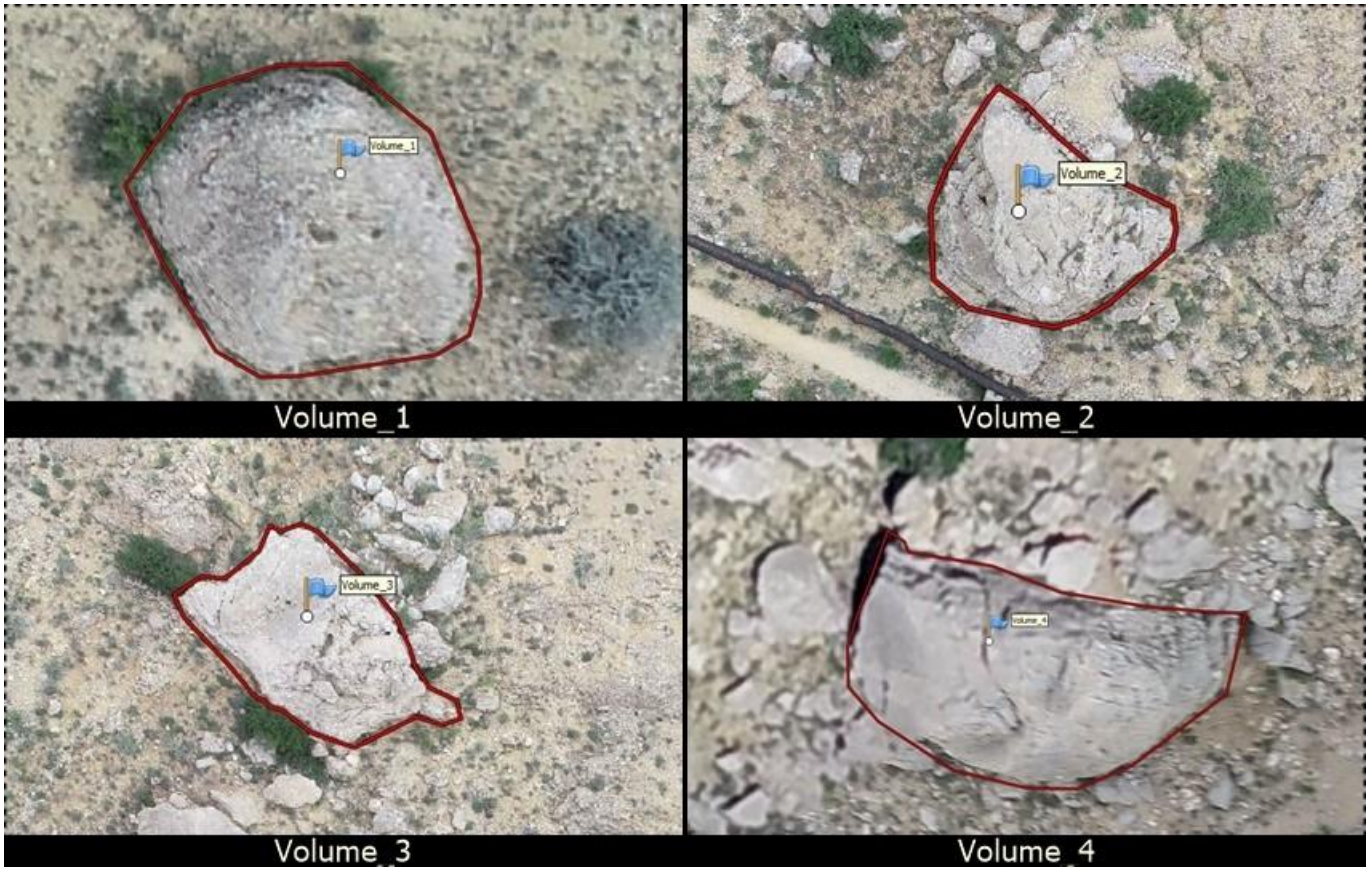

Figure 15. Volume measurements of 4 rock done within both models

Table 10. Volume measurements and RMSEs

First Study Area (Sivas) Volume Measurements					
Observation No.	**With GCPS (m^3)**	**Without GCPs (m^3)**	**Δi (m^3)**	**Relative Error %**	**RMSE (m^3)**
1	24.119	22.478	1.641	6.800	
2	101.393	104.088	-2.695	2.660	
3	52.881	54.043	-1.162	2.200	**2.301**
4	409.243	406.101	3.142	0.80	
		Mean	**2.160**	**3.115**	

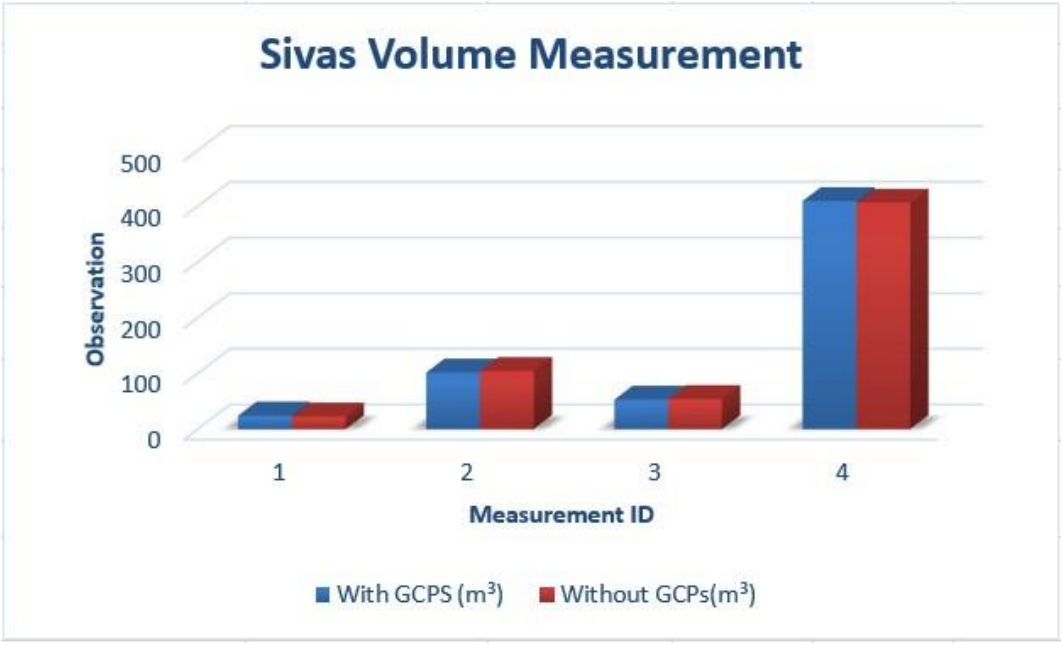

Figure 16. Volume measurements are shown graphically

6.2. Artvin Area's experimental studies (Second study area)

As in the last section, the length, area and volume measurements are conducted using the two models, and the results of the measurements obtained with both models (with and without GCPs) are given in Table 11.

6.2.1. Length measurements

The lengths of regions with different shapes were measured, as shown in Fig. 17, and the measurements are given in Table 12. A graphical interpretation of the length measurements is shown in Fig. 18.

6.2.2. Area measurements of the second study area (Artvin)

The areas of different objects are measured using both models, and the results are given in Fig. 19. A graphically representation of the area measurements is given in Fig. 20.

6.2.3. Volume measurements of second study area (Artvin)

The volumes of different objects are measured for the intended goal of investigating the usability of the model generated without GCPs, and the results are shown in Fig. 21.

6.2.4. Volume measurements of second study area (Artvin)

The volumes of different objects are measured for the intended goal of investigating the usability of the model generated without GCPs, and the results are shown in Fig. 21.

The measured volume values are given in Table 13. The volumes measured using both models are shown graphically in Fig. 22.

Table 11. Measured length values

Second Study Area (Artvin) Length Measurements					
Observation No.	**With GCPs (m)**	**Without GCPs (m)**	**Δi (m)**	**Relative Error %**	**RMSE (m)**
1	209.522	209.303	0.219	0.100	**0.153**
2	69.293	69.199	0.094	0.140	
3	58.667	58.552	0.115	0.200	
		Mean	**0.143**	**0.147**	

Table 12. Area measurements from both models

Second Study Area (Artvin) Area Measurements					
Observation No.	**With GCPs (m^2)**	**Without GCPs (m^2)**	**Δi (m^2)**	**Relative Error %**	**RMSE (m^2)**
1	215.045	212.828	1.207	0.560	**1.726**
2	27.967	26.494	1.473	5.270	
3	65.567	63.263	2.304	3.510	
		Mean	**1.661**	**3.113**	

Table 13. Volume measurements and RMSEs

Second Study Area (Artvin) Volume Measurement					
Observation No.	**With GCPS (m^3)**	**Without GCPs (m^3)**	**Δi (m^3)**	**Relative Error %**	**RMSE (m^3)**
1	2129.885	2118.759	11.126	0.520	**7.061**
2	161.364	158.123	3.241	2.010	
3	779.396	775.485	3.911	0.502	
		Mean	**6.093**	**1.011**	

Figure 17. Length measurements for third study area

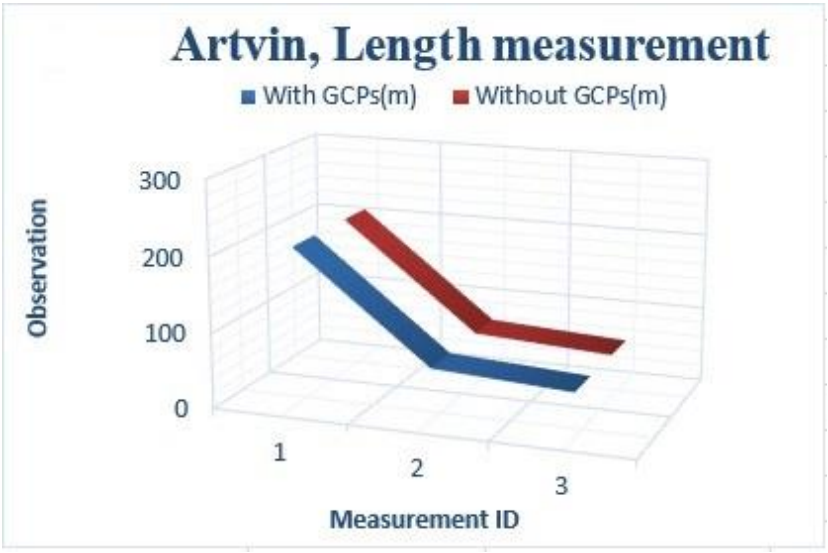

Figure 18. Graphical vision of length measurements

Figure 19. Areas measured in two models

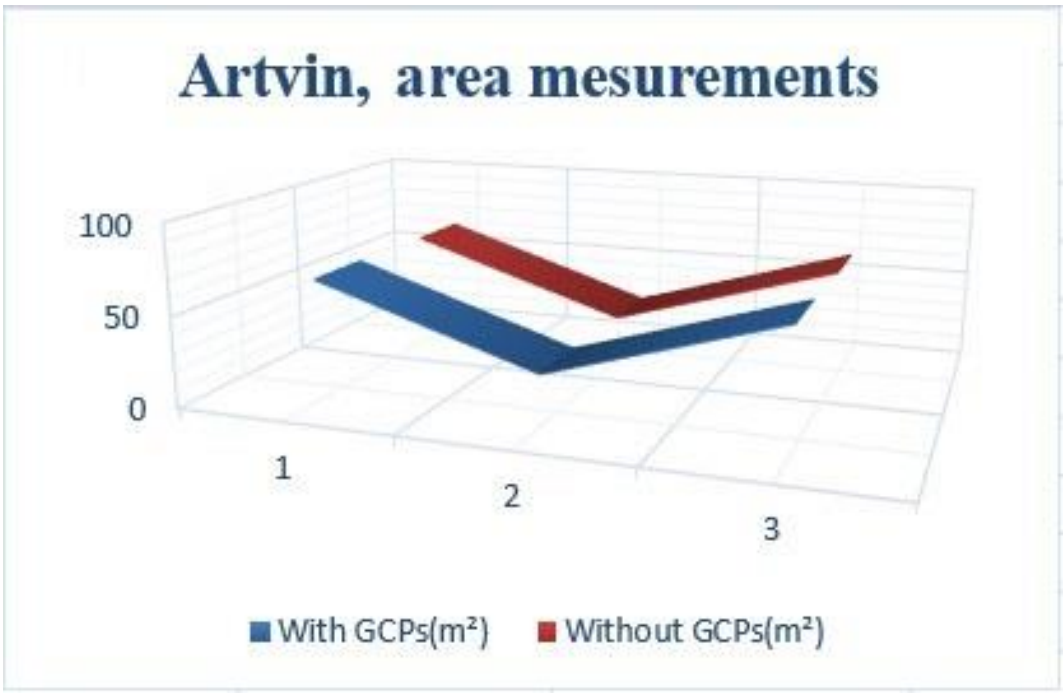

Figure 20. Graphically representation of area measurements

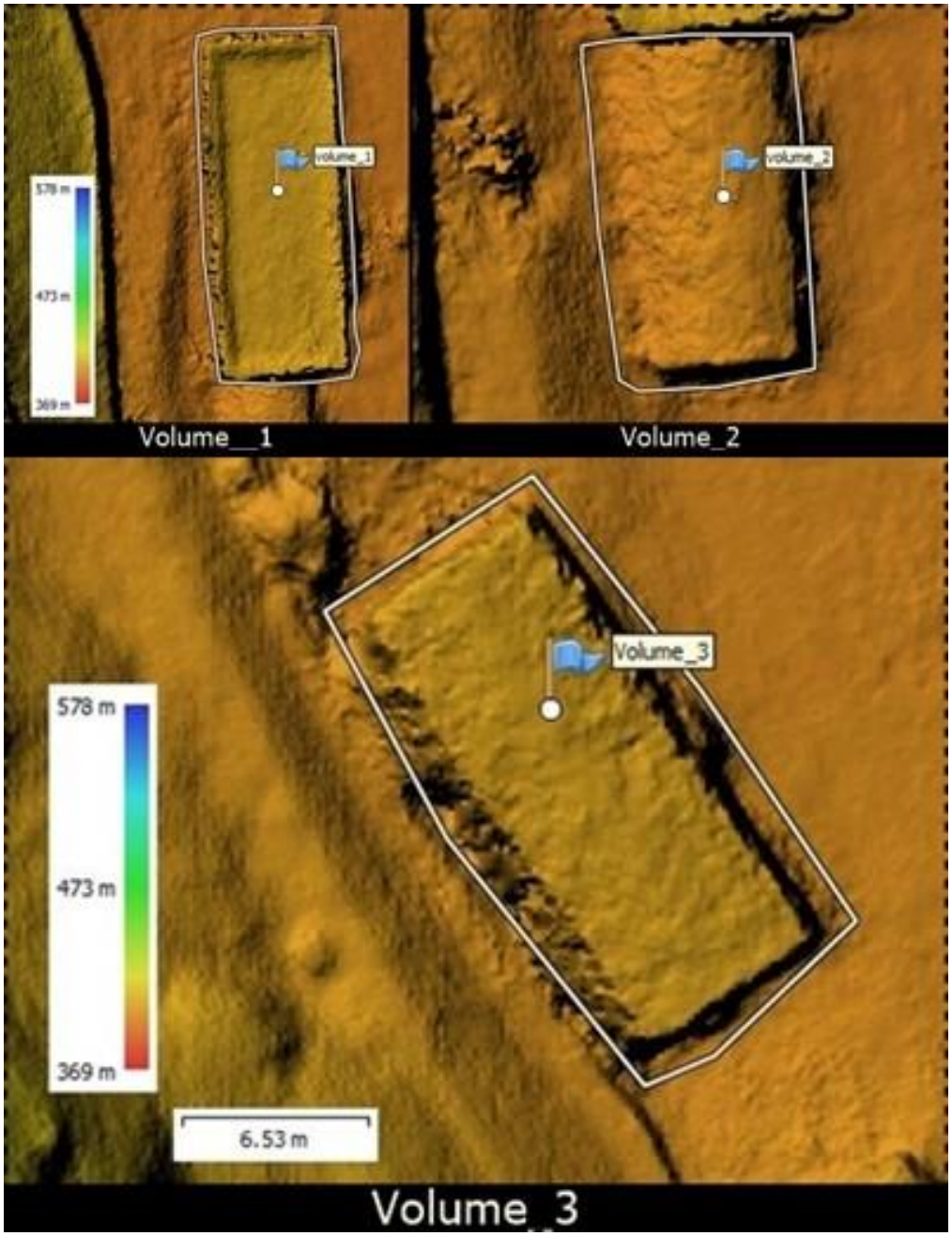

Figure 21. Volume measurements

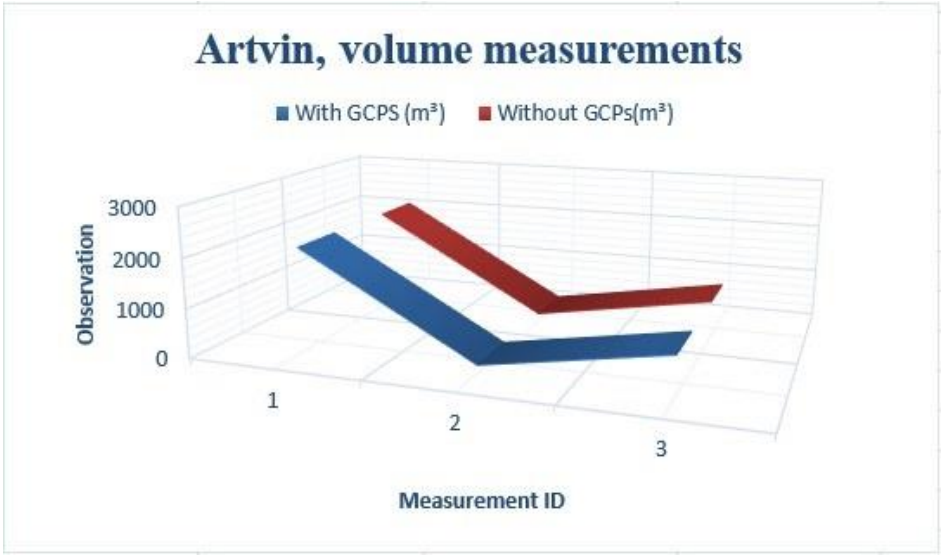

Figure 22. Graphic representation of volume measurements

7. Discussion

These studies were conducted to investigate the usability of 3D photogrammetric models produced without any GCPs; to reach this goal, two different areas were modelled twice each: once with GCPs and once without GCPs. To achieve the goal of this study, the lengths, areas and volumes of the same areas were measured using both models. The results obtained from the models generated with GCPs were accepted as the true values (reference values), and the results obtained from the models generated without GCPs were compared to the reference values. The relative errors as well as the RMSEs were also calculated and are given in tables above.

7.1. Length Measurement Assessment

The length measurement results provided various levels of success. The accuracy of each measurement was assessed by comparing the reference data (obtained from the model with GCPs) to the estimations determined through the photogrammetric models without GCPs. In the first study area (Sivas), length measurements were conducted on three types of terrain (flat, sloping and rocky terrain). As shown in Table 5, the length measurement errors are lower in flat areas than in inclined areas; similarly, the length measurement errors of inclined areas are lower than the errors of rocky areas. It is important to know that some objects used for the length measurements, especially those in the in inclined areas, were in close proximity to other objects and were sufficiently complex. However, overall, the first study area exhibited very promising results in measuring length, with a relative error of less than 1% and an RMSE of 0.139 m; these results are sufficiently accurate.

In the second study area (Artvin), the lengths of various objects are measured. The relative error value is 0.15%, and the RMSE is 0.153 m; these errors are also within acceptable error limits.

In an analysis of the length measurements performed using models generated with and without GCPs, no marked difference was found. The majority of relative error calculations output values less than 1%. The influence of the shape, size and configuration of the target object on the accurate estimation of the length obtained from the models without GCPs was examined in this study. Areas with greater slopes and complexity contain more errors than flat areas. In the first study area, the flat area has a majority relative error of 0.10%, whereas the inclined area has a majority relative error of 0.20%; finally, the lengths measured in the rocky area have a relative error of 0.36%. The rocky area has the highest error as well as the most complex structure in the first study area. As a result, the higher the inclination and complexity of the object area, the greater the error is.

The maximum relative errors of the length measurement between the study areas is 0.36%, which is an acceptable length accuracy. Given acceptable accuracy assessments in various fields, it is possible to conclude that photogrammetric models produced without GCPs are adequate for estimating the lengths of objects for different engineering applications, for some quantity estimations within civil engineering projects, and for disciplines that do not require very high accuracies; however, these models may not be suitable for disciplines that require very high levels of accuracy (millimetric accuracy). According to the above descriptions, we can conclude that models generated without GCPs can be used for length measurements as accurate length measurement tools.

7.2. Length Measurement Assessment

The area estimations show varying results. The accuracy of each estimation (measurement) was assessed by comparing the reference data (obtained from the model with GCPs) to the estimations determined using the photogrammetric models without GCPs.

In the area estimations, out of 8 areas measured within three study areas, five have relative errors less than 1%. One of the areas has a relative error of less than 2%, one has a relative error of 3.51%, and the last one has the maximum relative error of 5.27%. The influence of the shape and size of the area can be seen, as in the length measurements. As seen in Table 6 representing the first study area, the flat area has a majority relative error of 0.16%, whereas the inclined area has a majority relative error of 1.05%. As described for the length measurements, the higher the inclination and complexity of an object are, the greater the error is.

7.3. Volume Measurement Assessment

The results of the volume estimations obtained from the two study areas are convincing. Within the first study area (Sivas), the largest area exhibited a relative error of 0.8%, and the maximum volume estimation relative error is 6.8%. While this error appears to be slightly high, the absolute error is no more than 1.641 m^3.

The average relative error is calculated as 3.115%, and the RMSE is calculated as 2.301 m^3; these errors likely result from the failure of the software to properly model the object structure.

Similarly, for the volume estimations of the second study area, a maximum relative error of 2.01% was identified, with an RMSE of 7.061. It should be noted that the objects with the lowest-accuracy results have poor photo coverage, which is sometime caused by the location of an object in the edge of a study area or by insufficient image overlap or is sometimes due to external factors. By considering these factors, the errors can be reduced.

8. Conclusion

It is a known fact that photogrammetrically correct results can be obtained if GCPs are used. However, establishing and measuring GCPs is not always possible or preferred due to the associated costs. Today, orthophoto and digital terrain model production with unmanned aerial vehicles for use in many engineering projects can be performed without GCPs with some margin of error. The results obtained from this study and the literature review strengthen this thesis.

Based upon the obtained results, several conclusions can be made regarding the decision to accept or reject the usability of models produced without GCPs. Considering the errors calculated above, the following conclusions pertain to the ability of photogrammetric models with no GCPs.

- Photogrammetric models generated with no GCPs are usable for different engineering applications.
- Photogrammetric models produced with no GCPs can be used as accurate length-measuring tools within the modelled areas.
- Relative errors of 0.12% in the first study area (Sivas) and 0.143% in the second study area (Artvin) are obtained.
- Photogrammetric models with no GCPs can be used as accurate area-measuring tools within the modelled areas.
- The relative error in the case of the area measurement of first study area (Sivas) is 0.306%, and that of the second study area (Artvin) is 3.11%.
- Photogrammetric models with no GCPs can calculate accurate object volumes and areas with different shapes and slopes.
- A 3.115% relative error of volume measurement is calculated for the first study area (Sivas), while this value is 1.01% for the second study area (Artvin).
- The length measurements conducted by the model within flat areas are more accurate than those conducted within inclined or rocky areas.
- The area measurements conducted in flat areas are also more accurate than those conducted in inclined areas.
- The area measurements of objects with smooth shapes are more accurate than those of objects with complex shapes.
- The accuracy of the volume measurements is based on the identified base surface; if the surface is identified accurately, there is no effect on the shape or slope of the object.
- The studies above are conducted in two areas with different characteristics, such as different elevations above sea level, different climate conditions, different study area topographies, and different flight plans, but the results, accuracies, relative errors and absolute errors of these models are approximately the same. As a result, it can be indicated that the above principles (the usability of models with no GCPs) are acceptable and applicable for all conditions.

Considering the results obtained in our study, it can be seen that length, area and volume measurements can be performed with orthophotos and digital surface models produced without using GCPs with an average relative error of 0.1-3%. In light of this information, the orthophoto and digital terrain model needs of many engineering projects can be effectively met without using GCPs using images obtained by unmanned aerial vehicles.

Author contributions

Erdem Emin Maraş: Designed the study and performed the experiments, analyzed the data, wrote the manuscript. **Mohammad Noman Nasery:** Designed the study and performed the experiments.

Conflicts of interest

The authors declare no conflicts of interest.

References

1. Yastikli, N. (2007). Documentation of cultural heritage using digital photogrammetry and laser scanning. Journal of Cultural heritage, 8(4), 423-427.
2. McCarthy, J. (2014). Multi-image photogrammetry as a practical tool for cultural heritage survey and community engagement. Journal of Archaeological Science, 43, 175-185.
3. Berni, J. A., Zarco-Tejada, P. J., Suárez, L., & Fereres, E. (2009). Thermal and narrowband multispectral remote sensing for vegetation monitoring from an unmanned aerial vehicle. *IEEE Transactions on geoscience and Remote Sensing*, *47*(3), 722-738.
4. Xiang, H., & Tian, L. (2011). Development of a low-cost agricultural remote sensing system based on an autonomous unmanned aerial vehicle (UAV). *Biosystems engineering*, *108*(2), 174-190.
5. Jauregui, L. M., & Jauregui, M. (2000). Terrestrial photogrammetry applied to architectural restoration and archaeological surveys. *International Archives of Photogrammetry and Remote Sensing*, *33*(B5/1; PART 5), 401-405.
6. Bianchi, G., Bruno, N., Dall'Asta, E., Forlani, G., Re, C., Roncella, R., ... & Zerbi, A. (2016). Integrated survey for archıtectural restoratıon: A methodologıcal comparıson of two case studıes. *International Archives of the Photogrammetry, Remote Sensing & Spatial Information Sciences*, *41*, 175-182.
7. Kucukkaya, A. G. (2004). Photogrammetry and remote sensing in archeology. *Journal of Quantitative Spectroscopy and Radiative Transfer*, *88*(1-3), 83-88.
8. Guidi, G., Russo, M., Ercoli, S., Remondino, F., Rizzi, A., & Menna, F. (2009). A multi-resolution methodology for the 3D modeling of large and complex archeological areas. *International Journal of Architectural Computing*, *7*(1), 39-55.
9. Patikova, A. (2004) Digital photogrammetry in the practice of open pit mining. Int. Arch. Photogramm. Remote Sens. Spat. Inf. Sci. 34, 1-4.
10. Sheng, Y. H., Yan, Z. G., & Song, J. L. (2003). Monitoring technique for mining subsidence with digital terrestrial photogrammetry. *Journal of China University of Mining & Technology*, *32*(4), 411-415.
11. Murfitt, S. L., Allan, B. M., Bellgrove, A., Rattray, A., Young, M. A., & Ierodiaconou, D. (2017). Applications of unmanned aerial vehicles in intertidal reef monitoring. *Scientific reports*, *7*(1), 1-11.
12. Yalcin, G., & Selcuk, O. (2015). 3D city modelling with Oblique Photogrammetry Method. *Procedia Technology*, *19*, 424-431.
13. Danahy, J. (1997). A set of visualization data needs in urban environmental planning & design for

photogrammetric data. In *Automatic extraction of man-made objects from aerial and space images (II)* (pp. 357-366). Birkhäuser, Basel.
14. Döner, F. & Bıyık, C. Management of three dimensional objects in spatial database. Chamb. Surv. Cadastre Eng. Geod. Geoinf. Mag. 100, 27 (2009).
15. Yılmaz, H. M., Mutluoglu, O., Ulvi, A., Yaman, A., & Bilgilioglu, S. S. (2018). Created Tree Dimensional Model of Aksaray University Campus with Unmanned Aerial Vehicle. *Journal of Geomatics*, *3*(2), 103-107.
16. Choudhury, M. A. M., Costanzini, S., Despini, F., Rossi, P., Galli, A., Marcheggiani, E., & Teggi, S. (2019, May). Photogrammetry and Remote Sensing for the identification and characterization of trees in urban areas. In *Journal of Physics: Conference Series* (Vol. 1249, No. 1, p. 012008). IOP Publishing.
17. Wu, B., Xie, L., Hu, H., Zhu, Q., & Yau, E. (2018). Integration of aerial oblique imagery and terrestrial imagery for optimized 3D modeling in urban areas. *ISPRS journal of photogrammetry and remote sensing*, *139*, 119-132.
18. Goetz, J., & Brenning, A. (2019). Quantifying uncertainties in snow depth mapping from structure from motion photogrammetry in an alpine area. *Water Resources Research*, *55*(9), 7772-7783.
19. Chudley, T. R., Christoffersen, P., Doyle, S. H., Abellan, A., & Snooke, N. (2019). High-accuracy UAV photogrammetry of ice sheet dynamics with no ground control. *The Cryosphere*, *13*(3), 955-968.
20. Casella, V. and Franzini, M. (2016) Modelling steep surfaces by various configurations of nadir and oblique photogrammetry. ISPRS Annals of the Photogrammetry. Remote Sensing and Spatial Information Sciences, III-1, 175-182.
21. Tomaštík, J., Mokroš, M., Surový, P., Grznárová, A., & Merganič, J. (2019). UAV RTK/PPK method—An optimal solution for mapping inaccessible forested areas?. *Remote sensing*, *11*(6), 721.
22. He, F., Zhou, T., Xiong, W., Hasheminnasab, S. M., & Habib, A. (2018). Automated aerial triangulation for UAV-based mapping. *Remote Sensing*, *10*(12), 1952.
23. Gerke, M., & Przybilla, H. J. (2016). Accuracy analysis of photogrammetric UAV image blocks: Influence of onboard RTK-GNSS and cross flight patterns. *Photogrammetrie, Fernerkundung, Geoinformation (PFG)*, (1), 17-30.
24. Turk, T. & Ocalan, T. (2020). Examining the Accuracy of Photogrammetric Products Obtained by Unmanned Aerial Vehicles with PPK GNSS System with Different Approaches. Turkish Journal of Photogrammetry, 2 (1), 22-28.
25. Eling, C., Klingbeil, L., & Kuhlmann, H. (2014). Development of an RTK-GPS system for precise real-time positioning of lightweight UAVs.
26. Takasu, T. (2021) RTKLIB, Open-Source Program Package for RTK-GPS. https://github.com/tomojitakasu/RTKLIB

International Journal of Engineering and Geosciences
https://dergipark.org.tr/en/pub/ijeg
e-ISSN 2548-0960

A linear approach for wheat yield prediction by using different spectral vegetation indices

Yunus Kaya[*1], **Nizar Polat** [1]

[1]*Harran University, Geomatics Engineering Department, Türkiye*

Keywords
Yield estimation
Vegetation indices
Wheat
Sentinel-2
Landsat-8

Research Article
DOI: 10.26833/ijeg.1035037

Received: 10.12.2021
Accepted: 03.02.2022
Published: 13.04.2022

Abstract

Yield prediction before harvest is one of the important issues in terms of managing agricultural policies and making the right decisions for the future. Using remote sensing techniques in yield estimation studies is one of the important steps for many countries to reach their 21st-century agricultural targets. The aim of this study is to develop a wheat yield model using Landsat-8 and Sentinel-2 satellite data. In this study, the development stages of winter wheat were examined with the help of satellite images obtained between the years 2015-2018 of a selected region in Sanliurfa, Turkey, and it was aimed to predict the yields for other years by establishing a yield estimation model. The yield estimation model was established with the help of Normalized Difference Vegetation Index (NDVI), Soil-adjusted Vegetation Index (SAVI), Green Normalized Difference Vegetation Index (GNDVI) and Modified Soil-adjusted Vegetation Index (MSAVI) obtained from remote sensing satellite images. Linear regression analysis was established between calculated NDVI, SAVI, GNDVI, MSAVI indices, and actual yield values on the pre-flowering, flowering stage, and post-flowering stage. As a result of the study, the highest correlation coefficient was found in the flowering stage between the vegetation indices values and the actual yield values. The values of NDVI, SAVI, GNDVI, and MSAVI and correlation coefficients are obtained in the flowering stage were 0.82, 0.80, 0.86, and 0.87, respectively. With the established model, yield values in 2019 were tried to be estimated for three different fields. The highest correlations were seen in the flowering stage for MSAVI and GNDVI, pre-flowering stage for NDVI and post-flowering stage for SAVI. This clearly shows that the satellite images can be used in yield estimation studies with a remarkable correlation between vegetation indices and actual yield values.

1. Introduction

Nutrition is the basis of human survival and development [1]. Increasing population [2], air pollution, and reduction of cultivated lands have serious impacts on cereal crops [3] and food security has become a serious problem worldwide. Especially, for agriculture depended on economies like Turkey [4], yields prediction is vital for determining a sustainable supply-demand statistic [5]. In addition, considering in a timely manner predicting yields a few months earlier before harvest provides great advantages for securing national demand, organizing food transport [6,7], forecasting agricultural imports and exports, regulating grain markets, and managing plantations [8,9]. Previously, yield prediction studies were based on field measurements and observations. This traditional method is often subjective, costly, and prone to large errors [10]. Today, thanks to the developments in remote sensing techniques, it is possible to get more reliable results in agricultural applications by using satellite data. Aside from other possibilities, the satellite systems present high spatial resolution data and the multispectral information about the plants [11]. These possibilities allow us to analyze growth stages and physical conditions. Moreover, compared to terrestrial observations, satellite systems are more economical, more consistent, and more holistic. Pre-harvest yield prediction studies are not only advantageous in predicting yields for specific crops but also in controlling possible disease and pest control during the growing period [12]. Pre-harvest yield prediction and crop monitoring are a common issue for many countries [13]. The use of remote sensing in yield prediction studies is a very active research area [14,15]. There are many studies in the literature to predict pre-harvest yield. The known

* **Corresponding Author**

*(yunuskaya@harran.edu.tr) ORCID ID 0000-0003-2319-4998
(nizarpolat@harran.edu.tr) ORCID ID 0000-0002-6061-7796

Cite this article

Kaya, Y., & Polat, N. (2023). A linear approach for wheat yield prediction by using different spectral vegetation indices. International Journal of Engineering and Geosciences, 8(1), 52-62

earlier studies on the yield prediction model are AgRISTARS [16] and the Large Area Crop Inventory Experiment (LACIE) [17]. The Monitoring Agriculture with Remote Sensing (MARS) project in Europe and the National Agricultural Statistics Service (NASS) service of the US Ministry of Agriculture are play important role in remote sensing studies [18]. [19,20] reported that vegetation indices gave successful results in predicting yield before harvest. [21] used the AgroMetShell model developed by FAO and predict the wheat yield with, a correlation of R^2 = 0.9067 between predict and actual yield. [22] used the BBCH scale to monitor the developmental stages of sunflower and wheat plants. [23] used Sentinel-2 data and vegetation indices to monitor the phenological stages of the sunflower plant. Among the VIs, they obtained the best forecast with NDVI (R^2=0,74) when three months before harvest of sunflower. [24,25] reported that NDVI based pre-harvest yield prediction includes a 10% error rate. [26] examined the performance of Landsat-8 and Sentinel-2 satellites in their efficiency estimation studies. In Skakun's study, yield estimation was made using only Landsat-8, only Sentinel-2 and NDVI value obtained from the combined model and R^2 values were found to be 0.64, 0.88, and 0.90, respectively. [27] compared the NDVI and SAVI results and they indicated that SAVI performed better than NDVI.

In this study, the success of NDVI, SAVI, GNDVI and MSAVI values obtained from Landsat-8 and Sentinel-2 satellite data provided free of charge for a selected region, unlike previous studies, was examined. The phenological stages of the wheat plant were examined with the vegetation indices obtained from satellite images. A linear regression model was established between the vegetation indices obtained for pre-flowering, flowering, and post-flowering stage, and yield values. The yield prediction model was applied for 2018-2019 data and a model performance accuracy was made.

2. Method

2.1. Study area and data

2.1.1. Study area

The study was conducted in a planting area dominated by winter wheat agricultural city, Şanlıurfa (38°45'E to 38°53'E and 37°06'N to 37°14'N), in the south-eastern part of Turkey (Fig. 1). The region covers approximately 1633 km^2. The prevailing planting pattern is dominated by an intensive dual-cropping system based on winter wheat, including barley, cotton, maize, isot pepper, lentil [28]. Şanlıurfa has a hot and dry summer climate, and a rainy and mild winter climate. The city, which is close to the Equator in terms of mathematical location, has a continental climate. The region is suitable for wheat agriculture Due to enough rainfall, groundwater, and suitable temperature.

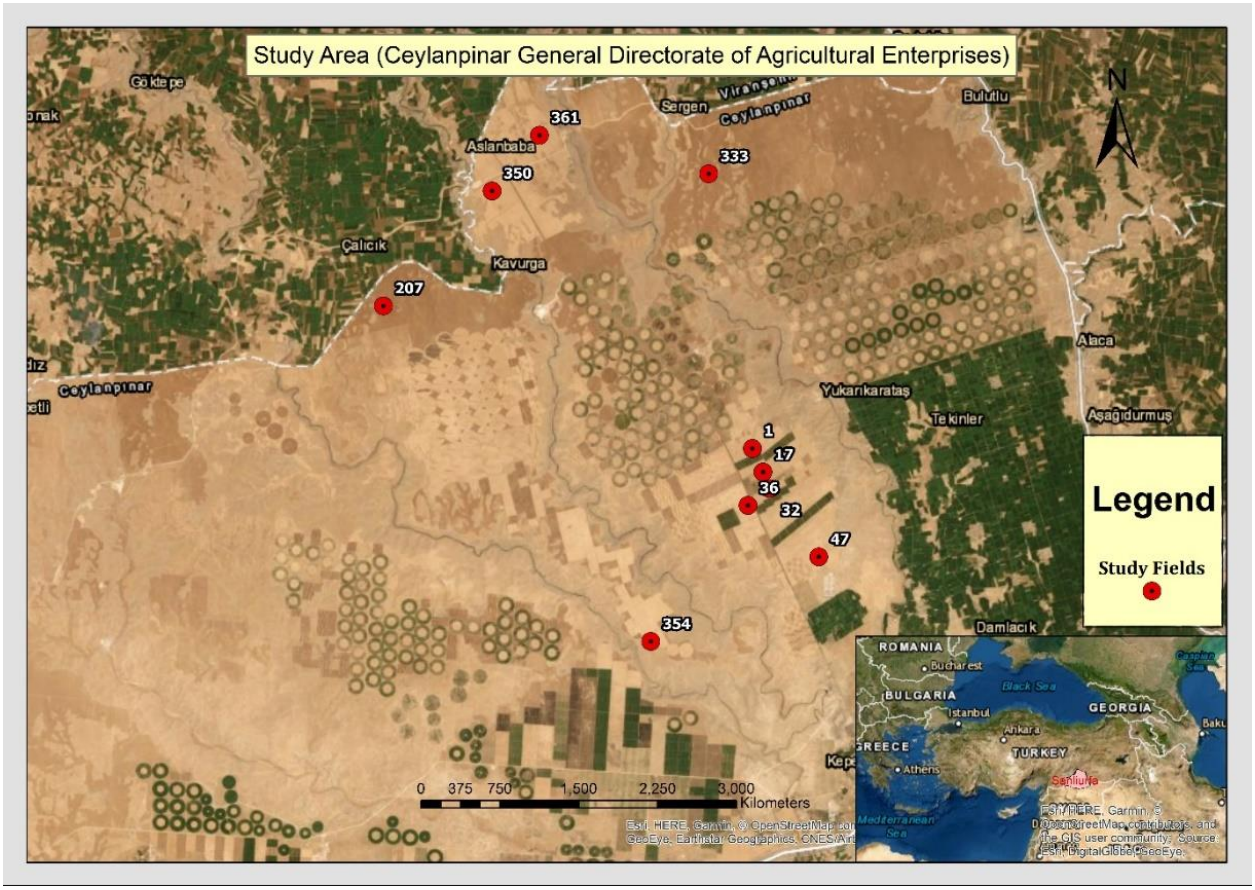

Figure 1. Location of the study area and of the sample plots in the TIGEM of south-eastern Turkey

2.1.2. Satellite data

We used Landsat-8 and Sentinel-2 data to monitor wheat fields. Because Landsat-8 and Sentinel-2 satellites have different temporal resolution [29], and they scan the same region at different times. Therefore, it is advantageous to use two satellite data in combination to monitor changes in plant growth. Landsat-8 data is shared free of charge by a collaboration of the National Aeronautics and Space Administration (NASA) and the United States Geological Survey (USGS). Landsat-8 satellite was launched into space on February 11, 2013. It orbits at an altitude of 705 kilometers and completes one tour in 16 days. Operational Land Imager (OLI) and Thermal Infrared Sensor (TIRS) sensors were used on the Landsat-8 satellite [30,31]. The Sentinel-2 satellite mission was developed by the European Space Agency (ESA) and is shared free of charge on the internet. The Sentinel-2 mission consists of two polar-orbiting satellites phased at 180 degrees to each other placed in the same orbit. It scans between 56° south and 84° north latitudes. Its temporal resolution is 10 days at the equator. However, since there are 2 satellites in the system, the same place is displayed every 5 days. It has a temporal resolution of 3 days at 45° latitude. Band properties used in the study are shown in Table 1.

In the study, the vegetation indices were created using satellite images obtained between 2015-2019 (3 seasons for the model and 1 season for the test). Satellite images obtained in certain periods from sowing to harvest were downloaded for each season. For 2015-16, 2016-17 and 2017-18 seasons, 8 Landsat-8 and 33 Sentinel-2A satellite images were used from the sowing time (December) to the harvest time (June) of wheat, where the study area was cloudless (Table 2).

2.1.3. Reference data

The yield values of the study area were provided by the General Directorate of Agricultural Enterprises (TIGEM). Since it is forbidden to fly UAVs and measure land in the study area, the field study has not been conducted. Yield values and information on the land were obtained from the institution. In the study, 5 irrigated agricultural lands and 5 dry agricultural lands were used. Wheat plant is not generally cultivated every year [32]. Therefore, wheat cultivation was not made in some fields in some seasons. These fields have been removed from the data set. The parcel yields of the data set used in the study are shown in Table 3.

Table 1. Feature of Landsat-8 and Sentinel-2

	Landsat 8 OLI-TIRS			Sentinel-2		
Scene size (km)	185 x 180			290		
Radiometric Resolution (bit)	12			8		
Band Name	**Band Count**	**Wavelength (µm)**	**Spatial Resolution (m)**	**Band Count**	**Wavelength (µm)**	**Spatial Resolution (m)**
Blue	Band 2	0.45-0.51	30	Band 2	0.490	10
Green	Band 3	0.53-0.59	30	Band 3	0.560	10
Red	Band 4	0.64-0.67	30	Band 4	0.665	10
Near Infrared	Band 5	0.85-0.88	30	Band 8	0.842	10

Table 2. Dates of satellite data (* refers Landsat-8 images)

	2015-2016	**2016-2017**	**2017-2018**
December	05.12.2015 19.12.2015 * 25.12.2015	09.12.2016	04.12.2017 08.12.2017 * 14.12.2017
January		08.01.2017 18.01.2017	09.01.2018 * 13.01.2018
February		07.02.2017 17.02.2017 23.02.2017 *	02.02.2018
March	08.03.2016 * 24.03.2016		19.03.2018
April	23.04.2016	28.04.2017	08.04.2018 13.04.2018 23.04.2018
May	03.05.2016	8.05.2017 14.05.2017 * 30.05.2017 *	18.05.2018 23.05.2018
June	02.06.2016 12.06.2016 22.06.2016 28.06.2016 *	07.06.2017 17.06.2017 27.06.2017	07.06.2018 12.06.2018 17.06.2018 22.06.2018 27.06.2018

2.2. Methodology

Health status, growth etc. has a direct impact on yield. Using remote sensing methods, the health status of the plant, its growth rate and the rate of foliage can be determined quickly. The satellite data used for this must go through certain phases. In this study, yield estimation was made using Sentinel-2 and Landsat-8 satellite images. This topic can best be treated under three headings: detection of phenological stage, yield estimation model and application of yield estimation model to test data. Firstly, we applied pre-processing operations on satellite images. The workspace was in two different scenes in Sentinel-2 satellite data. For this reason, Sentinel-2 images were mosaic processed in ENVI software. Secondly, since Sentinel-2 (10 m) and Landsat-8 (30 m) satellite images have different spatial resolution, Landsat-8 images were resampled to 10 m. In the next step, vegetation indices were then created. NDVI and SAVI were used to determine the phenological stages. Then 4 different indices values were determined for each field in the study area. A yield estimation model was established for three stages between index values and yield values. Finally, the model was applied to the same region for the 2018-2019 season. Model performance accuracy was performed for the obtained results (Fig. 2).

2.2.1. Decision of phenological stage

Plants are living things that show continuous development from the sowing period to the harvest period. Therefore, it does not make sense to wait for the harvest period to decide about the health and development of plants. BBCH-scale was used to determine the growth stages of the wheat plant from sowing to harvest [33] (Table 4).

Due to the temporal and spatial resolution of satellite data and cloud conditions, all stages of plant development could not be monitored. Therefore, the growing stages of the wheat plant can be examined in 4 basic stages.

Germination and seedling stage: Germination begins with water intake by a wheat kernel, which ends the postharvest sleeping period. At the germination stage, enough temperature and humidity are needed for wheat seeds to germinate. The optimum temperature at the germination stage of wheat seeds is between 12 ºC and 25 ºC. Under favorable conditions, seedling emergence usually takes place within seven days. The seedling stage begins with the emergence of the first leaf and the top of the plant usually becomes apparent after the third leaf.

Tillering and stem elongation: Sprouts appear shortly after crown formation and crown root system develops. The crown root system provides nutrients and water to the plant during the growing season. After this stage, the wheat plant starts in the stem elongation stage. Most short season wheat produces 7-8 leaves on the stem before stem elongation.

Heading and flowering: This stage is the stage when the wheat ear comes out of the stem completely. After this stage, the plant begins to grow and bloom. During flowering, high temperature and drought reduce the grain yield.

Ripening and senescence: The senescence stage begins after the flowering stage. Ripening takes place in four stages: milk, soft dough, hard dough and finally mature. Meanwhile, the wheat plant turns straw color, and the grain becomes very hard.

Flowering phase is very important for yield estimation of wheat plant. During the flowering phase, the chlorophyll content of the wheat plant reaches its highest level and reaches its greenest form. In the study, by examining the NDVI and SAVI indexes, the flowering phase was determined for each season, and the previous satellite image was evaluated as the pre-flowering phase and the next satellite image post-flowering phase.

Table 3. Wheat Yield (kg/daa) (* refers fallowing field)

CEYLANPINAR TIGEM WHEAT YIELDS (kg/daa)										
	Irrigated Agricultural Fields					Dry Agricultural Fields				
Cropland Number / Season	1	17	32	36	47	207	333	350	354	361
2015-2016	496.9	*	*	*	*	285.6	359.9	*	161.0	*
2016-2017	*	627.0	411.0	397.0	532.8	*	*	167.3	*	249.6
2017-2018	506.2	558.4	403.1	371.8	445.0	125.1	46.6	*	37.3	*

Table 4. Phenological Stage of Wheat in the BBCH-Scale (Meier 2001)

BBCH-Scale	Principal Growth Stage	Stage
0-10	Stage 0	Germination
10-20	Stage 1	Leaf development
20-30	Stage 2	Tillering
30-40	Stage 3	Stem elongation
40-50	Stage 4	Booting
50-60	Stage 5	Inflorescence emergence, heading
60-70	Stage 6	Flowering, anthesis
70-80	Stage 7	Development of fruit
80-90	Stage 8	Ripening
90-100	Stage 9	Senescence

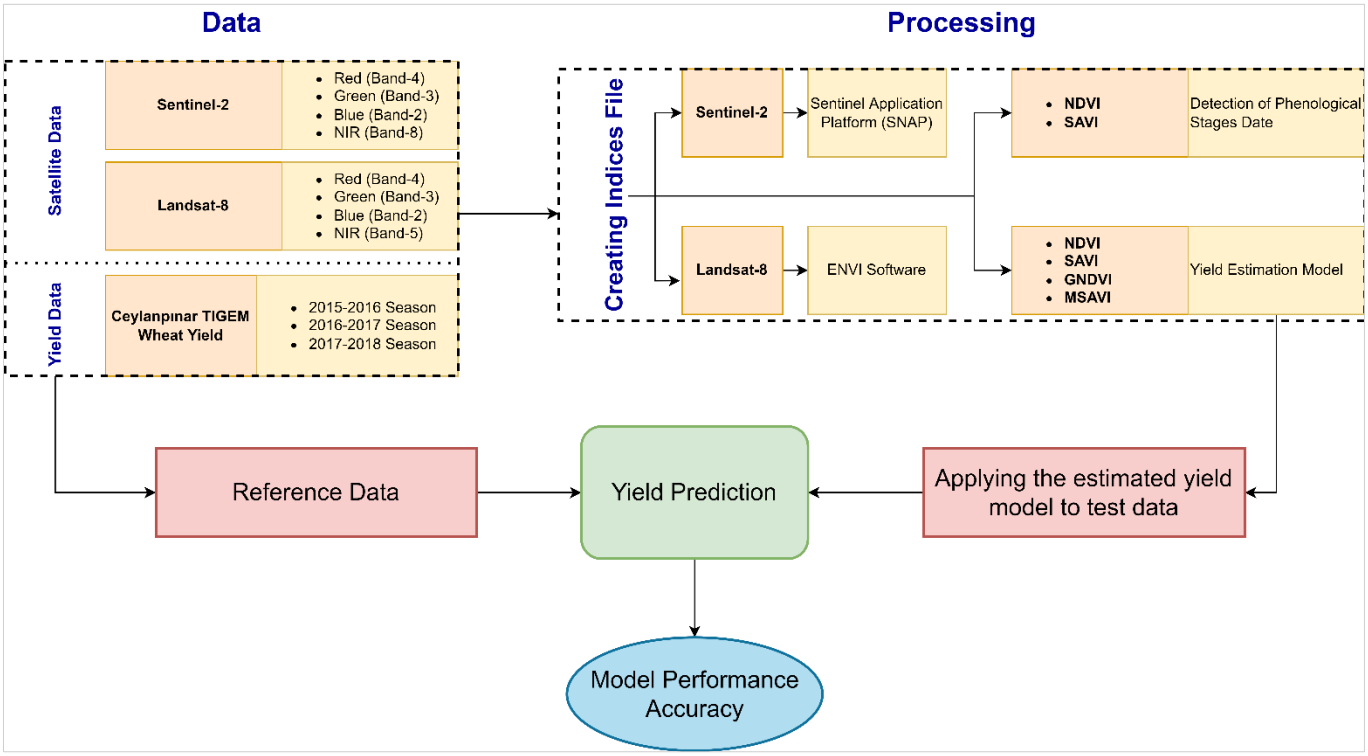

Figure 2. Flow-process diagram

2.2.2. Vegetation indices

Vegetation density is one of the important indicators in the plant, soil, and climate formation [34,35]. In vegetation determination studies, the original spectral bands on satellites may not always be enough to determine the characteristic spectral features of the vegetation in the target region [36]. In this case, vegetation indices, which are frequently used in remote sensing studies, help to understand the characteristic features of vegetation [37,38].

The NDVI designed to monitor biomass [39,40] and makes use of the reflection near-infrared (NIR) and red spectrum [41]. The NIR is between 0.76 nm and 0.90 nm in the TM sensor and 0.77-0.90 in the ETM sensor. The red spectrum is between 0.63-0.69 in the TM and ETM sensors. High NDVI values refer to green and healthy plants, low NDVI values indicate that the plant is not green or low amounts of vegetation. Unlike the NDVI, GNDVI uses green wavelength instead of visible red wavelength. GNDVI is useful in calculating photosynthesis rates and monitoring plant stress. SAVI is basically like NDVI. However, in SAVI, unlike NDVI, the effect of land areas is more. Therefore, the soil correction (L) is used in SAVI calculations according to the vegetation density in the field. [42] reported that the L parameter should take a value close to 0 or very close to 0 in regions with dense vegetation, and a value close to 1 or 1 in areas where vegetation is sparse. The soil correction is expressed with a variable L, for which we select 0.50. Changes occur in the L factor in the SAVI value according to the density of the vegetation. When the L factor is 0, the SAVI value is equal to the NDVI value. However, the soil correction factor (L) must vary according to the amount of vegetation available in order to obtain the optimum setting for the effect of the soil. Thus, the modified SAVI (MSAVI) index is obtained [43] (Table 5).

Table 5. Equations of Vegetation Indices

Index	Equation	References
NDVI	$\frac{NIR - Red}{NIR + Red}$	**[44]**
GNDVI	$\frac{NIR - Green}{NIR + Green}$	**[45]**
SAVI	$\frac{NIR - Red}{NIR + Red + L} x(1 + L)$	**[46]**
MSAVI	$\frac{2xNIR + 1 - \sqrt{(2xNIR + 1)^2 - 8x(NIR - Red)}}{2}$	**[47]**

$$Yield\ prediction\ = a\ x\ Vegetation\ Index + b \quad (1)$$

The peak date of the vegetation indices values (NDVI, GNDVI, SAVI and MSAVI) during the year is the heading and flowering stage. While establishing the yield model in the study, pre-flowering, flowering stage and post-flowering reflectance values were evaluated separately and the relationship between each stage and yield was investigated. The average values of each field were matched with the amount of yield in the season and linear regression analysis was performed between these two variables. The yield prediction model is established by the equation 1.

3. Results

First step of the yield prediction is to determine the phenological stages of the wheat. Hence a continuous remote sensing data set is required. In this section, determination of phenological stages and establishment of yield estimation model will be explained, respectively. Finally, the obtained yield prediction model was tested for the season of 2018-2019 and the model accuracy was determined.

3.1. Detection of phenological stages

The development processes of plants can be determined numerically with the vegetation indices obtained from satellite images, and it is possible to comment on the analyzed field with the help of the graphics. NDVI and SAVI values were obtained from all available satellite images in the process from sowing to harvest for the investigation of phenological stages. The changes in NDVI and SAVI values were examined for each season. The peaks of the index values were determined as the flowering stage, the previous date pre-flowering stage, and the next date the post-flowering stage. (Table 6).

Table 6 shows that the flowering stage is towards the end of April in the 2015-2016 season and at the beginning of May in the 2016-2017 season. In the 2017-2018 season, the flowering stage occurred in the middle of March (19 March).

In the yield prediction model, the indices value pre-flowering, flowering and post-flowering period were used. NDVI, GNDVI, SAVI and MSAVI values for three seasons in three periods are shown in Table 7.

3.2. Yield estimation model

We used simple linear regression model, that is, a model with a single regressor x that has a relationship with a response y that is a straight line. Simple linear regression model is given in equation 2.

$$Y = \beta_0 + \beta_1 X + \varepsilon \qquad (2)$$

where the intercept β_0 and the slope β_1 are unknown constants and ε is a random error component. The error does not depend on the value of other error. Correlation coefficient is calculated by equation 3.

$$r = \frac{n(\sum xy) - (\sum x)(\sum y)}{\sqrt{[n\sum x^2 - (\sum x)^2][n\sum y^2 - (\sum y)^2]}} \qquad (3)$$

Linear regression analysis was performed between NDVI, GNDVI, SAVI and MSAVI values and actual yield values in wheat cultivated areas. A yield estimation model has been established to determine yield values. Yield equations, correlation coefficients and determination coefficients are shown in Table 8(a).

Table 8(a) shows that when all indices are examined, the correlation coefficient obtained during the flowering period is higher than the other stages. The highest correlation coefficient was determined in MSAVI (0.87). Correlation coefficients for GNDVI, NDVI and SAVI were 0.86, 0.82 and 0.80, respectively.

3.3. Model performance accuracy

The yield estimation model obtained from experiments shown in Fig. 3. Position number 1 in Fig. 3 is in the same position as the reference data used in the yield estimation model. Field numbers 2 and 3 are approximately 72 km from field number 1.

NDVI, GNDVI, SAVI and MSAVI indices were generated from remote sensed Landsat-8 and Sentinel-2A satellite data at certain time intervals from planting to harvest. The obtained index values were determined pre-flowering, flowering stage, and post-flowering, and the indices values at these dates were applied to the equation obtained in the yield model. The yield values of the cultivated fields have been tried to be estimated by using all indices values for every three periods and the results are shown in Table 8(b, c and d) for test areas 1, 2, and 3, respectively. Model accuracy was calculated with equation 4.

Table 8(b) shows that the most suitable result out of four indexes is during flowering with MSAVI. GNDVI and MSAVI also achieved 95.88% and 99.99% accuracy at the flowering stage, respectively. In NDVI, the highest accuracy was achieved pre-flowering (95.80%). In addition, high accuracy was obtained in other periods (88.76% for flowering and 87.98% for post-flowering). SAVI is the only index with more than 90% accuracy in all three periods. Although the highest accuracy was achieved after flowering (98.62%), high accuracies were also obtained pre-flowering and during the flowering phase (97.11% for pre-flowering and 93.47% for the flowering period) (Fig. 4).

$$\text{Model Accuracy} = \left(1 - \frac{|\text{Estimated Yield} - \text{Actual Yield}|}{\text{Actual Yield}}\right) * 100 \qquad (4)$$

Table 6. Dates of Phenological Stages

Season	Pre-Flowering Date	Flowering Date	Post-Flowering Date
2015-2016	24.03.2016	23.04.2016	03.05.2016
2016-2017	28.04.2017	08.05.2017	14.05.2017
2017-2018	02.02.2018	19.03.2018	18.05.2018

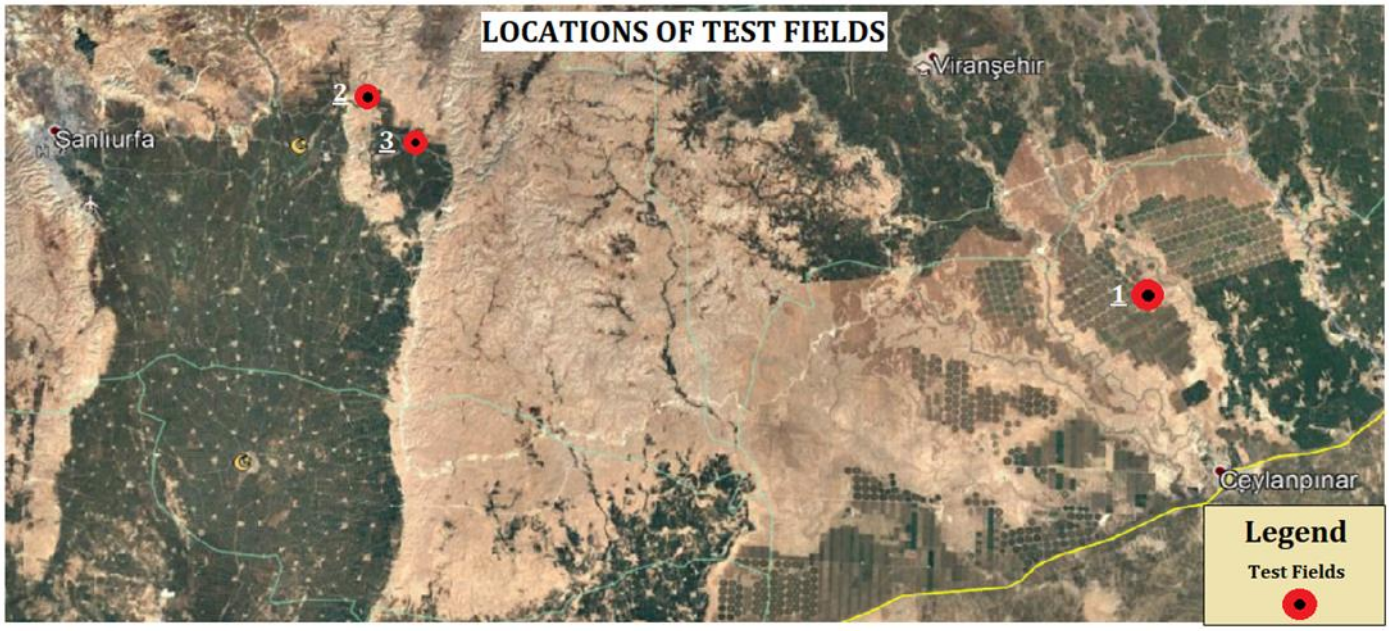

Figure 3. Locations of Test Fields

Table 7. Indices Values for Pre-flowering, flowering and post-flowering seasons (a) NDVI, (b) GNDVI, (c) SAVI, (d) MSAVI

Season	Field Number	(a) NDVI			(b) GNDVI			(c) SAVI			(d) MSAVI		
		Pre-Flowering	Flowering	Post-Flowering	Pre-Flowering	Flowering	Post-Flowering	Pre-Flowering	Flowering	Post-Flowering	Pre-Flowering	Flowering	Post-Flowering
2015-2016	1	0.64	0.81	0.41	0.55	0.7	0.37	0.51	0.59	0.27	0.45	0.63	0.24
	350	0.65	0.67	0.51	0.58	0.59	0.47	0.54	0.64	0.34	0.49	0.48	0.31
	354	0.37	0.4	0.29	0.32	0.3	0.25	0.29	0.3	0.13	0.67	0.09	0.08
	361	0.66	0.75	0.6	0.58	0.67	0.54	0.53	0.6	0.44	0.48	0.6	0.43
2016-2017	17	0.56	0.72	0.43	0.51	0.63	0.56	0.43	0.65	0.44	0.42	0.5	0.4
	32	0.62	0.74	0.44	0.55	0.64	0.57	0.46	0.66	0.45	0.46	0.51	0.42
	36	0.66	0.73	0.43	0.58	0.63	0.54	0.49	0.65	0.4	0.48	0.51	0.39
	47	0.61	0.74	0.44	0.55	0.65	0.58	0.46	0.66	0.48	0.46	0.53	0.43
	207	0.49	0.52	0.28	0.45	0.5	0.39	0.36	0.41	0.23	0.34	0.34	0.18
	333	0.47	0.63	0.31	0.44	0.56	0.44	0.37	0.46	0.24	0.35	0.4	0.24
2017-2018	1	0.48	0.81	0.5	0.42	0.68	0.45	0.29	0.59	0.31	0.27	0.62	0.28
	17	0.49	0.81	0.49	0.44	0.68	0.36	0.3	0.64	0.3	0.28	0.68	0.18
	32	0.47	0.82	0.44	0.41	0.69	0.41	0.28	0.6	0.26	0.25	0.64	0.24
	36	0.39	0.75	0.37	0.38	0.46	0.42	0.25	0.46	0.28	0.23	0.35	0.26
	47	0.52	0.8	0.46	0.44	0.67	0.43	0.31	0.57	0.28	0.28	0.6	0.25
	350	0.47	0.69	0.34	0.46	0.35	0.6	0.3	0.49	0.19	0.27	0.17	0.48
	354	0.24	0.34	0.12	0.3	0.27	0.28	0.09	0.12	0.06	0.11	0.06	0.08
	361	0.37	0.49	0.27	0.41	0.36	0.56	0.23	0.42	0.18	0.21	0.15	0.41

Table 8. (a) Yield equations (y refers yield value; x refers indices value) and Model performance accuracy calculations for phonological stages per vegetation index: (b) Test field 1, (c) Test field 2, (d) Test field 3

(a)					(b)			(c)			(d)		
					Test Field 1			Test Field 2			Test Field 3		
Indices	Stage	Equations	Correlation coefficients (R)	Determination coefficient (R^2)	Index Value	Estimated Yield (kg/daa)	Actual Yield (kg/daa)	Index Value	Estimated Yield (kg/daa)	Actual Yield (kg/daa)	Index Value	Estimated Yield (kg/daa)	Actual Yield (kg/daa)
NDVI	Pre-Flowering	y= 894.5x-111.36	0.59	0.35	0.47	310.33	297.3	0.6	420.87	450	0.86	657.91	700
	Flowering	y= 1006x-340.5	0.82	0.67	0.67	334.96	297.3	0.71	373.76	450	0.9	564.9	700
	Post-Flowering	y= 1159x-114.11	0.73	0.53	0.39	337.9	297.3	0.52	488.57	450	0.86	876.84	700
SAVI	Pre-Flowering	y= 698.68x+92.319	0.48	0.23	0.28	288.95	297.3	0.34	326.38	450	0.68	563.93	700
	Flowering	y= 987.73x-178.09	0.8	0.64	0.46	279.09	297.3	0.48	293.55	450	0.67	486.16	700
	Post-Flowering	y= 1147.5x+8.0299	0.74	0.55	0.25	293.27	297.3	0.29	340.8	450	0.71	817.02	700
GNDVI	Pre-Flowering	y=980.68x-113.13	0.48	0.23	0.46	340.78	297.3	0.41	288.95	450	0.71	583.15	700
	Flowering	y=1044.6x-239.74	0.86	0.74	0.5	285.54	297.3	0.63	418.36	450	0.81	601.16	700
	Post-Flowering	y=356.08x+180.76	0.64	0.4	0.41	326.75	297.3	0.46	342.78	450	0.76	451.38	700
MSAVI	Pre-Flowering	y=301.09x+234.53	0.71	0.5	0.32	331.31	297.3	0.24	305.29	450	0.48	377.55	700
	Flowering	y=771.23x+7.5578	0.87	0.75	0.38	297.32	297.3	0.48	377.75	450	0.57	443.3	700
	Post-Flowering	y=325.98x+247.37	0.64	0.41	0.22	318.15	297.3	0.28	338.64	450	0.47	398.95	700

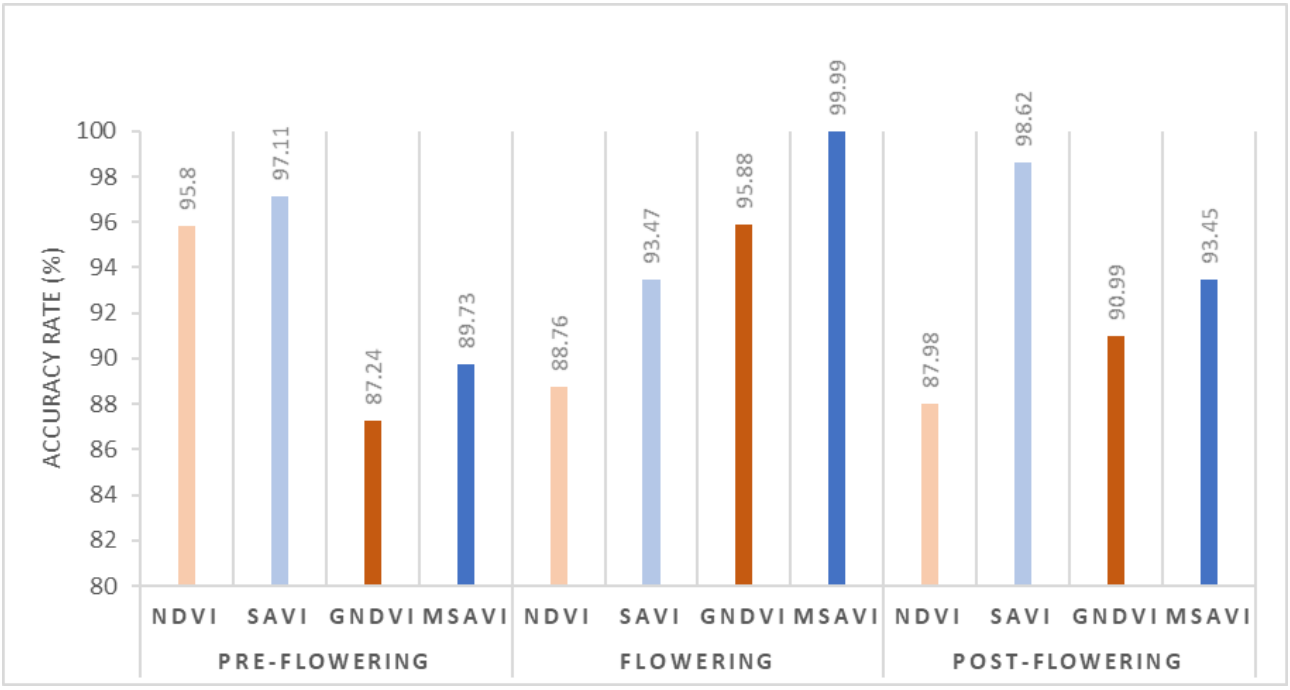

Figure 4. Model Performance Accuracy Analysis for all phenological stages per index for test field 1

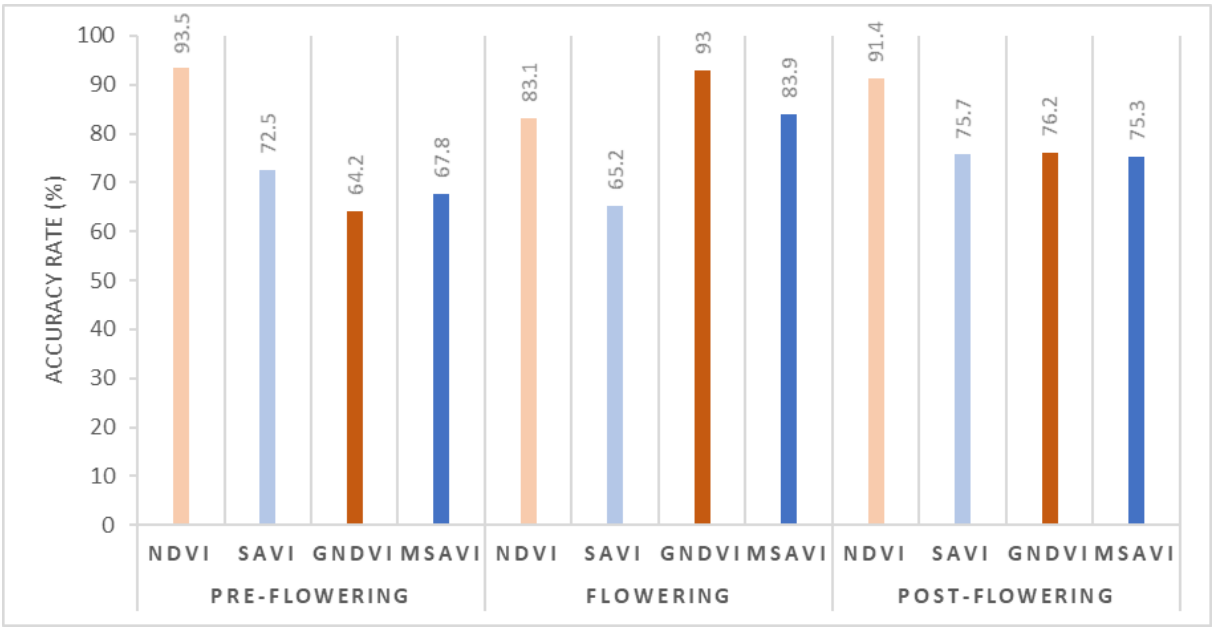

Figure 5. Accuracy Analysis for all phenological stages per index for test field 2

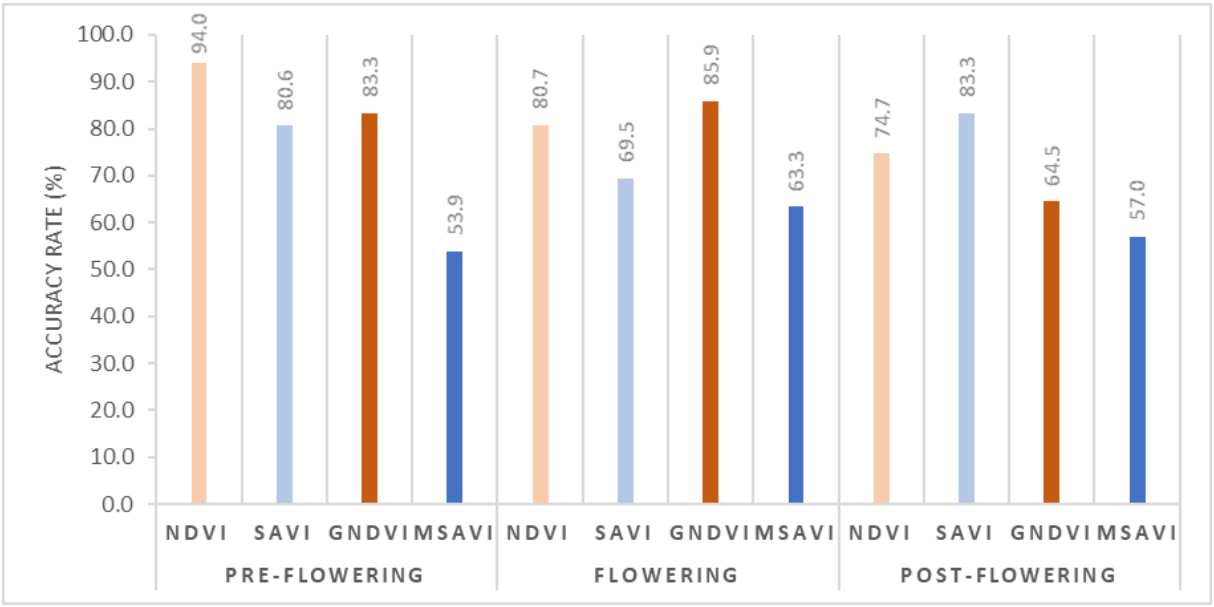

Figure 6. Accuracy Analysis for all phenological stages per index for test field 3

Table 8(c) shows that the highest accuracy is achieved with NDVI pre-flowering. GNDVI and MSAVI achieved 93% and 83.9% accuracy at the flowering stage, respectively. Although the highest accuracy was obtained pre-flowering (93.5%) in NDVI, high accuracy was also obtained in other stages. The highest accuracy in SAVI was obtained post-flowering (75.7%) (Fig. 5).

Table 8(d) shows, as Table 8(c), that the highest accuracy is achieved with NDVI (94%) pre-flowering. The second highest accuracy was obtained with GNDVI in the flowering stage (85.9%). While 83.3% accuracy was obtained post-flowering with SAVI, 63.3% accuracy was obtained at the flowering stage with MSAVI (Fig. 6).

When Table 8(b, c and d) are evaluated together, GNDVI and MSAVI gave more accurate results in the flowering stage compared to the other stages. In addition, compared to other stages, the highest accuracy was obtained pre-flowering in NDVI while it was obtained post-flowering in SAVI.

4. Conclusion

The main aim of this study was to establish a yield estimation model by using four widely used spectral indices. Since the life cycle of a vegetation starts with sowing, passes from several stages, and ends with harvest, firstly a phenological stages determination process was applied to get yearly proper dates for spectral indices. In the next step, a linear regression model was established between vegetation indices and actual yield values for pre-flowering, flowering, and post-flowering stages. The highest correlation of the generated model was observed in MSAVI with a coefficient of r = 0.87. The other correlation coefficients were calculated as GNDVI (r = 0.86), NDVI (r = 0.82) and SAVI (r = 0.80). The generated yield estimation model was applied to get predict actual yield of 3 different test field and compared with its actual value. According to the index-based results, the NDVI was the most successful

index to predict yield with an 87.77% mean accuracy value. GNDVI, SAVI, and MSAVI had 82.36%, 81.78%, and 76.04% mean accuracy value, respectively. Besides, in a phenological stages manner, NDVI was more successful in Pre-Flowering stage with a 94.43 % mean accuracy rate. In Flowering stage, GNDVI reach the best mean accuracy rate with 91.59%. In Post-Flowering stage the SAVI showed the highest mean accuracy rate 85.87%.

Although this comprehensive study reached notable results yet includes limitations. Firstly, the resolution of the satellite images has direct effect on the results. Secondly the generated model could not apply different fields due to the model is depending on the reference data. This means, for a region which has similar conditions the model should be re generated.

In future studies, it is planned to develop a wider range of yield estimation models from satellite images with higher spatial resolution and images obtained with hyperspectral cameras. In addition, further studies need to be carried out in order to validate field measurements.

Acknowledgement

We thank the General Directorate of Agricultural Enterprises for providing data.

Author contributions

Yunus Kaya: Methodology, Data curation, Writing-Original draft preparation, Software **Nizar Polat:** Conceptualization, Reviewing and Editing

Conflicts of interest

The authors declare no conflicts of interest.

References

1. Wang, Y., Xu, X., Huang, L., Yang, G., Fan, L., Wei, P. & Chen, G. (2019). An improved CASA model for estimating winter wheat yield from remote sensing images. Remote Sensing, 11(9), 1088.
2. Selim, S., & Demir, N. (2019). Detection of ecological networks and connectivity with analyzing their effects on sustainable urban development. International Journal of Engineering and Geosciences, 4(2), 63-70.
3. Godfray, H. C. J., Beddington, J. R., Crute, I. R., Haddad, L., Lawrence, D., Muir, J. F., Pretty, J., Robinson, S., Thomas, S. M. & Toulmin, C. (2010). Food security: The challenge of feeding 9 billion people. Science, 327(5967), 812-818.
4. Uyan, M. (2019). Comparison Of Different Interpolation Techniques in Determining of Agricultural Soil Index on Land Consolidation Projects. International Journal of Engineering and Geosciences, 4(1), 28-35.
5. Knox, J. W., Haro-Monteagudo, D., Hess, T., & Morris, J. (2018). Forecasting Changes in Agricultural Irrigation Demand to Support a Regional Integrated Water Resources Management Strategy. Advances in Chemical Pollution, Environmental Management and Protection, 3, 171-213.
6. Bastiaanssen, W. G. M. & Ali, S. (2003). A new crop yield forecasting model based on satellite measurements applied across the Indus Basin, Pakistan. Agriculture, Ecosystems and Environment, 94(3), 321–340.
7. Apaydin, C., & Abdikan, S. (2021). Fındık bahçelerinin Sentinel-2 verileri kullanılarak piksel tabanlı sınıflandırma yöntemleriyle belirlenmesi. Geomatik, 6(2), 107-114.
8. Li, H., Chen, Z., Liu, G., Jiang, Z. & Huang, C. (2017). Improving Winter Wheat Yield Estimation from the CERES-Wheat Model to Assimilate Leaf Area Index with Different Assimilation Methods and Spatio-Temporal Scales. Remote Sensing, 9(3), 190.
9. Lipper, L., Thornton, P., Campbell, B. M., Baedeker, T., Braimoh, A., Bwalya, M., Caron, P., Cattaneo, A., Garrity, D., Henry, K., Hottle, R., Jackson, L., Jarvis, A., Kossam, F., Mann, W., McCarthy, N., Meybeck, A., Neufeldt, H., Remington, T., Sen, P. T., Sessa, R., Shula, R., Tibu, A. & Torquebiau, E. F. (2014). Climate-smart agriculture for food security. Nature Climate Change, 4(1068-1072).
10. Reynolds, C. A., Yitayew, M., Slack, D. C., Hutchinson, C. F., Huete, A. & Petersen, M. S. (2000). Estimating crop yields and production by integrating the FAO Crop Specific Water Balance model with real-time satellite data and ground-based ancillary data. International Journal of Remote Sensing, 21(18), 3487–3508.
11. Liu, W. T., & Kogan, F. (2002). Monitoring Brazilian soybean production using NOAA/AVHRR based vegetation condition indices. International Journal of Remote Sensing, 23(6), 1161–1179.
12. Pinter, P. J., Hatfield, J. L., Schepers, J. S., Barnes, E. M., Moran, M. S., Daughtry, C. S. T., & Upchurch, D. R. (2003). Remote sensing for crop management. Photogrammetric Engineering and Remote Sensing, 69(6), 647-664.
13. Fernandez-Ordonez, Y. M., & Soria-Ruiz, J. (2017). Maize crop yield estimation with remote sensing and empirical models. In International Geoscience and Remote Sensing Symposium (IGARSS), Institute of Electrical and Electronics Engineers Inc., 3035-3038.
14. Salazar, L., Kogan, F. & Roytman, L. (2007). Use of remote sensing data for estimation of winter wheat yield in the United States. International Journal of Remote Sensing, 28(17), 3795–3811.
15. Ahmad, I., Saeed, U., Fahad, M., Ullah, A., ur Rahman, M. H., Ahmad, A. & Judge, J. (2018). Yield forecasting of spring maize using remote sensing and crop modeling in Faisalabad-Punjab Pakistan. Journal of the Indian Society of Remote Sensing, 46(10), 1701-1711.
16. Ferguson, M.C. (1982). Evaluation of Trends in Yield Models: Agristars Supporting Research. December, SR J1-04157, JSC-17428.
17. Tucker, C. J., Holben, B. N., Elgin, J. H. & McMurtrey, J. E. (1981). Remote sensing of total dry-matter accumulation in winter wheat. Remote Sensing of Environment, 11, 171-189.
18. Craig, M. E. (2001). A resource sharing approach to crop identification and estimation. In ASPRS 2001 Proceedings of the 2001 Annual Conference.

19. Raun, W. R., Solie, J. B., Johnson, G. V., Stone, M. L., Lukina, E. V., Thomason, W. E., & Schepers, J. S. (2001). In-Season Prediction of Potential Grain Yield in Winter Wheat Using Canopy Reflectance. Agronomy Journal, 93(1), 131–138.
20. Ren, J. Q., Chen, Z. X., Zhou, Q. B., & Tang, H. J. (2010). LAI-based regional winter wheat yield estimation by remote sensing. Chinese Journal of Applied Ecology, 21(11), 2883-2888.
21. Şimşek, O., & Çakmak, B. (2012). Agrometshell modeli ile buğdayda geleceğe dönük senaryolar ve risk analizi. Tarım Bilimleri Dergisi, 18(3), 187-196.
22. Narin, O. G., Noyan, O. F., & Abdikan, S. (2021). Monitoring Vegetative Stages of Sunflower and Wheat Crops with Sentinel-2 Images According to BBCH-Scale. Journal of Agricultural Faculty of Gaziosmanpasa University, 38(1), 46-52.
23. Narin, O. G., & Abdikan, S. (2020). Monitoring of phenological stage and yield estimation of sunflower plant using Sentinel-2 satellite images. Geocarto International, 1-15.
24. Becker-Reshef, I., Vermote, E., Lindeman, M., & Justice, C. (2010). A generalized regression-based model for forecasting winter wheat yields in Kansas and Ukraine using MODIS data. Remote Sensing of Environment, 114(6), 1312–1323.
25. Mkhabela, M. S., Bullock, P., Raj, S., Wang, S., & Yang, Y. (2011). Crop yield forecasting on the Canadian Prairies using MODIS NDVI data. Agricultural and Forest Meteorology, 151(3), 385–393.
26. Skakun, S., Vermote, E., Roger, J. C. & Franch, B. (2017). Combined Use of Landsat-8 and Sentinel-2A Images for Winter Crop Mapping and Winter Wheat Yield Assessment at Regional Scale. AIMS Geosciences, 3(2), 163–186.
27. Gontia, N. K., & Tiwari, K. N. (2011). Yield Estimation Model and Water Productivity of Wheat Crop (Triticum aestivum) in an Irrigation Command Using Remote Sensing and GIS. Journal of the Indian Society of Remote Sensing, 39(1), 27–37.
28. Benek, S. (2006). Şanlıurfa ilinin tarımsal yapısı, sorunları ve çözüm önerileri. Turkish Journal of Geographical Sciences, 4(1), 67-91.
29. Yağmur, N., Tanık, A., Tuzcu, A., Musaoğlu, N., Erten, E., & Bilgilioglu, B. (2020). Oppurtunities provided by remote sensing data for watershed management: Example of Konya closed basin. International Journal of Engineering and Geosciences, 5(3), 120-129.
30. Zabci, C. (2021). Çok bantlı Landsat 8-OLI ve Sentinel-2A MSI uydu görüntülerinin karşılaştırmalı jeoloji uygulaması: Örnek çalışma alanı olarak Doğu Anadolu Fayı boyunca Palu–Hazar Gölü Bölgesi (Elazığ, Türkiye). Geomatik, 6(3), 238-246.
31. Ahady, A. B., & Kaplan, G. (2022). Classification comparison of Landsat-8 and Sentinel-2 data in Google Earth Engine, study case of the city of Kabul. International Journal of Engineering and Geosciences, 7(1), 24-31.
32. Tanaka, D. L. (1989). Spring Wheat Plant Parameters as Affected by Fallow Methods in the Northern Great Plains. Soil Science Society of America Journal, 53(5), 1506–1511.
33. Meier, U. (2001). Growth stages of mono- and dicotyledonous plants. BBCH Monograph.
34. Gündeş, S., & Peştemalci, V. (2008). Türkiye'nin Bitki Örtüsü Değişiminin NOAA Uydu Verileri ile Belirlenmesi. Ç. Ü. Fen Bilimleri Enstitüsü, 17(6).
35. Kundu, A., Dwivedi, S., & Dutta, D. (2016). Monitoring the vegetation health over India during contrasting monsoon years using satellite remote sensing indices. Arabian Journal of Geosciences, 9(2), 1–15.
36. Üstüner, M., Şanli, F. B., & Abdikan, S. (2016). Bitki örtüsü indekslerinin tarimsal ürün deseni tespitindeki etkisinin araştırılması. In Proceedings of VI. RS&GIS Symposium (VI. UZAL&CBS Sempozyumu), Adana, Turkey.
37. Aboelghar, M., Ali, A. R., & Arafat, S. (2014). Spectral wheat yield prediction modeling using SPOT satellite imagery and leaf area index. Arabian Journal of Geosciences, 7(2), 465–474.
38. Jackson, R. D., & Huete, A. R. (1991). Interpreting vegetation indices. Preventive Veterinary Medicine, 11(3–4), 185-200.
39. Konda, V. G. R. K., Chejarla, V. R., Mandla, V. R., Voleti, V., & Chokkavarapu, N. (2018). Vegetation damage assessment due to Hudhud cyclone based on NDVI using Landsat-8 satellite imagery. Arabian Journal of Geosciences, 11(2), 1–11.
40. Peng, W., Wang, J., Zhang, J., & Zhang, Y. (2020). Soil moisture estimation in the transition zone from the Chengdu Plain region to the Longmen Mountains by field measurements and LANDSAT 8 OLI/TIRS-derived indices. Arabian Journal of Geosciences, 13(4), 1–13.
41. Tucker, C. J. (1979). Red and photographic infrared linear combinations for monitoring vegetation. Remote Sensing of Environment, 8(2), 127-150.
42. Ray, T. R. (1994). Vegetation indices in Remote Sensing. A FAQ on Vegetation in Remote Sensing.
43. Richardson, A. J., & Wiegand, C. L. (1977). Distinguishing vegetation from soil background information. Photogrammetric Engineering and Remote Sensing, 43(12), 1541-1552.
44. Rouse, W., Haas, R. H., & Deering, D. W. (1974). Monitoring vegetation systems in the Great Plains with ERTS. Third ERTS-1 Symposium, 309-329.
45. Gitelson, A. A., Kaufman, Y. J., & Merzlyak, M. N. (1996). Use of a green channel in remote sensing of global vegetation from EOS- MODIS. Remote Sensing of Environment, 58(3), 289–298.
46. Huete, A. (1988). A soil-adjusted vegetation index (SAVI). Remote Sensing of Environment, 25(3), 295-309.
47. Qi, J., Chehbouni, A., Huete, A. R., Kerr, Y. H., & Sorooshian, S. (1994). A modified soil adjusted vegetation index. Remote Sensing of Environment, 48(2), 119-126.

International Journal of Engineering and Geosciences
https://dergipark.org.tr/en/pub/ijeg
e-ISSN 2548-0960

Determination of the appropriate zone on dam surface for floating photovoltaic system installation using RS and GISc technologies

Osman Salih Yılmaz [*1], **Fatih Gülgen** [2], **Ali Murat Ateş** [3]

[1] *Manisa Celal Bayar University, Geographical Information Systems Department, Türkiye*
[2] *Yıldız Technical University, Geomatics Engineering Department, Türkiye*
[3] *Manisa Celal Bayar University, Computer and Instructional Technologies Department, Türkiye*

Keywords
Remote sensing
GIS
Google Earth Engine
Solar power plant
Solar analysis

Research Article
DOI: 10.26833/ijeg.1052556

Received: 02.01.2022
Accepted: 11.02.2022
Published: 13.04.2022

Abstract

This study aims to reveal suitable places where floating photovoltaic-solar power plants (FPV-SPPs) can be installed on the dam surface using the possibilities of remote sensing (RS) and geographical information science (GISc) technologies. Past satellite images from Landsat and Sentinel platforms allow researchers to analyse shoreline changes in the dam surface. Shoreline extraction is a crucial process for the FPV-SPP to stay afloat despite external constraints. In this study, changes in dam water levels were determined by classifying 20-year satellite images and analysing a 32-year global surface water dynamics dataset. The water surface area was calculated as 1,562.40 ha using the random forest (RF) algorithm and the normalized differences water index (NDWI) on Google Earth Engine (GEE) cloud platform. In addition, solar analysis was carried out with GISc using annual solar radiation maps shuttle radar topography mission (SRTM) data, which directly affects the energy production of FPV-SPPs. It has been calculated that the solar radiation on the water surface varies between 1,554 kWh/m^2-year and 1,875 kWh/m^2-year. These calculated values were divided into five different classes, and it was observed that 88.5% of the dam surface had a very high level of solar radiation compared to other areas. Higher efficiency will be obtained from the FPV-SPP to be installed in this region compared to the systems to be installed in other regions. It has been observed that the radiation values in other parts of the water surface are lower due to topographic shading. These analyses revealed energy zones with high production potential, thereby easing the decision-making process for investors planning to establish FPV-SPPs.

1. Introduction

Ensuring sustainability of water resources is very important in environmental, economic, and strategic terms for humans, animals, plants and the ecosystem [1]. One of the water resources is the dams that produce hydroelectric energy and at the same time are built to prevent floods in places with abundant rainfall [2]. The amount of water in dams changes frequently due to uses for agricultural irrigation, energy production activities, and climatic changes. Monitoring these changes is a necessity within the scope of understanding hydrological processes and good management of water resources [3]. Remote sensing technology, with its advantages of continually, rapidly, informatively and dynamically monitoring the large-scale environment, is one of the important tools in terms of obtaining information about the change in the dam coastal region [4, 5]. and tracking the water dynamics [6]. Changes in physically inaccessible regions can be quickly, cost-effectively, and advantageously monitored using medium-resolution optical images obtained from satellites, such as Landsat and Sentinel [7].

Rapid population growth and industrial investments exponentially increase countries' need for energy. Approximately 81% of the total energy consumption in the world is met by fossil fuel resources [8]. The intensive use of fossil fuels causes the emission of harmful gases and the deterioration of the natural balance. Renewable energy systems that transform natural resources into electrical energy stand out as alternatives to fossil fuels. Among these systems, solar power plants (SPPs)

* **Corresponding Author**
*(osmansalih.yilmaz@cbu.edu.tr) ORCID ID 0000 - 0003 - 4632 - 9349
(fgulgen@yildiz.edu.tr) ORCID ID 0000 - 0002 - 8754 - 9017
(murat.ates@cbu.edu.tr) ORCID ID 0000-0002-2815-1404

Cite this article
Yılmaz, O. S., Gülgen, F., & Ateş, A. M. (2023). Determination of the appropriate zone on dam surface for floating photovoltaic system installation using RS and GISc technologies. International Journal of Engineering and Geosciences, 8(1), 63-75

producing electricity from solar insolation are the most prominent. The conversion from solar to electrical energy is made by photovoltaic (PV) cells, which have been used since the 1950s. PV-SPPs comprise many solar panels, and the total radiation coming to the surface of the panels directly affects the efficiency of the system [9]. The direct solar radiation and the absence of shadows on the module surfaces provide maximum efficiency in PV-SPPs throughout the year. Shading in SPPs installed on building roofs or facades is generally high due to environmental factors. It is desirable to place the panels in the most appropriate position and angle to reduce the shading effect in collecting solar insolation [10].

SPPs can be installed on marginal agricultural lands [11], roofs [12, 13] or hydrographic surfaces, such as seas, lakes, dams, and canals [14, 15]. In floating PV (FPV) plants installed on the water surface, the environmental impact causing shading is reduced, and more solar radiation is used. Moreover, FPV-SPPs generate more energy than terrestrial systems, as they reduce the panel temperature of water [16]. The panels that cover the water surface also reduce the amount of evaporation, prevent sunlight from penetrating deep, reduce algae growth, and keep the water clean [17]. Particularly, FPV-SPPs aiming to make idle water surfaces usable for energy production are used in several countries, such as the US, Australia, Japan, China, South Korea, Brazil, and India [18].

Hydroelectric power plants (HPPs) are one of the most suitable surfaces for FPV-SPP installation due to the existing electrical energy infrastructure. However, the dynamic water level of dams can cause radical changes in shoreline boundaries. In this case, the FPV plant, which is planned to float continuously, may go aground and its electrical efficiency may decrease. Also, sharp rocks below the water level in the reservoir may rise to the surface with the withdrawal of water and damage the panels. To prevent these problems, the plant's design

should be made by considering in advance the possible changes in the dam boundaries [19]. These changes can be determined from evaluations made from the past to the present.

Energy efficiency for FPV-SPPs installed on water surfaces is usually calculated by ignoring the shading effect [20]. However, the topography of the land around the dam and other artificial elements in the area can create a shading effect on the water surface throughout the day. Various software developed to process geographical data includes analysis tools that gauge the amount of shading in a region during the day. For instance, hillshade analysis tools of geographical information system (GIS) software can be used to determine the shading effect. Solar analysis tools that consider the shading effect can be used to calculate solar radiation values for a given geographical location in certain periods [21]. Topographical factors such as differences in elevation and slope changes that make up the terrestrial shapes in the region are the main factors used in calculating the amount of shading and solar radiation [22].

RS and geographical information science (GISc) technologies include highly effective tools for monitoring water dynamics and changes in surface boundaries, shading, and solar radiation analysis from past to present [5]. In this study, the minimum limits due to the reduction in dam waters were determined by supervised classification using Landsat-5 Thematic Mapper (TM), Top of Atmosphere (TOA), Landsat-8 Operational Land Imager (OLI), and Sentinel-2 Multi-Spectral Instrument (MSI) L2A satellite images. The small islets formed from sharp rocks, which prevent the installation of FPV-SPP on the water surface, have emerged with the withdrawal of the dam water. These islets, whose positions and geometric shapes cannot be easily detected with traditional terrestrial surveying methods, can be easily detected by RS from the classified images. The water dynamics in this study area were extracted from the dataset created by Pekel et al. [6] using 32-year Landsat images. The calculated dam boundaries and water dynamics relationships were then compared. Later, an annual solar radiation map was created using the ArcGIS solar analysis tool. The area on the dam water surface in the prepared annual insolation map is classified according to solar energy potential. This study revealed the importance of RS and GISc opportunities in the facility of FPV-SPPs.

1.1. Literature Review

Water dynamics and surface boundary changes can be determined by pixel-based classification techniques using Landsat and Sentinel images [23]. There is various commercial software, such as ENVI, ERDAS, and eCognition, that can run supervised and unsupervised classification algorithms. Also, Google Earth Engine (GEE) platform, which can process big data and work in the cloud, is frequently used in pixel-based classification studies.

It is possible to determine the changes in large water masses up to 40 years with RS. However, computer systems with a powerful CPU and enough storage space are required to download and process many satellite images taken periodically. The long-term analyses conducted contribute to additional costs in the project budgets [24]. To eliminate this disadvantage today, Google has developed the GEE platform to map large areas of human settlements, analyse past changes and constantly update current estimates [25]. Operating in a cloud environment, GEE can simultaneously and easily access all the archives of Landsat and Sentinel images [26]. The GEE application interface allows development with JavaScript and Python scripting languages to access and analyse petabytes of data [27]. GEE is an effective platform for determining water dynamics, investigating temporal changes in water bodies, and monitoring seasonal changes [28]. Pekel et al. [6] analysed 32 years of water dynamics between 1984 and 2015, using more than three million Landsat images on a world scale with GEE. Chen et al. [29], Wang et al. [30], Xia et al. [31], and Deng et al. [32] have used GEE for making lake maps in China, determining maximum and minimum water coverage, and monitoring water surface changes. Nguyen et al. [33] performed a fully automated water surface extraction for New Zealand using Automated Water Extracting Index derived from Landsat-8 OLI images on the GEE platform. Jena et al. [34] and Bi et al.

[35] used the GEE platform to detect the seasonal variation of water surfaces.

It is vital to determine the appropriate locations where panels can be placed for FPV-SPPs to be installed on the water surface. Surface boundaries should be monitored in the long term for SPPs to be established, especially in dams, where water dynamics change rapidly [19]. Today, FPV systems are used less often than terrestrial PV systems. For this reason, an adequate academic examination of the issues facing the use of the FPV-SPP plant has not been established. There are quite a few studies where shading analysis is performed on the surfaces where they are installed due to the shading effect of PV systems to be installed on terrestrial surfaces [13]. For systems to be installed on marginal agricultural lands, many criteria, such as proximity to the road and transformer centre, land use, and topographic features, are considered. Approaches such as Multiple-Criteria Decision-Making [36] Analytic Hierarchy Process [37] and Artificial Neural Networks [38] are used to determine the effects of these criteria. Enough work has not been done to investigate the effect of shading on water surfaces in the installation of FPV systems. Song and Choi [20] performed a shading analysis using a digital elevation model with a fish-eye lens camera in a mine lake in Korea. Sahu et al. [39] suggested using RS and GIS-based techniques to increase the efficiency potential of FPV projects. Kumar [40] aimed to find the solar energy potential for the southern part of India through the application of different solar radiation, geology, topography, atmospheric conditions, slope, and geospatial technology. Abid et al. [15] In the 2MW FPV system in India, the shading of artificial elements around the lake was considered. However, determining the water surface boundaries where an FPV-SPP will be established and locating the facility in the region where the highest efficiency will be obtained is vital for researchers and investors.

2. Method

2.1. Study Area

This study was conducted in the Demirköprü Dam, which is in Manisa Province in the southwest of Turkey, which was put into operation for irrigation, flood control, and energy production in 1960 (Fig. 1). Demirköprü Dam is fed by the Demirci Stream from the north, Gediz River and Deliniş Stream from the East. The topography around the dam is in a wavy form, and this region is covered by oak forests, farmlands and bare lands. The area and water volume of the dam, which is the earth's body fill type, are 3,000 ha and 4,300,000 m^3, respectively [41]. The irrigation of 99,220 ha of agricultural land in the region is carried out from the Demirköprü Dam. A Hydro-electric Power Plant (HPP) with a 69 MW generating 193 GWh of electrical energy annually has been installed on the dam. The dam boundaries and water volume often vary depending on irrigation uses, electricity generation, and seasonal transitions. Agricultural irrigation activities are performed annually in the region from the beginning of August to the end of October. Concurrently, the amount of evaporation increased due to hot climatic conditions in the region between July and November. During this period, the water level usually dropped below average.

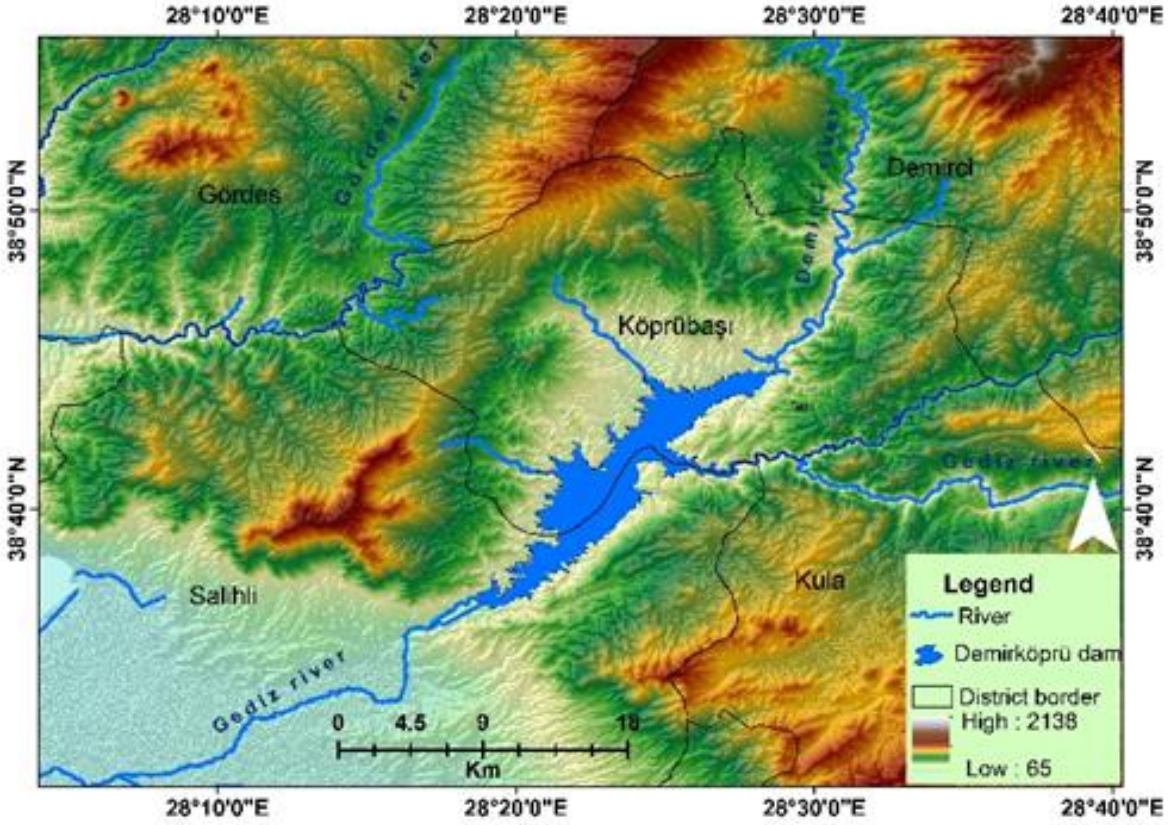

Figure 1. Location of the study area: Demirköprü Dam

2.2. Process steps in the article

In this study, changes in water surface boundaries and annual total solar insolation values were calculated based on the amount of shading on the water surface. These changes were then classified to determine the appropriate regions for the FPV-SPPs to be installed on the surface of the Demirköprü Dam. Changes in dam boundaries have been studied using two different methods. First, based on classification processes performed on images taken from satellite platforms. Second, the water surface changes in the dam area were monitored based on the surface water dynamics analysis proposed by Pekel et al. [6]. The analysis study was conducted using 3,066,080 images obtained from Landsat - 5 (TM), Landsat - 7 (ETM +), and Landsat - 8 (OLI) satellites covering the years 1984–2015. Landsat images have a temporal resolution of 16 days and a spatial resolution of 30 m. The constellation Sentinel-2A and Sentinel-2B together have a temporal resolution of 5 days. Sentinel satellite images provide data with 13 spectral bands, 12-bit radiometric resolution, and spatial resolution between 10-60 m.

The minimum limit for the installation of FPV-SPPs was determined by evaluating the information regarding the shoreline changes obtained from these two methods. Later, a solar insolation map was created considering the shading on the water surface within these boundaries using 30 m Shuttle Radar Topography Mission (SRTM) data covering the dam and its immediate surroundings. This insolation map is classified according to solar energy potential using the Jenks Natural Break (JNB) algorithm. The flow chart of the process steps is given in Fig. 2.

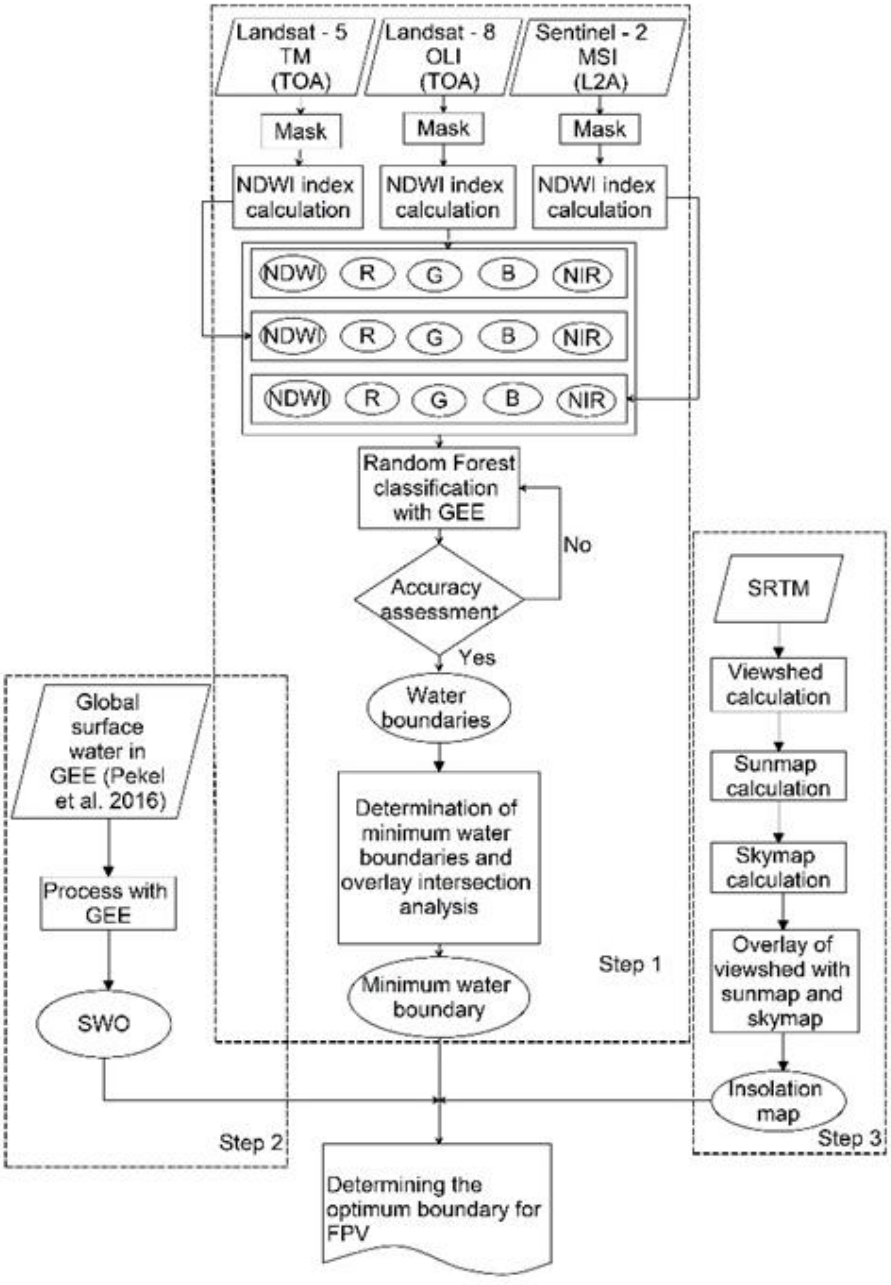

Figure 2. Flow chart of the analysis methodology

3. Results

3.1. Investigation of dam water surface change using satellite images

There are oak forests, planted agricultural areas, and bare areas around Demirköprü Dam. To detect the changes in these areas, 55 satellite images covering a span of 20 years from 1999–2019 have been classified. These images taken from Landsat-5, Landsat-8, and Sentinel-2 platforms in August, September, and October, when the dam water level was lowest, were classified by the RF algorithm in the GEE platform.

The red, green, blue, and infrared band data of each satellite image were used to distinguish the shoreline of the dam from other details. In addition to these bands, NDWI values suitable for the general characteristics of the region were calculated and included in the classification to extract the dam surface more sensitively. The accuracies of the performed classification operations were analysed by calculating producer's accuracy (PA), user's accuracy (UA), overall accuracy (OA), and kappa (K) values for each class. Among the images with an OA value over 90%, the water surface areas calculated as less than the 2,000-ha threshold are given in Table 1.

Table 1. High accuracy image classification results for Demirköprü Dam

Date	Spacecraft ID/Sensor	Area (ha)	PA (%)	UA (%)	OA (%)	K
14.08.2001	Landsat-5 (TM)	1741.6	100.0	99.9	92.0	0.882
15.09.2001		1711.5	100.0	99.9	94.8	0.924
01.10.2001		1694.7	100.0	99.9	93.1	0.899
10.09.2005		1979.6	100.0	100.0	93.1	0.899
15.08.2007		1625.2	100.0	99.8	93.1	0.898
16.09.2007		1601.8	100.0	99.7	93.2	0.901
21.08.2008		1603.2	99.7	99.8	95.1	0.928
07.09.2017	Sentinel-2 L2A (MSI)	1794.0	100.0	100.0	92.2	0.882
01.08.2018		1883.2	100.0	99.9	93.2	0.893
02.09.2018		1754.0	100.0	100.0	92.9	0.893
07.09.2019		1877.5	100.0	100.0	92.5	0.886

Among the 11 high-accuracy water surfaces derived by classification processes, five surfaces whose area values are smaller than the others are shown in Fig. 3 (a-e). The smallest surface found by the intersection of the dam surfaces derived by the classification defines the minimum boundaries of the Demirköprü Dam that constantly retains water Fig. 3 (f). This intersection area has been calculated as 1,562.4 ha [19].

On the dates when the dam's water level and surface area decrease, some small islets not visible at other times appear near the shores. Since these islets can damage FPV panels, their location and shape should be precisely established in advance. Furthermore, they can also be used as the fixing point of the panels as required. Their positions can be determined from Sentinel images with higher resolutions than Landsat images. Some of the islets determined from the classification are shown in red ellipses in Fig. 4. It is complex to determine their positions and shapes using classical terrestrial survey methods. The islets were precisely determined using high-resolution satellite images of these dates after determining that the dates of the dam water level were low.

3.2. Water dynamics for the Demirköprü Dam

Global surface water dynamics have been analysed by classifying spatial detail and accuracy levels at intervals of 5–10 years using medium-resolution Landsat satellite images covering 32 years [6]. In this study, NDWI was used to separate water from other details, and Hue-Saturation-Value (HSV) colour-space was used for image enhancement. Thematic maps were produced to characterize the water transitions between the first observation year and the last observation year. In the thematic maps produced, they stated that there was no significant change in the water in the black areas between 1984 and 2015, that the water increased in the green areas and decreased in the red areas. In addition, they divided the passages of water into different categories in their study. These categories are permanent water surfaces, new permanent water surfaces, lost permanent water surfaces, seasonal water surfaces, new seasonal water surfaces, lost seasonal water surfaces, conversion of permanent water into seasonal water.

Spectral library equations defining the classes used in the study were created through visual analysis. The performance of the global classification processes has been evaluated using 40,124 control points, and it has been proven that the accuracy is around 99% in the calculation. The derived global dataset has facilitated modelling of the water surface, mapping long-term changes in global water formation, tracking changes in freshwater resources, such as lakes and rivers, and tracking climatic changes.

During the monitoring period, the surface areas where water resources, such as waterbeds, rivers, dams, and lakes, remain constant have been determined. The permanent state of surface water is presented based on a single map called Surface Water Occurrence (SWO). Monthly SWO data were calculated using Eq.1 [6].

$$SWO^{month} = \sum WD^{month} / \sum VO^{month} \quad (1)$$

Where, WD is the monthly amount of water detected and VO is the number of valid observations.

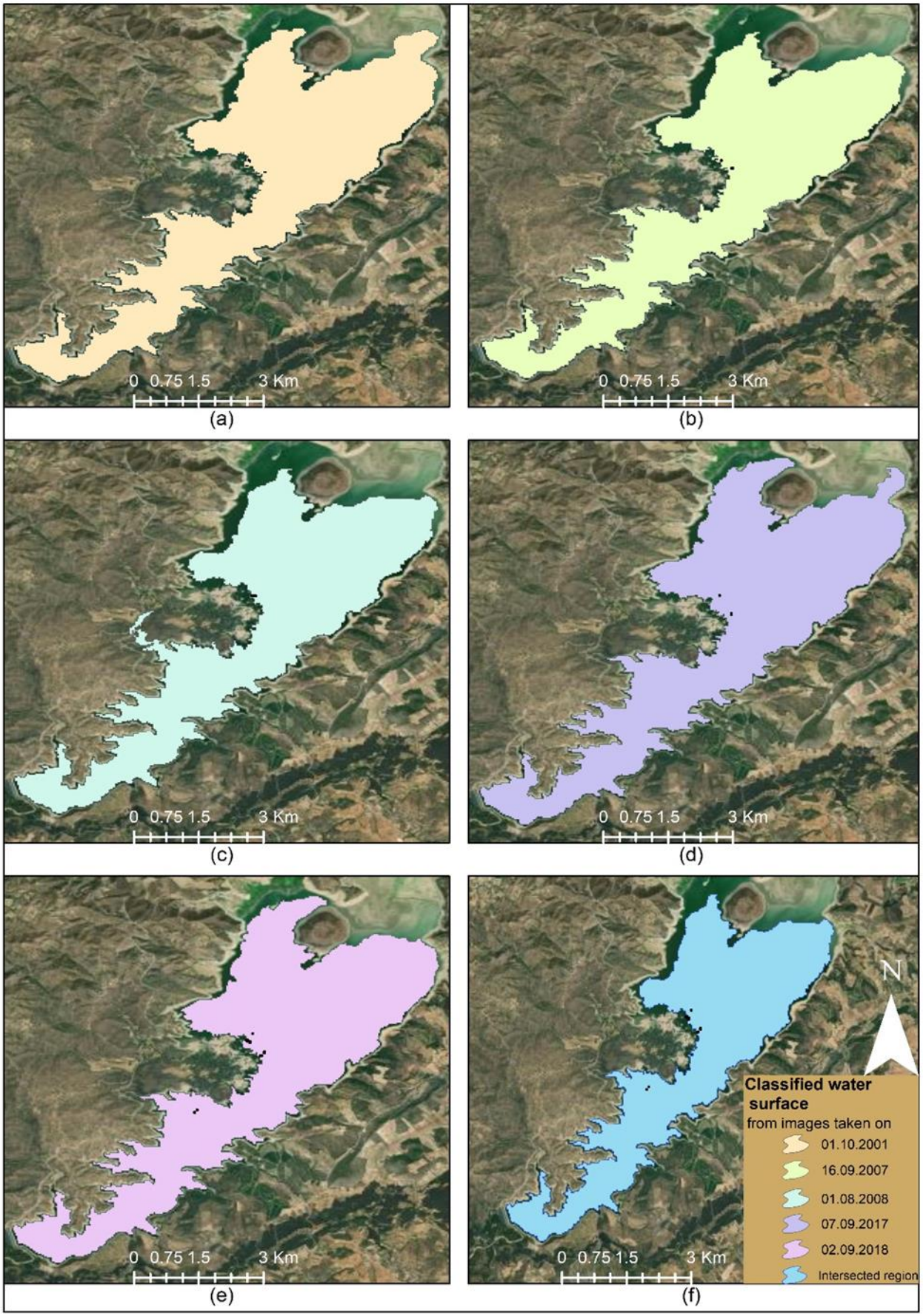

Figure 3. Five classifications with the smallest surface area (a–e) and the intersection of the surfaces (f)

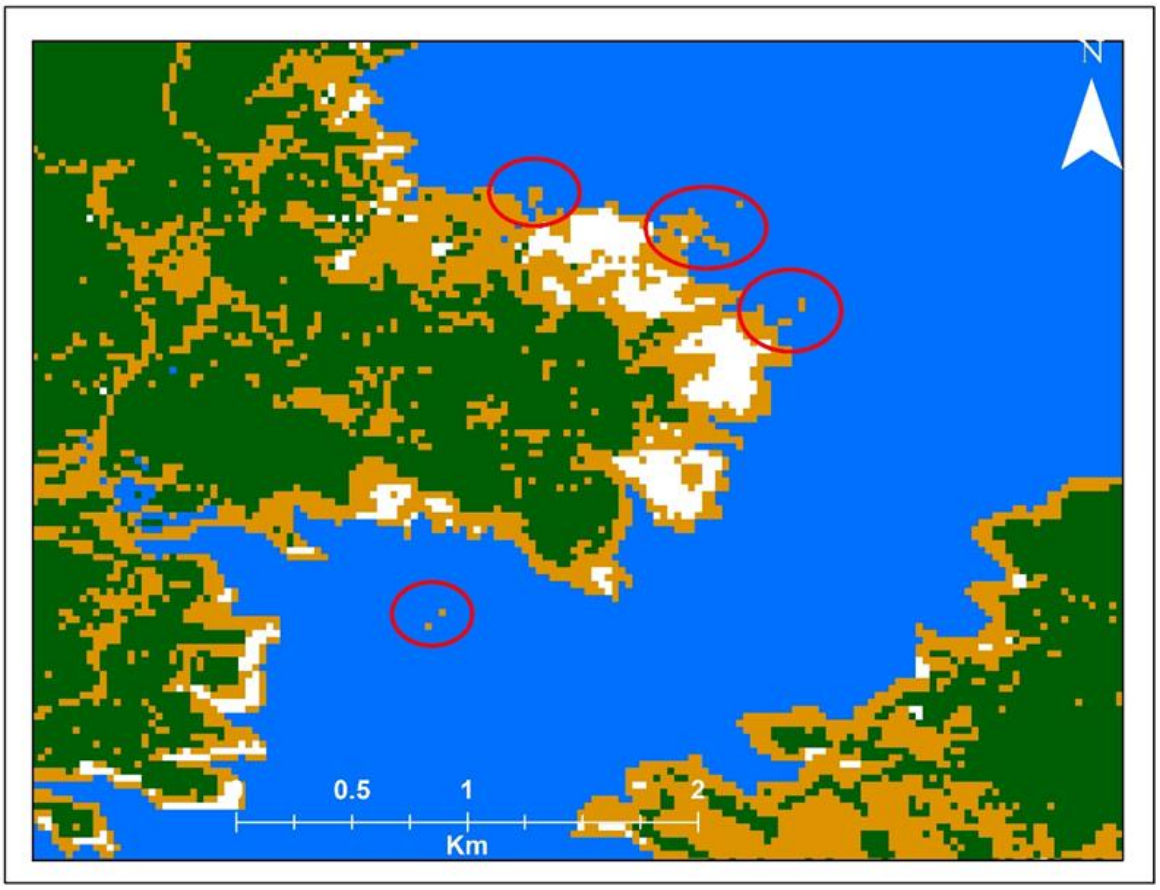

Figure 4. Islets extracted with the Sentinel 2A image dated 02.09.2018 are marked with red ellipses

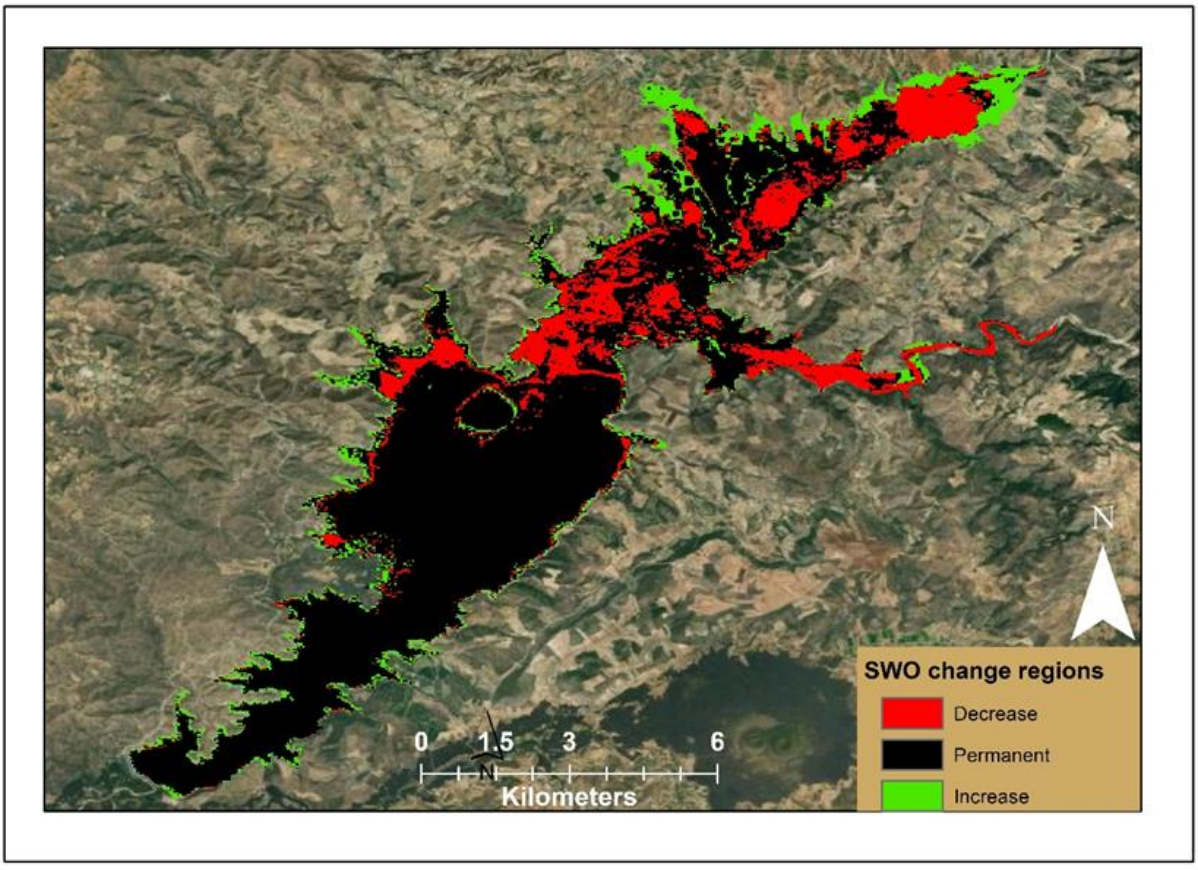

Fig. 2 SWO change map between 1984–2015 for Demirköprü Dam

This study, which is very useful in terms of interpreting the analyses and validating the methods used and carried out by writing code on the GEE platform, can be used as a ready data set in many academic studies.

32 years of global water dynamics analysis provides a map explaining the water dynamics in Demirköprü Dam. The change in the dam is in the form of continuous advancement and withdrawal of the shoreline. Increases in water formation are represented in green and decrease in red on the SWO map (Fig. 5). The regions with permanent water and no significant change in water formation between 1984 and 2015 are shown in black.

The region from the south to the middle of the dam is where water is constantly available. Time-dependent increases are observed in the coastal areas of this region. In contrast, the water is more dynamic in the northern part of the dam. Demirci Stream feeding from the north, Deliniş Stream, and Gediz River feeding on the east make Demirköprü Dam dynamic. Depending on the topographical formation, the transitivity that triggers the increases and decreases in the water level in the northern region is revealed by the SWO map. The currents formed in the northern part of the dam indicate that this area is unsuitable for FPV SPP installation.

The coherence between the SWO map and the Demirköprü Dam surface map obtained by the classification method was examined with the Kappa statistical test using randomly selected 1,000 points (Table 2). Kappa value calculated between the SWO map and the dam surface maps derived from the images dated September 2005, August 2018, and September 2019 are over 0.8. Kappa values higher than the threshold value indicate a very high agreement between the SWO map and the classified maps [42]. The areas with a Kappa value of less than 0.8 were found to be relatively lower than those in the fields on other dates. In this case, it was determined that the compatibility of these maps with the SWO map was lower, so according to the SWO map, the water level at those dates decreased more than the usual situation.

Consequently, in the last two decades, it has been determined that the withdrawal of water in Demirköprü Dam was high in August 2001, September 2001, October 2001, August 2007, September 2007, August 2008, September 2017, and September 2018.

Table 2. Accuracy test of the SWO map with images of the lowest water surface area maps

SWO change map	Date	Spacecraft ID/Sensor	K
Permanent data	14.08.2001	Landsat-5 (TM)	0.792
	15.09.2001		0.790
	01.10.2001		0.782
	10.09.2005		0.828
	15.08.2007		0.744
	16.09.2007		0.732
	01.08.2008		0.708
	07.09.2017	Sentinel-2 L2A (MSI)	0.790
	01.08.2018		0.808
	02.09.2018		0.770
	07.09.2019		0.810

3.3. Insolation map

The efficiency of PV systems depends on the amount of incident solar radiation on the panels' surfaces [43]. Topographical factors such as elevation, aspect, and slope affect the amount of incident solar radiation on the panel surface (Fig. 6). The spatial and temporal variations of this amount are revealed by solar radiation modeling. Modeling shows the effects of the sun on a geographical area for certain periods by spatial analysis based on topographic data [44]. Today, it is possible to produce solar radiation maps for a region using the solar analysis tools provided by GISc over the digital elevation model (DEM) dataset [45].

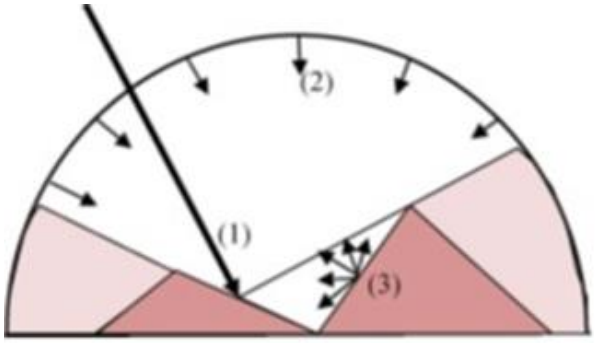

Figure 6. Solar energy sources on a surface: (1) direct radiation, (2) diffuse radiation reflected from the sky, and (3) diffuse radiation reflected from land [21]

In this study, solar radiation maps were created using the ArcGIS/Area Solar Radiation tool of ESRI, which offered comprehensive geometric modeling, high calculation speed, and accuracy [46]. A 30 m spatial resolution SRTM dataset was used to regionally map the amount of solar radiation that varies depending on the land topography and sun incidence angles. The annual total radiation of 2020 was calculated for each pixel in the area that includes Demirköprü Dam (Fig. 7). In the annual radiation calculation, the general parameters used according to the latitude of the region and the calculation period were selected as day interval 14, hour interval 0.5, and SkySize 200 [47]. Topographic and radiation parameters are given in Table 3.

Annual insolation map with 30 m spatial resolution for Demirköprü Dam and its near surroundings using SRTM DEM data overlaps with the smallest dam area given in Fig. 3 (f) and given in Fig. 5 (a). Solar radiation values calculated within the intersection field vary between 1,554 kWh/m^2-year and 1,875 kWh/m^2-year. This change is due to the shading caused by the topography around the dam. To reveal the effect of shading on the intersection region, 30 m resolution pixels were reclassified using the JNB algorithm according to the insolation value Fig. 7 (b). The classification made into five categories showed that insolation in the regions close to the shoreline of the dam was lower than in the inner regions (Table 4).

Table 3. Solar radiation parameters used in this study

Topographic parameters			Radiation parameters				
Z factor	Calculation directions	Calculation direction	Zenith divisions	Azimuth divisions	Diffuse model type	Diffuse Proportion	Transitivity
1	DEM	16	8	8	Standard overcast sky	0.5	0.5

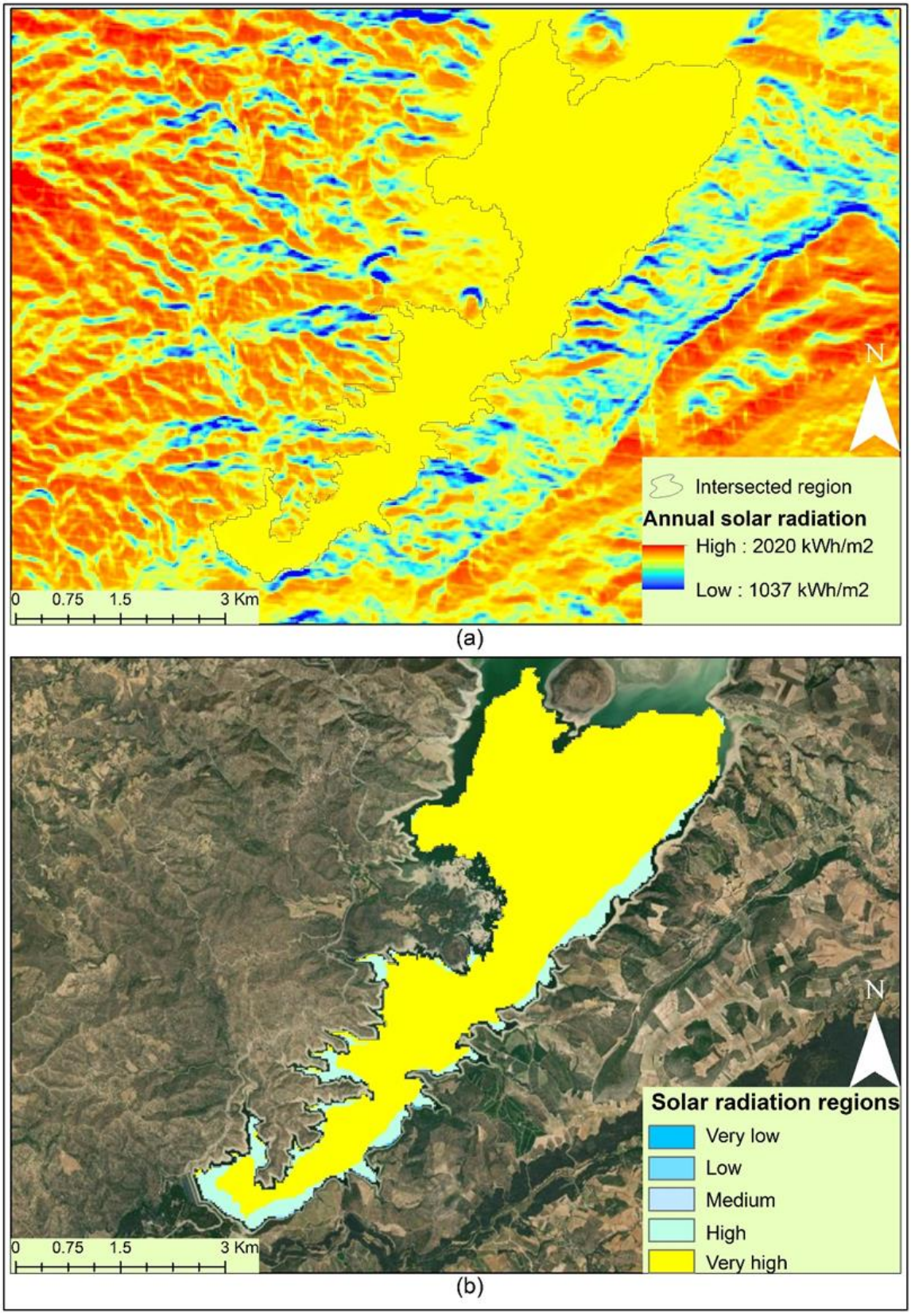

Figure 3. a) Annual insolation map of Demirköprü Dam and its near surround, b) classified solar radiations in the dam surface

Table 4. Classes calculated according to the JNB algorithm

Solar radiation value (kWh/m²)	Category	Area (ha)	Percentage (%)
1,796.8-1,875.2	Very High	1383.1	88.5
1,782.1-1,796.8	High	169.8	10.9
1,729.3-1,782.0	Medium	7.3	0.5
1,648.6-1,729.0	Low	1.4	0.1
1,554.0-1,648.6	Very Low	0.8	0.1

The area with very high insolation covers 88.5% of the dam area. Regions with medium, low, and very low insolation amounts constitute 0.6% of the total dam area. The insolation values of the regions on the shoreline in the east, south, and west of the dam basin are due to the wavy structure of the dam's shoreline and sharp rocks. The 10.9% of parts of the dam, which is a little further from the shoreline, is classified as high regarding insolation. Although this region is classified as high, it appears that there is some shading effect. When investing in FPV systems, it is important to valorise the shadowing effect in this region.

4. Discussion

The application of PV systems to water surfaces is a new and rapidly developing application in the world. A limited number of studies have been found on investigating the shading effect on water surfaces. For the installation of FPV systems, it is very important to calculate the water surface boundaries with the least error and to choose the most suitable places for installation. In the literature review, it is seen that RS and GIS techniques are widely used in determining the appropriate location of FPV systems. Especially in water surface applications, Sahu et al. [39] suggested the use of RS and GIS techniques in terms of increasing efficiency. In this study, the 20-year change in the area was examined by using RS to determine the suitable area for the FPV-GES installation on the Demirköprü dam water surface and was confirmed by the study by Pekel et al. [6].

The most important factor in the generation of electrical energy of photovoltaic systems is the amount of radiation falling on the module surface. Shading of the solar radiation of some module surfaces in the array due to any environmental factor affects the module efficiency, array efficiency and thus the efficiency of the PV system [48–52]. Various techniques are applied to reduce the shading effect [53]. However, applying strategies such as electrical interconnection changes or using microinverters in large-scale systems makes the system complex and increases its cost. The most practical and economical method to minimize the effect of shading is to determine the no shading or least shading areas. The ArcGIS solar radiation tool is frequently used to detect the total radiation in an area along with the effect of topography [54–58].

When the studies on FPV systems were examined, Kim et al. [59] focused on the selection of suitable sites. In their study, they created a water depth database using OpenAPI and estimated the radiation distribution using meteorological and topographical data. While the depth of the water was taken into account in that study, in our study, the surface area of the water, and therefore the horizontal shoreline change, was taken into account, since it was aimed to use the entire surface. In addition, the importance of topography in radiation distribution has been revealed. Lee and Lee [60] identified suitable locations for FPV systems with the Analytical Hierarchy Process (AHP) considering terrain and climatic factors. In their study, suitable river surface areas for FPV installation were determined using GIS techniques, while in this study, suitable areas of the dam surface were determined. Both studies are similar in this aspect.

5. Conclusion

The minimum areas in the classifications made using the RF Algorithm and NDWI over the Landsat and Sentinel satellite images of the Demirköprü Dam for the last 20 years were analyses with the GIS overlay tool, and the optimum area was calculated as 1,562.4 ha. Since the investment costs of FPVs are high, it is vital to precisely establish the water surfaces. Also, it was concluded that the detection of small islands caused by the decrease of the water level by remote sensing will be important in the net detection and fixation of the installation areas of FPV systems. According to this result, the regions with islets can only be used for fixation purposes.

Pekel et al. [6], a global water-formation study conducted on a world scale was applied for Demirköprü dam and the results were consistent with the determined dam boundaries. It has been realized that both approaches can be used as alternatives to each other in monitoring changes on the dam surface.

Shading on the surfaces of PV panels reduces their efficiency. Classification of annual solar analysis results for the dam surface is invaluable in determining the regions where maximum energy efficiency can be achieved. Although the total radiation is high in the middle parts of the reservoir, the total amount of radiation falling on the surface decreases in the regions close to the shoreline due to the effect of the shading caused by the topography. This will cause a decrease in the amount of electrical energy to be generated from the FPV panels installed in regions close to the shoreline of the reservoir. As a result, this study revealed the importance of using RS and GISc technologies in determining the optimum region for FPV power plants to be installed on dam water surfaces.

Acknowledgement

This research did not receive any specific grant from funding agencies in the public, commercial, or not-for-profit sectors and it was prepared from a part of the first author's doctoral dissertation.

Author contributions

Osman Salih Yılmaz: Conceptualization, Methodology, Software, Field study **Fatih Gülgen:** Data curation, Writing-Original draft preparation, Software, Validation., Field study **Ali Murat Ateş:** Visualization, Investigation, Writing-Reviewing and Editing.

Conflicts of interest

The authors declare no conflicts of interest.

References

1. Du, Z., Bin, L., Ling, F., Li, W., Tian, W., Wang, H., ... & Zhang, X. (2012). Estimating surface water area changes using time-series Landsat data in the Qingjiang River Basin, China. *Journal of Applied Remote Sensing*, *6*(1), 063609. https://doi.org/10.1117/1.jrs.6.063609
2. Molden, D. J., Vaidya, R. A., Shrestha, A. B., Rasul, G., & Shrestha, M. S. (2014). Water infrastructure for the Hindu Kush Himalayas. *International Journal of Water Resources Development*, *30*(1), 60-77.
3. Du, Y., Zhang, Y., Ling, F., Wang, Q., Li, W., & Li, X. (2016). Water bodies' mapping from Sentinel-2 imagery with modified normalized difference water index at 10-m spatial resolution produced by sharpening the SWIR band. *Remote Sensing*, *8*(4), 354. https://doi.org/10.3390/rs8040354
4. Yang, X., & Chen, L. (2017). Evaluation of automated urban surface water extraction from Sentinel-2A imagery using different water indices. *Journal of Applied Remote Sensing*, *11*(2), 026016.. https://doi.org/10.1117/1.JRS.11.026016
5. Su, H., Peng, Y., Xu, C., Feng, A., & Liu, T. (2021). Using improved DeepLabv3+ network integrated with normalized difference water index to extract water bodies in Sentinel-2A urban remote sensing images. *Journal of Applied Remote Sensing*, *15*(1), 018504.
6. Pekel, J. F., Cottam, A., Gorelick, N., & Belward, A. S. (2016). High-resolution mapping of global surface water and its long-term changes. *Nature*, *540*(7633), 418-422. https://doi.org/10.1038/nature20584
7. Arekhi, M., Goksel, C., Balik Sanli, F., & Senel, G. (2019). Comparative evaluation of the spectral and spatial consistency of Sentinel-2 and Landsat-8 OLI data for Igneada longos forest. *ISPRS International Journal of Geo-Information*, *8*(2), 56. https://doi.org/10.3390/ijgi8020056
8. Dehwah, A. H., Asif, M., & Rahman, M. T. (2018). Prospects of PV application in unregulated building rooftops in developing countries: A perspective from Saudi Arabia. *Energy and Buildings*, *171*, 76-87. https://doi.org/10.1016/j.enbuild.2018.04.001
9. Singh, A. K., Boruah, D., Sehgal, L., & Ramaswamy, A. P. (2019). Feasibility study of a grid-tied 2MW floating solar PV power station and e-transportation facility using 'SketchUp Pro'for the proposed smart city of Pondicherry in India. *Journal of Smart Cities*, *2*(2), 49-59. https://doi.org/10.18063/jsc.2016.02.004
10. García-Pérez, S., Sierra-Pérez, J., & Boschmonart-Rives, J. (2018). Environmental assessment at the urban level combining LCA-GIS methodologies: A case study of energy retrofits in the Barcelona metropolitan area. *Building and Environment*, *134*, 191-204. https://doi.org/10.1016/j.buildenv.2018.01.041
11. Merrouni, A. A., Elalaoui, F. E., Mezrhab, A., Mezrhab, A., & Ghennioui, A. (2018). Large scale PV sites selection by combining GIS and Analytical Hierarchy Process. Case study: Eastern Morocco. *Renewable energy*, *119*, 863-873.
12. Yilmaz, S., Ozcalik, H. R., & Dincer, F. (2015). Remote detection and assessment of solar energy potential analysis based on available roof surface area: case study in Kahramanmaras, Turkey. *Journal of Applied Remote Sensing*, *9*(1), 097698. https://doi.org/10.1117/1.jrs.9.097698
13. Gagnon, P., Margolis, R., Melius, J., Phillips, C., & Elmore, R. (2018). Estimating rooftop solar technical potential across the US using a combination of GIS-based methods, lidar data, and statistical modeling. Environmental Research Letters, 13, 1748–9326. https://doi.org/10.1088/1748-9326/aaa554
14. Czirjak, D. W. (2017). Detecting photovoltaic solar panels using hyperspectral imagery and estimating solar power production. *Journal of Applied Remote Sensing*, *11*(2), 026007. https://doi.org/10.1117/1.jrs.11.026007
15. Abid, M., Abid, Z., Sagin, J., Murtaza, R., Sarbassov, D., & Shabbir, M. (2019). Prospects of floating photovoltaic technology and its implementation in Central and South Asian Countries. *International Journal of Environmental Science and Technology*, *16*(3), 1755-1762. https://doi.org/10.1007/s13762-018-2080-5
16. Pimentel Da Silva, G. D., & Branco, D. A. C. (2018). Is floating photovoltaic better than conventional photovoltaic? Assessing environmental impacts. *Impact Assessment and Project Appraisal*, *36*(5), 390-400. https://doi.org/10.1080/14615517.2018.1477498
17. Mansouri Kouhestani, F., Byrne, J., Johnson, D., Spencer, L., Hazendonk, P., & Brown, B. (2019). Evaluating solar energy technical and economic potential on rooftops in an urban setting: the city of Lethbridge, Canada. *International Journal of Energy and Environmental Engineering*, *10*(1), 13-32. https://doi.org/10.1007/s40095-018-0289-1
18. Ranjbaran, P., Yousefi, H., Gharehpetian, G. B., & Astaraei, F. R. (2019). A review on floating photovoltaic (FPV) power generation units. *Renewable and Sustainable Energy Reviews*, *110*, 332-347. https://doi.org/10.1016/j.rser.2019.05.015
19. Ates, A. M., Yilmaz, O. S., & Gulgen, F. (2020). Using remote sensing to calculate floating photovoltaic technical potential of a dam's surface. *Sustainable Energy Technologies and Assessments*, *41*, 100799. https://doi.org/10.1016/j.seta.2020.100799

20. Song, J., & Choi, Y. (2016). Analysis of the potential for use of floating photovoltaic systems on mine pit lakes: case study at the ssangyong open-pit limestone mine in Korea. *Energies*, *9*(2), 102.
21. Charabi, Y., & Gastli, A. (2010). GIS assessment of large CSP plant in Duqum, Oman. *Renewable and Sustainable Energy Reviews*, *14*(2), 835-841.
22. Dubayah, R., & Rich, P. M. (1995). Topographic solar radiation models for GIS. *International journal of geographical information systems*, *9*(4), 405-419.
23. Zhang, Y., Gao, J., & Wang, J. (2007). Detailed mapping of a salt farm from Landsat TM imagery using neural network and maximum likelihood classifiers: a comparison. *International Journal of Remote Sensing*, *28*(10), 2077-2089. https://doi.org/10.1080/01431160500406870
24. Zurqani, H. A., Post, C. J., Mikhailova, E. A., & Allen, J. S. (2019). Mapping urbanization trends in a forested landscape using Google Earth Engine. *Remote Sensing in Earth Systems Sciences*, *2*(4), 173-182.
25. Patel, N. N., Angiuli, E., Gamba, P., Gaughan, A., Lisini, G., Stevens, F. R., ... & Trianni, G. (2015). Multitemporal settlement and population mapping from Landsat using Google Earth Engine. *International Journal of Applied Earth Observation and Geoinformation*, *35*, 199-208. https://doi.org/10.1016/j.jag.2014.09.005
26. Xiong, J., Thenkabail, P. S., Gumma, M. K., Teluguntla, P., Poehnelt, J., Congalton, R. G., ... & Thau, D. (2017). Automated cropland mapping of continental Africa using Google Earth Engine cloud computing. *ISPRS Journal of Photogrammetry and Remote Sensing*, *126*, 225-244. https://doi.org/10.1016/j.isprsjprs.2017.01.019
27. Dong, J., Xiao, X., Menarguez, M. A., Zhang, G., Qin, Y., Thau, D., ... & Moore III, B. (2016). Mapping paddy rice planting area in northeastern Asia with Landsat 8 images, phenology-based algorithm and Google Earth Engine. *Remote sensing of environment*, *185*, 142-154. https://doi.org/10.1016/j.rse.2016.02.016
28. Pekel, J. F., Cottam, A., Clerici, M., Belward, A., Dubois, G., Bartholome, E., & Gorelick, N. (2014, December). A Global Scale 30m Water Surface Detection Optimized and Validated for Landsat 8. In *AGU Fall Meeting Abstracts* (Vol. 2014, pp. H33P-01).
29. Chen, B., Xiao, X., Li, X., Pan, L., Doughty, R., Ma, J., ... & Giri, C. (2017). A mangrove forest map of China in 2015: Analysis of time series Landsat 7/8 and Sentinel-1A imagery in Google Earth Engine cloud computing platform. *ISPRS Journal of Photogrammetry and Remote Sensing*, *131*, 104-120. https://doi.org/10.1016/j.isprsjprs.2017.07.011
30. Wang, C., Jia, M., Chen, N., & Wang, W. (2018). Long-term surface water dynamics analysis based on Landsat imagery and the Google Earth Engine platform: A case study in the middle Yangtze River Basin. *Remote Sensing*, *10*(10), 1635. https://doi.org/10.3390/rs10101635
31. Xia, H., Zhao, J., Qin, Y., Yang, J., Cui, Y., Song, H., ... & Meng, Q. (2019). Changes in water surface area during 1989–2017 in the Huai River Basin using Landsat data and Google earth engine. *Remote Sensing*, *11*(15), 1824.
32. Deng, Y., Jiang, W., Tang, Z., Ling, Z., & Wu, Z. (2019). Long-term changes of open-surface water bodies in the Yangtze River basin based on the Google Earth Engine cloud platform. *Remote Sensing*, *11*(19), 2213. https://doi.org/10.3390/rs11192213
33. Nguyen, U. N., Pham, L. T., & Dang, T. D. (2019). An automatic water detection approach using Landsat 8 OLI and Google Earth Engine cloud computing to map lakes and reservoirs in New Zealand. *Environmental monitoring and assessment*, *191*(4), 1-12. https://doi.org/10.1007/s10661-019-7355-x
34. Jena, R., Pradhan, B., & Jung, H. (2020). Seasonal water change assessment at Mahanadi River, India using multi-temporal data in Google earth engine. Korean Journal of Remote Sensing, 36, 1–13
35. Bi, L., Fu, B. L., Lou, P. Q., & Tang, T. Y. (2020). Delineation water of pearl river basin using Landsat images from Google Earth Engine. *The International Archives of Photogrammetry, Remote Sensing and Spatial Information Sciences*, *42*, 5-10. https://doi.org/10.5194/isprs-archives-XLII-3-W10-5-2020
36. Pohekar, S. D., & Ramachandran, M. (2004). Application of multi-criteria decision making to sustainable energy planning—A review. *Renewable and sustainable energy reviews*, *8*(4), 365-381.
37. Palmas, C., Abis, E., von Haaren, C., & Lovett, A. (2012). Renewables in residential development: an integrated GIS-based multicriteria approach for decentralized micro-renewable energy production in new settlement development: a case study of the eastern metropolitan area of Cagliari, Sardinia, Italy. *Energy, Sustainability and Society*, *2*(1), 1-15. https://doi.org/10.1186/2192-0567-2-10
38. Yadav, A. K., & Chandel, S. S. (2014). Solar radiation prediction using Artificial Neural Network techniques: A review. *Renewable and sustainable energy reviews*, *33*, 772-781.
39. Sahu, A., Yadav, N., & Sudhakar, K. (2016). Floating photovoltaic power plant: A review. *Renewable and sustainable energy reviews*, *66*, 815-824. https://doi.org/10.1016/j.rser.2016.08.051
40. Kumar, D. (2019). Mapping solar energy potential of southern India through geospatial technology. *Geocarto International*, *34*(13), 1477-1495. https://doi.org/10.1080/10106049.2018.1494759
41. Kokpinar, M. A., Kumcu, S. Y., Altan-Sakarya, A., & Gogus, M. (2010). Reservoir sedimentation in the Demirköprü Dam, Turkey. *River Flow*, 1125-1130.
42. Landis, J. R., & Koch, G. G. (1977). An application of hierarchical kappa-type statistics in the assessment of majority agreement among multiple observers. *Biometrics*, 363-374.
43. Duffie, J.A., & Beckman, W. A. (2013). Solar engineering of thermal processes. John Wiley & Sons
44. Kumar, D. (2020). Satellite-based solar energy potential analysis for southern states of India. *Energy Reports*, *6*, 1487-1500.

45. Wate, P., & Saran, S. (2015). Implementation of CityGML energy application domain extension (ADE) for integration of urban solar potential indicators using object-oriented modelling approach. *Geocarto International*, *30*(10), 1144-1162. https://doi.org/10.1080/10106049.2015.1034192
46. Falklev, E. H. (2017). *Mapping of solar energy potential on Tromsøya using solar analyst in ArcGIS* (Master's thesis, UiT The Arctic University of Norway).
47. Fu, P., & Rich, P. M. (1999, July). Design and implementation of the Solar Analyst: an ArcView extension for modeling solar radiation at landscape scales. In *Proceedings of the nineteenth annual ESRI user conference* (Vol. 1, pp. 1-31). USA: San Diego.
48. Belhachat, F., & Larbes, C. (2021). PV array reconfiguration techniques for maximum power optimization under partial shading conditions: A review. *Solar Energy*, *230*, 558-582. https://doi.org/10.1016/j.solener.2021.09.089
49. Eke, R., & Demircan, C. (2015). Shading effect on the energy rating of two identical PV systems on a building façade. *Solar Energy*, *122*, 48-57. https://doi.org/10.1016/j.solener.2015.08.022
50. Mehedi, I. M., Salam, Z., Ramli, M. Z., Chin, V. J., Bassi, H., Rawa, M. J. H., & Abdullah, M. P. (2021). Critical evaluation and review of partial shading mitigation methods for grid-connected PV system using hardware solutions: The module-level and array-level approaches. *Renewable and Sustainable Energy Reviews*, *146*, 111138. https://doi.org/10.1016/j.rser.2021.111138
51. Saiprakash, C., Mohapatra, A., Nayak, B., & Ghatak, S. R. (2021). Analysis of partial shading effect on energy output of different solar PV array configurations. *Materials Today: Proceedings*, *39*, 1905-1909. https://doi.org/10.1016/j.matpr.2020.08.307
52. Seapan, M., Hishikawa, Y., Yoshita, M., & Okajima, K. (2020). Detection of shading effect by using the current and voltage at maximum power point of crystalline silicon PV modules. *Solar Energy*, *211*, 1365-1372. https://doi.org/10.1016/j.solener.2020.10.078
53. Yang, B., Ye, H., Wang, J., Li, J., Wu, S., Li, Y., ... & Ye, H. (2021). PV arrays reconfiguration for partial shading mitigation: Recent advances, challenges and perspectives. *Energy Conversion and Management*, *247*, 114738. https://doi.org/10.1016/j.enconman.2021.114738
54. Charabi, Y., Gastli, A., & Al-Yahyai, S. (2016). Production of solar radiation bankable datasets from high-resolution solar irradiance derived with dynamical downscaling Numerical Weather prediction model. *Energy Reports*, *2*, 67-73. https://doi.org/10.1016/j.egyr.2016.05.001
55. Gassar, A. A. A., & Cha, S. H. (2021). Review of geographic information systems-based rooftop solar photovoltaic potential estimation approaches at urban scales. *Applied Energy*, *291*, 116817. https://doi.org/10.1016/j.apenergy.2021.116817
56. Kumar, D. (2021). Spatial variability analysis of the solar energy resources for future urban energy applications using Meteosat satellite-derived datasets. *Remote Sensing Applications: Society and Environment*, *22*, 100481. https://doi.org/10.1016/j.rsase.2021.100481
57. Oh, M., & Park, H. D. (2018). A new algorithm using a pyramid dataset for calculating shadowing in solar potential mapping. *Renewable Energy*, *126*, 465-474. https://doi.org/10.1016/j.renene.2018.03.068
58. Settou, B., Settou, N., Gahrar, Y., Negrou, B., Bouferrouk, A., Gouareh, A., & Mokhtara, C. (2022). Geographic information-driven two-stage optimization model for location decision of solar power plant: A case study of an Algerian municipality. *Sustainable Cities and Society*, *77*, 103567. https://doi.org/10.1016/j.scs.2021.103567
59. Kim, S. M., Oh, M., & Park, H. D. (2019). Analysis and prioritization of the floating photovoltaic system potential for reservoirs in Korea. *Applied Sciences*, *9*(3), 395. https://doi.org/doi:10.3390/app9030395
60. Lee, K. R., & Lee, W. H. (2016). Floating photovoltaic plant location analysis using GIS. *Journal of Korean Society for Geospatial Information Science*, *24*(1), 51-59.

International Journal of Engineering and Geosciences
https://dergipark.org.tr/en/pub/ijeg
e-ISSN 2548-0960

Design of ultra-wide band dual-polarized quad ridged horn antenna for obstacle penetrating radar imaging applications

Betül Yılmaz[*1]

[1]*Mersin University, Department of Electrical-Electronics Engineering, Türkiye*

Keywords
Antenna Design
Horn Antenna
CAD
Radar Imaging
Quad ridged Horn Antenna

Research Article
DOI: 10.26833/ijeg.1053213

Received: 04.01.2022
Accepted: 04.02.2022
Published: 13.04.2022

Abstract

In this study, a high-gain and dual-polarized Quad Ridged Horn Antenna (QRHA) is proposed and designed to be used in Obstacle Penetrating Imaging Radar (OPIR) applications. The quad ridged design is developed and then optimized by using the antenna design simulator software; CST Microwave Studio. The antenna parameters including the center frequency, frequency bandwidth and the antenna radiation pattern beam width are considered based on the requirements of OPIR applications. The final design is obtained for the center frequency of 2.785 GHz with a -10 dB bandwidth of at least 2.5 GHz. The final designed QRHA is able to provide a gain of 12.4 dB with a beam width of 36° at the center frequency of 2.785 GHz.

1. Introduction

As the new antenna applications are emerging thanks to improvements in signal processing algorithms [1] and developments on near field antenna application such as indoor radar imaging and car-to-car communication, the need for ultra-wideband (UWB) antenna technologies are increasing vastly. Among these applications, near-field radar imaging technologies [2] have also gaining much attention thanks to developments in microwave electronic circuitries [3-5]. For such applications including thru-wall imaging radar (TWIR) [6-8] and ground-penetrating radar (GPR) [9-11] or more generally obstacle penetrating imaging radar (OPIR), the scene is at the near-field of the radar antenna. Therefore, this necessitates the resolution of the image to be on the order of a few centimeters or less. This requirement; of course, forces the bandwidth of the radar antenna to be as large as possible [12] and preferably have UWB feature.

Some candidate UWB antennas including biconical antenna [13], helical antenna [14], log-periodical antenna [15-16], Vivaldi antenna [17] and ridge-horn antenna [18], have been well studied by many researchers. Among them, Vivaldi Antenna, Antipodal Vivaldi microstrip patch antenna, and double ridged horn antenna are widely considered due to suitable for OPIR applications since they have the attractive features such as high gain, relatively narrow beam width, directional antenna pattern and UWB operation. While patch antennas have the advantage of being compact, light and small [19-21]; their frequency bandwidth features are not that good when compared to horn antennas.

We have previously presented an optimized design of double ridged horn antenna (DRHA) that can be practically used for OPIR applications [22]. This antenna had the ability to offer UWB usage with a directional pattern that was specifically designed and produced for TWIR practices. For the recent couple of years, researchers have shown that the use of multiple polarization could increase the probability of detection and also facilitate the classification of the targets [23-24].

In this paper, a novel dual-polarized Quad Ridged Horn Antenna (QRHA) is designed for the OPIR applications such as GPR and TWIR. In the next section, the basic design steps are shared for the dual-polarized QRHA. The full EM simulation of the antenna is performed by the commercially available CST® Microwave Studio [25]. The optimization parameters and also the optimized design of the targeted antenna are

* **Corresponding Author**
*(betuly@mersin.edu.tr) ORCID ID 0000-0001-7404-8312

Cite this article
Yılmaz, B. (2023). Design of ultra-wide band dual-polarized quad ridged horn antenna for obstacle penetrating radar imaging applications. International Journal of Engineering and Geosciences, 8(1), 76-82

given in this section as well. In the third section, the antenna parameter fulfillments are presented to reflect the successfulness of the designed antenna. The final section is dedicated to the conclusion of the work and the possible usage of the designed antenna.

2. Design and the CST Simulation of Dual-Polarized Qrha

The proposed the dual-polarized QRHA is designed and simulated with commercially available full-wave electromagnetic (EM) simulator tool of CST Microwave Studio [25]. The required characteristics of the designed antenna are listed below:

i. An operational bandwidth was aimed to be at least 2.5 GHz around center frequency of 2.75 GHz.
ii. Beam-width of the main lobe was objected to be approximately 30° to 40° at the center frequency of the bandwidth.
iii. The size of the complete antenna is to be compact. Our goal was to have a design to be shorter than 35 cm.

First, a preliminary design based on the double ridged horn antenna theory Yılmaz and Özdemir [22] is applied to be able to attain a starting point before optimization. During the optimization, the Trust Region Framework algorithm is utilized inside CST such that finite difference accuracy value of 0.01 had been targeted. Then, the QRHA is optimized based on the antenna parameter constraints that are listed above using the optimization tool of CST Microwave Studio. As a result, the final design for the QRHA is obtained as shown in Fig. 1. The perspective, side, front, inner and, back views of the final QRHA is given in Fig. 1 (a), (b), (c), (d), and (e), respectively.

The critical dimensions of the final, designed QRHA are listed in Table 1.

Table 1. Dimension parameters of QRHA

Parameter	Description	Value (mm)
W_L	Wave-guide length	161.61
H_L	QRHA total length	319.55
A_w	Aperture width	227.36
A_h	Aperture height	224.00
R_w	Ridge width	10.68
L_d	Ridge separation	11.65
W_w	Wave-guide width	67.96
W_h	Wave-guide height	67.96

3. Simulation results

Based on the final optimized design parameters that are listed in Table 1, the QRHA is taken into simulation using CST. All of the critical antenna parameters are obtained and shared below:

The return loss performance of the QRHA is given for both co-polarization and cross polarization cases in Fig. 2 that also indicate the practical operational band width of the antenna.

In Fig. 2(a), co-polarization returns loss parameters of S_{11}, and S_{22} are given between 1 to 6 GHz. It can be easily noted from the figure that the -10 dB frequency bandwidth of the designed QRHA is from 1.47 GHz to 4.1 GHz that gives us a bandwidth of approximately 2.63 GHz at the center frequency of 2.785 GHz. Therefore, the fractional bandwidth is approximately equal to

$$B_{fr} = \frac{B}{f_c} = \frac{2.63\ \text{GHz}}{2.785\ \text{GHz}} = 94.43\% \qquad (1)$$

Above results obviously show that the designed QRHA yields an attractive UWB feature. In Fig. 2(b), the cross-polarization isolation plots; that is S_{21}, S_{12} of the designed antenna. From the figure, one can easily notice that the isolation between the dual-polarization ports of QRHA is successfully low; providing isolation power levels always less than -28.8 dB for all the frequencies within the bandwidth. On average, isolation power is around -34.8 dB inside the operational bandwidth.

In Fig. 3, the Voltage Standing Wave Ratio (VSWR) performance of the designed QRHA is given. In Fig. 3(a), VSWR of port 1 is plotted; where as in Fig. 3(b), that of port 2 is drawn. Both graphs show that VSWR is always less than 2 for the defined frequency bandwidth from 1.47 GHz to 4.1 GHz as expected.

In Fig. 4, far-field gain patterns at the center frequency of 2.785 GHz are given. When each port is used as stand-alone which means that the other port is not activated, the far field gain pattern of port #1 and port #2 are plotted in Fig. 4(a), and (b), respectively. It can be seen that the gains at the center frequency of operation is around 12.4 dBi for both ports when they are used in linear polarization mode of either Vertical (V) or Horizontal (H). When the designed QRHA is used in the circular polarization (CP), corresponding far-field gain patterns are given in Fig. 4(c) and (d), for the right-hand circular polarization (RHCP) and the left-hand circular polarization (LHCP), respectively. It can also be seen from the figure that the gains for both RHCP and LHCP are about the same performance of 12.4 dBi.

To evaluate the beam widths of the main beam of the designed QRHA, -3dB beam width analysis along the both E-plane and H-plane directions was performed thru the 2D far-field gain patterns at the center frequency of 2.785 GHz as depicted in Fig. 5. In Fig. 5(a) and (b), -3dB beam widths for linear polarization cases of H-plane and E-plane patterns of port #1 is plotted for the maximum radiation angle cut-direction, respectively. It can be easily read from the figures that half power beam width (HPBW) performances are resulted to be 41.1°, and 31.3° for port #1's H-plane and E-plane patterns, respectively. Similar analysis was also done for port #2 as well. In Fig. 5(c) and (d), -3dB beam widths for H-plane and E-plane patterns of port #2 is depicted for the maximum radiation angle cut-direction, respectively. It can also be referred from the figures that HPBW performances are measured to be 41.1°, and 31.2° for port #2's H-plane and E-plane patterns, respectively that are very similar to the ones for the port #1. All of these 2D far-field radiation patterns in Fig. 5 clearly demonstrate that this antenna can be practically used in OPIR applications since it can produce the desired HPBW performances of around 30° to 40°.

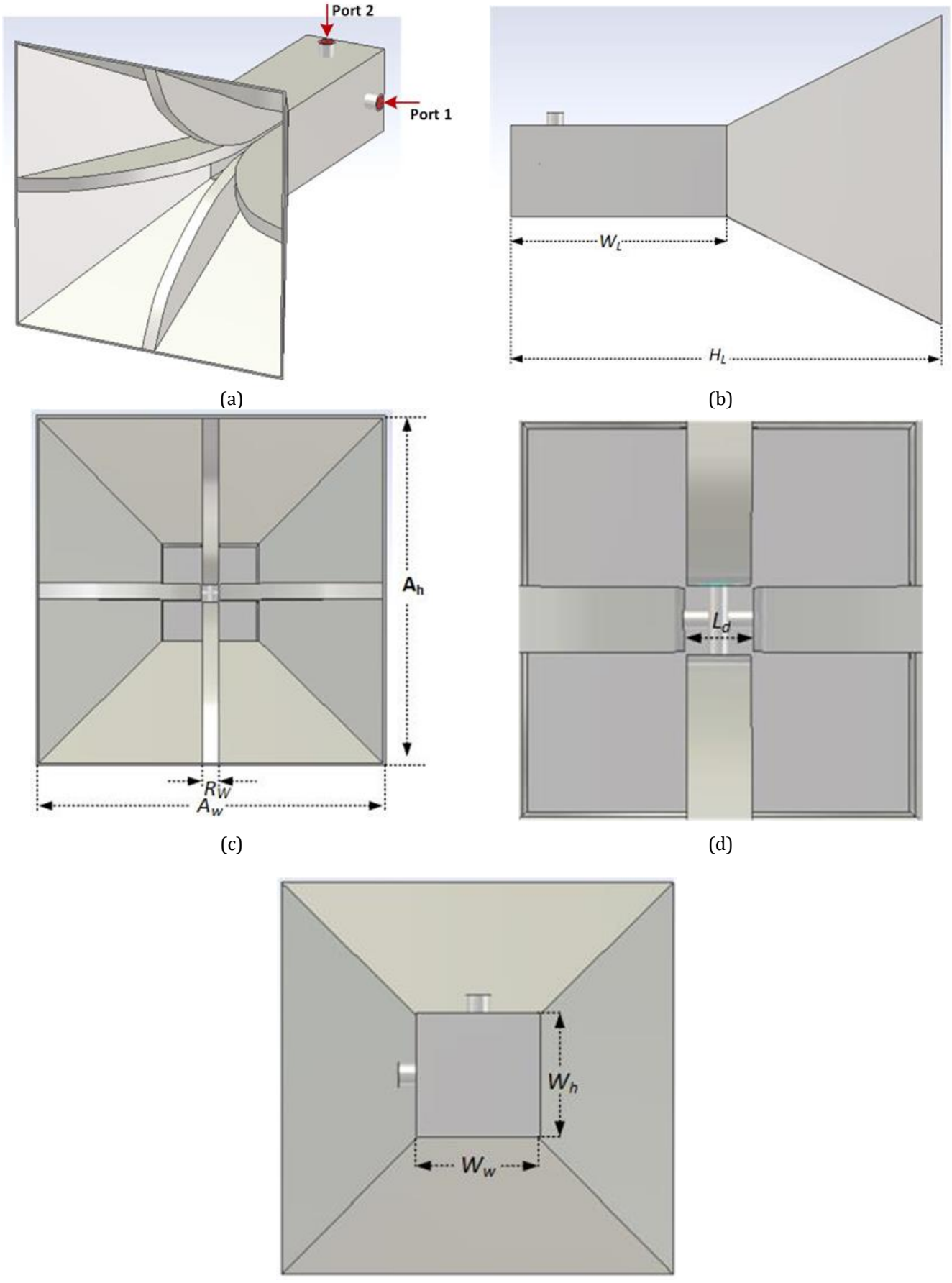

Figure 1. Designed QRHA with dimensions (a) perspective view, (b) side view, (c) front view, (d) a detailed view of the parameter for the width of the ridgeds, (e) back side

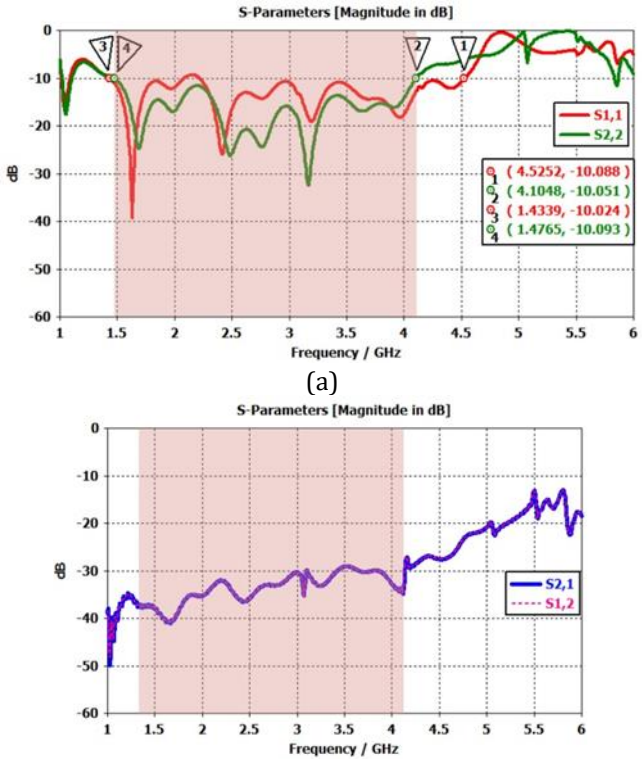

Figure 2. S-Parameters plots of the designed QRHA: (a) S_{11}, and S_{22} and (b) S_{21}, and S_{12}

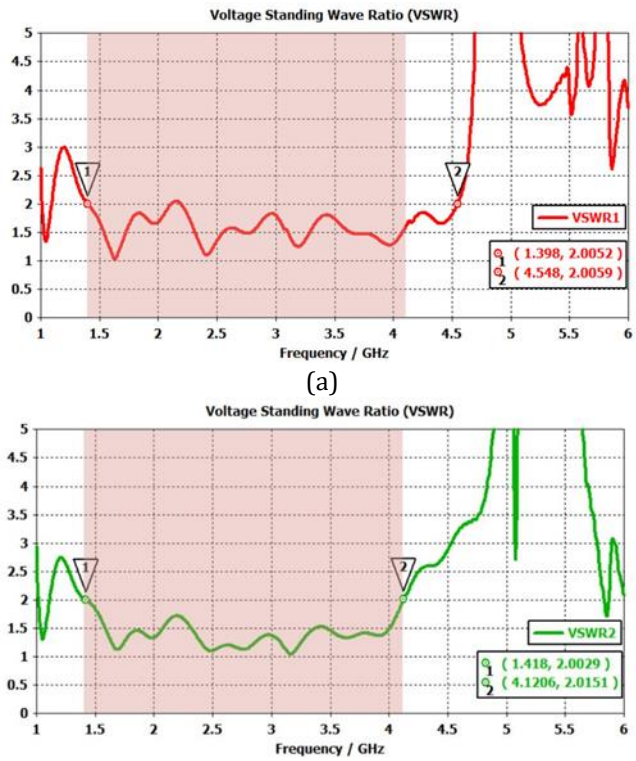

Figure 3. Voltage Standing Wave Ratio (VSWR) Results of the QRHA (a) for port 1, (b) for port 2

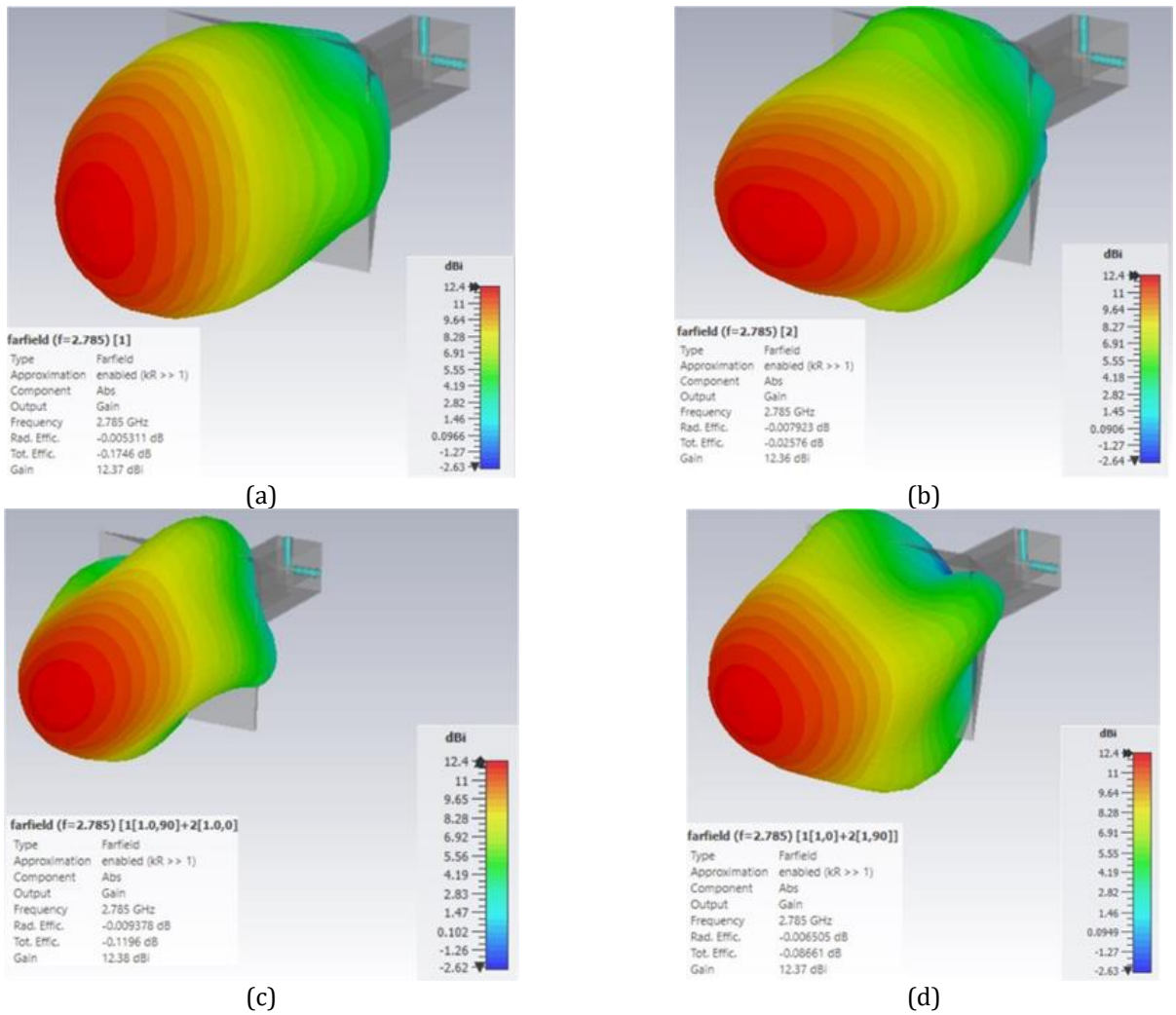

Figure 4. Far-field gain patterns at the center frequency of 2.785 GHz for (a) port #1, (b) port #2, (c) RHCP, and (d) LHCP

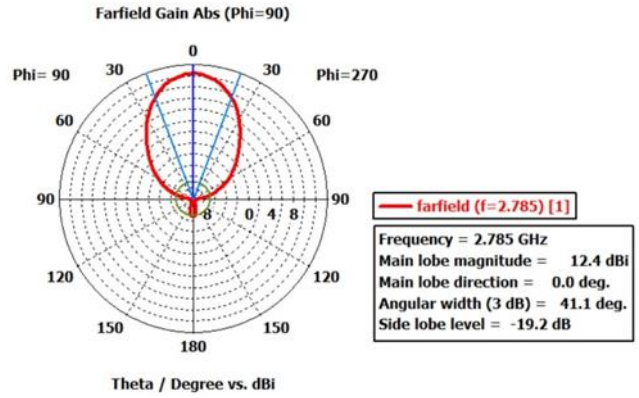

(a)

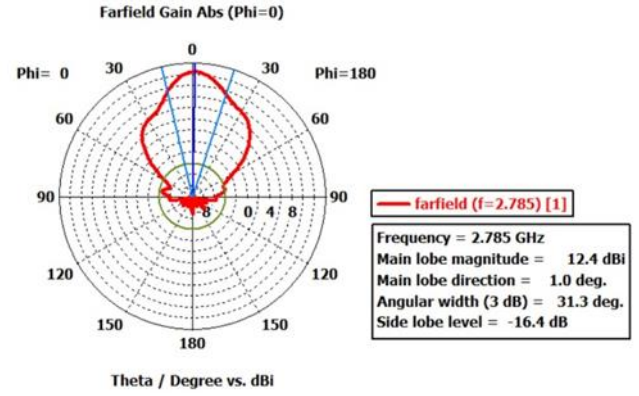

(b)

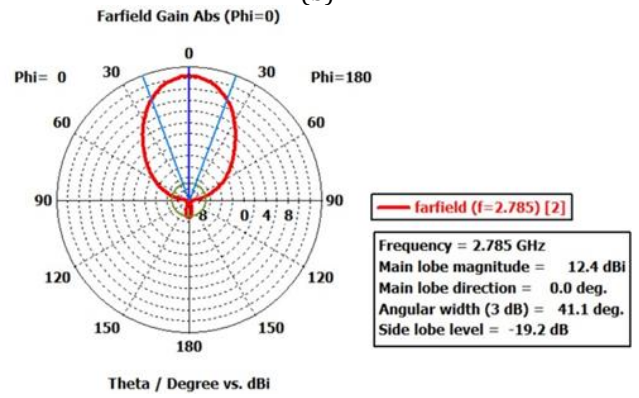

(c)

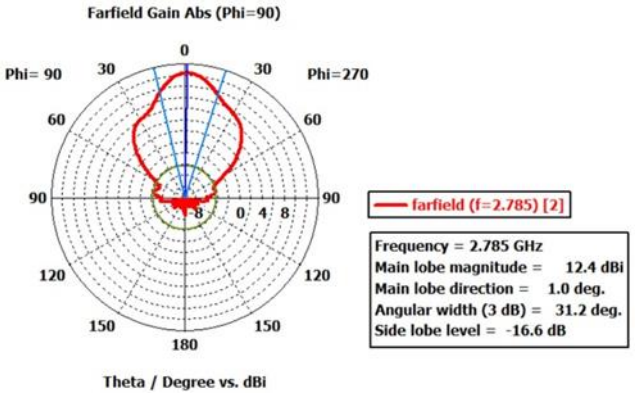

(d)

Figure 5. 2D Far-field radiation pattern cuts at 2.785 GHz in polar representation: (a) port #1 H-plane pattern, (b) port #1 E-plane pattern, (c) port #2 H-plane pattern, and (d) port #2 E-plane pattern

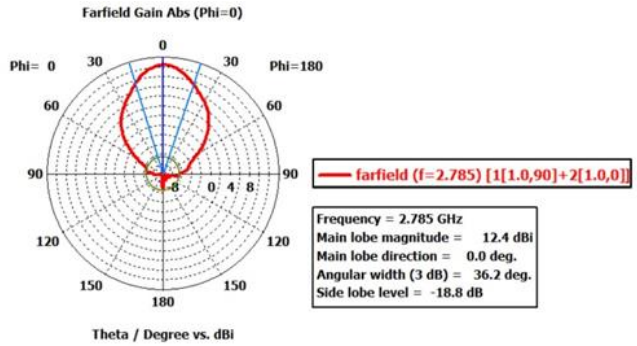

(a)

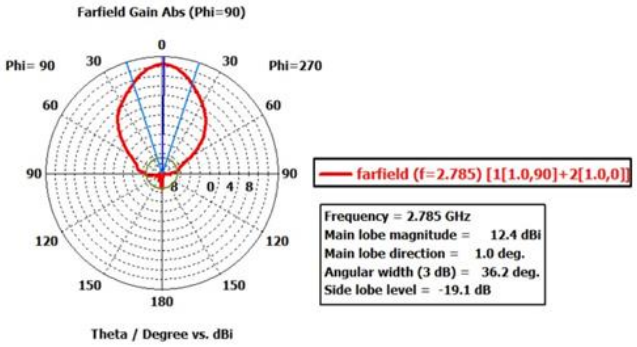

(b)

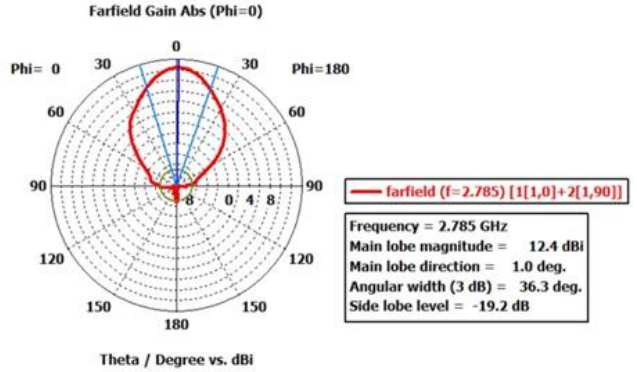

(c)

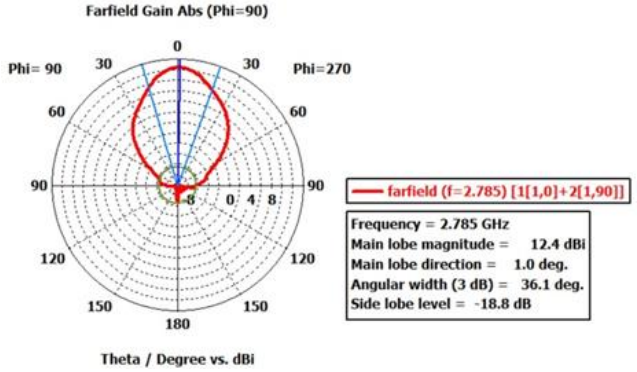

(d)

Figure 6. 2D Far-field radiation pattern cuts at 2.785 GHz in polar representation: (a) LHCP in x-z plane, (b) LHCP in y-z plane, (c) RHCP in x-z plane, (d) RHCP in y-z plane

In a further study, HPBW analysis was also performed for the CP usage of the designed QRHA. To achieve this, both ports are simultaneously activated while one of the ports is 90° in advance with respect to other port to yield LHCP or RHCP operation of the designed QRHA.

First, 2D far-field radiation pattern cuts of LHCP case at the center frequency of 2.785 GHz is considered thru Figs. 6(a) and 6(b). Fig. 6(a) represents the 2D far-field RHCP radiation pattern cut at $y = 0$ plane yielding a HPBW of 36.2° while, Fig. 6(b) stands for the same LHCP radiation pattern cut; but this time at $x = 0$ plane providing a HPBW of 36.2°. In Fig. 6(c) represents the 2D far-field RHCP radiation pattern cut at $y = 0$ plane with a HPBW performance of 36.3°. Whereas, Fig. 6(c) yields a HPBW of 36.1° for the same RHCP radiation pattern cut; but this time at $x = 0$ plane. Again, CP operation of the designed QRHA can provide directional usage of the antenna around 36° that is almost the mid-way of the design parameter.

4. Conclusion

In this study, a high-gain and dual-polarized horn antenna has been designed and optimized and to be practically used in OPIR applications. The final, optimized QRHA can be preferred for such practices thanks to its attractive antenna parameters that are validated by CST simulations. First of all, the final QRHA can provide a frequency band width of 2.63 GHz around the center frequency of 2.785 GHz providing an UWB operation of around %94.43 fractional band width. Secondly, the resultant QRHA has another attractive feature of yielding directive pattern of around 30° to 40° for either linear polarizations (H and/or V) and circular polarizations (RHCP and/or LHCP). Furthermore, the gain performance of the final QRHA is around 13 dB that can also be regarded as effective if this antenna is to be used to penetrate through a wall or a ground for a possible TWIR or GPR application. Also, the designed QRHA is directive to be operated effectively in OPIR operation by providing HPBW performances around 30° to 40 ° for LP usages and around 36° for CP usages. These results are in compliance with the results of DRHA design and optimization study that was reported earlier [22].

Conflicts of interest

The authors declare no conflicts of interest.

References

1. Ozdemir, C., & Ling, H. (1997). Joint time-frequency interpretation of scattering phenomenology in dielectric-coated wires. IEEE Transactions on Antennas and Propagation, 45, 1259- 1264.
2. Demirci, S., Ozdemir, C., Akdagli, A., & Yigit, E. (2008). Clutter reduction in synthetic aperture radar images with statistical modelling: An application to MSTAR data. Microwave and Optical Technology Letters, 50, 1514-1520.
3. Ahmed, S. S., Schiessl, A., Gumbmann, F., Tiebout, M., Methfessel, S. (2012). Advanced microwave imaging. IEEE Microwave Magazine, 13, 26-43.
4. Sheen, D. M., McMakin, D. L., & Hall, T. E. (2010). Near-field threedimensional radar imaging techniques and applications. Applied Optics, 49, E83–E93.
5. Yarovoy, A. G., Savelyev, T. G., Aubry, P. J., Lys, P. E., & Ligthart, L. P. (2007). UWB array-based sensor for near-field imaging. IEEE Trans on Microwave Theory and Techniques, 55, 1288–1295.
6. Baranoski, E. J. (2008). Through-wall imaging: historical perspective and future directions. Journal of the Franklin Institute, 345, 556–569.
7. Wang, G. Y., & Amin, M. G. (2006). Imaging through unknown walls using different standoff distances. IEEE Transactions on Signal Processing, 54, 4015–4025.
8. Zhu, F., Gao, S., Ho, A. T. S., Brown, T. W. C., Li, J. Z., & Xu, J. D. (2011). Low-profile directional ultra-wideband antenna for see-through-wall imaging applications. Progress In Electromagnetics Research, 121, 121-139.
9. Dou, Q., Wei, L., Magee, D. R., & Cohn, A. G. (2017). Real-Time Hyperbola Recognition and Fitting in GPR Data. IEEE Transactions on Geoscience and Remote Sensing, 55, 51-62
10. Gu, K., Wang, G., & Li, J. (2004). Migration based SAR imaging for ground penetrating radar systems. IEE Proceedings - Radar, Sonar and Navigation, 151, 317-325.
11. Soldovieri, F., Lopera, O., & Lambot, S. (2011). Combination of Advanced Inversion Techniques for an Accurate Target Localization via GPR for Demining Applications. IEEE Transactions on Geoscience and Remote Sensing, 49, 451-461.
12. Özdemir, C. (2021). Inverse Synthetic Aperture Radar Imaging with MATLAB Algorithms, Second Edition. Wiley. ISBN: 978-1119521334
13. Ghosh, C., Sarkar, T. K. (2009). Design of a wide-angle biconical antenna for wideband communications. Progress in Electromagnetics Research B, 16, 229-245.
14. Tang, X., Li, R., Pei, J., & Long, Y. (2014). An Ultra Wideband Printed Helical Antenna with Low Profile. Progress in Electromagnetics Research Symposium (PIERS), 2014, 1499–1502.
15. Islam, M. A., Istiak, S. M. S., Rahman, I., Tonmoy, S. A. U., & Ali, S. M. R. (2017). Design and Performance Analysis of a Log Periodic Dipole Antenna with a Frequency Range of 1350 to 2690 MHz. Journal of Microwave Engineering and Technologies, 4, 6–12.
16. Kubacki, R., Czyewski, M., & Laskowski, D. (2020). Enlarged Frequency Bandwidth of Truncated Log-Periodic Dipole Array Antenna. Electronics, 9, 1300.
17. Mehdipour, A., Aghdam, K. M., & Faraji-Dana, R. (2007). Completed dispersion analysis of Vivaldi antenna for ultra-wideband applications. Progress In Electromagnetics Research, 77, 85–96.
18. Bruns, C., Leuchtman, P., & Vahldieck, R. (2003). Analysis and simulation of a 1–18 GHz broadband double-ridged horn antenna. IEEE Transactions on Electromagnetic Compatibility, 45, 55–60.

19. Toktas, A. (2016). Log-periodic dipole array-based MIMO antenna for the mobile handsets. Journal of Electromagnetic Waves and Applications, 30, 351-365.
20. Toktas, A. (2016). Scalable notch antenna system for multiport applications. International Journal of Antennas and Propagation, 2016, 1-8.
21. Toktas, A. (2017). G-shaped band-notched ultra-wideband MIMO antenna system for mobile terminals. IET Microwaves, Antennas & Propagation, 11, 718-725.
22. Yılmaz, B., & Özdemir, C. (2017). Design and Prototype of a Compact, Ultra Wide Band Double Ridged Horn Antenna for Behind Obstacle Radar Applications. Turkish Journal of Engineering, 1, 76-81.
23. Novak, L. M, Owirka, G. J., & Netishen, C. M. (1993). Performance of a high resolution, polarimetric SAR automatic target recognition system. Lincoln Laboratory Journal, 6, 11-24.
24. Van Zyl, J. J. (1989). Unsupervised classification of scattering behavior using radar polarimetry data. IEEE Transactions on Geoscience and Remote Sensing, 27, 36- 45.
25. CST. (2012). CST Microwave Studio Advanced Topics. Technical report, CST-Computer Simulation Technology.

International Journal of Engineering and Geosciences
https://dergipark.org.tr/en/pub/ijeg
e-ISSN 2548-0960

Performance analysis of rule-based classification and deep learning method for automatic road extraction

Zeynep Bayramoğlu[*1], **Melis Uzar** [1]

[1]*Yıldız Technical University, Department of Geomatics Engineering, Türkiye*

Keywords
Automatic road extraction
Remote Sensing
Deep Learning
Ontology
UAV

Research Article
DOI: 10.26833/ijeg.1062250

Received: 24.01.2022
Accepted: 25.02.2022
Published: 13.04.2022

Abstract

The need for accurate and up-to-date spatial data by decision-makers in public and private administrations is increasing gradually. In recent decades, in the management of disasters and smart cities, fast and accurate extraction of roads, especially in emergencies, is quite important in terms of transportation, logistics planning, and route determination. In this study, automatic road extraction analyses were carried out using the Unmanned Aerial Vehicle (UAV) data set, belonging to the Yildiz Technical University Davutpasa Campus road route. For this purpose, this paper presents a comparison between performance analysis of rule-based classification and U-Net deep learning method for solving automatic road extraction problems. Objects belonging to the road and road network were obtained with the rule-based classification method with overall accuracy of 95%, and with the deep learning method with an overall accuracy of 86%. On the other hand, the performance metrics including accuracy, recall, precision, and F1 score were utilized to evaluate the performance analysis of the two methods. These values were obtained from confusion matrices for 4 target classes consisting of road and road elements namely road, road line, sidewalk, and bicycle road. Finally, integration of classified image objects with ontology was realized. Ontology was developed by defining four target class results obtained as a result of the rule-based classification method, conceptual class definition and properties, rules, and axioms.

1. Introduction

Roads are one of the important parts of the transportation infrastructure in spatial systems, especially for cities. In addition to the general management of urban areas, road maps are basic components of effective and planned management before and after disasters. Especially in emergencies, the management of roads with fast and up-to-date data is vital in solving transportation problems. To solve the requirements, the extraction of roads is carried out by spending a long time with traditional methods (e.g., manual digitizing) depending on the operators. Road extraction by the use of the classical methods such as pixel-based classification carries forward to time and resolution-related errors with misclassification problems. Moreover, most of the results of these methods are full of incomplete and erroneous data. Such errors negatively affect the accuracy of analyses for extracting roads. For that reason, automatic road extraction is aimed to solve these problems. At the stage of processing the data, determining the road network with photogrammetry and remote sensing methods is significant in terms of obtaining up-to-date, fast, and accurate data. For this purpose, in addition to using existing orthophoto and satellite images, Unmanned Aerial Vehicles (UAV) are preferred, which provide the opportunity to obtain fast, economical, and up-to-date data. The method of classifying objects to make inferences from the image is a method frequently

* **Corresponding Author**

*(zynpbayramoglu@gmail.com) ORCID ID 0000-0003-0324-3561
(auzar@yildiz.edu.tr) ORCID ID 0000-0003-0873-3797

Cite this article

Bayramoğlu, Z., & Uzar, M. (2023). Performance analysis of rule-based classification and deep learning method for automatic road extraction. International Journal of Engineering and Geosciences, 8(1), 83-97

preferred by researchers [1]. Generally, object-based and pixel-based classification methods are used for object extraction. In the case of non-homogeneous objects with various spectral values on the image, class confusion problems occur when using pixel-based methods [2]. For that reason, an object-oriented rule-based classification method is preferred to eliminate the problem of class confusion in automatic object extraction. In this method, spectral information with the properties of objects such as size, shape, texture, location was used to develop rules for extracting target classes. The analyses of segmentation and classification steps of the method are utilized to increase the accuracy of the target classes. A summary review of the recent state of the art in road extraction can be found in [3-4]. In addition, [5-7] utilized object-oriented classification methods for road extraction.

Deep learning has become popular in big data analysis and plays a big role in object detection, semantic segmentation and classification. Deep learning can be a bridge filling the gap between object extraction and remote sensing. The convolutional neural network (CNN) model, which can automatically extract objects and make classifications through sequential convolutional and fully connected layers, is used to improve efficiency and accuracy in remote sensing applications with the development of deep learning architectures. U-Net is the one of the most famous CNN architectures that is widely used for object segmentation and extraction. The U-Net architecture is based on fully convolutional networking. The advantage of the U-Net is that it works with fewer training images, providing more precise segmentation and allowing very fast results.

Today, the use of deep learning algorithms for the automatic extraction of roads [8-10] and feature information with machine learning has become prevalent. Particularly, studies conducted with remote sensing images and U-Net architecture are becoming widespread, [11-14]. In addition, there are also scientific studies in the literature that perform the classic methods with deep learning methods [15-16]. On the other hand, [17-21] employ deep learning methods for extraction of roads.

Ontology is used for presenting data and performing logical inference operations, as well as for leveraging and sharing these data by different systems and processing them syntactically and semantically by computers [22]. Ontology has been developed to identify and explain related concepts, establish the logical structure, and create taxonomic relationships. The difference in the result obtained from the image due to the user interpretation of the data creates the semantic gap problem [23-24]. To solve this problem, it is necessary to customize the a priori and extract information from the image by incorporating the conceptualization into image analysis systems [25]. Therefore, there is a need for a structure that can formalize field knowledge and expert knowledge. This structure should be in a state that can be applied to the image which will be classified. The concept of ontology, which helps to conceptualize a particular field, responds to this need by connecting spatial contents and presenting a formalized structure. The availability of geospatial data with ontology integration is increasing in recent years. Sener and Uzar [26] developed ontology by defining conceptual class definitions, object and data properties, rules, and axioms. Another study of geospatial ontology to define multi-scale representations and detailed cardinality relations of the building features was developed by [27].

In this study, automatic road extraction possibilities were investigated by using rule-based classification and U-Net [28] architecture. In addition, an ontology with classified objects was developed. The remainder of this paper is organized as follows. The properties of the study area and the dataset obtained by the UAV system are presented in the next section, followed by an explanation of the methodology adopted. The results of the experiment are reported along with an accuracy assessment of the automatic road extraction results with the comparison of two methods, i.e., rule-based classification and U-Net deep learning analyses, in the Results and Discussion section, and the conclusion is given in the last section.

2. Method

Object-oriented rule-based classification and U-Net deep learning methods were utilized for the automatic road extraction analysis, with the data obtained with UAV. The proposed methodology workflow is given in Fig. 1. In the rule-based classification method, orthophoto, DSM, and DTM were produced during data preparation. For automatic road extraction with deep learning U-Net architecture, data preparation, i.e., labeling, pre-processing, training and test data separation, has been completed. The performance analysis of target classes (road, sidewalk, road line, and bicycle road) was evaluated with both methods and then accuracy analyses were performed. Thus, it is aimed to solve the automatic road extraction problems with performance analysis of two methods using remote sensing and photogrammetric data. In this study, Pix4D software was used for photogrammetric data production processes using UAV images. The e-Cognition Developer software was used to develop a rule set with segmentation and classification analyses. In the deep learning method, the labeling processes of the target classes were created using GNU Image Manipulation Platform (GIMP) software. Accuracy, F1 score, precision, and recall parameters were evaluated for performance analysis of two methods. Finally, an ontology was developed to conceptualize the semantic information of objects and object classes with each other. And then the integration of classified image objects with ontology was carried out. Java-based and open-source Protégé was utilized for the creation of the semantic model and ontology development processes.

2.1. Study area and dataset

In this study, a road route was chosen as a study area found in the Davutpasa Campus of Yildiz Technical University in Istanbul, Turkey (Fig. 2).

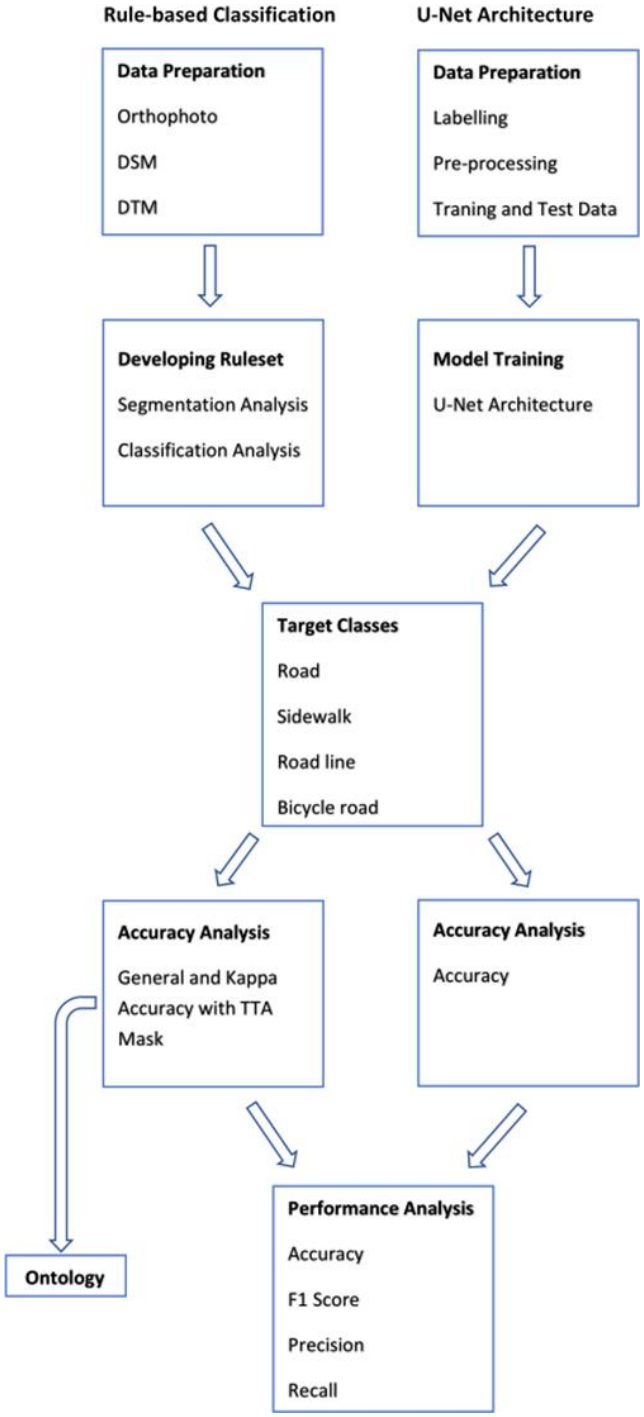

Figure 1. Workflow for the proposed methodology

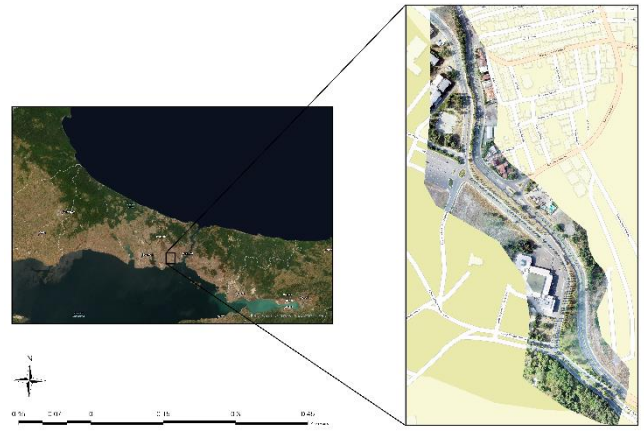

Figure 2. Study area

The data set was obtained with the UAV system, including DJI Phantom 4 Pro, GPS/IMU, and a digital camera positioned at the same platform. The UAV flight was carried out on 25.07.2019 with a flight altitude of 103 m. The images collected with the UAV were examined and the images with high error values and missing orientation parameters were eliminated. At this point of view, 157 images out of 182 images were used for method analysis. The FC6310R digital camera used in the UAV system was calibrated and Ground Control Points (GCP) were also measured. GCP and Root Mean Square (RMS) Errors are shown in Table 1.

Table 1. GCP and RMS Error

GCP	Error X(m)	Error Y(m)	Error Z(m)	Error (pixel)
10	0.004	0.001	-0.000	0.567
11	0.013	0.010	0.014	0.544
12	0.006	-0.013	0.038	0.340
RMS Error(m)	0.008	0.0094	0.0236	

After the measurement of the GCPs, the three-dimensional dense point cloud data was automatically generated in the TUREF/TM30 coordinate system. It was determined that the parameter obtained in the camera calibration report, camera distortion errors, and standard deviations were suitable for photogrammetric data generation [29]. A three-dimensional model was produced by a mesh model and texture from the point cloud data. A digital surface model (DSM), a digital terrain model (DTM) and an orthophoto with 2.55 cm ground sampling interval were produced from point cloud (Fig. 3).

2.2. Rule-Based classification method

In this study, by developing a rule set for automatic road extraction with object-based image analysis method, target classes were defined as road, road line, sidewalk, and bicycle road. And also additional classes, namely, green area, shadow, ground, sidewalk, and non-road were created to avoid class confusion. At the first stage, segmentation and classification analyses were performed to solve the class confusion problem, and rules were created as a result of the appropriate parameter estimation. In the second stage, a rule set was developed using brightness, texture analysis with a gray level co-occurrence matrix (GLCM) entropy, normalized digital surface model (NDSM) analysis, band combinations, and digital image processing techniques. Band combinations used to develop the ruleset are shown in Table 2 (Eq. 1-6). At the final stage, the error matrix based on the Test and Training Area (TTA) mask method was performed to test the accuracy of the proposed approach. In the TTA mask method, kappa, the overall, producer's and user's accuracies were computed. As a result, target classes are extracted using an original ruleset after the accuracy analysis for the performance analysis of two methods.

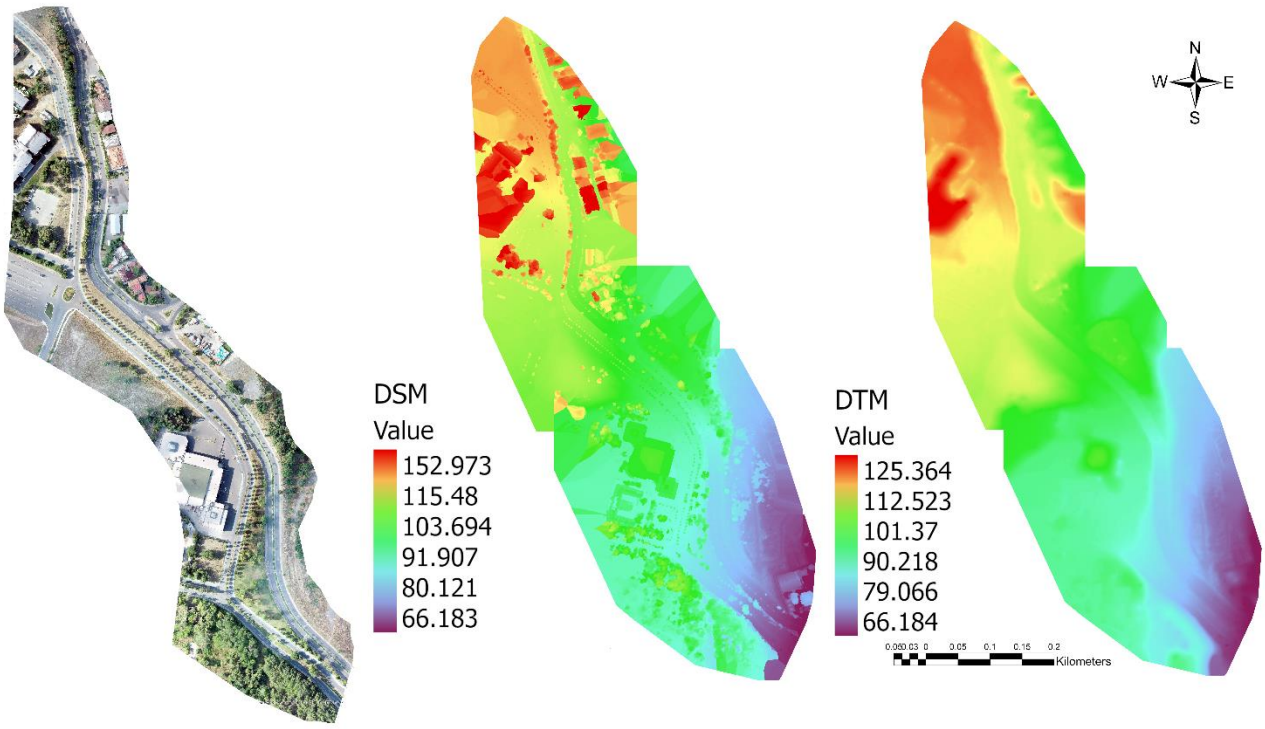

Figure 3. Orthophoto, DSM, and DTM

Table 2. Band combinations

Method	Abbr.	Formula	Eq. No
Brightness	B	$\frac{R+G+B}{3}$	1
Red Green Band Difference	R-G	$R-G$	2
Excess Index	RGI	$(2xG)-B-R$	3
Green Leaf Area Index	GLI	$\frac{((2\times G)\ -\ B-R)}{((2\times G)\ +\ B+R)}$	4
The Triangular Greenness Index	TGI	$G-(0.39R-0.69B)$	5
Haralick	H	$\frac{(0.5*(R-G)+(R-B))}{((R-G)^2+(R-B)(G*B))^{0.5}}$	6

2.3. *U-Net Architecture*

A Fully Convolutional Neural Network (FCNN) based U-Net architecture, which allows provides the use of global location and global context simultaneously with a few training samples, consists of the contracting path and the expansive path, also known as the encoder and decoder for analysis and synthesis path, respectively. The contracting path utilizes a typical CNN. It consists of two consecutive 3x3 convolutions followed by a batch normalization layer, a Rectified Linear Unit (ReLU) activation unit and a 2x2 max-pooling layer. This order is repeated as the number of downsampling operations. It should be noted that after each downsampling, the number of feature channels to be extracted is doubled [30] (Bayrak 2020). The expansive path includes an upsampling of the feature map by 2x2 transpose convolution to halve the number of feature channels and concatenation with the corresponding feature map from the contracting path. The final layer employs a 1x1 convolutional layer to classify each pixel. U-Net architecture for road extraction is given in Fig. 4.

2.3.1. *Training Details of U-Net Architecture*

Target classes (bicycle road, sidewalk, road, and road line) were annotated in GIMP software. U-Net implementation was performed using Keras 2.3.1 and the train/test process was made on a single NVIDIA RTX 2080 GPU. Firstly, the study area and corresponding annotated image were split into the sub-images with the size of 512×512 pixels and the numbers of train/test images and batch size were set as 320/140 and 8, respectively. Secondly, minimum maximum (min-max) normalization technique was applied to images due to data imbalance between classes. No pre-trained models were loaded; hence, the network was trained from scratch. Finally, the initial number of feature channels was set as 64 and after each downsampling, it is doubled and iterated 4 times. Adam optimizer with a learning rate of 1e-3 and exponential learning rate decay of 0.90 applied after each epoch (Table 3).

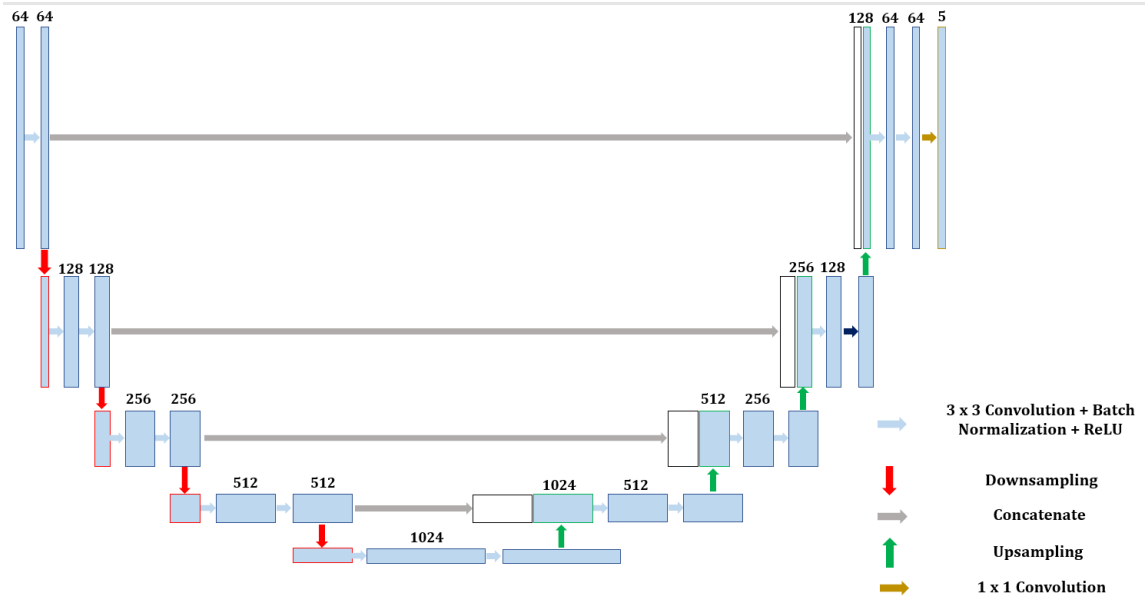

Figure 4. U-Net architecture [28]

Table 3. GCP and RMS Error

Train/Test Ratio	Optimizer	Learning Rate	Epoch Number
320/140	Adam	0.001	30

The model hyperparameters are given in Table 3. Loss calculation was performed by Dice Similarity Coefficient (DSC) [31] loss function in 30 epochs (Fig. 5). To evaluate the predictions, final feature maps were thresholded at 0.5 to obtain the masks, before comparison with ground truth annotations.

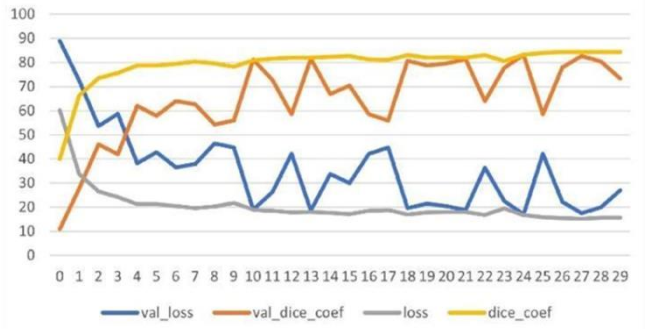

Figure 5. U-Net results

2.4. Developing ontology with classified image objects

In this study, shapefile data format was used for exporting data. The main reason for this approach is to preserve the properties of the classified image objects and to use them in information representation and ontology. This stage includes class definitions, object and data relations definitions, axiom, and rule definitions. The defined classes are shown in Fig. 6.

For the integration of classified object images with ontology, the data in shapefile format was converted into Web Ontology Language (OWL) format using the Comma Separated Value (CSV) as an intermediate format. After that step, the semantic model definition was completed. The QGIS program was used for conversion to CSV data format. The properties of image objects classified in CSV format are preserved. The data in CSV format was converted to an .xlsx file with excel and used as input in the ontology development platform. The steps required to create a file in OWL format are shown in Fig. 7.

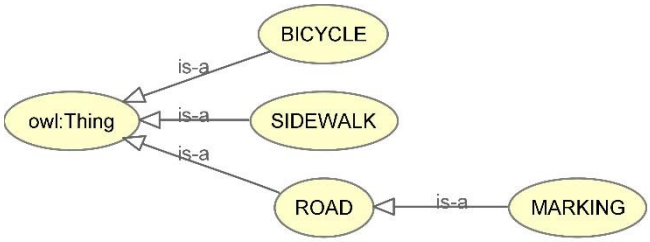

Figure 6. Classes in Ontology

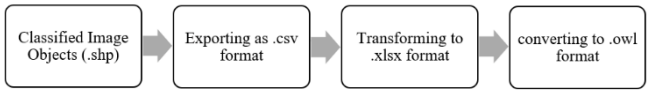

Figure 7. Converting shapefile to .owl format

After developing an ontology and integrating object instances into the ontology, the first requirement is the definition of data properties. For this purpose, the data properties defined for the integration of image objects into the ontology are given in Fig. 8.

These data features were determined by analysis after image segmentation. After defining data properties, axioms and rules are defined and ontology is developed. The rules used in transferring the data to the Protege program are shown in Fig. 9. An example representation of the developed ontology is given in Fig. 10.

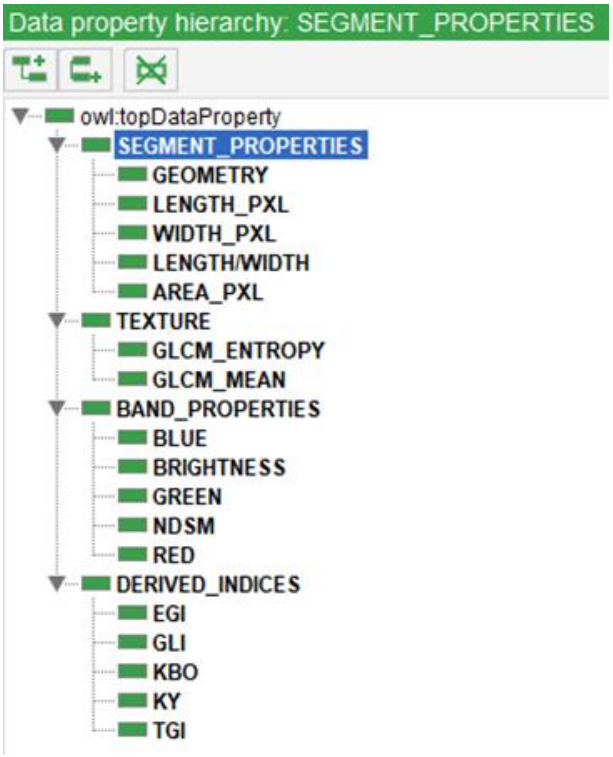

Figure 8. Defined data properties for Ontology

Figure 9. The image of the transfer process of rules

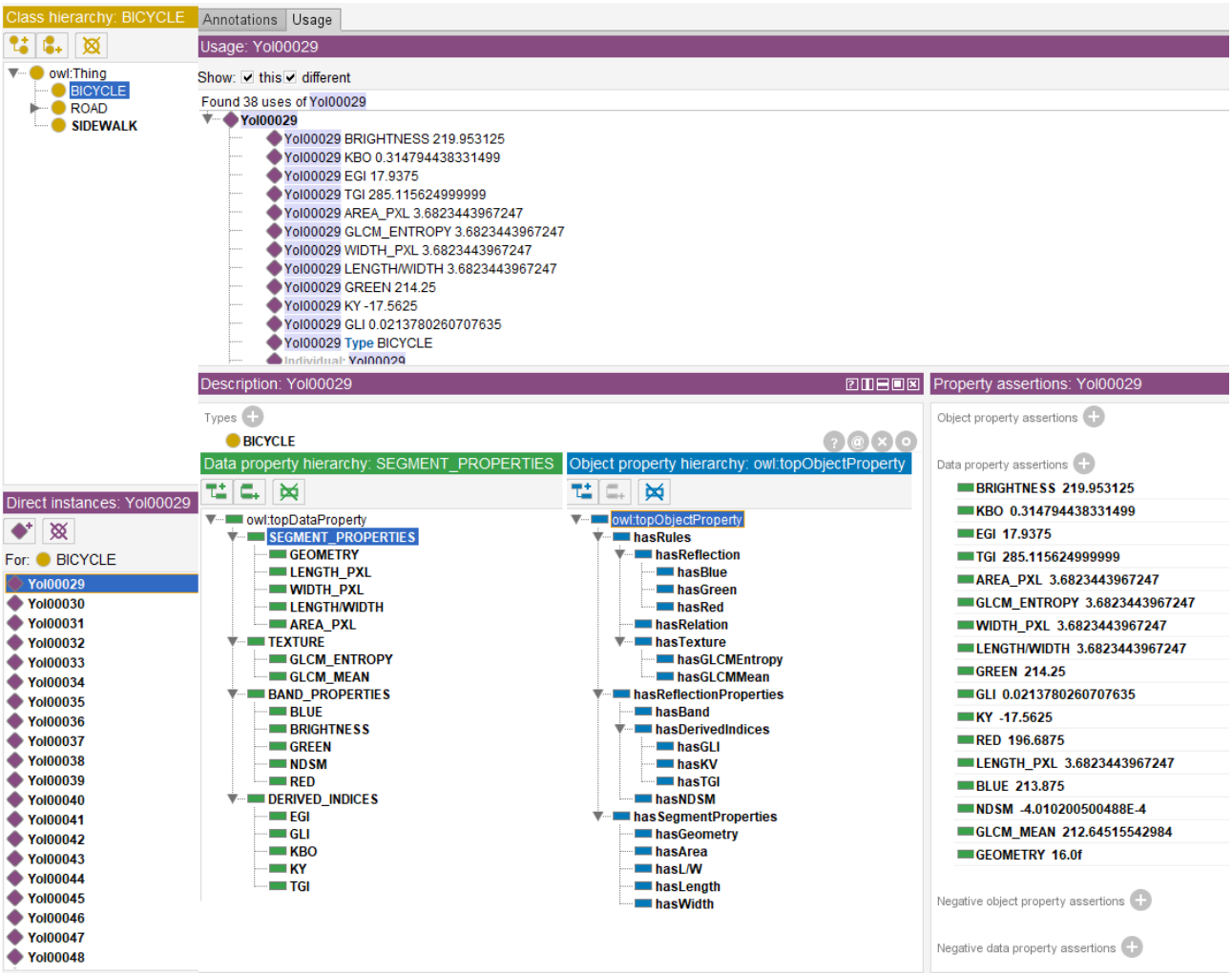

Figure 10. Ontology developed for the target classes

2.4.1. Evaluation parameters for performance analysis

A confusion matrix was used to perform the performance analysis in this study (Table 4). A confusion matrix is made up of four components, namely, True Positive (TP), True Negative (TN), False Positive (FP), and False Negative (FN) [32-33]. The assessment metrics engaged here are accuracy, precision, recall, and F1 score (Eq.7-10). True Positive (TP) refers to the number of predictions that correctly predict the object in reality. True Negative (TN) refers to the number of predictions that correctly predict the object that does not exist in reality. False Positive (FP) refers to the number of predictions in which it incorrectly predicts the object that does not exist in reality. And finally, False Negative (FN) refers to the number of predictions that incorrectly predict the object in reality. Precision shows how many of the positively predicted objects are Positive. The sensitivity indicates how many of the transactions that should be predicted as positive are predicted as positive. F1 Score value shows the harmonic mean of Precision and Sensitivity values. Accuracy is used to find the rate of correct predictions.

Table 4. Confusion matrix and evaluation metrics

		Prediction	
		Positive	Negative
Reference	Positive	True Positive	False Positive
	Negative	False Negative	True Negative

$$Precision=TP/ (TP+FP) \quad (7)$$

$$Recall= TP/ (TP+FN) \quad (8)$$

$$F1\ Score = 2*((P*R)/ (P+R)) \quad (9)$$

$$Accuracy= (TP+TN)/ (TP+FP+FN+TN) \quad (10)$$

3. Results and Discussion

3.1. Automatic extraction of road using the rule-based classification method

Segmentation, which is the first stage of the rule-based classification method, is the process of dividing the image into smaller parts by creating meaningful segments. These segments are created according to scale, shape, compactness, contrast difference, brightness, and statistical parameter values. A multi-resolution segmentation algorithm using shape, compactness, and scale factor was used. Analyses were carried out to determine the appropriate parameters and as a result, it was decided to prefer shape, integrity, and scale factors as 0.3, 0.8, and 20, respectively. The classes, parameters and analysis results created for the rule set developed for automatic road extraction are given in Table 5.

Table 5. Band combinations

Parameter	Analysis	Execution Class	Target Class
NDSM data	NDSM≥1		Non-road
GLI combination	threshold value ≥0.1		Green area
Length Width analysis	threshold value≥4		Line
GLCM Entropy	2≥threshold value≤6		Road
GLCM Mean	threshold value ≤170		Shadow
Classification		Unclassified	Ground
R-G	threshold value ≤-16	Road	Bicycle road
EGI	-8≥ threshold value ≤9	Bicycle road	Road
TGI	285≤ threshold value≥ 350	Road	Sidewalk
Brightness	230≤ threshold value ≥ 350	Road, Ground	Sidewalk
Hue	0.56≤ threshold value≥ 0.6	Shadow	Road
EGI/Road relation	value ≤-4 / 0.4≥ value	Shadow	Road
Area	100000	Road	Road
Boundary relationship with road	threshold value ≥0.1	Line	Road line
Area	600	Bicycle road	Ground

In this study, a rule set for automatic road extraction was developed by using the appropriate parameters obtained as a result of the analysis to prevent class confusion. Initially, the normalized digital surface model (NDSM) was obtained to distinguish between ground and non-ground objects. In this analysis, segments with an NDSM value greater than 1 were assigned as a non-road class. The proposed method improves the target class with rules using brightness, texture analysis with a gray level co-occurrence matrix (GLCM) entropy, NDSM analysis, band combinations, and digital image processing techniques. To classify the segments of the road, Haralick GLCM entropy texture analysis was performed and values between 2≥ value ≤ 6 were assigned as road class. The bicycle roads in the study area were obtained by taking the difference of the red and green bands. And the green leaf index (GLI) band combination was used to classify the green areas. Excess

green index (EGI) and triangular greenness index (TGI) band combinations were used to generate the road class and improve the classification.

One of the most common problems in object classification analysis is a shadow in the study area. Hue analysis was used to separate the road class from the shadow class. As a result, the classification was performed with the defined rules, and the results were improved with additional classes; Green area, Line, Shadow, Ground, Non-road to accurately represent the target classes. The processing step of target classes' improvement was implemented in Table 8 with several special indices and methods, such as boundary relationship, area determination, rectangular fitting, and merge classes. The image of classification results of additional and target classes is given in Fig. 11. Finally, automatic road extraction was performed using the defined rules with the proposed approach as shown in Fig. 12. Subsequently, TTA Mask analysis was used to evaluate the accuracy. For the selection of sample areas to be used in the test, multi-resolution segmentation was performed with the same parameters at a different level. TTA Mask was created with selected sample segments and the classes obtained in the study were compared with the reference data set. As a result of the accuracy analysis, 89% and overall accuracy of 95% were yielded for the target classes (Table 6).

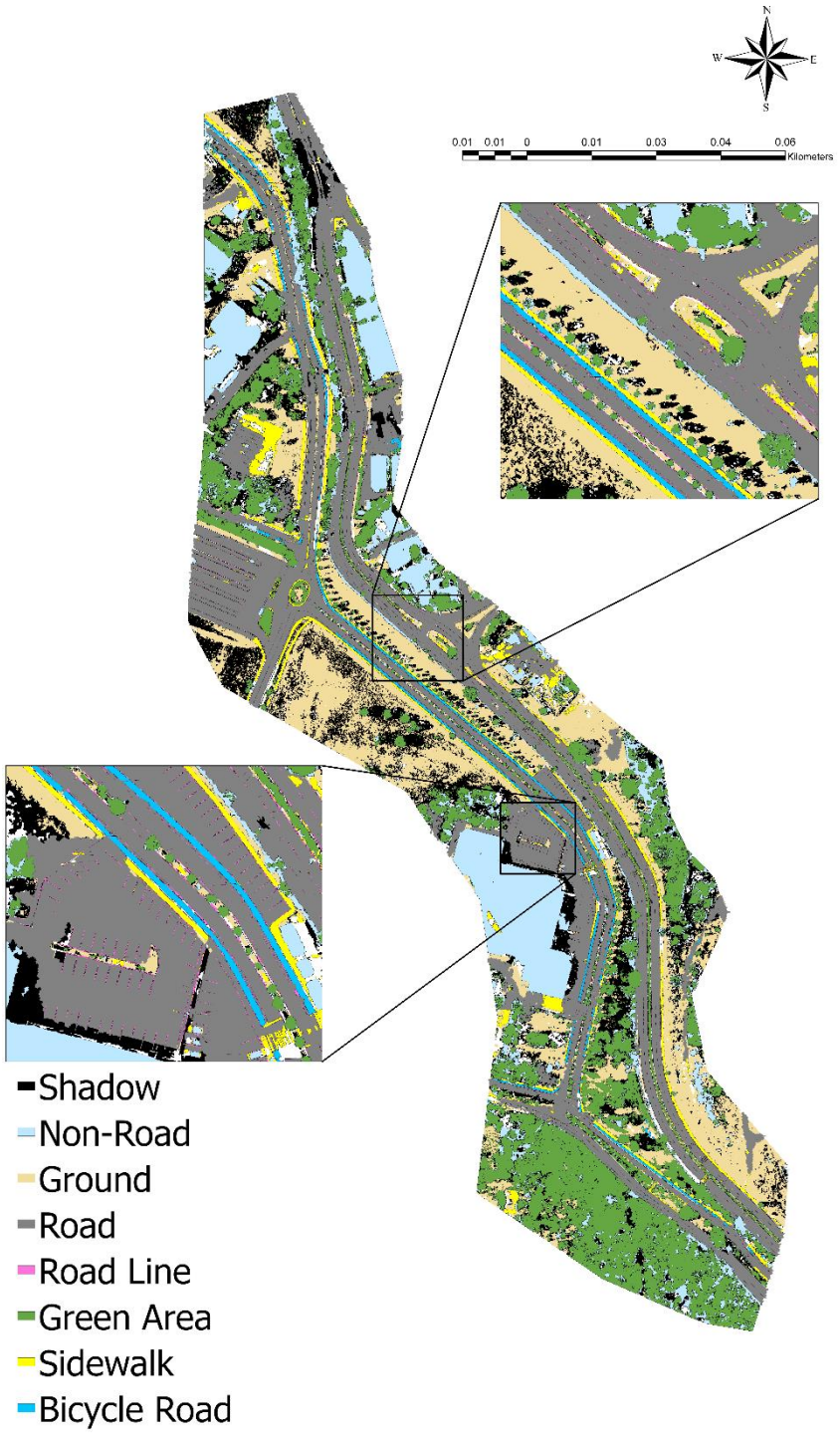

Figure 11. The image of classification results of additional and target classes

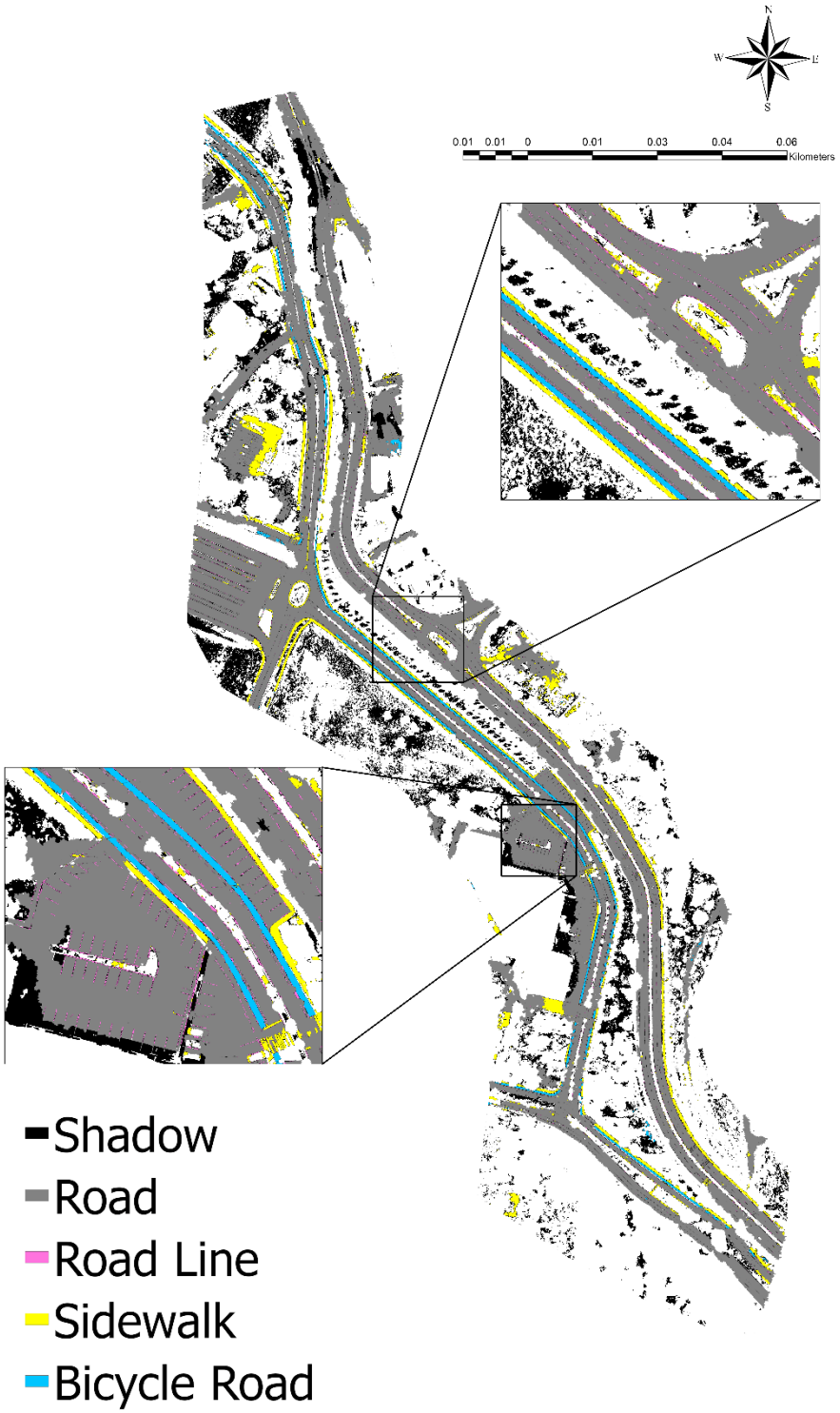

Figure 12. The image of the target classes and shadow class with the rule-based classification method

Table 6. Accuracy analysis results of rule-based classification

User/Reference Class	Bicycle Road	Side walk	Road	Road Line	Sum	User
Bicycle Road	65903	0	0	0	65903	1.00
Side walk	0	187654	4152	2425	194231	0.97
Road	14194	27847	907900	3364	953305	0.95
Road Line	371	0	2091	35819	38281	0.94
Sum	80468	215501	914143	41608	1251720	
Producer	0.82	0.87	0.99	0.86	Overall Acc.	0.95
					Kappa	0.89

3.2. Automatic extraction of road using U-Net architecture

To obtain the U-Net architecture's performance, a quantitative comparison between ground truth annotation and segmented images was employed by confusion matrix elements. Table 7 which covers the results of U-Net architecture includes Accuracy, Sensitivity, Specificity, and F1-Score metrics for each target class. According to Table 7, U-Net architecture achieved 92.4%, 97.9%, 70.5%, and 97.9% accuracy for sidewalk, road line, road, and bicycle road classes, respectively. However, U-Net architecture obtained 0 value for road line class in terms of Sensitivity and F1-Score value, due to lack of road line class in the study area. It means that U-Net architecture was under-fitted for the road line class. Even though the accuracy value of sidewalk and bicycle road classes' accuracy is greater than 90%, the Sensitivity and F1-Score values (0.320 and 0.639) of these classes show that U-Net architecture was under-fitted for both classes, too. Besides that, 61.7% and 50.3% for Sensitivity and F1-Score values for road class proved the same reason, so the lack of data in the small study area. The image of U-Net's classification results of target classes is given in Fig. 13.

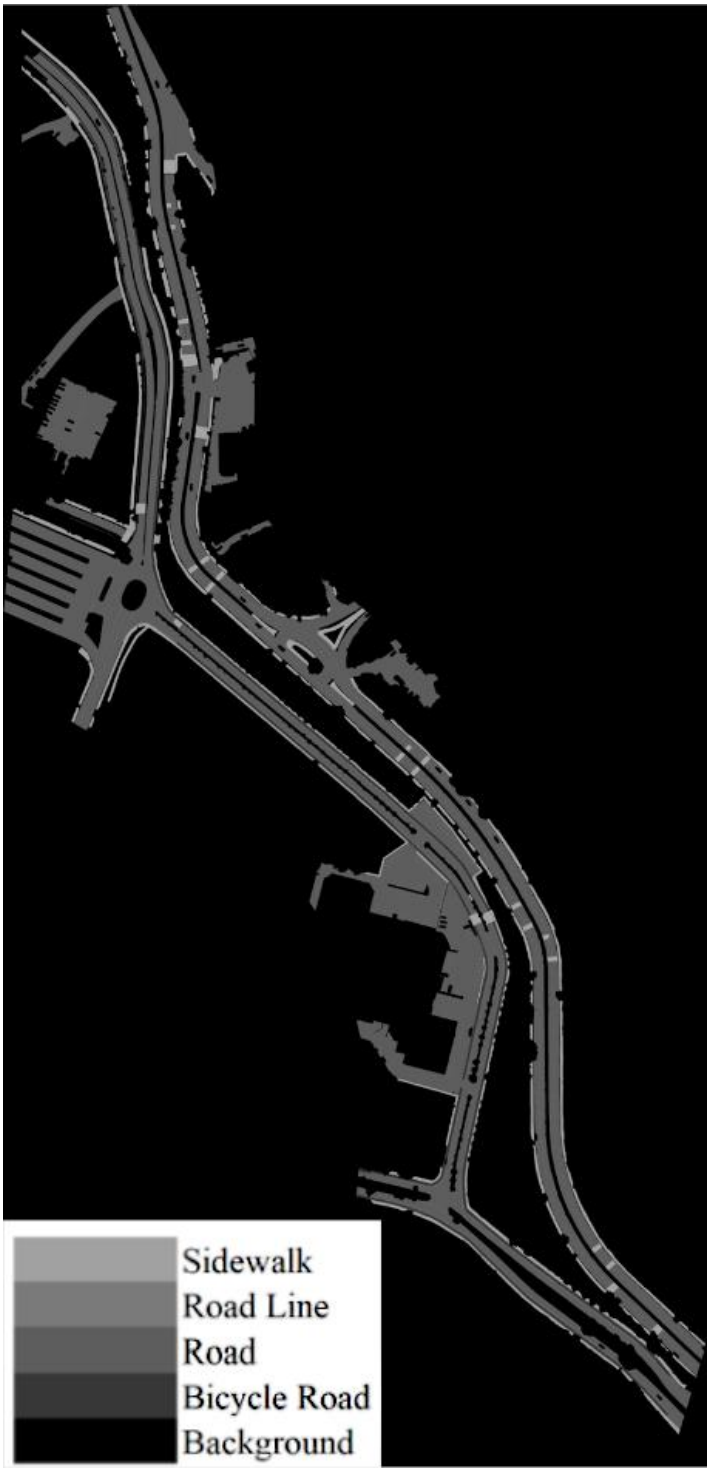

Figure 13. The image of the target classes with U-Net architecture

3.2.1. Performance analysis of target classes extraction with rule-based classification and U-Net architecture

In this study, performance analysis of object-oriented rule-based classification and U-Net architecture was produced by a confusion matrix according to accuracy, recall, precision, and F1 score values. As can be seen in Table 8, the accuracies of the rule-based classification method and U-Net architecture were 96% and 71% for the road class, 99% and 98% for the road line class, 97% and 92% for the sidewalk class, and 92% for the bicycle road class 99% and 98%, respectively.

Inaccuracy analysis of object extraction, calculating the only parameter of accuracy value does not always give the correct class accuracy in terms of completeness and quality. For that reason, precision, recall, accuracy, and F1 score parameters were calculated for the performance analysis of the target classes obtained according to the performance of both methods. The details of accuracy analysis according to two method performance are given in Table 8.

Table 7. Quantitative results of U-Net architecture

	Accuracy	Sensitivity	Specificity	F1-Score
Bicycle Road	0.979	0.639	0.985	0.517
Side walk	0.924	0.320	0.953	0.281
Road	0.705	0.617	0.733	0.503
Road Line	0.979	0.000	0.979	0.000

Table 8. Accuracy analysis of target classes according to two method's performance

	Confusion Matrix Elements	Bicycle Road	Side walk	Road	Road Line
Rule-Based Classification	Accuracy	0.988	0.972	0.959	0.993
	Precision	0.819	0.871	0.993	0.861
	Recall	1	0.966	0.952	0.936
	F1-Score	0.9	0.916	0.972	0.897
U-Net Architecture	Accuracy	0.979	0.924	0.705	0.979
	Precision	0.434	0.251	0.424	0
	Recall	0.639	0.32	0.617	-
	F1-Score	0.517	0.281	0.503	0

4. Discussion

In this study, it is aimed to obtain fast and accurate information in regard to the current spatial attributes of roads in case of any emergency, at the Davutpasa Campus of Yildiz Technical University. Therefore, an area with 244000m^2 was chosen as the study area. The advantages and disadvantages of rule-based classification and U-Net architecture were determined by comparing the performance analysis with target classes; a road, road line, sidewalk, bicycle road. The accuracy of target classes obtained from the rule-based classification method has outperformed U-Net architecture, because of the study area's size, since the rule-based classification method utilizes task-specific defined rules whereas U-Net architecture requires a large number of training images. Despite the lack of training data, Deep networks have proven to outperform at extracting mid-and high-level abstract and discriminative semantic features from images [34]. In such a study area, the similar or same textures which belong to different classes may provide an advantage for the rule-based classification method, whereas it became a disadvantage for U-Net in multiclass segmentation tasks.

In the rule-based classification method, a mixture of classes was prevented by creating auxiliary classes such as green area, shadow, ground, sidewalk, and non-road with scale, shape, and compactness analyses. In addition, with the defined rules, the class features were improved and classification accuracy was increased. More accurate results were obtained with the rule-based classification method by developing a rule set as follows: height, NDSM, pattern, color, texture, band combination, length, width, brightness, etc. to eliminate class confusion between target classes. All of these processes were performed to obtain a high accuracy for the target classes.

When we analyzed the properties of the study area, data distribution was found as follows: (i) 54% of the study area belong to the background, (ii) 6% to the sidewalk, (iii) 2% to the road line, (iv) 35% to the road and (v) 3% to the bicycle road classes. Therefore, the difference in classification results between target classes arose owing to a class imbalance in the study area (Table 8). It is thought that this problem may be solved by expanding the study area, namely the percentages of the sidewalk, road line, and bicycle road class. Despite these circumstances, U-Net architecture achieves more accurate segments on images with noise and variable details. From literature, it is known that deep learning networks are capable of classifying the objects under different conditions, although the spectral values of the target class vary, through medium and high-level feature extraction. Qualitative and quantitative analysis results showed that target classes could not be segmented since road lines, sidewalks and pedestrian crossings have variable characteristics and there are no adequate land-cover structures for training. In Fig. 14, the sample images of U-Net and Rule-based classification results for target classes are analyzed. When Fig. 14 is examined sequentially, bicycle road (Fig. 14a), shadow effect (Fig.

14b), road line and sidewalk (Fig. 14c), road and road line (Fig. 14d), and road (Fig. 14e) extraction results were given as examples. Two different situations were encountered in U-Net architecture when the extraction results of the bicycle road were analyzed. The bicycle road could not be extracted because it was not labeled as seen in Fig. 14 (a), while in Fig. 14 (b), the U-Net architecture was able to detect the bicycle road correctly. One of the main problems encountered in the automatic extraction of roads is the shadow effect (Fig. 14b). In the rule-based classification method, the objects representing shadow on the road are assigned to the road class by creating auxiliary classes using band combinations and texture properties. Also, the objects representing shadows on the sidewalk and road lines caused mix-classification. This situation was resolved by improving the classes created by length, width, and brightness analysis. In the U-Net architecture, it has been determined that the existence of shadows in the images does not pose a problem, especially in the segmentation of roads. For example, although there is a shadow on the bicycle road in the image, all the details were captured with the U-Net architecture, and classes were created correctly. In Fig.14 (c), the target class of road line, sidewalk, and road were analyzed. When the road lines are clear and have equal marking in aerial photos, the rule-based classification method detects and classifies the objects correctly with the analysis of pattern, color, and texture. However, in the U-Net architecture, the road line class could not be extracted correctly because the model could not fit due to insufficient segmentation of the road line training data. Contrary to this, the extraction of the road and sidewalk were obtained with successful results in U-Net architecture.

Another important condition in the extraction of roads that affects the accuracy is that roads have different textures in the aerial images. The structural material of roads; such as asphalt, ground fill, paint, patch, etc. have different textures. Because of that, different reflection values have emerged and this has prevented the model from learning in U-Net architecture. Qualitative results prove this as seen in Fig.14 (d) and Fig.14 (e). In Fig.14 (d) the road could not be extracted even though the road class was labeled in U-Net architecture. The result of a similar faulty road extraction is seen in Fig.14 (e). Despite these erroneous road extraction results, rule-based classification results were quite successful. The main reason for this is that the developed rule set increases the accuracy and improves the classes. On the other hand, it should also be noted that the U-Net architecture also gave successful results for this test area for the study.

5. Conclusion

In this study, object-oriented rule-based classification and U-Net deep learning architecture methods were utilized for automatic road extraction performance analysis using aerial images obtained by UAVs. Firstly, the object-oriented rule-based classification method was applied and the target classes of roads, road lines, sidewalks, and bicycle roads were extracted. After determining the appropriate parameter values obtained as a result of segmentation and classification analyses with the proposed method, the developed ruleset was created. With this ruleset, class confusions were removed and target classes were improved. In addition, auxiliary classes such as green area, shadow, and ground class were also extracted to eliminate class confusion and increase the accuracy of target classes. As a result of the original ruleset developed, 85% kappa accuracy and 90% overall accuracy were obtained for the accuracy analysis of the extracted target classes. Secondly, automatic road extraction was performed with the U-Net algorithm, which is one of the deep learning architectures, using data from the same study area. Along with the road class, road lines, sidewalks, bicycle roads, and background were labeled. In the deep learning method, an overall accuracy of 86% was obtained. Thirdly, for the performance analysis in this study, a confusion matrix was created for the target classes obtained for both methods and the results were compared with accuracy, recall, precision, and F1 score. In this context, the advantages and disadvantages of two different methods on the road route belonging to the same study area were investigated in the performance analysis and were given with details in the discussion section.

An important work step within the scope of this study is ontology. After the object extraction process, studies were carried out for the development of the ontology. Developing the ontology is aimed to define the high-level semantic concept of the image objects, automate the process of classifying image objects and discover the implicit knowledge in the classified image objects. After the conceptual design, the properties of image objects are defined in the ontology. By defining rules between data properties and segmented objects, classified objects are integrated with ontology. In order to use spatial data in operations regarding roads, various heterogeneity in the image object data should be solved. For this purpose, in this study, ontology was developed to conceptualize the semantic knowledge of image objects and target classes for road networks. As a result of associating the ontology with target classes, the spatial data has become reusable, fully semantic and interoperable.

As a result of this study, two different methods were utilized for the performance evaluation of the proposed automatic road approach. The obtained accuracy analysis as a result of the two different performance evaluations confirms the success of the approach for automatic road extraction due to its high accuracy, reliability, speed, and automation. Alternatively, the classification performance of road unit classes that have a low percentage in the study area may increase by utilizing object detection deep neural networks such as You Look Only Once (YOLO) and R-CNN. Considering this study, the rapid and accurate extraction of roads belonging to small study areas and its applicability for the whole region of the same area will be a source for future studies.

In particular, the correct use of road data in disaster and city administrations and the rapid transfer of these updated data in cooperation with different institutions are important. In this study, it has been determined that developed ruleset with rule-based classification and U-Net architecture deep learning methods can be used in

automatic road extraction according to the performance analysis results. It has been observed that the products obtained as a result of both methods can be used as reference data in the determination of post-disaster damages and inventory transportation to the needy, in route creation applications, in smart city systems, in the creation of city plans, in the follow-up of rapid construction, in the working areas of public and private administrations.

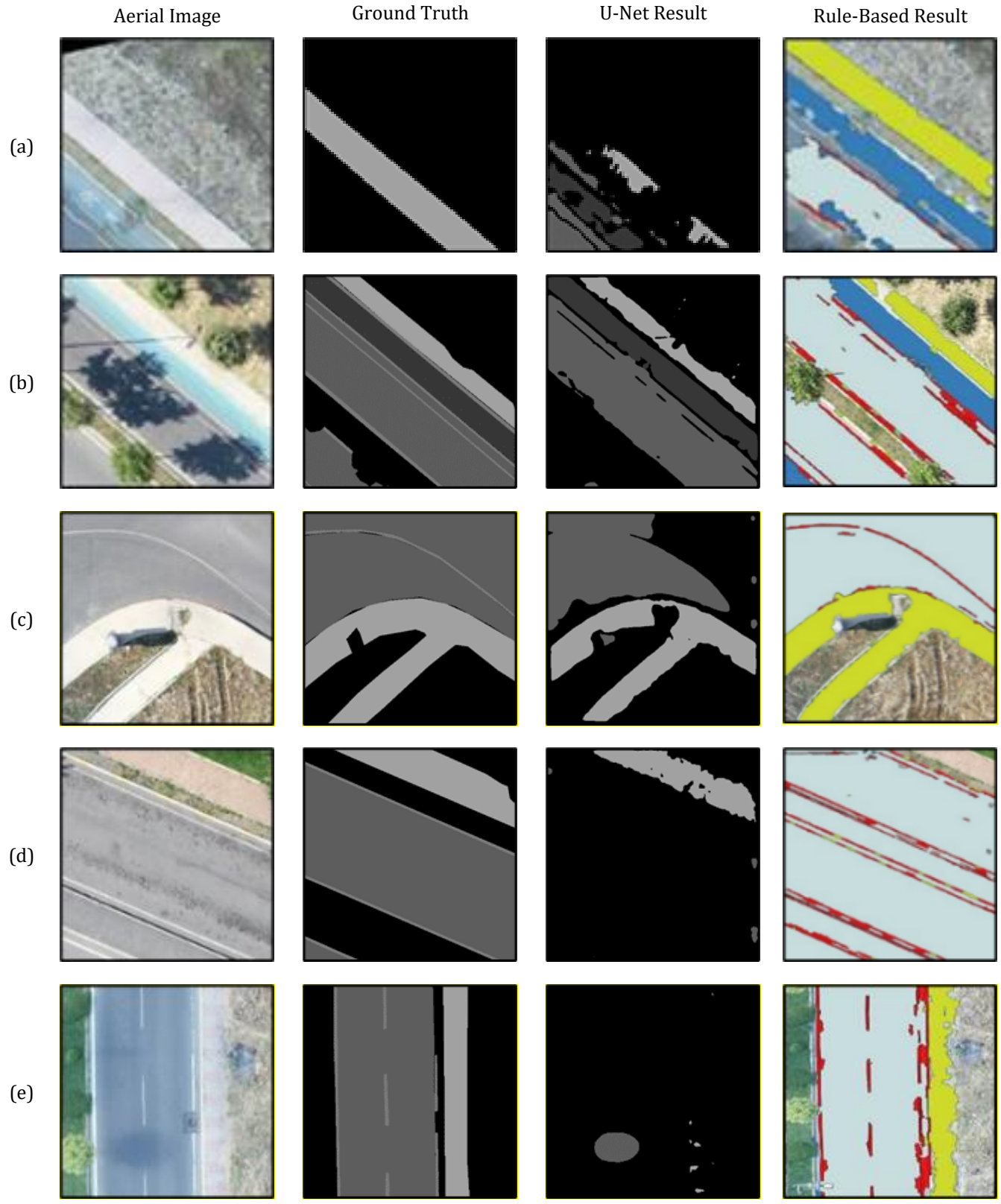

Figure 14. The sample images of U-Net and Rule-based classification results for target classes; a: bicycle road, b: shadow effect, c: road line and sidewalk, d: road and road line, and e: road

Author contributions

Zeynep Bayramoğlu: Methodology, Software, Data curation, Visualization, Writing-Reviewing and Editing.
Melis Uzar: Conceptualization, Methodology, Software, Investigation, Validation, Writing-Original draft preparation.

Conflicts of interest

The authors declare no conflicts of interest.

References

1. Fetai, B., Ostir, K., Kosmatin, F. M. & Lisec, A. (2019). Extraction of visible boundaries for cadastral mapping based on UAV ımagery. Remote Sensing, 11(13), 2-20.
2. Kavzoğlu, T., & Tombul, H. (2017). Nesne Tabanlı Sınıflandırmada Segmentasyon Kalitesinin Sınıflandırma Doğruluğu Üzerine Etkisinin İncelenmesi. Afyon Kocatepe Üniversitesi Fen ve Mühendislik Bilimleri Dergisi, 17(1), 118-125.
3. Abdollahi, A., Pradhan, B., Shukla, N., Chakraborty, S. & Alamri, A. (2020). Deep Learning Approaches applied to remote sensing datasets for road extraction: A state of the art review. Remote Sensing, 12(9), 4-22.
4. Lian, R., Wang, W., Mustafa, N., & Huang, L. (2020). Road Extraction Methods in High-Resolution Remote Sensing Images: A Comprehensive Review. IEEE journal of selected topics in applıed earth observations and remote sensing, 11(5), 552, 2-16.
5. Yadav, D. P., Nagarajan, K., Pande, H., Tiwari, P., & Narawade, R. (2020). Automatic urban road extraction from high resolution satellite data using object based ımage analysis: a fuzzy classification approach. Journal of Remote Sensing & GIS, 9(1), 279, 1-8.
6. Yiğit, A. Y., & Uysal, M. (2020). Automatic road detection from orthophoto images. Mersin Photogrammetry Journal, 2(1), 10-17.
7. Zhang, X., Han, L., & Zhu, L. (2020). How well do deep learning based methods for land cover classification and object detection perform on high resolution remote sensing imagery. Remote Sensing, 12(3), 2-29.
8. Senthilnath, J., Varia, N., Dokania, A., Anand, G., & Benediktsson, J. A. (2020). Deep TEC: Deep transfer learning with ensemble classifier for road extraction from UAV imagery. Remote Sensing, 12(2), 245-264.
9. Zhang, Z., & Wang, Y. (2019). JointNet: A common neural network for road and building extraction. Remote Sensing, 11(6), 696-718.
10. Gao, L., Song, W., Dai, J., & Chen, Y. (2019). Road extraction from high-resolution remote sensing imagery using refined deep residual convolutional neural network. Remote Sensing, 11(5), 552-568.
11. Zhang, Z., Liu, Q., & Wang, Y. (2017). Road extraction by deep residual U-Net. IEEE Geoscience and Remote Sensing Letters, 5(15), 749-753.
12. Huang, Z., Cheng, G., Wang, H., Li, H., Shi, L., & Pan, C. (2016). Building extraction from multi-source remote sensing images via deep deconvolution neural networks. IEEE International Geoscience and Remote Sensing Symposium, 1835-1838, Beijing, China.
13. Abderrahim, N. Y. Q, Abderrahim, S. & Rida, A. (2020). Road segmentation using U-Net architecture. IEEE International Conference of Moroccan Geomatics, 1-4, Casablanca, Morocco.
14. Emek, R., & Demir, N. (2020). Building detection from SAR images using U-Net deep learnıng method. The International Archives of the Photogrammetry, Remote Sensing and Spatial Information Sciences, Volume XLIV-4/W3-2020, 5th International Conference on Smart City Applications, 215-218, Virtual Safranbolu, Turkey.
15. Xiaoqiang, Lu, Gong, T., & Zheng, X. (2020). Multisource compensation network for remote sensing cross-domain scene classification, IEEE Trans. Geoscience Remote Sensing, 58(4), 2504-2515.
16. Sarıturk, B., Bayram, B., Duran, Z., & Seker, D. Z. (2020). Feature extraction from satellite images using SEGNET and fully convolutional networks (FCN) International Journal of Engineering and Geosciences, 5(3), 138 - 143.
17. Cheng, G, Xie, X., Han, J., Guo, L., & Xia, G. (2020). Remote sensing ımage scene classification meets deep learning: challenges, methods, benchmarks, and opportunities. IEEE Journal of Selected Topics in Applied Earth Observations and Remote Sensing, 13(1), 3735-3756.
18. Cira, C. I., Alcarria, R., Manso-Callejo, M. Á., & Serradilla, F. (2020). A deep learning-based solution for large-scale extraction of the secondary road network from high-resolution aerial orthoimagery. Applied Sciences, 10(20), 2-18.
19. Filin, O., Zapara, A. & Panchenko, S. (2018). Road detection with EOSResUNet and post vectorizing algorithm. IEEE/CVF Conference on Computer Vision and Pattern Recognition Workshops (CVPRW), 211-215, Salt Lake City, UT, USA.
20. Zhang, L., Zhang, L., & Du, B. (2016). Deep learning for remote sensing data: a technical tutorial on the state of the art. IEEE Geoscience and Remote Sensing Magazine, 4(2), 22-40.
21. Zhang, Z., Liu, Q., & Wang, Y. (2018). Road extraction by deep residual U-net. IEEE Geoscience and Remote Sensing Letters, 15(5), 749-753.
22. Sener, Z. (2020). Ontology use and evaluation in spatial object extraction from multi sensor system data. Doctoral Thesis, Yıldız Technical University, Institute of Science, Istanbul, 159p
23. Bouyerbou, H., Bechkoum, K., Benblidia, N., & Lepage, R. (2014). Ontology-based semantic classification of satellite images: Case of major disasters. IEEE Geoscience and Remote Sensing Symposium, 2347-2350, Quebec City, Canada.
24. Smeulders, A. W. M., Worring, M., Santini, S., Gupta, A. & Jain, R. (2009). Content-based image retrieval at the end of the early years. IEEE Transactions on Pattern Analysis and Machine Intelligence, 22(12), 1349-1380

25. Belgiu, M., & Thomas, J. (2013). Ontology based interpretation of very high-resolution imageries-grounding ontologies on visual interpretation keys AGILE Conference, 14-17, Leuven.
26. Sener, Z., & Uzar, M. (2020). New trend in object oriented image analysis - ontology. Journal of the Faculty of Engineering and Architecture of Gazi University, 35(1), 479-493.
27. Memduhoglu, A., & Basaraner, M. (2022). An approach for multi-scale urban building data integration and enrichment through geometric matching and semantic web. Cartography and Geographic Information Science, 49(1), 1-17.
28. Ronneberger, O., Fischer, P., & Brox, T. (2015) U-Net: Convolutional networks for biomedical image segmentation. In: Navab N, Hornegger J, Wells W, Frangi A. (eds) Medical Image Computing and Computer-Assisted Intervention MICCAI 2015. Lecture Notes in Computer Science, 234-241, Springer, Cham. ISBN 978-3-319-24574-4
29. https://www.tmmob.org.tr/en
30. Bayrak, O. C. (2020). Segmentation of liver and brain lesions by deep learning approach from medical images. Master's Thesis, Yıldız Technical University, Institute of Science, Istanbul, 54p.
31. Sørensen, T. (1948). A method of establishing groups of equal amplitude in plant sociology based on similarity of species, and its application to analyses of the vegetation on Danish Commons, Kongelige Danske Videnskabernes Selskab, Biologiske Skrifter, 5, 1-34.
32. Savoy, J., Gaussier, E., Savoy, J., & Gaussier, E. (2010). Information retrieval. In N. Indurkhya & F. Damerau (Eds.), Handbook of natural language processing. Boca Raton Chapman; Hall/CRC, 455-484. ISBN: 1420085921
33. Rutzinger, M., Rottensteiner, F., & Pfeifer, N. (2009). A comparison of evaluation techniques for building extraction from airborne laser scanning. IEEE Journal of Selected Topics in Applied Earth Observations and Remote Sensing, 2(1), 11-20.
34. Benbahria, Z., Sebari, I., Hajji, H., & Smiej, M. F. (2021). Intelligent mapping of irrigated areas from Landsat 8 images using transfer learning. International Journal of Engineering and Geosciences, 6(1), 40 - 50.

International Journal of Engineering and Geosciences
https://dergipark.org.tr/en/pub/ijeg
e-ISSN 2548-0960

Investigation and modeling of physical development of urban areas and its effects on light pollution using night light data

Samaneh Bagheri [*1], **Sadra Karimzadeh** [1], **Bakhtiar Feizizadeh** [1]

[1]*University of Tabriz, Department of Remote Sensing and GIS, Iran*

Keywords
VIIRS
NPP
Light Pollution
Physical Development
GIS

Research Article
DOI: 10.26833/ijeg.976495

Received: 08.11.2021
Accepted: 15.02.2022
Published: 13.04.2022

Abstract

The expansion of urbanization and unbalanced urban growth has attracted the attention of many urban planners and decision makers to the issues and consequences of urban population growth. In general, monitoring how urban areas are developed on a large scale is very important in order to plan urban development. However, in most cases, the lack of basic information in this area, especially in developing countries is one of the main obstacles to achieve this. With the development of human civilization and urbanization, the demand for artificial light has increased and this growth will continue. Found. Due to its lack of direct impact on daily life, light pollution has remained largely unknown and has rarely been studied. In this regard, the role of remote sensing techniques and data in identifying changes in the physical development of cities and changes in the amount of light is clearer than other methods. Using VIIRS satellite imagery, other satellite, digital and GIS data can measure and measure the physical growth of cities as well as the spatial and temporal distribution and extent of this type of pollution, and can even manage the risk of this pollution and Reach zoning. High-risk and dangerous areas. In this study, NPP images, travel time layer of Landsat 7 and 8 images have been used, which have been analyzed with the help of remote sensing and GIS techniques. The time frame considered in this study is 2012 to 2020.

1. Introduction

The world is urbanizing rapidly. The process of urbanization in different parts of the world is the result of interactions between various factors, including social, economic, political, geographical and cultural, and has had consequences. Pollution is one of the most important consequences of urban civilization. Of the various types of pollution, light pollution may be one of the emerging pollutants in the field of environmental damage. Despite the introduction in recent years, this pollution continues to grow due to poor urban management. Disrupting or causing adverse effects on the environment and the health of organisms is called pollution. Light pollution is a type of pollution that is called over-illumination of an environment by artificial light. This pollution is a branch of environmental studies that has become important in the last two decades, and experts have begun studies due to the effects that this pollution causes on humans and nature, especially animals. Therefore, identification and zoning of areas sensitive to light pollution in order to assess the environment of these areas seems necessary. Recently, advances in data collection and sharing in many aspects of urban life have provided us with better clues about the characteristics of cities [1-3]. In this regard, the effectiveness of remote sensing techniques and data in detecting changes, whether physical or optical changes, has been more than other methods. Night light observations through remote sensing allow us to evaluate human activities. In this study, we will follow a new multi-stage approach to examine the rate of physical growth of cities and light pollution in them. The main purpose of this study is to evaluate the efficiency of satellite remote sensing (NTL) to determine the causes of changes and various factors affecting the development and growth of urban areas and light pollution and to make a comparison between Tehran and Tabriz cities.

* **Corresponding Author**

*(samanehbagheri99@gmail.com) ORCID ID 0000-0003-3889-6685
(sadra.karimzadeh@gmail.com) ORCID ID 0000-0002-5645-0188
(Feizizadeh@tabrizu.ac.ir) ORCID ID 0000-0002-5645-0188

Cite this article

Bagheri, S., Karimzadeh, S., & Feizizadeh, B. (2023). Investigation and modeling of physical development of urban areas and its effects on light pollution using night light data. International Journal of Engineering and Geosciences, 8(1), 98-110

2. Material, Methods and Case Studies

In order to study the physical development of cities and light pollution, we use two remote sensing data classes: built-up area and night lights. We also use travel time based on openly available street maps. Some authors such as [4-6] used these data in their studies. In this study, Landsat 7, Landsat 8 satellite images, VIIRS night light images and travel time raster images were used. Landsat 7 images were used to produce the ground cover layer in 2012 and Landsat 8 images were used for the years 2013 to 2020. The night light images for the years 2012 to 2020 are all for the SOUMI NPP satellite VIIRS sensor. The Visible Infrared Imaging Radiometer Suite (VIIRS) Day/Night Band (DNB) collects global low-light imaging data that have significant improvements over comparable data collected for 40 years by the DMSP Operational Linescan System. One of the prominent features of DNB data is the detection of electric lighting present on the Earth's surface. Most of these lights are from human settlements. VIIRS collects source data that could be used to generate monthly and annual science grade global radiance maps of human settlements with electric lighting. There are a substantial number of steps involved in producing a product that has been cleaned to exclude background noise, solar and lunar contamination, data degraded by cloud cover, and features unrelated to electric lighting (e.g., fires, flares, volcanoes), [7]. The flow chart of the adopted methodology is depicted in Figure1. In this study, we will go through three steps to measure urban growth: the first step is to produce land cover, the second step is to classify the night light image, and the third step is to calculate travel time. Each of these steps has its own processing. Each of these datasets has advantages and disadvantages that. For example, Landsat provides the free optical remote sensing imagery of medium resolution (30m). Surface classification using Landsat is limited by cloud obscuration, the similarity of radiance signatures among surface types and incomplete training data. Another problem with land cover is the occurrence of gaps when we focus on one class (built up in the present study). Unlike Landsat, the Nighttime Light (NTL) products do not show any gaps over a city area. However, due to their large pixel size, NTL products provide ambiguous information at the edges of the cities and on coastlines. Travel time provides evidence on the connectivity of a city but not whether this is associated with population so it cannot define urban extent alone. If logically combined, show the physical growth of the city. The algorithm used in this study is called BUNTUS (ground cover, night light and travel time) algorithm [8], which will use remote sensing and GIS techniques to calculate the physical growth of the city. We will also use the Google Earth Engine system to check the amount of light pollution. In the following, we will show our study areas and explain each step separately and examine their composition and the final result. The general framework of the work is shown in Figure 1.

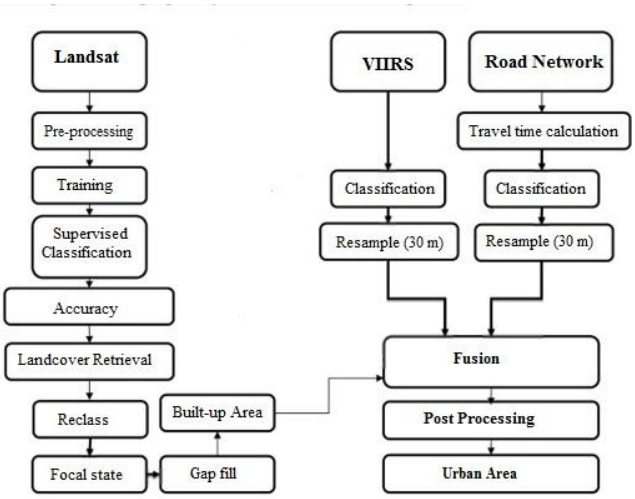

Figure 1. Methodology flowchart of fusion of Landsat, Nighttime light product of Visible Infrared Imaging Radiometer Suite (VIIRS) and travel time

2.1. Case Studies

In this study, we selected two metropolises of Iran, namely the cities of Tehran and Tabriz as study areas (see Figure 2) to examine the various aspects of the BUNTUS algorithm on them and to challenge the progress of light pollution. The figure 2 shows the study areas.

2.2. Land Cover Classification

Landsat Enhancement Thematic Mapper (ETM) and Landsat Operational Line Imager (OLI) images were used to produce the land cover map. ETM images were used to map the land cover for 2012 and Landsat 8 images for 2013-2020. First, the necessary preprocessions such as radiometric correction and atmospheric correction were performed in ENVI image review software, then the images were classified using SVM method. Initially, each image was classified into four classes of built-up areas, water, plants, and soil, and then we categorized those four classes into two classes to extract urban built-up and non-built-up areas. In selecting the training data, Google Earth was used to classify it correctly.

2.2.1. Accuracy Assessment

Error matrix method was used to evaluate the classification accuracy. A confusion matrix is a summary of prediction results on a classification problem. The results showed that the accuracy of the four classified classes was between 85 and 90%.

2.2.2. Urban Area Generation

The land cover produced had 4 classes. The higher number of classes minimizes the effect of mixed pixels. In order to separate built-up and non-built-up urban areas, we divided the 4 classes into two classes. A value of 1 was assigned to build areas and a value of 0 was assigned to non-built-up areas. Since our main focus was on built-up areas, we re-evaluated the accuracy of the two classes. Our two-class classification was more than 90% successful in all datasets. Finally, Focal Statistics analysis

was performed on a two-tier image in ArcGIS software and the ground cover layer was ready to be collected with other data.

2.3. Nighttime Light Data Processing

Nighttime light (NTL) satellite images are a class of remote sensing products, globally available for multiple years. The global open-source night light images are available from two sensors; The Operational Line scan System (OLS) instrument mounted on the United States Air force Defense Meteorological System Program (DMSP) and the Visible Infrared Imaging Radiometer Suite (VIIRS) sensor mounted and flown on NASA/NOAA Suomi-National Polar-Orbiting Operational Environmental Satellite System (SNPP) [8]. In this research, we use VIIRS images and various strategies. To find the DN threshold for urban areas for multivariate analysis, we categorized NTL images into five classes to establish the relationship between DN and ground cover. We categorized the VIIRS datasets into five classes at their native resolutions of 742 meters. Figures 3 and 4 show the NTL classified image map of Tehran and Tabriz.

Using these thresholds, we classified VIIRS data into two classes: for the city of Tehran, the range is between 0 - 26.6 class one, which is not related to the built-up areas, and the value of 0 is assigned to it, and the range is between 26.6 - 149.25 is the second class, which is related to urban areas and the value of 1 is assigned to it. For the city of Tabriz, the range between 0 - 22.99 is class one (unbuilt areas, and has a value of 0), and the range between 22.99 - 168.64 is the second class (built areas of the city), to which value one is assigned. Figures 5 and 6 show Two-class night light image map for Tehran and Tabriz for 2020.

2.4. Travel Distance Raster Creation

Meaning of travel time is usually specified period of time spent in traveling at work or from the entrance of a business establishment to the place where work is actually done (as in portal-to-portal travel or deadheading) for which compensation may be demanded or paid. The road network provides a third view of the urban area as it measures the connection of space. Therefore, complete and accurate geographic road network data is a valuable data set. Open Street Maps (OSM) provide the spatial data of the road network globally and at no cost [8]. In the present study, we used OSM data because they are readily available. To create the travel distance layer, the OSM platform and ORS command in QGIS software were used. This tool calculates the travel time by introducing the city center to it, without considering any restrictions such as traffic, and based on the speed considered in each route. Finally, the final layer became a raster in ArcGIS software. Figure 7 and 8 show Travel distance raster map for Tehran and Tabriz.

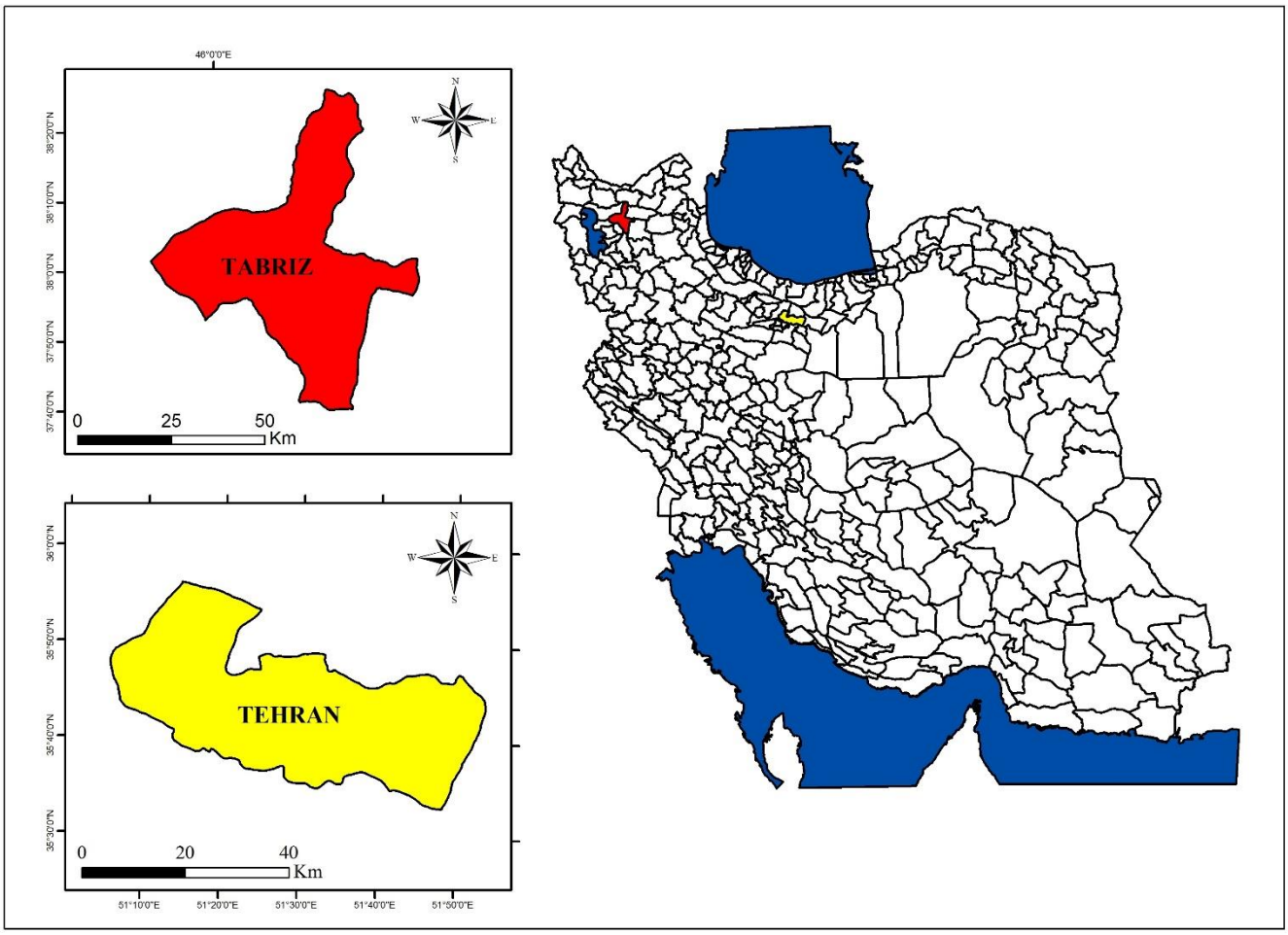

Figure 2. Study area

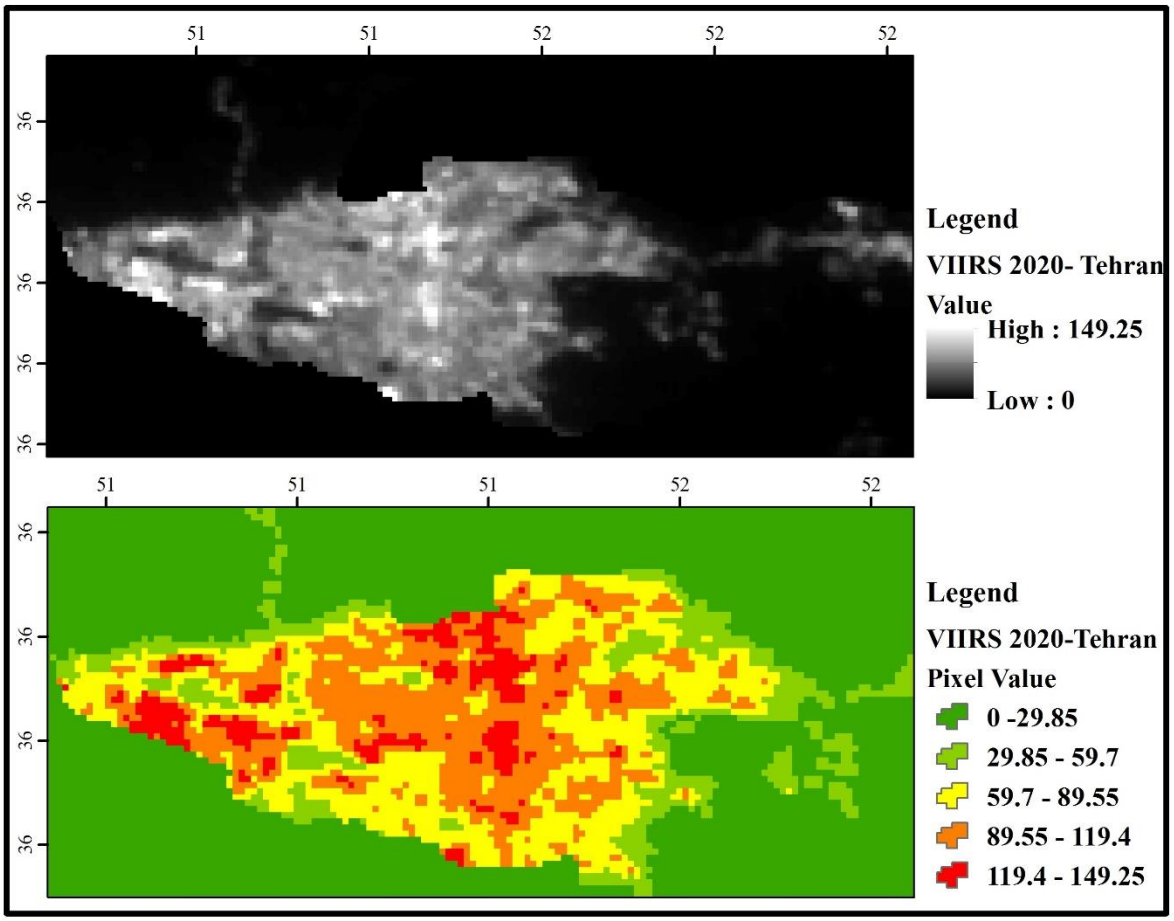

Figure 3. Classified NTL image map of Tehran

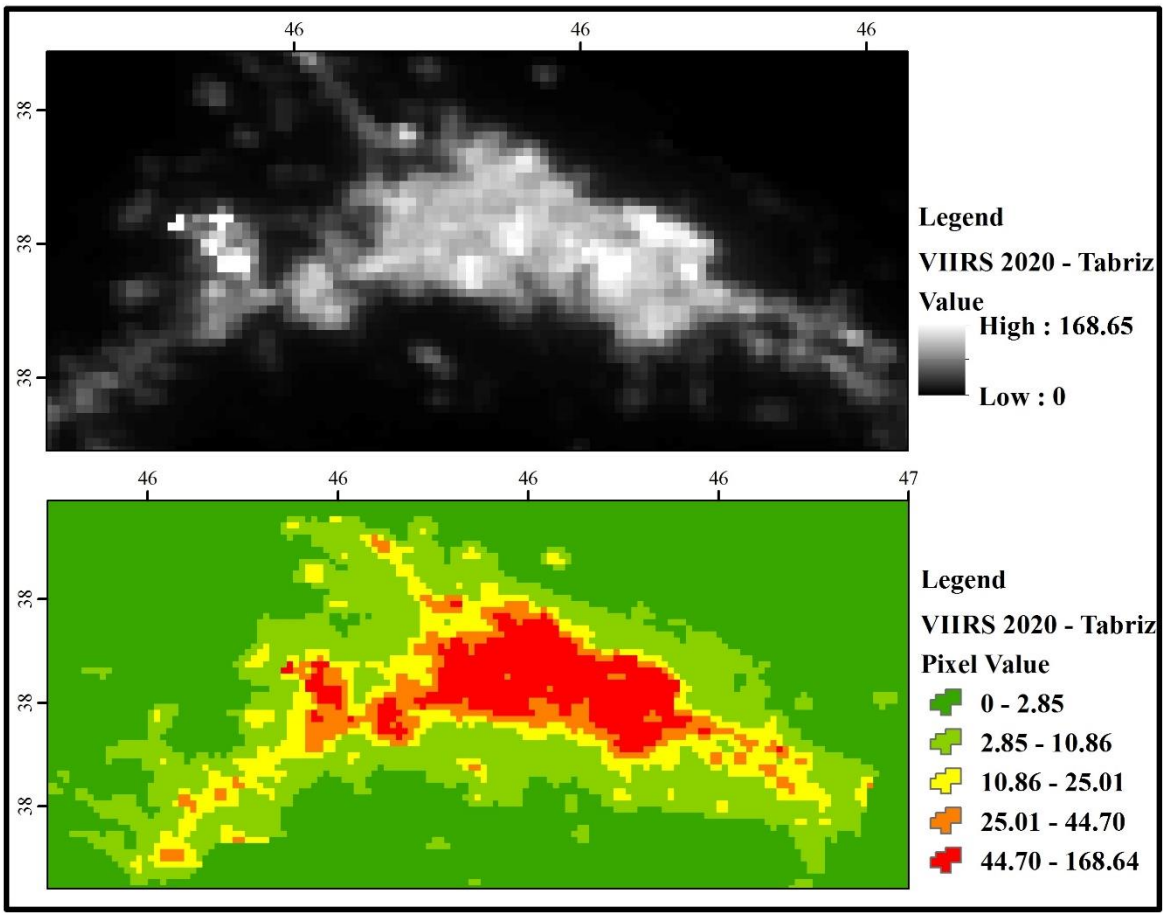

Figure 4. Classified NTL image map of Tabriz

2.5. Fusion of Datasets

After generating three rasters, namely the ground cover layer, the travel time raster, and the night light image, we merged these three layers. A simple sum of three raster is generated according to the following formula:

DNout = DNB + DNNTL + DNTT

Finally, in order to extract the urban boundary, we divided the generated layer into two classes according to the logical threshold. We then selected the largest adjacent urban area, which included the urban core, and converted it to a data vector polygon. Then we adapted it to Google Earth images. These steps are shown in the figure below, respectively. Figure 9 and 10 show Fusion of three datasets (DNTT, DNB, DNNTL) for Tehran and Tabriz in 2020.

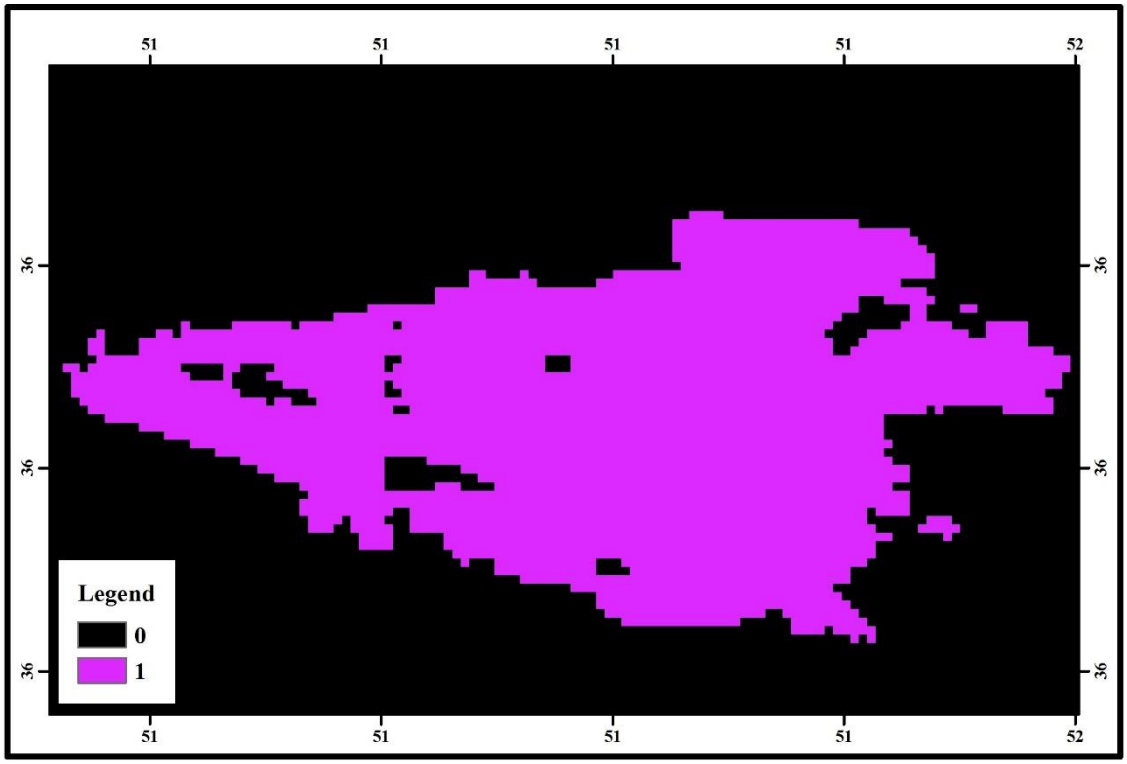

Figure 5. Two-class night light image map for Tehran for 2020

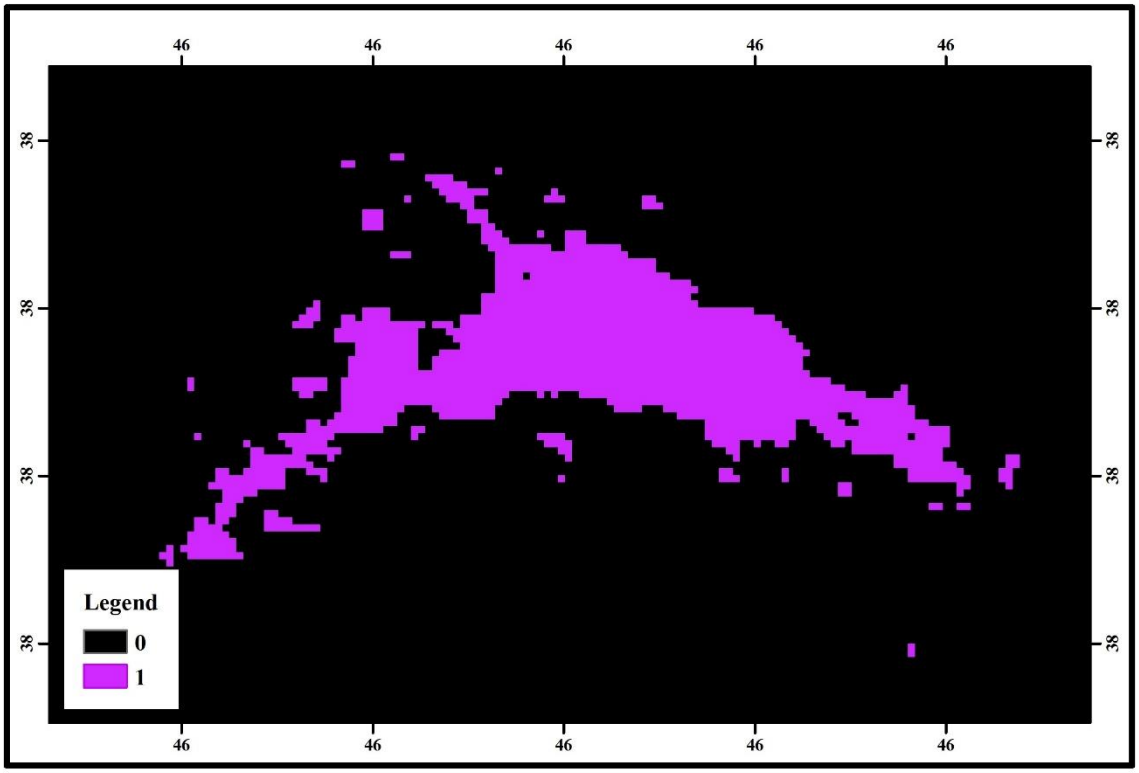

Figure 6. Two-class night light image map for Tabriz for 2020

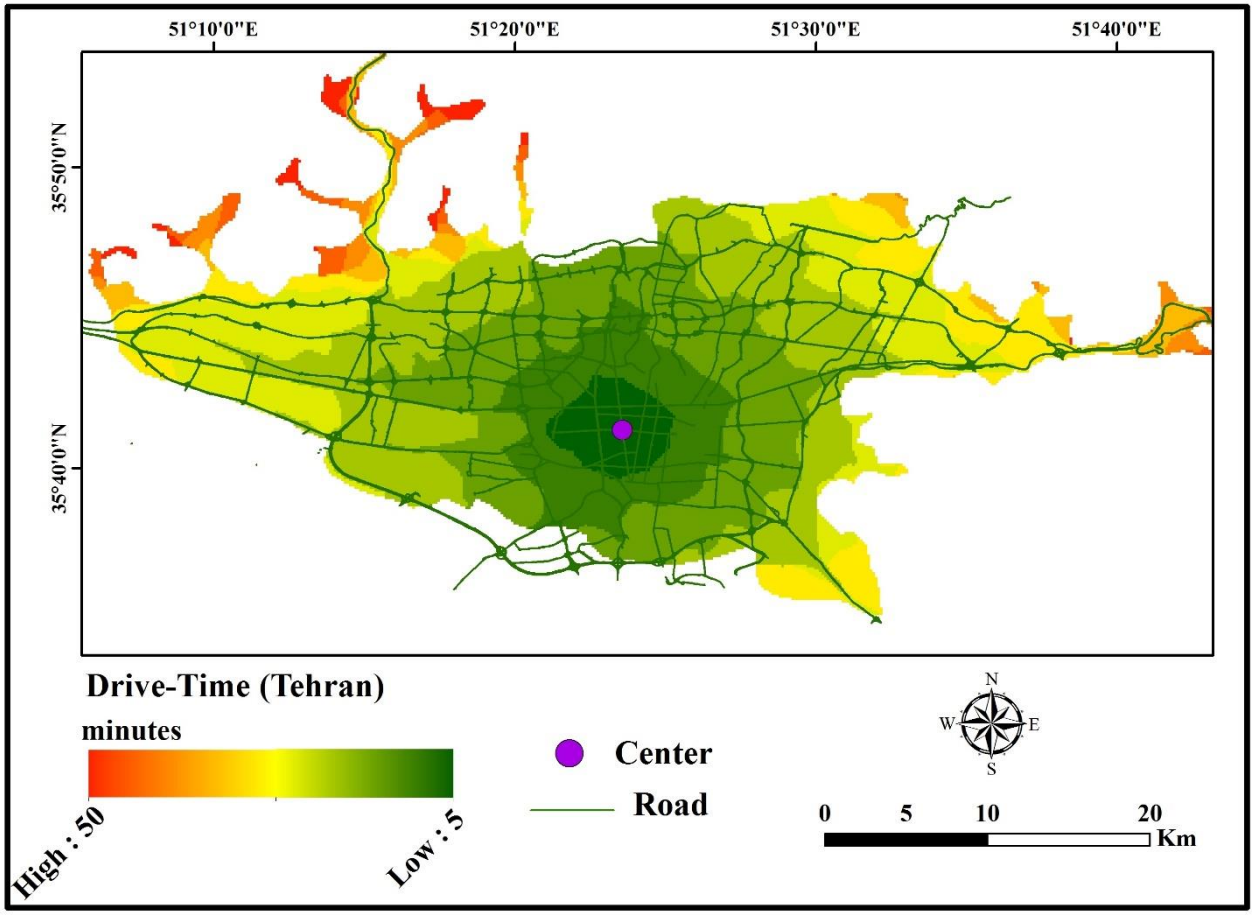

Figure 7. Travel distance raster map for Tehran

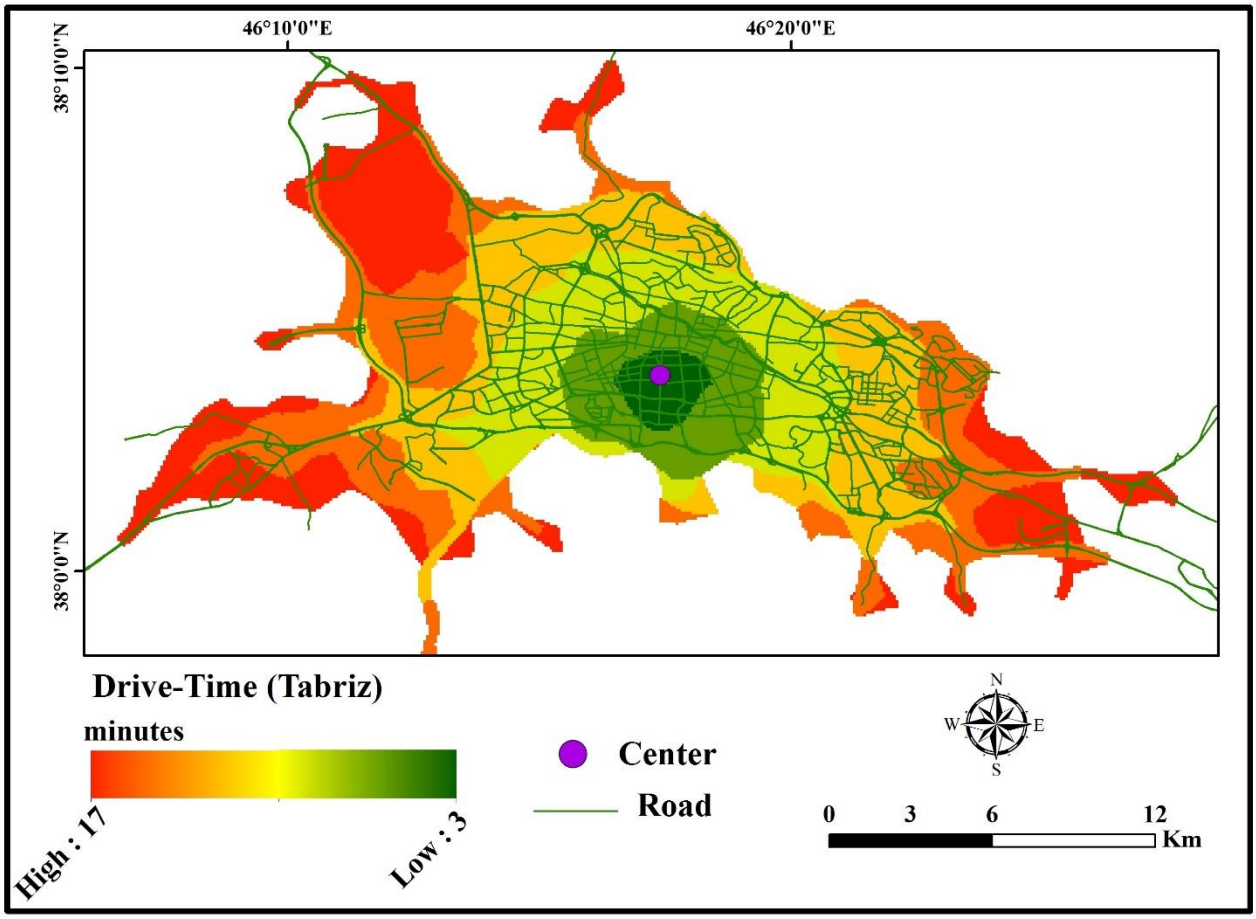

Figure 8. Travel distance raster map for Tabriz

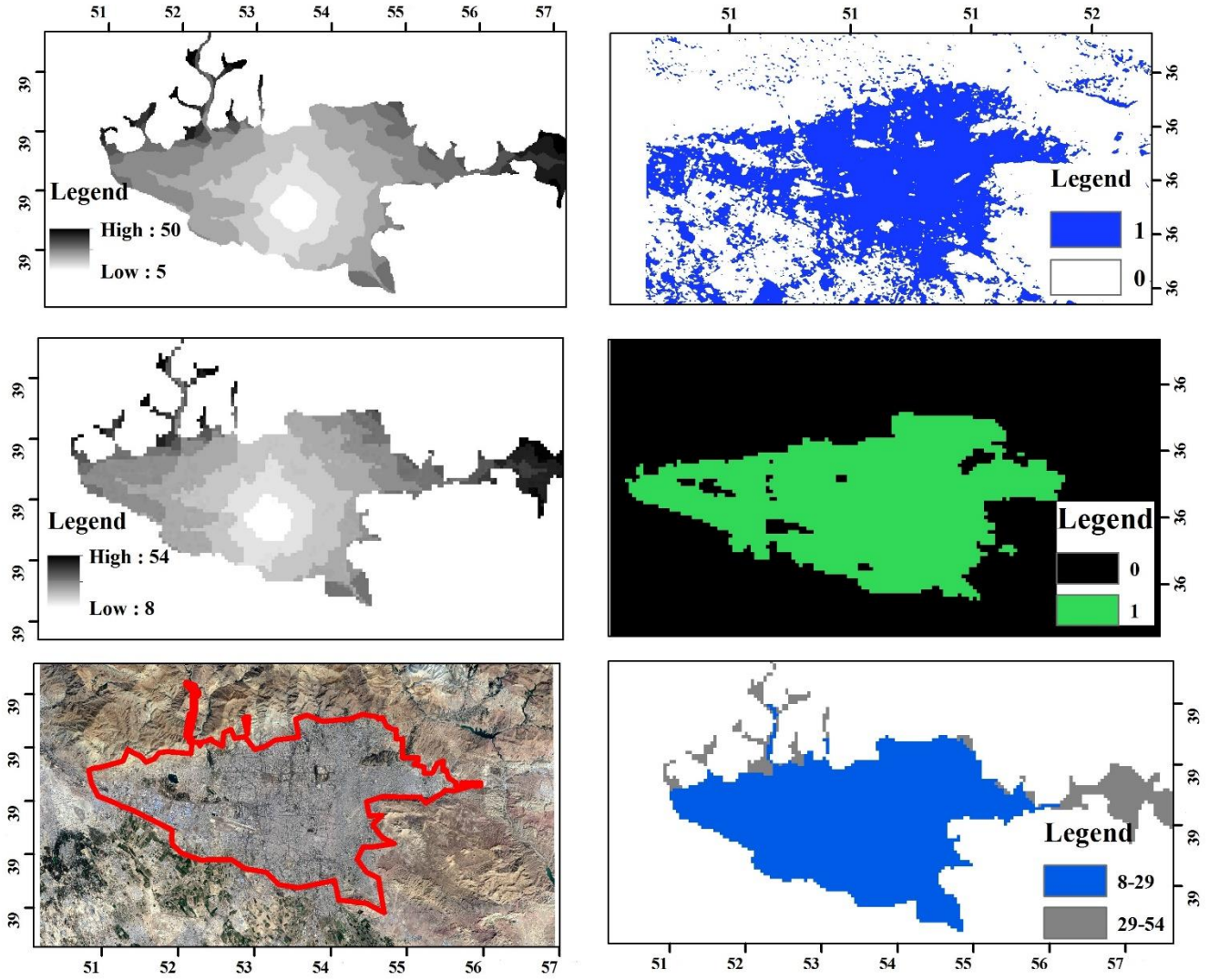

Figure 9. Fusion of three datasets (Tehran in 2020). Plate (A) represents the travel time raster (DNTT), plate (B) represents the built-up area (DNB), plate (C) represents the Nighttime Light classified raster (DNNTL), plate (D) represents the fusion of all three datasets (DNout), plate (E) represents the classified sum with a threshold value 1.5, and plate F represents the largest contiguous urban area boundary

2.6. Light pollution

In the astronomical classification of the sky, there are three categories: dark, marginal and catastrophic. According to the evidence, the capital sky is in the category of a catastrophic sky. What is more important than air pollution, improper and uncontrolled expansion of cities, widespread and uncontrolled use of non-standard lamps, lack of awareness of people in the correct use of light and its means of production and incorrect policies of urban management in using street lighting and Passages have placed Tehran at the top of Iran's polluted cities in terms of light pollution [9]. In order to calculate the level of pollution in the two cities studied, Google earth Engine software was used.

The results obtained in this study also show an increasing trend of light pollution in Tehran and Tabriz between 2012 and 2020. As you can see, in 2012, the central centers of Tehran had moderate light pollution, while in 2020, the amount of light pollution in the central and western regions has increased. Billboard lights, street and highway lights, lighting of urban elements such as flags, statues, stairs, etc., lighting of buildings and towers, recreational places, etc. are among the causes of light pollution. And every year we see a sharp increase in these cases. Figure 9 shows Night light images for Tehran for 2012 and 2020. Also Figure 12 and 13 show Graph of changes in light pollution in Tehran and Tabriz between 2012 and 2020.

Due to the increasing expansion of urbanization and the consequences of urbanization of cities and uncontrolled migration of light has also increased. Although this pollution is not comparable in appearance and sight to the naked eye, but it is an unfortunate environmental reality that lurks in the health of creatures and humans. By using new methods and techniques for measuring the distance, these contaminants can be mapped and appropriate measures can be taken to deal with and reduce them. If in an area with a high degree of light pollution and its negative effects on humans, it may be possible to prevent or relocate endangered individuals and organisms [9].

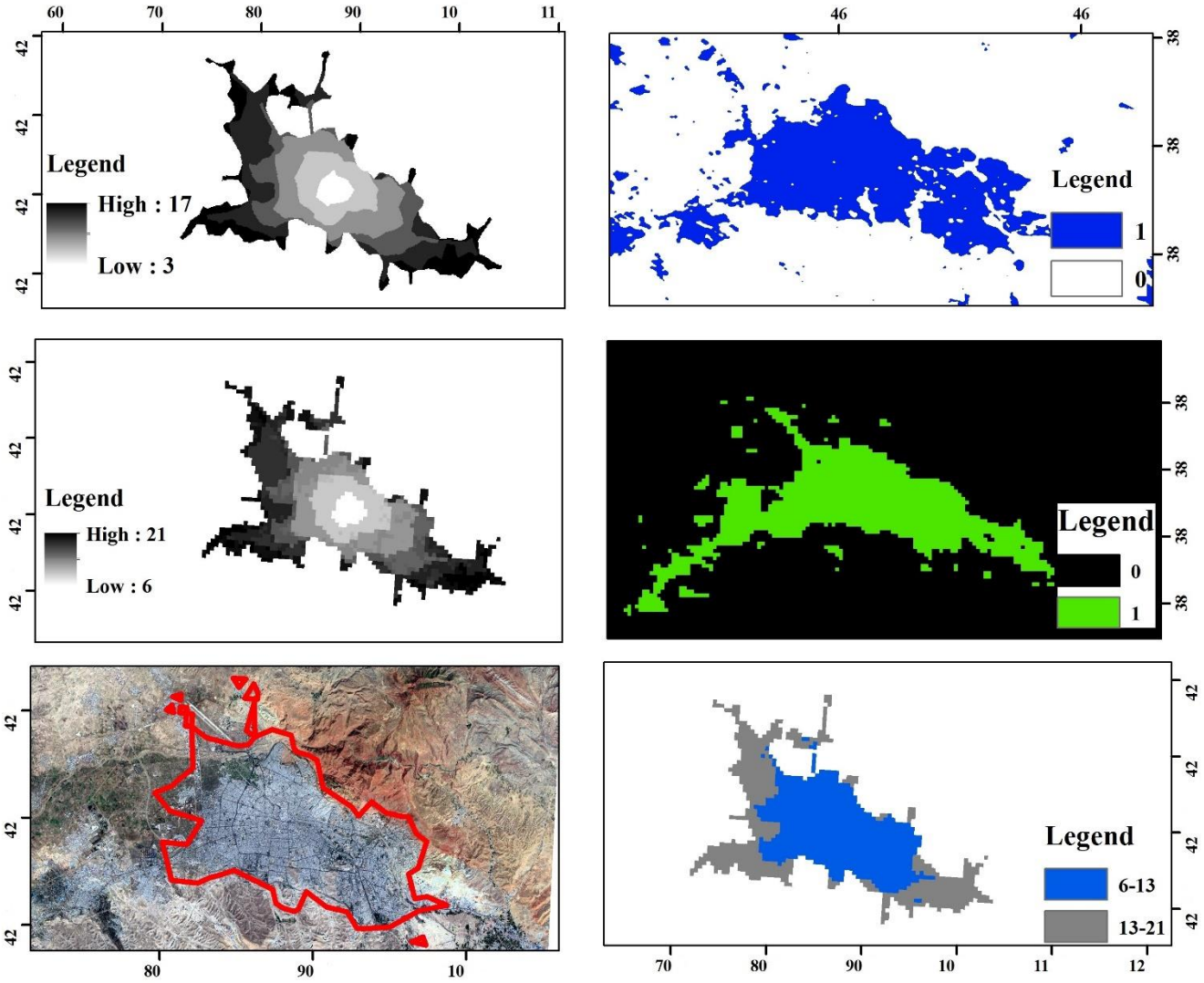

Figure 10. Fusion of three datasets (Tabriz in 2020). Plate (A) represents the travel time raster (DNTT), plate (B) represents the built-up area (DNB), plate (C) represents the Nighttime Light classified raster (DNNTL), plate (D) represents the fusion of all three datasets (DNout), plate (E) represents the classified sum with a threshold value 1.5, and plate F represents the largest contiguous urban area boundary

3. Results

3.1. BUNTUS validation

A little direct validation of BUNTUS is difficult. No other dataset has a separation of time and place for complete comparison. More seriously, the definition of urban sprawl is arbitrary [8]. Our task is to capture urban dynamism. Therefore, we can compare the ranking size of changes from BUNTUS and other datasets. The most commonly used method is direct comparison with urban images. The following figures show the BUNTUS borders of Tehran and Tabriz cities from 2012 to 2020 on Google Earth images, respectively. The maps below show the changes of the urban border in this period in these two cities well. The city of Tehran has expanded from the east and north to other urban areas. The city of Tabriz has also had a gentle growth in all directions. Figures 14 and 15 show the changes in the border between Tehran and Tabriz between 2012 and 2020.

3.2. Urban expansion

The following figures are useful for understanding how urban areas grow over time. For example, the city of Tehran shows more growth on the north side and on the northeast and northwest sides, and the city of Tabriz has been accompanied by growth in almost all directions, albeit with a gentle slope. Figure 16 Shows Boundaries of the urban area of Tehran and Tabriz (2012-2020).

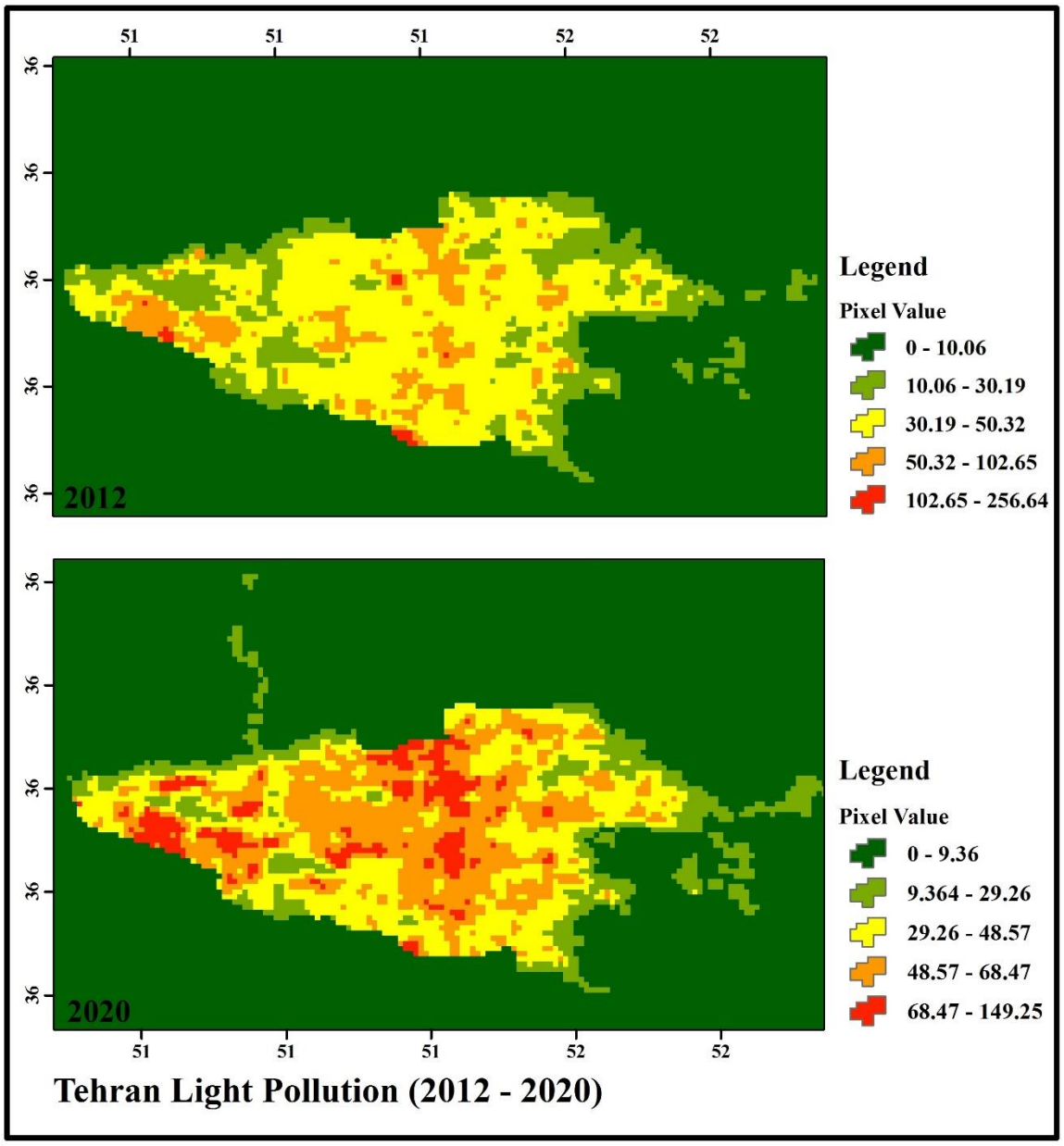

Figure 11. Night light images for Tehran for 2012 and 2020

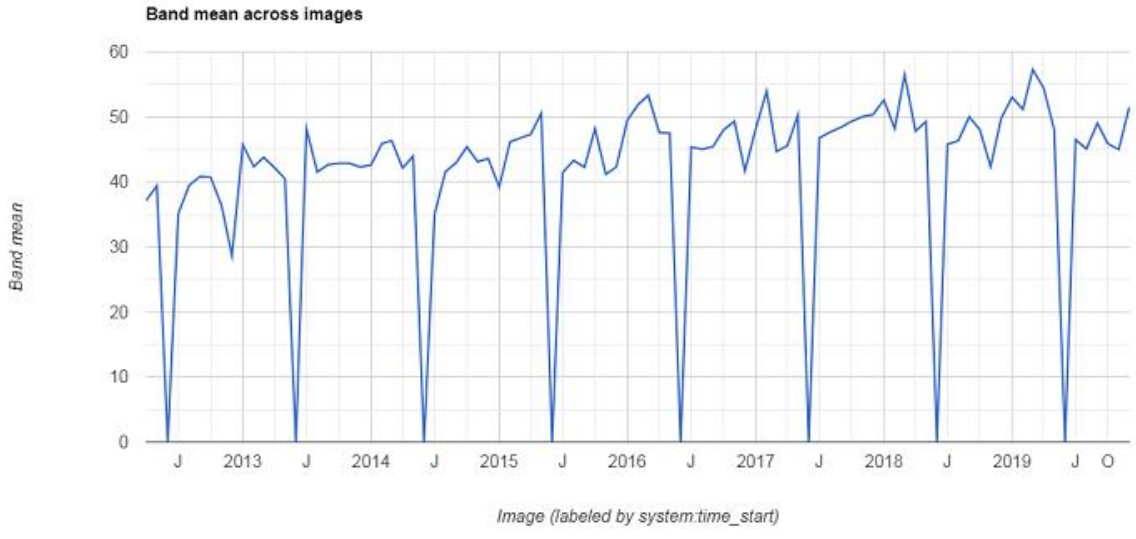

Figure 12. Graph of changes in light pollution in Tehran between 2012 and 2020

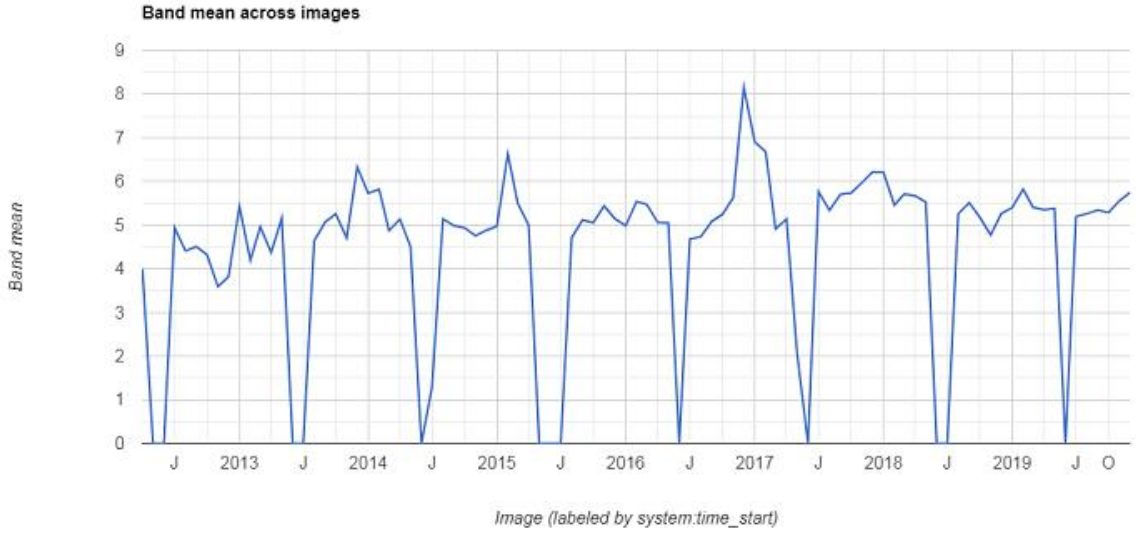

Figure 13. Graph of changes in light pollution in Tehran between 2012 and 2020

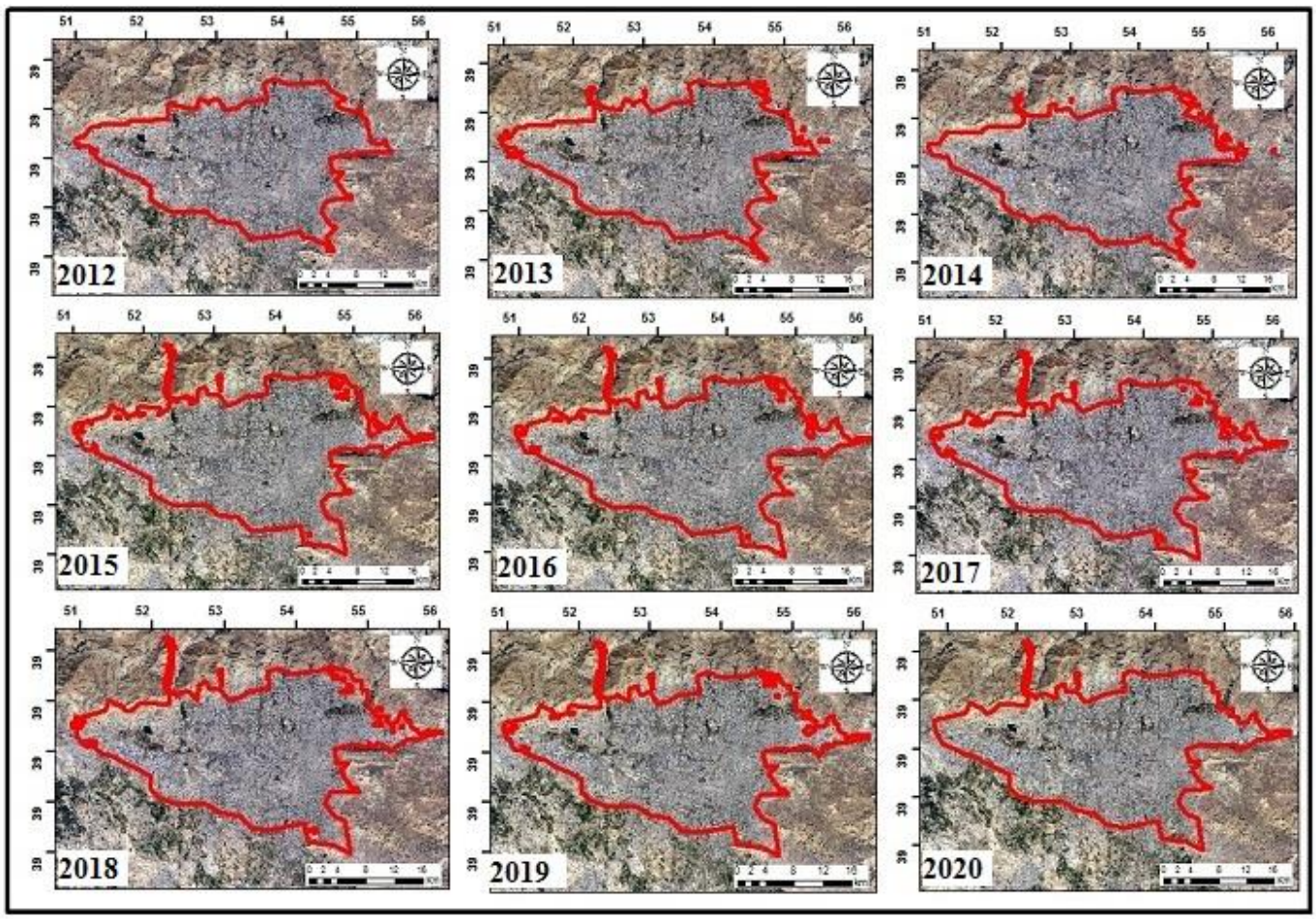

Figure 14. Built-in areas, night light image and travel time raster for urban size borders (BUNTUS) Tehran on Google Earth images from 2012 to 2020

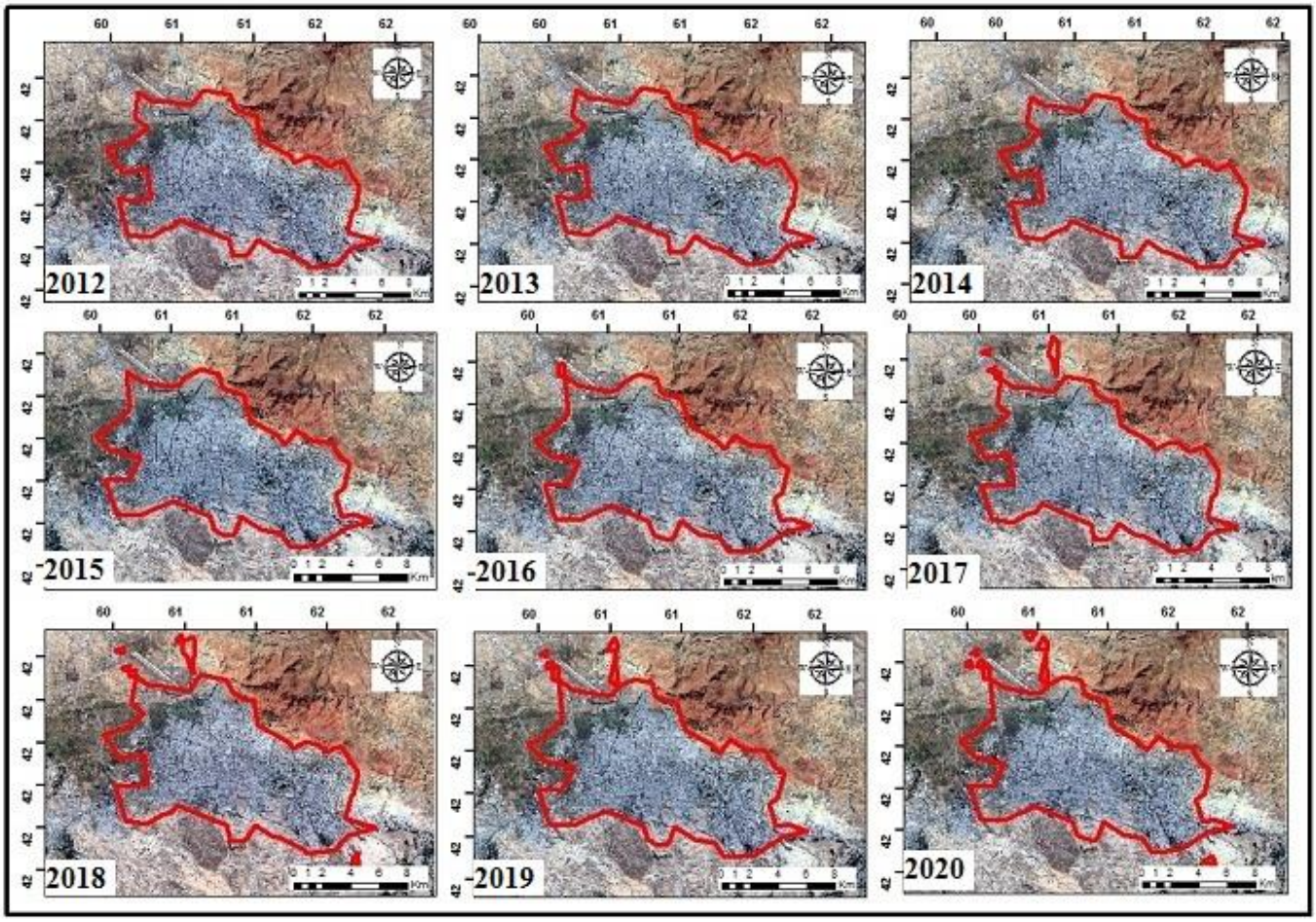

Figure 15. Built areas, night light image and travel time raster for Tabriz city size borders (BUNTUS) on Google Earth images from 2012 to 2020

Generally, urban area does not shrink except during war or natural disasters. We can take advantage of this fact by making the boundary calculation purely additive, i.e., once a pixel is included in a city it remains there. Figure (17) shows the area diagram of Tehran and Tabriz cities from 2012 to 2020. The chart, for both cities, shows continuous annual growth, and only the city of Tehran in 2014 showed more growth than other years. Figure 17 Shows Urban area versus year plot for Tehran and Tabriz.

4. Discussion

T Considering the performance of various algorithms and analyzes regarding the study and modeling of physical growth in the studied cities and its effect on light pollution, we saw that the results showed continuous growth, but with a gentle slope in the studied cities. his program should be kept in mind when evaluating the usefulness of a data set such as BUNTUS. This is true for any urban data set because no single definition is sufficient for all applications, even if there is data to determine it. Our task here is to define an algorithm that is strong, consistent, and efficient enough to define global urban dispersion trends for many cities over decades [8]. The results of this study showed that the metropolises of Tehran and Tabriz did not have significant physical growth in this period. The metropolitan area of Tehran has increased by about 66 square kilometers in this 9-year period and the city of Tabriz by about 5 square kilometers. One of the limitations that can be mentioned is that the BUNTUS algorithm depends on the quality of the data and if the data is of lower quality, the result will be less accurate. For example, due to the unavailability of cloudless satellite imagery, the accuracy of classification made for some areas and years is reduced. Also, the presence of chat in Landsat 7 images for 2012 creates many problems. Although this problem can be largely solved, some processes such as classification on these images are very time consuming and slow. Another limitation is the difference in resolution of the different data sets, resulting in mixed pixels. Though we tried to minimize the effect of mixed pixels when dealing with the coarser resolution datasets by resampling, they still play a role smaller scale. Regarding light pollution, due to its increase from 2012 to 2020, especially in the central parts of the city, plans should be made to reduce or control this type of pollution, which has a great impact on humans, animals, plants, energy.

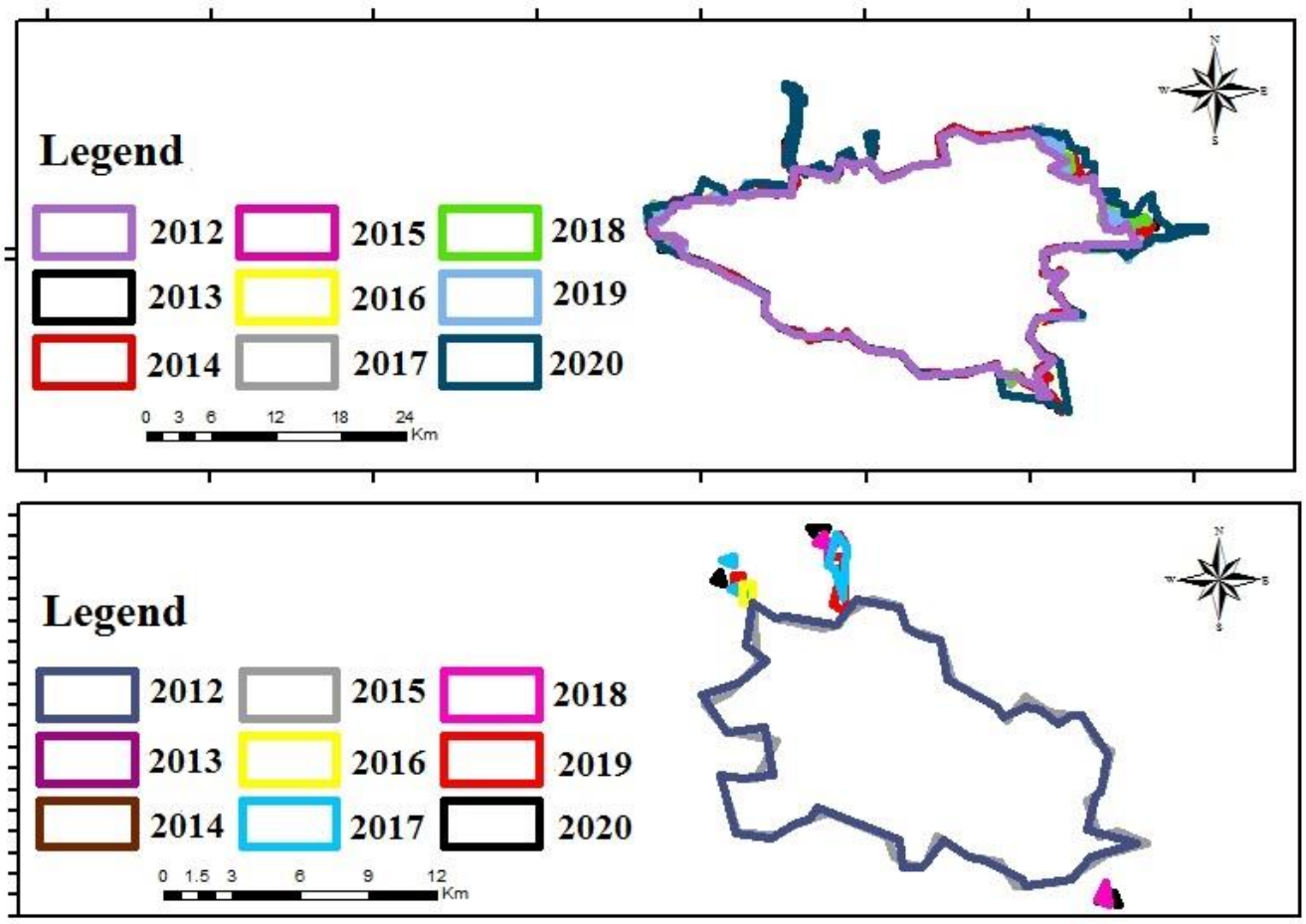

Figure 16. Boundaries of the urban area of Tehran and Tabriz (2012-2020)

Figure 17. Urban area versus year plot

5. Conclusion and Suggestions

With advances in NTL satellite sensors and technologies, NTLs viewed from satellites have emerged as unique geographic data products that measure the brightness of light observed at night from space. This study proposes a set of NTL urban dispersion indices that intend to use quantitative DN values to quantify urban dispersion. These NTL indicators can provide a general idea of urban sprawl and are very easy to calculate, especially for a large group of areas. In this study, efficient methods and algorithms for studying and modeling the physical development of urban areas and the effect of light pollution were investigated. The results

showed that by combining Landsat information, night light image and travel time information, urban growth trend can be studied with high accuracy. This method is relatively robust to the quality and availability of data variables and a fully automatic and general algorithm. The results of the studies on the studied cities showed that the cities of Tehran and Tabriz have had a gentle slope of growth over a nine-year period. The results of studies on light pollution also showed an increase in light pollution from 2012 to 2020 in the studied cities.

The following are suggested from the studies and results obtained in this study:

- More uses of night light images in various projects as a useful source in the fields of economy, urban growth, traffic and ...
- Using the urban budget for the growth of all urban areas and not just a specific area
- Using night light images in environmental fields, especially in the field of light pollution (these images have proven their high efficiency in this field).

Author contributions

Samaneh Bagheri: Conceptualization, Methodology, Software, Data curation, Writing-Original draft preparation, Validation, Investigation, Visualization, **Sadra Karimzadeh**: Conceptualization **Bakhtiar Feizizadeh:** Conceptualization.

Conflicts of interest

The authors declare no conflicts of interest.

References

1. Karimzadeh, S., Miyajima, M., Hassanzadeh, R., Amiraslanzadeh, R., & Kamel, B. (2014). A GIS-based seismic hazard, building vulnerability and human loss assessment for the earthquake scenario in Tabriz. *Soil Dynamics and Earthquake Engineering*, *66*, 263-280.
2. Karimzadeh, S., & Matsuoka, M. (2020). Remote Sensing X-Band SAR Data for land subsidence and pavement monitoring. *Sensors*, *20*(17), 4751.
3. Karimzadeh, S., & Matsuoka, M. (2021). Development of nationwide road quality map: Remote sensing meets field sensing. *Sensors*, *21*(6), 2251.
4. Jaeger, J. A., Bertiller, R., Schwick, C., Cavens, D., & Kienast, F. (2010). Urban permeation of landscapes and sprawl per capita: New measures of urban sprawl. *Ecological Indicators*, *10*(2), 427-441.
5. Kasanko, M., Barredo, J. I., Lavalle, C., McCormick, N., Demicheli, L., Sagris, V., & Brezger, A. (2006). Are European cities becoming dispersed?: A comparative analysis of 15 European urban areas. *Landscape and urban planning*, *77*(1-2), 111-130.
6. Poelmans, L., & Van Rompaey, A. (2009). Detecting and modelling spatial patterns of urban sprawl in highly fragmented areas: A case study in the Flanders–Brussels region. *Landscape and urban planning*, *93*(1), 10-19.
7. Elvidge, C. D., Baugh, K., Zhizhin, M., Hsu, F. C., & Ghosh, T. (2017). VIIRS night-time lights. *International Journal of Remote Sensing*, *38*(21), 5860-5879.
8. Luqman, M., Rayner, P. J., & Gurney, K. R. (2019). Combining measurements of built-up area, nighttime light, and travel time distance for detecting changes in urban boundaries: introducing the BUNTUS algorithm. *Remote Sensing*, *11*(24), 2969.
9. Fardad, M., Yosefi, M. (2011). Evaluation of light pollution, investigation and zoning of its environmental effects using remote sensing and GIS techniques, The 5th National Conference & Exhibition on Environmental Engineering